



UNIVERSITAT DE  
BARCELONA

## Functionalized coatings by Cold Spray for joint prosthesis

Anna Martín i Vilardell

**ADVERTIMENT.** La consulta d'aquesta tesi queda condicionada a l'acceptació de les següents condicions d'ús: La difusió d'aquesta tesi per mitjà del servei TDX ([www.tdx.cat](http://www.tdx.cat)) i a través del Dipòsit Digital de la UB ([diposit.ub.edu](http://diposit.ub.edu)) ha estat autoritzada pels titulars dels drets de propietat intel·lectual únicament per a usos privats emmarcats en activitats d'investigació i docència. No s'autoritza la seva reproducció amb finalitats de lucre ni la seva difusió i posada a disposició des d'un lloc aliè al servei TDX ni al Dipòsit Digital de la UB. No s'autoritza la presentació del seu contingut en una finestra o marc aliè a TDX o al Dipòsit Digital de la UB (framing). Aquesta reserva de drets afecta tant al resum de presentació de la tesi com als seus continguts. En la utilització o cita de parts de la tesi és obligat indicar el nom de la persona autora.

**ADVERTENCIA.** La consulta de esta tesis queda condicionada a la aceptación de las siguientes condiciones de uso: La difusión de esta tesis por medio del servicio TDR ([www.tdx.cat](http://www.tdx.cat)) y a través del Repositorio Digital de la UB ([diposit.ub.edu](http://diposit.ub.edu)) ha sido autorizada por los titulares de los derechos de propiedad intelectual únicamente para usos privados enmarcados en actividades de investigación y docencia. No se autoriza su reproducción con finalidades de lucro ni su difusión y puesta a disposición desde un sitio ajeno al servicio TDR o al Repositorio Digital de la UB. No se autoriza la presentación de su contenido en una ventana o marco ajeno a TDR o al Repositorio Digital de la UB (framing). Esta reserva de derechos afecta tanto al resumen de presentación de la tesis como a sus contenidos. En la utilización o cita de partes de la tesis es obligado indicar el nombre de la persona autora.

**WARNING.** On having consulted this thesis you're accepting the following use conditions: Spreading this thesis by the TDX ([www.tdx.cat](http://www.tdx.cat)) service and by the UB Digital Repository ([diposit.ub.edu](http://diposit.ub.edu)) has been authorized by the titular of the intellectual property rights only for private uses placed in investigation and teaching activities. Reproduction with lucrative aims is not authorized nor its spreading and availability from a site foreign to the TDX service or to the UB Digital Repository. Introducing its content in a window or frame foreign to the TDX service or to the UB Digital Repository is not authorized (framing). Those rights affect to the presentation summary of the thesis as well as to its contents. In the using or citation of parts of the thesis it's obliged to indicate the name of the author.



UNIVERSITAT DE  
BARCELONA

## FACULTAT DE FÍSICA

Departament de Ciència de Materials i Química Física  
H0D02 Enginyeria i Tecnologies Avançades 2013-2016

# Functionalized coatings by Cold Spray for joint prosthesis

Anna Martín i Vilardell

Memòria per optar al Grau de Doctor per la  
Universitat de Barcelona, presentada per  
sota la direcció de Dra. Núria Cinca Luis i  
Dra. Irene Garcia Cano

Barcelona, Novembre 2016



*Per a tots aquells qui han  
cregut i confiat en mi.*



## AGRAÏMENTS / ACKNOWLEDGEMENTS

El present treball va dirigit amb una expressió de gratitud al Centre de Projecció Tèrmica que m'ha acollit durant aquests 3 anys i mig com a part de la seva família i m'ha fet créixer tant en l'àmbit professional com personal, on no només he crescut com a investigadora sinó també com a persona.

He d'agrair de manera especial i sincera al Prof. Josep M<sup>a</sup> Guilemany per haver-me donat aquesta oportunitat dintre del centre i haver confiat en mi en tot moment, i per descomptat a les meves dues tutores, a la Dra. Núria Cinca per tot el seu suport actiu i il·limitada paciència, tanmateix que la seva gran disponibilitat i ganes de tirar sempre endavant, i a la Dra. Irene Garcia per haver-me tingut al seu costat tot aquest temps. A la resta de l'equip del CPT, per descomptat, per estar sempre presents amb el seu constat suport i ajuda.

Voldria agrair al ministeri d'economia i competitivitat pel suport financer del projecte MAT2013-46755-R, tanmateix com a la Universitat de Barcelona per la concessió de la beca predoctoral APIF dintre del departament de Ciència de Materials i Química Física.

Fer extensió de l'agraïment a tot l'equip de professionals dels CCI<sup>TUB</sup> de la Universitat de Barcelona, que sense ells aquesta tesi hagués costat de tirar endavant, com també tota la gent que ha mostrat interès en tots els aspectes relacionats de com el Prof. Müller del Dept. d'electroquímica per tots els seus valuosos coneixements de química i la Gemma del Dept. d'electrònica pel seu ajut en la microscopia de transmissió.

Vull expressar el meu sincer agraïment a tot l'equip del URFOA, en especial a la Dra. Natàlia Garcia-Giralt per haver-me acollit i endinsat en l'àmbit biològic, i sobretot a la Laureta, la Maria, la Marta, la Lara, l'Enrique i l'Ivan per haver compartit tots aquests bons moments que mai s'oblidaràn.

No vull acabar sense fer menció a tot el suport dels meus companys d'escola: tant de batxillerat (Sandra i Marta), d'universitat tant a escala nacional (Tamara) com internacional (Newsha i Latifa), d'idiomes (Àngela i Gemma) i de ball (SwingManiacs), que li han donat aquests anys una perspectiva diferent quan més ho necessitava, tanmateix com el gran assessorament i els bons consells rebuts que m'han guiat fins el dia d'avui (Chris).

Per últim, però no pel que menys, fer menció de tot el suport que m'ha donat la meva família, pare, mare, germana, tiets, cosina i avis, tant en els bons com mals moments, per haver-me escoltat, aconsellat i ajudat a veure la llum quan més ho necessitava...

... a tots GRÀCIES.

# TABLE OF CONTENTS

***Abstract***

***PREFACE***

<b>CHAPTER 1. State of art .....</b>	<b>1</b>
1.1. General considerations .....	3
1.2. Surface treatments and biocompatible coatings: current status .....	5
1.3. Biocoatings market for orthopaedic implants with focus on thermal spray .....	13
1.4. Thermal spray processes .....	16
1.4.1. Conventional technologies .....	16
1.4.1.1. Advantages of conventional technologies .....	17
1.4.1.2. Limitations of conventional technologies .....	18
1.4.2. Cold spray technique .....	19
1.4.2.1. Advantages of cold spray technology .....	20
1.4.2.2. Process parameters of cold spray technology .....	22
1.4.3. Biocoatings via cold spray .....	23
1.4.3.1. Metal biocoatings .....	23
1.4.3.2. Ceramic-based biocoatings .....	26
a) Hydroxyapatite biocoatings .....	26
b) Hydroxyapatite-composite biocoatings .....	29
1.5. Clinical performance .....	31
1.6. Antibacterial/antimicrobial coatings .....	33
1.7. References .....	35
<b>CHAPTER 2. Motivation and objectives .....</b>	<b>51</b>
2.1. Motivation .....	53
2.2. Objectives of the thesis .....	54

**CHAPTER 3. Raw materials and experimental procedure ..... 55**

3.1. Raw materials ..... 57

    3.1.1. Commercial pure titanium powder ..... 57

    3.1.2. Calcium phosphate powders ..... 58

    3.1.3. Ti6Al4V alloy substrate ..... 59

3.2. Methods of powder characterization ..... 60

3.3. Coating production ..... 62

    3.3.1. Thermal spraying techniques ..... 62

    3.3.2. Nanotexturing surface treatments ..... 63

3.4. Methods of coating characterization ..... 63

    3.4.1. Microstructural coating characterization ..... 63

    3.4.2. Mechanical coating characterization ..... 65

    3.4.3. Biological coating characterization ..... 68

        3.4.3.1. Static testing ..... 68

        3.4.3.2. Dynamic testing ..... 70

3.5. References ..... 72

**CHAPTER 4. Results and discussion ..... 75**

4.1. Feedstock powders and substrate ..... 77

    4.1.1. Commercial pure titanium powder ..... 77

        4.1.1.1. Particle size distribution and flowability ..... 77

        4.1.1.2. Particle morphology ..... 78

        4.1.1.3. Particle microstructure ..... 79

        4.1.1.4. Phase composition: X-ray diffraction analysis ..... 80

    4.1.2. Hydroxyapatite powders ..... 81

        4.1.2.1. Particle size distribution ..... 81

        4.1.2.2. Flowability ..... 83

4.1.2.3. Particle morphology .....	84
4.1.2.4. General features of hydroxyapatite particles .....	86
4.1.2.5. Particle microstructure .....	87
4.1.2.6. Phase composition: X-ray diffraction analysis .....	90
4.1.3.7. Phase transformations: Fourier transform infrared spectroscopy .....	93
4.1.3. Ti6Al4V alloy substrate .....	94
4.2. Coatings .....	95
4.2.1. Highly rough titanium coatings .....	96
4.2.1.1. Introduction .....	96
4.2.1.2. Spraying conditions .....	98
4.2.1.3. Coating characterization .....	98
a) Correlation of spraying parameters with bonding features .....	98
b) Particle deformation and interfaces .....	100
c) Microstructure features .....	102
d) Surface features .....	104
➤ Top surface morphology .....	104
➤ Surface topography parameters .....	104
➤ Surface composition .....	112
➤ Surface wettability .....	114
4.2.1.4. Mechanical characterization .....	115
a) Tensile strength test .....	115
b) Fracture surface .....	117
c) Shear strength test .....	119
d) Abrasion test .....	121
4.2.2. Nanotexturing surface treatments on highly rough titanium coating .....	123
4.2.2.1. Introduction .....	123
4.2.2.2. Nanotexturing by anodic oxidation .....	123

a) Introduction .....	123
b) Functionalization by anodic oxidation .....	124
c) Surface features of titanium oxide nanotube layer onto cold gas commercial pure titanium coating .....	125
➤ Top surface morphology .....	125
➤ Surface composition .....	128
➤ Surface wettability.....	131
➤ Surface topography parameters .....	132
4.2.2.3. Nanotexturing by anodic oxidation .....	134
a) Introduction .....	134
b) Functionalization by alkaline treatment .....	134
c) Surface features of alkaline treatment onto cold gas commercial pure titanium coating .....	135
➤ Top surface morphology .....	135
➤ Surface composition .....	136
➤ Surface wettability.....	141
➤ Surface topography parameters .....	141
4.2.3. Hydroxyapatite coatings.....	143
4.2.3.1. Introduction .....	143
4.2.3.2. Spraying conditions .....	146
a) Splat characterization .....	146
b) Hydroxyapatite coatings .....	155
4.2.3.3. Coating characterization .....	160
a) Surface features .....	160
➤ Top surface morphology .....	160
➤ Surface wettability.....	162
➤ Surface topography parameters .....	163
➤ Phase composition: X-ray diffraction analysis.....	167

➤ Phase transformation: Fourier transform infrared spectroscopy .....	169
b) Coating microstructure .....	170
c) Mechanical properties .....	173
➤ Scratch test.....	173
4.2.3.4. Build up of agglomerate hydroxyapatite coating .....	176
4.2.4. Biological properties of the coating .....	181
4.2.4.1. In vitro comparison between low roughness sand blasted and highly rough commercial pure titanium coating by cold spray .....	181
a) Introduction .....	181
b) Cell viability and proliferation.....	184
c) Cell differentiation.....	187
d) Cell morphological aspects .....	188
4.2.4.2. In vitro comparison of different nanotextured treatments onto highly rough commercial pure titanium coating by cold spray .....	189
a) Introduction .....	189
b) Cell viability and proliferation.....	190
c) Cell differentiation.....	193
4.2.4.3. In vitro comparison between commercial pure titanium and hydroxyapatite coatings by cold spray .....	194
a) Introduction .....	194
b) Cell viability and proliferation.....	195
c) Cell morphological aspects.....	197
d) Cell differentiation .....	200
4.2.4.4. In vitro comparison of hydroxyapatite coatings obtained by plasma spray and cold spray.....	201
a) Introduction .....	201

b) Cell viability and proliferation.....	202
c) Cell morphology aspects .....	204
d) Cell differentiation .....	206
4.2.4.5. In vitro dynamic testing of cell attachment onto hydroxyapatite surface .....	207
a) Introduction .....	207
b) Multi-Parametric Surface Plasmon Resonance protein measurement .....	209
c) Multi-Parametric Surface Plasmon Resonance cell measurement .....	210
4.3. References .....	211
<b>CHAPTER 5. Conclusions .....</b>	<b>233</b>
Appendix I: Publications .....	241
I.1. Articles .....	243
I.1.1. Published articles.....	243
I.1.2. Submitted/accepted articles.....	243
I.1.3. To send to journals .....	244
I.2. Congresses.....	244
I.3. Trade secrets .....	245
Appendix II: On the understanding of cold spray .....	247
II.1. Introduction .....	249
II.2. Cold spray systems.....	250
II.2.1. Low Pressure cold spray system .....	250
II.2.2. High Pressure cold spray system .....	250
II.3. Deposition mechanism.....	251
II.4. Particle velocity and critical velocity .....	252

II.5. Influence of spraying parameters .....	253
II.5.1. Gas temperature and pressure .....	254
II.5.2. Stand off distance and spraying angle .....	254
II.5.3. Feeding rate.....	256
II.5.4. Spraying powder size and morphology .....	256
II.5.5. Gas type .....	256
II.6. References.....	257
Appendix III: Refinement of x-ray data .....	259
III.1. Introduction .....	261
III.2. Free profile fitting .....	261
III.3. Rietveld's method .....	262

*Resumen*



## ***Abstract***

The Cold Spray (CS) is a novelty technique for the production of coatings within the field of Thermal Spray. The use of low work temperatures (under the melting point of the material) is what makes it different from the other conventional spraying techniques. CS is an ideal technique to spray materials that are sensitive to temperature, such as nanostructured and amorphous materials, or sensitive to the oxygen, as could be titanium. These characteristics may be specially promising within the field of biomedical coatings. Compared to the conventional processes, it would allow to produce coatings in a more cost-effect and environmental friendly way.

The research is mostly focused on the obtaining of highly rough Commercial Pure Titanium (CP-Ti) and Calcium Phosphate (CP) coatings by CS for joint prosthesis application. An exhaustive development of coating parameter optimization has been developed and the different deposition mechanisms for each feedstock powder were analyzed as well. The mechanical and biological properties of the optimal coatings were evaluated consequently. The mechanical testing (e.g. Tensile and shear strength test and Taber test), was performed on the optimized CP-Ti coating overcoming the ASTM standard specifications for joint, shoulder and knee prosthesis; CP-Ti coating showed good bonding between particles as well with the substrate.

The used of coarse titanium particles provided high roughness ( $R_a=40\pm 12\ \mu\text{m}$  and  $R_z=235\pm 44\ \mu\text{m}$ ) that shows an increase in cell viability, proliferation and differentiation as well as mineralization, in comparison with a low-roughness titanium surface obtained by Sand Blasted (SB). Afterwards, additional surface modification procedures were investigated to obtain nanotextured surfaces on the highly rough as-sprayed CS CP-Ti coatings to evaluate their in-vitro cell response for comparison.

The anodic oxidation treatment leads to a  $\text{TiO}_2$  Nanotube (NT) layer with a pore diameter between 50-100 nm and a roughness of  $R_a=36.8\pm 4.6\ \text{nm}$ , whereas the alkaline treatment leads to a nanosurface of  $R_a=1.2\pm 0.2\ \text{nm}$ , composed by very fine porosity  $<100\ \text{nm}$ . The nanotextured treatments lead to an increase of cell viability in comparison with the as-sprayed CP-Ti coating as well as high cell differentiation due to its nanofeatures.

On the other hand, Hydroxyapatite (HA) coatings were well-deposited by CS without amorphization. Two different HA powders were used as feedstock, a sintered HA powder with a crystalline microstructure, and agglomerate HA feedstock powder with a nanocrystalline microstructure. Both powders show different deposition by CS according to their microstructure; particle deposition of sintered HA powder occurred by slight void collapse and dynamic fragmentation followed by cracking and crushing and reduction in crystal size by plastic deformation mechanisms, whereas agglomerate HA powder a consolidation between particles is caused by the tamping effect produced by the continuous impact of incoming particles onto the already adhered ones, leading to coating build up. Although sintered HA coatings show high cell differentiation, agglomerated HA coatings result in higher cell viability and proliferation, as well as a more homogeneous cell deposition along the coating; agglomerate HA coatings were compared to HA coatings obtained by conventional techniques (e.g. Plasma Spray), and an increase of cell viability and proliferation were observed according to the crystalline HA percentage (CS>PS).

To sum up, CS has shown to be suitable to produce metallic and ceramic coatings for joint applications, especially those dealing with materials that are sensitive to the temperature and oxygen. The non-microstructural changes from the feedstock powder to the coatings leads to a big advantage in CS to obtain customized coatings.

## **PREFACE**

The purpose of this research was to investigate the feasibility and development of functional coatings for orthopaedic joint replacement by means of the Cold Spray (CS) technology. The reason for choosing that theme was to explore the advantages of the technique in order to fulfil and improve the drawbacks that conventional thermal spray technologies have.

Thus, the **first chapter** of the thesis is focused on the state of the art of the CS technology in the biomedical field. It includes the status of the surface treatments and biocompatible coatings. Thermal spraying technologies are explained, emphasizing all the research performed with CS in the field of biocoatings, including its clinical performance as well as all work referring to antibacterial coatings.

In the **second chapter**, the objectives and the motivation to perform the current research are presented.

The **third chapter** entitled "Raw materials and experimental procedure" explains the election of the feedstock powders as well as the substrate. It exposes the list of methods of powder characterization, as well as the coating techniques used and methods of coating characterization and evaluation of properties.

In the **fourth chapter** of the thesis the results are presented and discussed. This chapter is divided in two main subchapters: (4.1) *Feedstock powders and substrate* and (4.2) *Coatings*; this last one is subdivided in subparts: (4.2.1) *Highly-rough titanium coatings*, (4.2.2) *Nanotexturing surface treatments on titanium coatings*, (4.2.3) *Hydroxyapatite coatings* and (4.2.4) *Biological properties of the coatings*. Each system and subsystem includes its own results and discussion as well as its own conclusions.

At the end, the **conclusions** are summed up, followed by the **appendixes**, which include a list of all the publications resulting from this research.

A Spanish summary (**Resumen**) of the thesis is included at the end of the thesis.

All the work presented henceforth was conducted in the Thermal Spray Centre (CPT) of the University of Barcelona in collaboration with the Barcelona Biomedical Research Park.



# CHAPTER 1

***STATE OF ART***

---



## **1.1. GENERAL CONSIDERATIONS**

The massive increase in human aging has affected different areas such as economical, social, and health, especially the last one, with the increase of chronic diseases. It is anticipated that elderly people (+65 years) will reach up to 20 % of European population in 2050, compared with the 10 % of nowadays [1]. For centuries, a diseased tissue was removed to improve marginally the quality of life. With the scientific advances in biomedical field, however, it has led to an increase in human survivability aversely to the quality of tissues, thus the arising need to replace tissues [2]. In terms of orthopedics, more and more patients will require the use of prostheses in order to replace critical parts of the skeletal system.

Current patients' complaint about conventional prostheses includes (i) socket-related problems of discomfort, sores, rashes, and pain, (ii) the difficulties on donning the prosthesis, (iii) the unreliability of prosthesis being securely suspended, and (iv) mobility difficulties. While innovation on new materials with better mechanical and biological properties is day by day carried out through the collaboration of many scientific disciplines, the osteointegration by the surface modification of conventional prosthetic materials can still offer many possibilities for the improvement of bone resorption decreasing the allergenic response. In addition, in many cases, the surgery for prosthesis replacement is extremely aggressive and the cost is high; therefore, whatever solution that can extend the prosthesis life will be very welcomed by clinical community.

The biomaterials field is always under development and has experienced considerable progress especially over the last 60–70 years [3, 4]. The definition of a biomaterial, currently proposed as “a non-viable material, used in a medical device, intended to interact with biological systems,” was definitely established by William in 1987 [5]. The development of biomaterials for medical applications has evolved through three generations, each with a distinct objective (Fig.1.1). Specific familiar terms such as bioinert, bioactive, or biodegradable allow their classification according to their characteristics within the body.

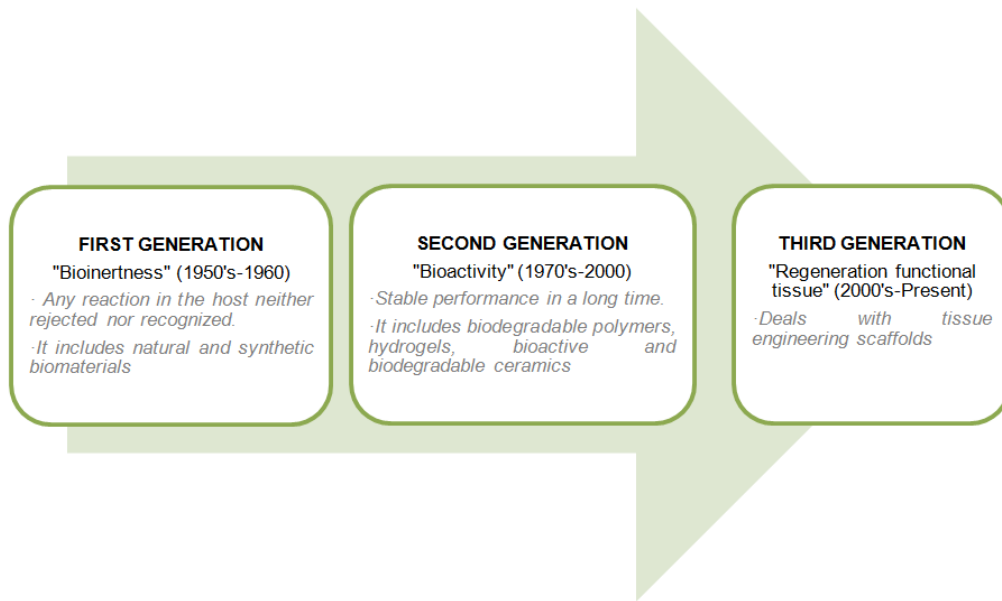


**Figure 1.1.** Evolution of biomaterials science and technology

Bioactive materials are an intermediate between resorbable and bioinert (Fig.1.2) [6]. The first denoted bioactive material was Bioglass®, also known as 45S5 bioactive glass in the late 1960s by Larry Hench [7], and the concept of using synthetic resorbable ceramics as bone substitutes was introduced in 1969 [8]; then, hydroxyapatite (HA) as well as some other glass–ceramics appeared within the market circa 1985s [9, 10]. Bioactive materials are classified in two categories: (i) osteopductive materials, that are recognized by the intracellular and extracellular responses elicited at their interfaces (e.g., Bioglasses), whereas (ii) osteoconductive materials only elicit an extracellular response at their interfaces (e.g., HA). Bioglasses induce integration between bone and implant in the form of a continuous interfacial layer, while osteoconductivity only induces bone growth directly at the implant surface and often results in a fibrous capsule between the implant surface and bone.

The two primary issues in biomaterials are biocompatibility and structural compatibility [11]. Considering the biocompatibility as “the ability of a material to perform with an appropriate host response in a specific application” [5], it implicitly refers two terms: biosafety and biostability, where the material does not have to provoke chronic inflammation/infection that may cause cell death or produce a dysfunction in cellular and tissue matrix [12]. Structural compatibility refers to mechanical properties and becomes especially important for prosthesis biomaterials.

Surface characteristics such as roughness [13] and porosity [14] influence cell attachment and promote bone ingrowth fixation between implant and host tissues due to its structure and free surface. The concept of bioactivity is actually highly related with those characteristics, which will be many times addressed along this work.

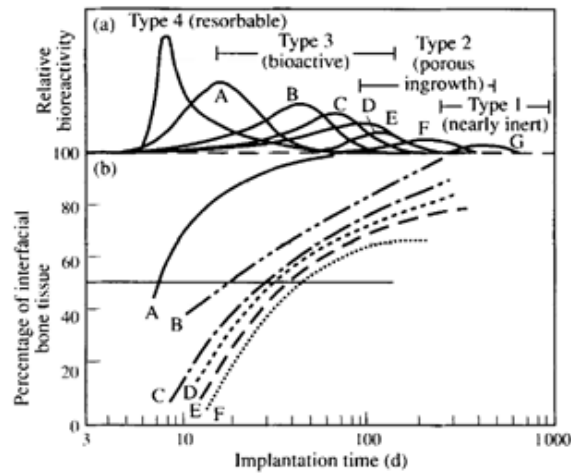


**Figure 1.2.** Bioactivity spectrum for various bioceramic implants: a) relative rate of bioactivity and b) time dependence of formation of bone bonding at an implant interface [A 45S5 Bioglass®, B Mina13 Ceravital®, C 55S4.3 Bioglass®, D A/W glass-ceramic, E HA, F KGy213 Ceravital®] [6]

## 1.2. SURFACE TREATMENTS AND BIOCOMPATIBLE COATINGS:

### CURRENT STATUS

Surface engineering has helped biomedical science to provide better understanding of implant-tissue interactions; the surface modification methods include both the chemical modification and surface roughness as well. The atoms on the surface are more prompt to undergo phase transformations, crystallization, or corrosion (dissolution) processes; this higher energy and higher reactivity are particularly important in view of adsorbates from the biological system. Cellular activity, protein adsorption, or tissue response has been specially induced in titanium (Ti) based alloys by surface roughening, acid treatment, anodization, and coating techniques, i.e., thermal spraying, methods that produce surface topography changes mainly at the microscale level [15]. Other attempts to improve osteoblast activity include the promotion of surface roughness with combined micrometer and nanometer structures such as photo, electron beam, and colloidal lithography or electrochemical anodization [12, 16].

Concerning metal coatings, vacuum plasma spraying (VPS) is, for example, widely used to prepare rough and porous titanium coatings [17–21]. Yang et al. [17] obtained titanium (Ti) coatings on Ti substrates consisting of an outer layer full of macropores with a surface roughness of approximately  $R_a = 100 \mu\text{m}$  (such macropores are reported to be beneficial for tissue ingrowth into the coating), a middle layer consisting of a mixture of micropores and macropores and an inner dense layer. By contrast, however, Borsari et al. [19] used the same technique to produce rough but dense VPS-Ti coatings with the purpose of avoiding as much the reduction in bone density, also known as “stress shielding,” as possible, and thus prolong the prosthesis lifespan. The aim of that study was to investigate the in vitro effect of high roughness ( $R_a = 73.75 \mu\text{m}$ ) and dense Ti surface in comparison with medium ( $R_a = 18.42 \mu\text{m}$ ) and high roughness ( $R_a = 39.64 \mu\text{m}$ ) and open porous coatings. Such new ultra-high rough and dense VPS coating provided a good biological response; at least in vitro, it behaved similarly to the coatings already used in orthopedics. The effect of the coating stability and ultra-high roughness level after surgical implantation and during dynamic bone healing and remodeling has yet to be established. Other titanium coatings for medical devices may include open porosity [17].

Other thermal spray (TS) metal coating attempts include tantalum (Ta) and silver (Ag). Tantalum coatings have an excellent corrosion, good formability, low coefficient of expansion, excellent wear resistance, and excellent biocompatibility and radio-opacity for biomedical applications. Recent in vitro, in vivo, and clinical studies demonstrated that tantalum is a promising bioactive metal [22, 23]. Since tantalum applications in biomedical devices have been limited by processing challenges rather than biological performance, Ta coatings have been achieved via plasma spray (PS) and high-velocity oxy-fuel (HVOF). Optimizing spraying parameters leads to minimum porosity and oxide content but without good corrosion protection [22, 23]; in addition, there are still some drawbacks such the high cost and the high reactivity at temperatures above  $500 \text{ }^\circ\text{C}$  where oxidation causes loss of ductility and cracking of the surface material. Other coatings methods by which tantalum have been deposited include LENSTM (Laser Engineered Net Shaping) [24], sputter deposition [25], chemical vapor deposition (CVD), and electrodeposition.

From another hand, silver has been highlight since ancient times for its antibacterial, antifungal, and antiviral properties; also its compounds, such as silver nitrate and silver

sulfadiazine, have been used for the treatment of burns, wounds, and several bacterial infections [26–28]. Pure silver coatings by different methodologies have been tested with very good results, especially in catheters [29–34]. Using thermal spray methods, however, silver has been co-deposited with many other materials [35–39]. For example, HA/silver composite coatings obtained via VPS proved to combine antibacterial and bioactivity properties; it was found non-cytotoxicity for the coatings and they were covered by bone-like apatite layer after immersed in simulated body fluids (SBF), suggesting that their bioactivity was not affected obviously by the addition of silver in the coatings [40].

Concerning ceramic coatings, plasma-sprayed alumina and zirconia are being used clinically, mostly due to their higher wear resistance than titania. However, alumina and zirconia coatings cannot bind directly to bone tissues due to their bioinert nature, thus limiting their use in hard tissue applications. Moreover, there is a controversy on the binding strength and on particle release from plasma sprayed coatings into the host tissue, caused by either dissolution or fretting. Therefore, the use of bioactive HA coatings produced by plasma spraying (PS) [41–44], high-velocity oxy-fuel (HVOF) [45–47], and flame spray as well [48] was a very successful achievement; in HVOF, particles reach lower temperatures and higher velocities that minimize the time of residence of the particles within the spray beam and therefore its thermal decomposition [1]. HA-coated prosthesis maximizes fixation and decreases the migration of microparticles along the prostheses [49]; they are a good alternative to cemented [50] prosthesis, which have high rates of loosening. In addition, Chern et al. [51] compared the coating–substrate bonding strength of HA with those of other bioactive coatings such as bioglass and bioglass-HA and found that bonding strength was  $33.0 \pm 4.3$ ,  $39.1 \pm 5.0$ , and  $52 \pm 11.7$  MPa for bioglass, bioglass-HA, and HA coatings, respectively. It was demonstrated that after 4 weeks bone ingrowth was significantly higher in bioglass and HA coatings but after 16 weeks only bioglass maintained its high percentages of bone ingrowth while in HA decreased with time [52]. Despite having excellent bioactivity, the mechanical properties of bioactive glasses are worse than those of bioactive HA; this problem can be solved by combining those bioactive materials with metals or polymers to produce a composite coating surface [53]. Cai et al. [54] developed a sintered Co–Cr–Mo/Bioglass composite coating for medical implant application in order to be compared to plasma-sprayed coatings. Those coatings show a more porous structure than plasma spray but less wear resistance. Nevertheless, an adequate bonding between Co–Cr–Mo/ Bioglass composite

coating was achieved and furthermore an apatite layer on top of the coating performed bioactivity. Moreover, more processes are used to fabricate composite bioglass coatings, such as sol–gel [55], electrophoretic deposition [56], and pulsed laser deposition [57].

Even enhanced biocompatibilities are achieved using nanocrystalline ceramics [58, 59]. HA particles' shape has a high influence in cell performance (e.g., needle-shaped particles promote inflammatory reaction, spherical-shaped particles show increased inhibition with time and concentration of those in U2-OS cancer cells, and irregular-shaped particles produce a greater response than spherical-shaped particles).

However, there is still some concern about the uniformity, the adherence of the coatings, and the dissolution rates due to crystalline issues affecting long-term stability. The lack of uniformity is related to the uncontrollable crystallinity within HA plasma coatings, leading to many different phases such as alpha tricalcium phosphate ( $\alpha$ -TCP), beta tricalcium phosphate ( $\beta$ -TCP), tetracalcium phosphate (TTCP), oxyapatite (OHA), and amorphous phases (ACP), whereas the concern on the adherence is attributed to the presence of amorphous phases at the coating–substrate interface. Ceramic bond coats based on zirconia and titania have been plasma sprayed in order to be employed to act as a chemical barrier against in vivo release of metal ions from the implant and improve the adhesive bond [60]. Table 1.1 includes the requirements of HA coatings for implants for surgery specified by different ISO and ASTM standards [61–65].

**Table 1.1.** Requirements of HA coatings for implants for surgery [61-65]

<b>Property</b>	<b>Specification</b>
<b>Ca/P ratio</b>	1.67-1.76
<b>Hydroxyapatite phase</b>	$\geq 50\%$
<b>Limits of specific trace elements</b>	50 mg/kg
<b>TCP, TTCP, CaO phases</b>	$\leq 5\%$ mass fraction
<b>Crystallinity</b>	$\geq 45\%$ of the 100 % crystalline HA
<b>Tensile Strength</b>	$\geq 15\text{MPa}$
<b>Shear Strength</b>	$\geq 22\text{MPa}$

Other coating technologies have also been employed for the production of HA coatings but are less cost effective when compared to thermal spray processes (TS). Table 1.2 shows some advantages and disadvantages of TS compared to such other possibilities.

**Table 1.2.** Advantages and inconvenients of TS to other technologies for HA spraying [66-69]

<b>Technique</b>	<b>Advantages</b>	<b>Inconvenients</b>
<b>Thermal spraying</b>	<ul style="list-style-type: none"> <li>-High deposition rates</li> <li>-Low cost</li> </ul>	<ul style="list-style-type: none"> <li>-Line of sight technique</li> <li>-High temperature induce decomposition</li> <li>-Rapid cooling produces amorphous coatings</li> <li>-Lack of uniformity</li> <li>-Crack appearance</li> <li>-Coating spalling and interface separation between the coating and the substrate</li> </ul>
<b>Sputter coating</b>	<ul style="list-style-type: none"> <li>-Uniform Coating thickness on flat substrates</li> <li>-Dense coating</li> <li>-Homogenous coating</li> <li>-High adhesion</li> </ul>	<ul style="list-style-type: none"> <li>-Line of sight technique</li> <li>-Expensive time consuming</li> <li>-Produces amorphous coatings</li> <li>-Low crystallite which accelerates the dissolution of the film in the body</li> </ul>
<b>Pulsed laser deposition</b>	<ul style="list-style-type: none"> <li>-Coating with crystalline and amorphous faces</li> <li>-Dense and porous coating</li> <li>-Ability to produce wide range of multilayer coating from different materials</li> <li>-Ability to produce high crystalline HA coating</li> <li>-Ability to restore complex stoichiometry</li> </ul>	<ul style="list-style-type: none"> <li>-Line of sight technique</li> <li>-Splashing or particle deposition</li> <li>-Need surface pretreatment</li> <li>-Lack of uniformity</li> </ul>

	-High degree of control on deposition parameters	
<b>Dip coating</b>	-Low cost -Quick technique -Produce complex coat substrates -High surface uniformity -Good speed of coating	-Requires high sintering temperatures -Thermal expansion mismatch -Crack appearance
<b>Sol-Gel</b>	-Can coat complex shapes -Low processing temperatures -Relatively cheap as coatings are very thin -Simple deposition method -High purity -High corrosion resistant -Fairly good adhesion	-Some processes require controlled atmosphere processing -Expensive raw materials -Not suitable for industrial scale -High permeability -Low wear resistance -Hard to control the porosity
<b>Electrophoretic deposition</b>	-Uniform coating thickness -Rapid deposition rates -Can coat complex substrates -Simple setup -Low cost -High degree of control on coating morphology -and thickness -Good mechanical strength -High adhesion for n-HA	-Difficult to produce crack-free coatings -Requires high sintering temperatures -HA decomposition during sintering stage -Substrate must have electrical conductivity
<b>Hot isostatic pressing</b>	-Produce dense coatings -Produce net-shape ceramics -Good temperature control -Homogeneous structure -High uniformity -High precision -No dimensional or shape limitation	-Cannot coat complex substrates -High temperature required -Thermal expansion mismatch -Elastic property differences -Expensive -Removal/interaction of encapsulation material

<b>Ion beam assisted deposition</b>	<ul style="list-style-type: none"> <li>-Low temperature process</li> <li>-High reproducibility and reliability</li> <li>-High adhesion</li> <li>-Wide atomic intermix zone are coating-to-substrate interface</li> </ul>	<ul style="list-style-type: none"> <li>-Crack appearance on the coated surface</li> </ul>
<b>Dynamic mixing method</b>	<ul style="list-style-type: none"> <li>-High adhesive strength</li> </ul>	<ul style="list-style-type: none"> <li>-Line of sight technique</li> <li>-Expensive</li> <li>-Produces amorphous coatings</li> </ul>
<b>Biomimetic coating</b>	<ul style="list-style-type: none"> <li>-Low processing temperatures</li> <li>-Can form bonelike apatite</li> <li>-Can coat complex shapes</li> <li>-Can incorporate gone growth stimulating factors</li> </ul>	<ul style="list-style-type: none"> <li>-Time consuming</li> <li>-Requires replenishment and a constant of pH of simulated body fluid</li> </ul>
<b>Solution deposition</b>	<ul style="list-style-type: none"> <li>-A low-temperature precipitation process resulting in a pure, highly crystalline, firmly adherent HA coating. Good for coating evenly for porous and beaded surfaces.</li> </ul>	<ul style="list-style-type: none"> <li>-Maximum thickness of 20 microns limits its use as a primary mode of fixation</li> </ul>
<b>Electrochemical deposition</b>	<ul style="list-style-type: none"> <li>-Uniform coating</li> <li>-Simply set up</li> <li>-Control morphologies coating</li> <li>-Low temperatures</li> <li>-Coat highly irregular objects</li> </ul>	<ul style="list-style-type: none"> <li>Low tear strength</li> <li>Poor adherence</li> </ul>
<b>Atomic layer deposition</b>	<ul style="list-style-type: none"> <li>-Suitable for preparation nanoscale HA and coating three-dimensional structures where exact film conformality is needed</li> </ul>	<ul style="list-style-type: none"> <li>Poor crystallinity</li> </ul>
<b>Physical vapor deposition</b>	<ul style="list-style-type: none"> <li>-Thin layers</li> <li>-More adherent to the underlying titanium surface than thermal spray</li> <li>less prone to crack formation</li> </ul>	<ul style="list-style-type: none"> <li>Expensive technique</li> </ul>

---

<b>Chemical vapor deposition</b>	-Ability to modulate precursor concentrations during deposition to create functionally graded coatings	Expensive technique
----------------------------------	--	---------------------

---

Some other variations of these types of coatings have been performed using HA–TiO<sub>2</sub> mixtures to improve mechanical properties, i.e., bond strength, fracture toughness, and wear resistance [70–72], fluorapatite–HA mixtures given that fluorapatite offers the potential for lower mineral ion release by dissolution [73], yttria-stabilized zirconia-reinforced HA/Ti–6Al–4V composites which leads to significantly higher mechanical properties than pure HA coatings (even after immersion in SBF solution) [74], Ta/ HA layers to improve the corrosion resistance and biocompatibility [75], Ag–HA mixtures to reduce bacterial adhesion [76–78], or using carbon-nanotube reinforcement imparting strength and toughness to brittle HA bioceramic coating [79].

All these surface modifications have been developed over the past decades to improve the bioactivity mostly of Ti-based implants and their bonding strength to the host tissue. However, although many research groups are still working on this topic, there has been more recently an upgrade on the study of polymer composite materials as an alternative choice to overcome the shortcomings of metals and ceramics [4]. The poly(ether ether ketone) (PEEK), for example, highlights for its biocompatibility, bioinertness, and similar elastic modulus to the bone and their good mechanical properties for hard tissue applications (hip and knee replacements) [80]; other polymers such as poly(lactic acid) (PLA)—bone plates, tendons, and ligaments—and poly-L-lactide (PLLA)—bone plates—stand out for their fully resorbable property; polyurethane (PU) and silicone rubber (SR) get distinguished because of their flexibility in catheters. Some of the attempts to improve the bioactivity of these polymers include coating with tantalum [81], gold, titanium dioxide (TiO<sub>2</sub>), diamond-like carbon (DLC), and tert-butoxides [82].

The bioactivity requirement, depending on the component application, can be also pursued by proper manufacturing routes [83]. In this direction, some researchers have developed human hip joint prosthesis made of fiber-reinforced poly(ether ether ketone) (CF/PEEK) and coated the stem with vacuum plasma-sprayed (VPS) Ti/HA coatings [84]; the mechanical tests of the prosthesis produced by Riner et al. indicated good long-term stability of the bone prosthesis system, while the in vitro and in vivo tests proved no cytotoxicity and necrotic effects in

rabbits. Apart from plasma spraying, HA coatings have been also produced on PEEK substrates by other processes such as RF magnetron sputtering and aerosol technique.

### **1.3. BIOCOATINGS MARKET FOR ORTHOPAEDIC IMPLANTS WITH FOCUS ON THERMAL SPRAY**

As shown in figure 1.1, after the first generation of loadbearing implants (cortical bone substitution) using bioinert materials [stainless steel 316L, cobalt chromium alloy, titanium, or titanium alloy (Ti6Al4V)], the second generation involving surface treatments emerged prominently in 1985 with the first HA-coated femoral prosthesis (Furlong®, JRI, London, UK) [85]. In general, in vitro and in vivo studies indicate that bioactive biomaterials' application in biomedical field increases the long-term durability of prostheses. Since first clinically reported trials of HA coatings on femoral stems, HA coatings were extensively used in dental and orthopedic prosthesis [86]. HA coatings are currently being used in total hip [87, 88] and knee [89] replacement implants, ankle and shoulder implants, and screws and pins in bone plates for fixing bone fractures. Medical studies were undergone in acetabular cups for total hip arthroplasty [90] and tibial component for total knee arthroplasty [91] at a minimum duration of follow-up of 5 years comparing different fixations like HA coatings, porous surfaces, and cemented fixations. HA coating surfaces stabilized after an initial period of early migration, whereas cemented components showed an initially lower but over time continuously increasing migration. Some of the biomaterials used in skeletal system applications are listed in table 1.3 together with medical market.

**Table 1.3.** The human impact and the size of the commercial market for biomaterials and medical devices [3]

<b>Application</b>	<b>Biomaterials used</b>	<b>Number/year</b> – <b>World (or World</b> <b>Market in US\$)</b>
<b>Joint replacements (hip, knee, shoulder)</b>	Titanium, stainless steel, polyethylene	2,500,000
<b>Bone fixation plates and screws</b>	Metals, poly(lactic acid) (PLA)	1,500,000
<b>Spine disks and fusion hardware</b>	-	800,000
<b>Bone cement</b>	Poly(menthyl methacrylate)	(\$600M)
<b>Bone defect repair</b>	Calcium phosphates	-
<b>Artificial tendon or ligament</b>	Polyester fibers	-
<b>Dental implant-tooth fixation</b>	Titanium	(\$4B)
<b>The biomaterials and healthcare market: Facts and figures (per year)</b>		
<b>Total US healthcare expenditures (1990)</b>		\$714 billion
<b>Total US healthcare expenditures (2009)</b>		\$2.5 trillion
<b>Total US health research and development expenditure (2009)</b>		\$139billion
<b>Number of medical device companies in the US</b>		12,000
<b>Jobs in the US medical device industry (2008)</b>		425,000
<b>Sales by US medical device industry (2008)</b>		\$136 billion
<b>World medical device market forecast for 2013</b>		\$286 billion

At the moment, some of the successful bioactive coatings for implants have been produced by electrodeposition and plasma spraying: Peri-apatite™, Biomet's Osteocoat®, and Corail®, among the most important. Other successful approaches have been (i) the development of a macro-sized interconnected porosity in the range of 100–500 μm within a metal coating with the aim to promote proper bone ingrowth, i.e., Regenerex™, Trabecular Metal™, and Arcam AB Trabecular Structures™ and (ii) nanoscale topographies, i.e., OsseoSpeed™ and Nanotite™. Table 1.4 presents some of the characteristics of the current commercial orthopedic implants [92].

**Table 1.4.** Surface description of some of the commercial orthopedic implants [92]

<b>Manufacturer</b>	<b>Surface description</b>
<b>Biomet</b>	-Regenerex™: porous Ti alloys -RoughCoat™: sintered Co-Cr bead porous coating with and without plasma-sprayed HA
<b>DePuy</b>	-Oription™: porous coating, porous pure Ti alloy coating -Purocoat®: porous coating, sintered Co-Cr beads -Duofix® HA: plasma sprayed HA over Purocoat® coating
<b>Smith &amp; Nephew</b>	-Stikite: porous three-dimensional asymmetric Ti powder coating -RoughCoat™: sintered Co-Cr bead porous coating with and without plasma-sprayed HA
<b>Stryker</b>	-PureFix™ HA: plasma-sprayed HA -Peri-Apatite™: solution deposited HA coating that uniformly coats three-dimensional porous ingrowth surfaces -Plasma sprayed CP-Ti with and without PureFix™ HA coating -Arc-deposited CP-Ti with PureFix™ HA coating
<b>Zimmer</b>	-Trabecular Metal™: open cell porous tantalum construct -CSTi™, Cancellous-Structured Titanium™ coating with and without plasma-sprayed HA coating -Fiber metal: Ti fiber with and without plasma-sprayed HA/TCP coating -CoCr-beaded ingrowth surfaces
<b>Arcam AB</b>	-Trabecular Structures™ : titanium deposition via Electron Beam Melting (EBM)
<b>Astra Tech AB</b>	OsseoSpeed™: grit blasting titania (TiO <sub>2</sub> ), followed by hydrofluoric acid (HF) treatment
<b>BIOMET 3i Implant Innovations</b>	Nanotite™: CaP nanoparticle features

## 1.4. THERMAL SPRAY PROCESSES

### 1.4.1. CONVENTIONAL TECHNOLOGIES

TS is a group of techniques to produce metallic and nonmetallic coatings where the feedstock is sprayed in molten or semi-molten state onto a prepared substrate. Their basic principle is to impart sufficient kinetic and thermal energy to the raw material (in powder, wire, or rod form) to create a confined high-energy particle stream and propel the energetic particles toward the substrate. Through the solidification of the droplets on impact with the substrate, they create cohesive bonds with each other and adhesive bonds with the substrate; many different spraying parameters need to be optimized to produce suitable coatings for the desired applications (Fig.1.3).

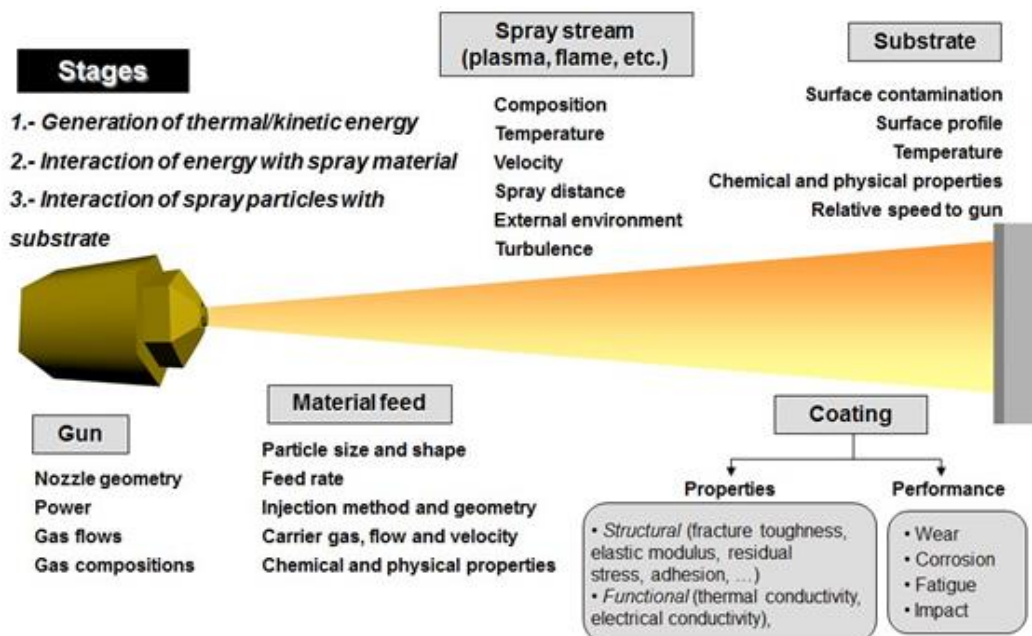


Figure 1.3. Variables and stages of coating formation in conventional thermal spray processes

The particles are heated by electrical (air plasma or arc wire spraying) or chemical (detonation gun, flame spraying, or high-velocity oxy-fuel) means. Droplets impact and start bonding onto the substrate due to high cooling rate, typically excess of  $10^6$  K/s for metals [93–95]. Coating properties directly depend on particle temperatures and speeds, which produce thin layers of lamellas, often called “Splats” that finally build up the deposit. There are three types of bonding mechanisms at interface substrate–coating, being predominant the mechanical bonding followed by metallurgical ones [95]:

- Mechanical bonding, particles, molten or semi-molten, impact onto surface substrate (previously grit-blasted), and remaining adhered due to its roughness.
- Metallurgical bonding, given by the occurrence of interdiffusion processes between substrate–coating and even though the formation of one new compound such as intermetallic phases.
- Physical bonding, reached by Van der Waals forces between substrate–coating.

Thermal spraying techniques are divided into three subgroups according to the energy source (Fig.1.4), and the selection of the appropriate spraying method will be determined by coating material characteristics, coating performance requirements, economics, and part size and portability.

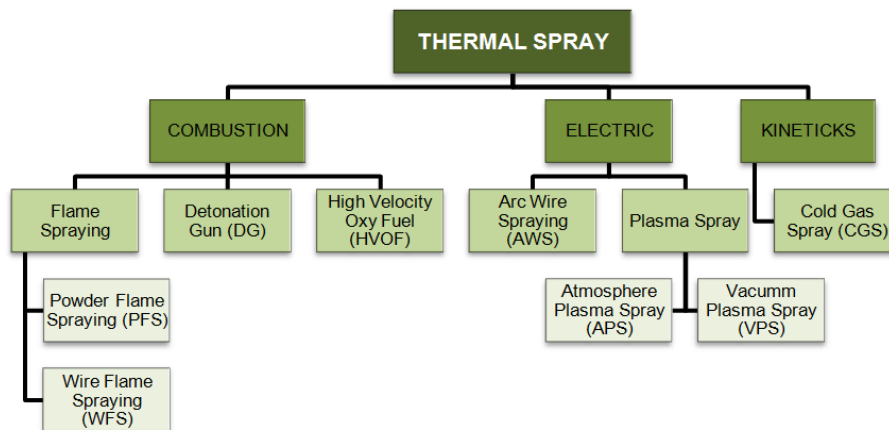


Figure 1.4. Schema of TS techniques according to energy source

#### 1.4.1.1. Advantages of conventional technologies

A big advantage of thermal spray processes is the ability to deposit an extremely wide range of materials. Virtually, any material that has a stable molten phase can be deposited, and even some materials that do not melt, such as graphite and many carbide or boride ceramics, can often be co-deposited with another sprayable material to create a composite coating material. Another one is that the range of suitable substrate materials is even greater than the range of sprayable materials. In addition to metals, ceramics, glasses, and polymers, thermal spray coatings have been successfully applied to many other substrate materials including wood. Conventional thermal spray also offers the advantage of high deposition rates, which are orders of magnitude higher than those of most alternative coating technologies, such as

electroplating or vapor deposition, where deposition occurs at the atomic or molecular level. When the objects to be coated are very large or difficult to move, the ability to apply coating in situ is also an advantage. Furthermore, coatings can be applied without significant heat input and it is possible to strip off and recoat worn or damaged coatings without changing part properties or dimensions. Further advantages of thermal spraying include its rapid coating deposition, low cost, high efficiency, and rapid execution process.

Although all the techniques exposed in Table 1.2 are suitable to produce bioactive HA layers, only thermal spraying, in particular plasma spraying, is the commercially accepted method by Food and Drug Administration (FDA), the USA for producing HA coatings [96].

#### **1.4.1.2. Limitations of conventional technologies**

TS deposition features depend on the used technique and the thermal and kinetic applied energy will be different. High temperatures cause oxide inclusions (overcoat metallic materials) as well as decomposition/degradation in oxygen-sensitive materials such titanium or HA, respectively. Oxide inclusions improve mechanical properties like wear resistance and hardness, but an excessive presence at intersplat regions leads to cohesive failure and wear debris [97]. Processes that minimize heating of the spray material, such as HVOF and D-Gun, typically result in lower oxide concentration and minimal changes in alloy chemistry. Also, the controlled inert atmosphere of VPS creates very little or no oxide during the deposition process; however, some changes in the alloy chemistry may still occur due to relatively high temperatures in the plasma jet. High porosity could be beneficial in some applications like in the case of prosthesis to promote a good bone ingrowth; conversely, excessive porosity can also be a problem if the coating is intended to protect the underlying substrate from species that can cause corrosion or other problems. Porosity depends moreover on size particle distribution and spray distance, producing “unmelted” particles according to their inertia when are fed into the plume. Also, low-velocity processes tend to have higher level of porosity in the range of 5–15 % volume, and higher velocity processes origin coatings with less porosity (3–8 % volume). Another limitation is the introduction of residual stresses that limit the maximum thickness due to the solidification of droplets when they cool down [98]. Finally, the deposition is limited to surfaces in a direct line of sight of the spray gun.

Cold spray (CS), a novel spray technique in the late 1980s, mainly arises from the limitations of some coating types of thermal spray that seem to be overcome for some materials. CS is a low-temperature process based on the plastic deformation of the spraying material, and it is suitable for the deposition of oxygen-sensitive materials or for temperature-sensitive materials like nanostructured and amorphous powders [97–100]. Moreover, it should also be noticed that, compared to the conventional thermal spray technologies and other coating alternatives like painting and electrodeposition, CS is an environmentally friendly approach since its effluents are easy to control and dispose and it is a non-combustion process.

### **1.4.2. COLD SPRAY TECHNIQUE**

CS is the newest recent spray technology from the thermal spray family from 1980s; it is based on the kinetic energy and stands above conventional spray techniques for its low temperature rates. Small particles (5–50  $\mu\text{m}$ ) are accelerated by a pre-heated gas temperature (25–1100  $^{\circ}\text{C}$ ) lower than the melting point of the material and propelled toward a prepared substrate at supersonic velocities (300–1200 m/s). Supersonic flows from gas dynamics are obtained within nozzle with the principal purpose to maximize the thrust and obtain a better coating quality. Nozzle design influences on particle velocity, depending basically on the type of nozzle and its geometry. From the three basic nozzles, convergent-barrel (CB nozzle), convergent-divergent (CD nozzle), and convergent-divergent-barrel (CDB nozzle), the one which achieves a higher particle velocity is CD nozzle, known also as Laval nozzle with its conical geometry.

Particle binding is made by kinetic energy when particle impacts onto a surface causing plastic deformation [98], becoming particle velocity an important parameter. Due to high kinetics, CS is able to produce quality dense coatings. However, depending on the spraying conditions, it is possible to obtain porous coatings if the application requires it. Figure 1.5 shows the schema of CS technique.

Instantly, the feedstock located in the feeder is propelled by gas (normally nitrogen) and pre-heated gas (nitrogen, air or helium) at determinate temperature and pressure, into the spray nozzle, to propel particles at high velocities to build up the coating. Stages of coating formation are shown in figure 1.6 [101].

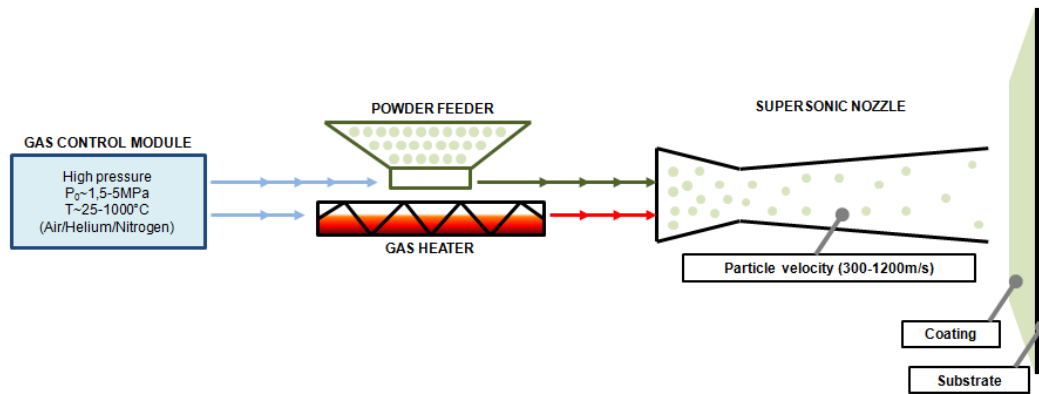


Figure 1.5. Schema of CS technique

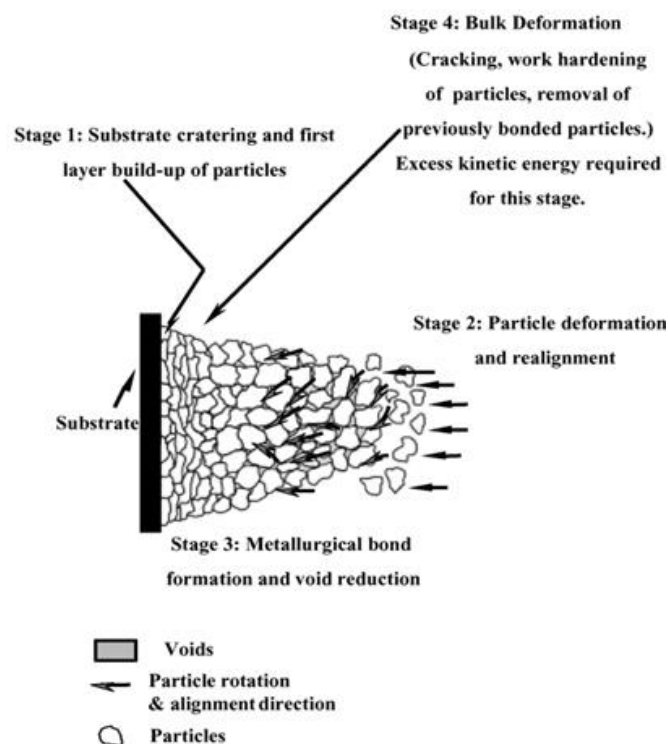


Figure 1.6. Stages of coating formation in the cold spray process [97]

### 1.4.2.1. Advantages of cold spray technology

The main advantage of the CS process is that it is a solid state process, which results in many unique coating characteristics. High deposition efficiency values have been achieved with metals, alloys, and composites; high deposition rates can produce a thick coating in a single pass (1–2 mm) due to its typical spray beam of about 10 mm diameter [98].

CS can be viewed as a triplex process (grit blast, spray coat, and shot peen), as expected to be caused by the velocity Gaussian distribution across the spray beam; flexibility in substrate–coating selection is good to produce coatings that could lead to unacceptable interfaces in PS or HVOF, i.e., intermetallic phases between Cu–Al with PS; minimum thermal input to the substrate facilitates the use of temperature- and oxygen-sensitive materials such as magnesium, titanium, and polymers. Moreover, residual tensile thermal stresses remain in a TS coating produced by a conventional process, whereas CS induces stresses mostly in compressive nature across the entire coating thickness, which improves mechanical properties such as fatigue. However, some investigations confirm that in specific cases neutral and tensile stresses may appear to be depending on substrate/coating combination and surface treatment. Suhoen et al. [102] deposited aluminum, titanium, and copper onto carbon steel, stainless steel, and aluminum substrates with different surface treatments. It has been shown that compressive residual stresses predominate in copper deposition onto the majority of the specimens; also titanium coatings may show compressive, neutral, or tensile residual stresses depending on the substrate; by contrast, aluminum coatings exhibited tensile residual stresses onto all the substrates.

Furthermore, compressive residual stresses may be detrimental if relatively thick coatings are sprayed onto thin substrates and they produce their deformation; also, they have to be taken into account in the case that they promote tensile stresses to the substrate. Therefore, residual stresses should be considered in any application where structures are required to carry load.

It has been demonstrated that metals, polymers, ceramics, and composite materials are able to be applied with CS technology in a wide range of applications that are in constant development, such as those involving corrosion protection, repairing structures, catalyst deposition, electromagnet transition, and electronic and medical devices [103, 104].

Depending on spraying materials' properties, grid blasting could be a good option to improve particle attachment onto substrate if a mechanical anchoring effect contributes in the bonding mechanism [105–107]. However, it might be detrimental if this induces hardening of the substrate surface since it would change the mechanical surface characteristics [108–110].

### 1.4.2.2. Process parameters of cold spray technology

The actual mechanism by which the solid particles deform and bond during CS is still not well understood. Particles undergo an extensive plastic deformation when impact onto the substrate, which results in the creation of jets, known as adiabatic shear bands (ASB), in the case of ductile materials such as metals. It is believed that the contact of substrate surface and particle with the high pressures is necessary for particle bonding. Actually, for metals which are the mostly deposited materials by CS, the resulting microstructure resembles that of a cold worked material, with elongated grains and even recrystallized areas at particle interfaces where a higher temperature is reached, a result of adiabatic shearing [111]; such microstructures have been well compared to those of powder-compacted and explosive-welded materials. A wide range of ductile materials (metallic and polymeric) have been successfully deposited by CS, whereas non-ductile materials such as ceramics are able to deposit onto ductile substrates where particle could be embedded.

Generally, for each material, there is a critical velocity ( $V_c$ ) for its successful deposition onto a certain substrate. Only those particles that exceed this critical velocity ( $V_p > V_c$ ) will be successfully deposited to build up a coating, but higher impact velocities may result in erosion of surface substrate.

This critical velocity depends, from one side, on the intrinsic characteristics of the spraying material, i.e., the physical and mechanical properties such as density, melting point, and ultimate strength, and from another side on the particle size, morphology, temperature, and substrate; in addition, the particle velocity ( $V_p$ ) also depends on the spray gun parameters, i.e., gas composition, gas preheat temperature, gas pressure, and nozzle geometry. An optimization of all these parameters is many times critical for a good deposition [100].

Metal, cermet, and polymeric coatings have been successfully produced onto different substrates, but ceramic coatings are still a challenge due to their intrinsic brittleness. Blends of metal–ceramic feedstock powders have been sprayed by CS leading to improved coating properties such as wear and hardness [112]; as it will be later discussed, this alternative has been successfully used to produce titanium–HA coatings.

### 1.4.3. BIOCOATINGS VIA COLD SPRAY

#### 1.4.3.1. Metal biocoatings

Biocompatible metals were the first family of materials to be sprayed via CS within this field due to their high plasticities and thus the feasibility to produce coatings with good efficiencies. The first metal coatings that were used for biomedical applications were of stainless steel (SS) and titanium. In analogy to porous PS Ti coatings, these have been also produced by CS with the aim to allow bone ingrowth.

By changing the spraying conditions, it is possible to reach different porosity levels. Li et al. [113] presented the microstructure of cold-sprayed Ti and Ti6Al4V coatings onto Ti6Al4V alloy substrates and the effect of heat treatment on coating microstructure. These authors achieved an average porosity of  $5.4 \pm 2.4$  and  $22.3 \pm 4.7$  % before the heat treatment; after the heat treatment, the porosity increased to  $21.6 \pm 4.6$  and  $29.7 \pm 5.1$  % probably by the healing of the incomplete interfaces through the atom diffusion during annealing treatment. In addition, Wong et al. is another example of how the authors achieve different degrees of porosity by a wide range of modification of the spraying conditions (Fig. 1.7) [114]. It might be also worth noting that the density of the microstructure can be influenced by the tamping effect; this is the successive impact of following particles, therefore leading to more porous structures on the top rather than near the interface with the substrate [115].

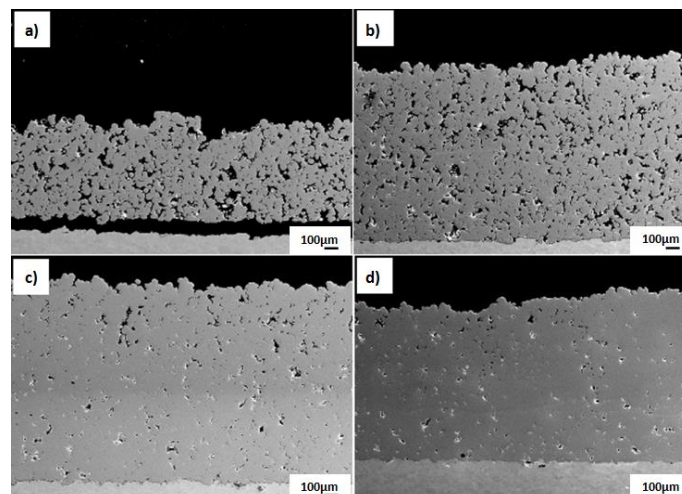


**Figure 1.7.** Porous Ti coatings by CS from less to high energetic conditions (a–d) [122]

On the other hand, some authors have used materials such as magnesium or aluminum to produce porosity. Sun et al. [116] produced porous titanium coatings spraying Mg+Ti powders

onto titanium, where the magnesium behaved as a space holder and is eliminated by vacuum sintering. Plasma-sprayed porous titanium coatings usually exhibit irregular porosity distribution and the pores are not well interconnected, while other methods such as sintering titanium beads or fibers have relatively low porosity (<37 %) and low cohesive and/or bond strength. By contrast, CS coatings of Mg + Ti resulted in an average porosity of 48.6 % and pore sizes in the range of 70–150  $\mu\text{m}$ . Bending modulus and compressive modulus of porous titanium coating were close to the bone and thus may be beneficial to reducing stress shielding. Qiu et al. used aluminum as a porogen to form porous titanium coatings [117], which was removed after spraying by alkaline leaching. Considering all tests, the average pore size was between 74 and 91  $\mu\text{m}$  and the pore percentage between 48 and 66 %. Figure 1.8 shows the porous morphologies and cross section of both studies with pore sizes of 50–150 and 70–150  $\mu\text{m}$ , respectively.

Furthermore, well-adhered, thick, and homogeneous titanium coatings have been also produced onto PEEK biopolymer without its degradation, with the aim to enhance PEEKs biocompatibility for implant applications [118]. This responds to the new emerging use of PEEK as a novel alternative within the biomedical field. Table 1.5 shows the CS spray conditions of metal coatings used for biocoatings. Spraying onto UHMWPE has also been produced with the aim to avoid having the polyethylene liner and the acetabular cup as two separate components. In such a way, the rough titanium shell and the polymer contacting the femoral head can be achieved within the same component; this was obtained through proper surface activation before spraying [119].

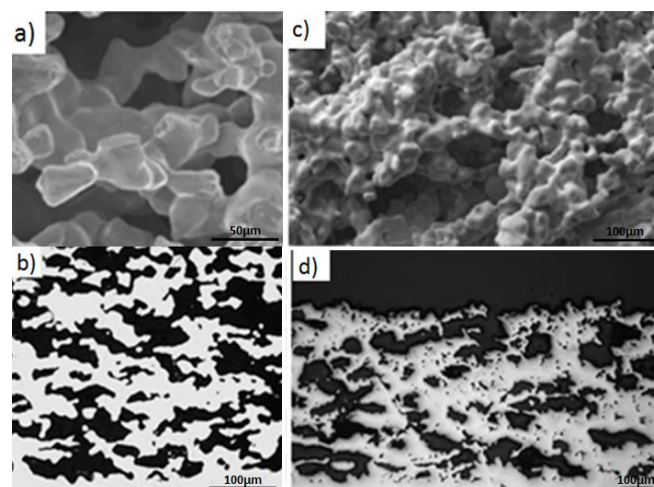


**Figure 1.8.** Porous Ti coatings a) SEM free surface image and b) MO cross section image [126], c) SEM free surface image d) SEM cross section image [127]

**Table 1.5.** CS conditions of metals coatings for biomedical applications

	Feedstock powder	Subs*	Gas	Gas T* (°C)	Gas P* (bars)	Standoff distance (mm)	Traverse Speed (mm/s)
Li et al. [113]	Ti Ti6Al4V	Ti6Al4V	Air	520	28	30	-
Sun et al. [116]	Ti+Mg	Titanium	He	340	10	-	-
Qiu al. [117]	CP-Ti+CPAI CP-Ti +CPAI+HA	Ti	He	370	6.9	12.5	1.66
Al-Mangour et al. [120]	SS 316 + L605alloy	Mild Steel	N <sub>2</sub>	700	40	80	300

\*Subs. (Substrate); Gas T. (Gas temperature); Gas P. (Gas pressure)

As the microstructure of feedstock powders is maintained in the coatings via CS, it is possible to obtain fine-grain coatings, which might be beneficial in biomedical field. For example, Al-Mangour et al. [120] performed mechanical and corrosion properties in stents coated by fine grain powders; they used a mixture of L605 cobalt–chromium (Co–Cr) alloy and 316-L SS onto mild steel, where it was observed that the addition of cobalt powders helped obtain dense coatings. A heat treatment improved then the densification and porosity reduction as well as a significant increase of ductility; although in vivo and in vitro tests are still pending, the Co–Cr alloy showed a lower corrosion rate than pure SS, making it suitable for the development of a new class of metallic biomaterials.

Other attempts were done with Tantalum (Ta). CS, as it works with low temperatures, is being studied to produce Ta coatings where it is observed good interface adhesion, low porosity, and increase of hardness [121].

Finally, metal coatings have also been produced by CS for bone fracture fixation systems in order to prevent bonding or one or more types of corrosion between the metallic fastener and the metallic bone plate [122]. Where the components of an internal fixation device subsequently bond together, the surgeon may have extreme difficulty in disengaging one

component from the other, such as disengaging a bone screw from within an opening in a bone plate. The bonding may prevent the separation of the components, and therefore it can result in injuries due to the prevention of the components being removed from the patient. This patented procedure comprises a cold-sprayed metallic coating either within the opening or on the metallic fastener. The cold-sprayed metallic coating comprises a biocompatible metallic material having a third composition that is different than the first and second compositions.

#### **1.4.3.2. Ceramic-based biocoatings**

Specifically, bioactive ceramic coatings highlight their direct bond to living tissues when implanted. Looking for fixation, bioactive fixation forms a bond with higher strength than mechanical fixation. Nevertheless, TiO<sub>2</sub> coatings are currently investigated by CS due to its good mechanical properties and biocompatibility. Kilemann et al. [123] studied the formation of TiO<sub>2</sub> particles onto metallic substrates. TiO<sub>2</sub> particles interact as solid spheres with the substrate bonding in a ring-like zone. Particles break into small remnants and remain in the bonding zones. Only if substrate material is brought to the surface and is available to bind other particles, a second layer or parts of it are likely to be attached to the coating on impact. Salim et al. [124] proposed a novel synthesis of TiO<sub>2</sub> powders for CS in which makes it possible the deposition of those particles by CS and the growing up of a layer without the addition of binder, but onto copper not in biocompatible material. Nevertheless, investigations are currently running out.

##### a) Hydroxyapatite biocoatings

Previously, the advantages of CS over conventional thermal spray processes have been mainly associated to high-temperature-related features. HA coatings have been found to promote fast and enhanced fixation strength, but the long-term stability of the fixation has been reported to still be a challenge in TS techniques; for this main reason, CS is proposed as an alternative to produce HA coatings with high density and controlled crystallinity. In front of other low-temperature processes such as sol-gel, biomimetic deposition, solution deposition, electrochemical deposition, and atomic layer deposition, HA cold spray technique highlights for its simple and economic process of producing coatings at low temperatures being able to control coatings' microstructure.

Despite the common sense that HA particles bombardment is like blasting the metal surface of the implant, some approaches have been applied in this direction [125–129] and even more successful by dealing with a shot-penning route [130]. Cold Gas Spray of ceramics has been actually compared to other low-temperature powder-based dry manufacturing processes, i.e., aerosol deposition (AD), sometimes known as vacuum cold spray (VCS) and nanoparticle deposition system (NPDS), which appeared in the 1990s and 2000s, respectively. AD is based on the acceleration of submicrometer particles, but low-vacuum conditions are necessary to control the supersonic flow. In NPDS, the source of bonding is attributed to the dissipation of the kinetic energy of the particles. The use of submicrometer feedstock particles seems to be also important, and some plasticity features have been revealed [131–133]. Dense HA coatings have been deposited on titanium by this method [134, 135].

Different numerical and simulation studies have been developed to come upon optimal conditions for cold spraying of spraying HA. Zhang et al. [136] studied the factors influencing HA particle acceleration using a computational fluid dynamics program FLUENT. The simulation results showed that the HA particle is accelerated by the combination of throat diameter and exit diameter whose expansion ratios lie within the optimal range of 1.5–4. HA particle velocity increases with the increasing of gas pressure notably from 0.2MPa (150 mm/s) to 0.6 MPa (360 mm/s) and with the decrease of HA particle size until a minimum of 5  $\mu\text{m}$ , where it decelerates steeply, being 5–20  $\mu\text{m}$  particle size suitable for spray with CS. The taguchi method was used by Singh [137] to optimize HA conditions in CS; they calculated the percentage contribution of all factors on exit particle velocity of HA powder, being as follows in descending order: gas type>particle diameter>gas inlet pressure>particle temperature>gas inlet temperature. Moreover, they observed that the combination of those parameters can alter the result [138]; the increase of gas pressure and particle temperature was found to increase the particle velocity, while the increase of HA particle diameter was found to decrease the particle velocity and its influence was found to be more than respective influences of gas pressure, gas temperature, and particle temperature. Therefore, HA particle velocity is inversely proportional to particle size, despite the increase of gas pressure and gas temperature.

Recent investigations concern biocompatible coatings on biodegradable implants and, for example, magnesium-based alloys. Despite its excellent properties, magnesium-based alloys have not seen tangible applications in biomedical field industry. To date, they have been studied within the development of cardiovascular stents, bone fixation material, and porous scaffolds for bone repair. Nevertheless, the main limitation to the medical application is their rapidly and localized corrosion behavior. In order to control the degradation rates, it is useful to coat with HA. PS studies have not been developed for its high temperatures that could melt magnesium substrate and decompose HA in other calcium phosphate phases, and the crystallinity of HA may also be lowered due to rapid solidifications. CS has offered solution to both problems [139].

On the other hand, pure HA coatings have been produced on PEEK substrates by CS, therefore providing bioactivity to a material that avoids the stress shielding phenomenon normally occurring between a metallic material and the bone and the weak mechanical properties of ceramic substrates [140]. Coating polymeric biomaterials with calcium phosphate is also one of the most effective methods to enhance biocompatibility. However, calcium phosphate ceramic coatings necessitate a heat treatment at a high temperature in order to induce crystallization of the coating layer, or necessitate a cost-consuming vacuum deposition method for low-temperature crystallization in order to control/obtain other calcium phosphate phases. In the case of polymeric biomaterials, a heat treatment at a high temperature brings about deformation of polymers, and such deformation eventually deteriorates the performance of polymers, preventing the polymers from being used as biomaterials. Furthermore, a vacuum deposition method at a low temperature may also damage the surfaces of polymers, causing deformation, and requires high production cost to increase productivity, which is not preferable. CS overcomes the limitations of various conventional coating methods and enables coating of the surfaces of polymeric biomaterials while maintaining the intrinsic properties of both the powder and the polymer, with low production cost and high productivity. This patent includes as bioactive coatings HA, bioglass compounds such as bioglasses containing CaO, SiO<sub>2</sub>, and P<sub>2</sub>O<sub>5</sub> as main ingredients, and crystallized bioglasses, and mixtures thereof [140]. Lee et al. [141] also evaluated the bioactivity of HA coatings on PEEK substrates by CS; these proved to be homogeneous and strongly adhered without any deformation of the substrate material.

### b) Hydroxyapatite-composite biocoatings

Due to the intrinsic brittle nature of ceramics, a direct deposition of a uniform layer with proper adhesion is still a challenge via CS, especially onto the typical metallic prosthesis, i.e., Ti and SS, on account of the inelastic deformation that ends in failure fragmentation. This has already been observed by the few studies reported in the previous section. For a better understanding of this behavior, lots of studies are being carried out on the investigation of failure mechanisms of ceramics at dynamic impacts [142, 143]. Significant efforts are thus addressed in the direction of using metal–ceramic and polymer–ceramic composite powders. Some works deal with HA–Ti mixtures [144, 145]. The results showed that, compared to pure Ti coating, cold-sprayed HA/Ti composite coating exhibits higher corrosion current and lower corrosion resistance. However, a post-spray heat treatment can improve the corrosion property of HA/Ti composite coating remarkably. In addition, the mechanical properties such as microhardness and ultimate shear strength of cold-sprayed 20wt% HAP/Ti composite coating also improved up to three times by a post-spray heat treatment process. Further, the recrystallization also favored the interfacial bonding and hence improved the mechanical properties [146]. Choudhuri et al. [147] also demonstrated that HA–Ti mixture powders can be cold sprayed achieving a better bond strength (24.45 MPa) than PS (~10–15 MPa); two different titanium powders were used in those mixtures: a vacuum atomized commercial pure titanium (CP-Ti) and a sponge titanium powder both from a particle size ~45  $\mu\text{m}$ .

CP-Ti showed difficulties to build up the coating by encapsulating HA particles, whereas the use of sponge Ti powder was more effective. The maximum incorporation of HA was of 20 %; above that percentage, it was found that HA particles got crushed into fragments due to high impacts.

As reported before, aluminum powders have been used as a porogen, in combination with titanium, to achieve porous titanium coatings with higher interconnected macroporosity and larger specific surface area; in order to make these coatings bioactive, HA was added to facilitate bone cell attachment and ingrowth, leading to outstanding in vitro HA mineralization, although long-term studies are required [117]. Such authors used two types of HA, a crystalline and an amorphous calcium phosphate nanocrystalline HA (NC-HA), where it could be observed that NC-HA reaches a maximum  $\text{Ca}^{2+}$  mineralization efficiency promoting an early bone fixation.

Other attempts in the case of cold-sprayed HA-composite coatings include HA–graphene nanohsheet (GN) [148], with the aim to avoid the concerns related to its long-term performance, i.e., the intrinsic brittleness and low fracture toughness of HA, and doping HA with silver [149], with the advantages that silver involves. The addition of graphene has been proved to be very suitable for load-bearing applications, exhibiting a very reasonable biocompatibility as well; it was even embedded in HA matrix and plastic deformation of certain nano HA particles was revealed. The GN-containing HA coatings markedly enhanced attachment and proliferation of the osteoblast cells, which is most likely attributed to fast adsorption of key serum proteins like fibronectin with elongated stretching conformation on GN. Table 1.6 shows different cases of CS conditions for biomedical applications.

**Table 1.6.** CS conditions of HA/Ti and HA coatings for biomedical applications

	<b>Feedstock powder</b>	<b>Sub*</b>	<b>Gas</b>	<b>Gas T*(°C)</b>	<b>Gas P* (bars)</b>	<b>Standoff distance (mm)</b>	<b>Traverse Speed (mm/s)</b>
<b>Qiu al. [117]</b>	CP-Ti+CP-Al CP-Ti+CP-Al +HA	Ti	He	370	6.9	12.5	1.66
<b>Noorakma et al. [139]</b>	HA	AZ51 alloy	Air	500-700	10	40	-
<b>Lee et al. [141]</b>	HA	PEEK	Air	200/300/ 400	7/14/20	30	-
<b>Zhou et al. [146]</b>	CP-Ti+HA	Ti	N <sub>2</sub>	700	35	15	-
<b>Choudhuri n et al. [147]</b>	CP-Ti Sponge Ti Sponge Ti+HA	Ti	N <sub>2</sub>	400-700	25-38	25	50-400

\*Subs. (Substrate); Gas T. (Gas temperature); Gas P. (Gas pressure)

## **1.5. CLINICAL PERFORMANCE**

This is a very novel topic and since many few researchers have optimized their coating systems, not many in vitro and in vivo results exist within the literature. In vitro performance can be measured by the evaluation of morphological changes of coatings after immersion in SBF. Qiu et al. [117] reported the formation of clusters of fine precipitates for their HA–Ti porous coatings, with similar calcium mineralization efficiencies when using either crystalline HA or amorphous nanocrystalline HA. In addition, these authors used the human osteosarcomaderived SaOS-2 line with the aim to evaluate the cytotoxicity; cell viabilities after 48 h proved that neither of the coatings was cytotoxic. On the other hand, Gardon et al. [150] studied the differentiation and proliferation of cultured trabecular bone of Ti coatings onto PEEK obtaining a better biological response from Ti than PEEK from 3 days of culture, although optimal properties were shown with nanostructured titanium dioxide. Lee et al. [141] performed similar studies with cultured Human bone marrow mesenchymal stem cells hBMSCs (Human Bone Marrow Stromal Osteoprogenitor Cells) on HA–CS-coated PEEK samples. The HA coating facilitated the differentiation and proliferation of cultured hBMSCs and promoted bone fusion with the surrounding iliac bone without the presence of any fibrous layer. Figure 1.9 illustrates some in vivo results showing an association of the cylinders with the bone tissue improved as the recovery period in HA-coated PEEK disk group was increased. In contrast, the association of the cylinders with the bone tissue decreased for the animals implanted with the bare PEEK cylinder. Noorakma et al. [139] deposited an HA layer onto magnesium alloy substrate and demonstrated that in vitro behavior and superior cells adherence with numerous cellular micro extensions on porous Ta samples compared to Ti samples clearly suggest that Ta surfaces are biocompatible and cause no inhibition to bone osteoblast cells adhesion and growth. Presence of relatively high extra cellular matrix (ECM) mineralization on porous Ta samples also indicates that osteoblast cells have started differentiating and ECM remodeling [151]. In vivo, this porous tantalum biomaterial has desirable characteristics for bone ingrowth; further studies are warranted to ascertain its potential for clinical reconstructive orthopedics [152].

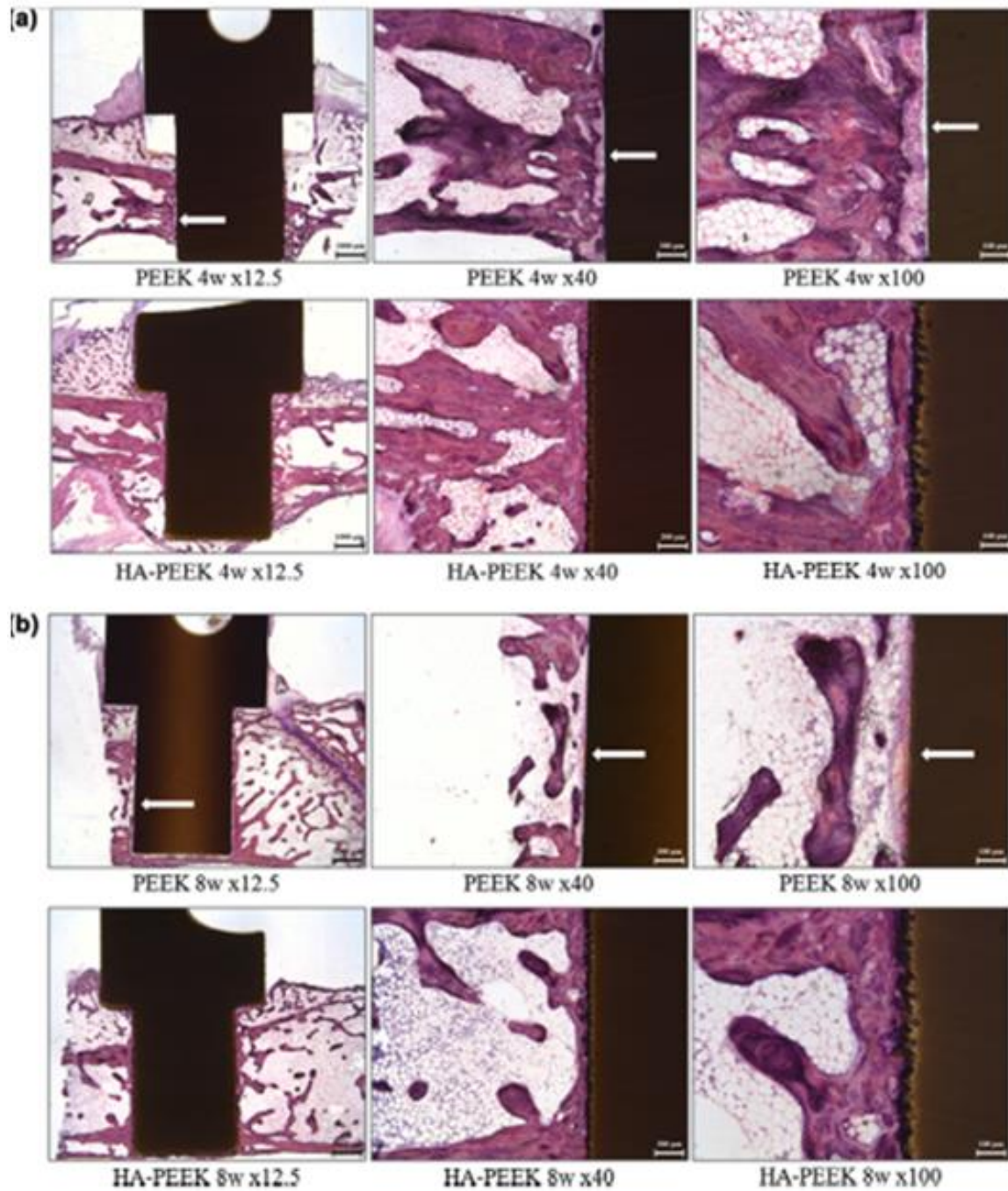


**Figure 1.9.** In vivo evaluation of bare PEEK and HA-PEEK at 4 weeks a) and 8 weeks b) [141]

The addition of graphene to HA coatings significantly enhanced the attachment and proliferation of human osteoblast cells, which is most likely attributed to fast adsorption of key serum proteins like fibronectin with elongated stretching conformation on graphene [143].

## **1.6. ANTIBACTERIAL/ANTIMICROBIAL COATINGS**

Although the use of titanium and its alloys in biomedicine is still important, the infection around the implants remains as a concern. Infection not only makes the patients suffer serious damage, but bacterial infection after implant placement can cause significant complications thereby increasing medical cost. The paradigm of bacterial attachment and proliferation on surfaces was first recognized in the 1930s. It was established that bacteria prefer to colonize a solid substrate than living in a planktonic state. The creation of antibacterial surfaces seeks to repel or resist the initial attachments of bacteria by either exhibiting an antibiofouling effect or by inactivating any cells coming into contact with the surface. Antibacterial surfaces can be divided in two groups: (i) antibiofouling surfaces that may resist or prevent cellular attachment due to the presence of an unfavorable surface topography or surface chemistry and (ii) bactericidal surfaces that disrupt the cell on contact, causing cell death. The CS process has also emerged as a promising process to functionalize surfaces in such way.

The use of inorganic antimicrobial agents has attracted interest for its improved safety and stability versus organic antimicrobial agents. There has been a great development during recent years in antibacterial coatings, but they are not still clinically much used; however, more developments and investigations are being explored to achieve both excellent tissue integration ability and good antibacterial properties [153]. Silver (Ag) has already been highlighted as an antibacterial material. The combination of bioactivity (HA) and antibacterial properties (Ag) has been previously reported, and the results indicated that the antibacterial activity increased with increasing HA–Ag nanopowder concentrations [144]. Alternatively, ceramic powder of zinc oxide (ZnO), calcium oxide (CaO), and magnesium oxide (MgO) has found antibacterial activity. Combinations of ZnO/Ti powders with different ratios have been performed to produce composite-coated implants [154]; the results show that the viability of cells on ZnO<sub>20</sub>/Ti<sub>80</sub> was higher than that on ZnO<sub>50</sub>/Ti<sub>50</sub> and ZnO<sub>80</sub>/Ti<sub>20</sub> samples, thus proving that the cell viability decreased with increasing ZnO concentration in the coating composition. On the other hand, the bactericidal effect of TiO<sub>2</sub> coatings has also been extensively studied; specifically, CS anatase coatings were investigated by Kliemann et al. [123]. A kill rate of 99.99 % was obtained after 5 min of exposition of the bacteria *Pseudomonas Aeruginosa* to UV light with a peak intensity of 360 nm. Certain stagnation of

the decay of the bacteria was found, which could be attributed to noncoated areas present due to the impossibility of covering all the surface of the substrate by means of anchoring TiO<sub>2</sub> particles. Other coatings that are committed to antibacterial properties thank to ZnO are made of Novaron VZ 600 (a commercial available inorganic antimicrobial powder made from glass, with the functional material being ZnO) onto Ti [155]. Those studies were developed to analyze the differences among surfaces using different processing pressures and analysis of the antimicrobial with CS due to the low heat powder resistance. Results have shown that *S. Aureus* cells on samples decreased after 24-h culture, even on non-coated plates. Two possibilities were reported: (i) Roughness can contribute to antimicrobial ability and (ii) medium concentration may have been too low for this bacterium.

Moreover, antibacterial coatings not only focus on orthopedic and implant applications, but also in touch surfaces where there is certain risk of infection. Metals like copper (Cu) have been employed for this purpose. In the case of copper, its antibacterial activity not only comes from itself but also the utilized technique. The specific mechanism by which copper affects cellular structures is not yet proven, but the active agent of cell destruction is generally considered to be the copper ion [156]. Since CS involves high strain rates which lead to extreme work hardening and high dislocation density within the deposit, it causes an increase of ion diffusion through the grain dislocations leading to microbial destruction [156]. Champagne et al. [156] produced copper surfaces onto aluminum using three thermal spray methods: plasma spray, wire spray, and CS, in order to analyze the microbiologic differences and decrease the risk of infection of bacterial contamination on touch surfaces such as hospital table. CS produced the minimum percentage of MRSA (Methicillin-Resistant *Staphylococcus Aureus*) due to the high number of dislocations within the coating.

Other attempts were performed with aluminum powder as ductile metal for blend antibacterial powders such as chitosan–Cu [157] and ZnO [158]. The use of aluminum is cause for a number of cosmetics used, repair, corrosion, and protection applications, also for its low density that could be accelerated to very high velocities in CS and the available commercial variety of composition of Al powders. Table 1.7 summarizes the CS spraying conditions used for the antibacterial coatings referenced within this section.

Table 1.7. CS conditions of antibacterial coating

	Feedstock powder	Sub*	Gas	Gas T* (°C)	Gas P* (bars)	Standoff distance (mm)	Traverse Speed (mm/s)
Sanpo et al. [149]	HA-Ag (Ag-doped HA) +PEEK	Glass	Air	150-160	11-12	15	50
Sanpo et al. [154]	ZnO+Ti	Al 6061	He	300-400	13-15	15	60
Tami et al.[155]	Novaron VZ 600	Ti	N	350	30	5	20

\*Subs. (Substrate); Gas T. (Gas temperature); Gas P. (Gas pressure)

## 1.7. REFERENCES

- [1] Gaona M (2007) Recubrimientos biocompatibles obtenidos por Proyección Térmica y estudio in vitro de la función osteoblástica. PhD thesis. Universitat de Barcelona
- [2] Hench LL (1998) Biomaterials: a forecast for the future. *Biomaterials* 19:1419–1423
- [3] Ratner BD, Hoffman AS, Schoen FJ, Lemons JE (2013) Introduction— biomaterials science: an evolving, multidisciplinary endeavor. In: Ratner BD, Hoffman AS, Schoen FJ, Lemons JE (eds) *biomaterials science*, 3rd edn. Academic Press, London
- [4] Ramakrishna S, Mayer J, Wintermantel E, Leong KW (2001) Biomedical applications of polymer composite materials: a review. *Compos Sci Technol* 61:1189–1224
- [5] William DF (1987) Consensus and definitions in biomaterials. In: de Potter C, de Lange K, de Groot K, Lee AJC (eds) *Advances in biomaterials*. Elsevier, Amsterdam, pp 11–16
- [6] Cao W, Hench LL (1996) Bioactive materials. *Ceram Inter* 22:493–507
- [7] Jones J, Clare A (2012) *Bio-glasses: an introduction*. Wiley, Chichester
- [8] Kalita S (2008) Nanostructured biomaterials. In: Seal S (ed) *Functional nanostructures*. Springer, New York

- [9] Bronzono JD (2000) The biomedical engineering handbook, vol 1, 2nd edn. CRC Press LLC, Boca Raton
- [10] Salinas AJ, Vallet-Regi M (2013) Bioactive ceramics: from bone grafts to tissue engineering. *RSC Adv* 3:11116–11131
- [11] Katti KS (2004) Biomaterials in total joint replacement. *Colloid Surf B* 39:133–142
- [12] Bauer S, Schmuki P, von der Mark K, Park J (2013) Engineering biocompatible implant surfaces: Part I: materials and surfaces. *Prog Mater Sci* 58:261–326
- [13] Khan SP, Auner GG, Newaz GM (2005) Influence of nanoscale surface roughness on neural cell attachment on silicon. *Nanomed Nanotechnol Biol Med* 1:125–129
- [14] Yun H-S, Park J-W, Kim S-H, Kim Y-J, Jang J-H (2011) Effect of the pore structure of bioactive glass balls on biocompatibility in vitro and in vivo. *Acta Biomater* 7:2651–2660
- [15] Singhatanadgit W (2009) Biological responses to new advanced surface modifications of endosseous medical implants. *Bone Tissue Regen Insights* 2:1–11
- [16] Lin L, Wang H, Ni M, Rui Y, Cheng T-Y, Cheng C-K (2014) Enhanced osteointegration of medical titanium implant with surface modifications in micro/nanoscale structures. *J Orthop Transl* 2:35–42
- [17] Yang YZ, Tian JM, Tian JT, Chen ZQ, Deng XJ, Zhang DH (2000) Preparation of graded porous titanium coatings on titanium implant materials by plasma spraying. *J Biomed Mater Res* 52:333–337
- [18] Endres S, Wilke M, Knoell P, Frank H, Kratz M, Wilke A (2008) Correlation of in vitro and in vivo results of vacuum plasma sprayed titanium implants with different surface topography. *J Mater Sci Mater Med* 19:1117–1125
- [19] Borsari V, Giavaresi G, Fini M, Torricelli P, Tschon M, Chiesa R (2005) Comparative in vitro study on a ultra-high roughness and dense titanium coating. *Biomater* 26:4948–4955
- [20] Chen Y, Zheng X, Ji H, Ding C (2007) Effect of Ti–OH formation on bioactivity of vacuum plasma sprayed titanium coating after chemical treatment. *Surf Coat Technol* 202:494–498

- [21] Jaeggi C, Mooser R, Frauchiger V, Wyss P (2009) 3D characterization of open porous vacuum plasma sprayed titanium coatings by means of high resolution micro computer tomography. *Mater Lett* 63:2643–2645
- [22] Kinoshita T, Chen SL, Siitonen P, Kettunen P (1996) Densification of plasma-sprayed titanium and tantalum coatings. *JTST* 5:439–444
- [23] Stanislav J, Kosikowsky D, Mohanty PS (2005) High temperature erosion behavior of thermal sprayed tantalum. In: Sudarshan TS, Stiglich JJ (eds). *Proceedings of the 19th International Conference on Surface Modification Technologies*, pp 28–33. ASM International, Materials Park
- [24] Balla VK, Bodhak S, Bose S, Bandyopadhyay A (2010) Porous tantalum structures for bone implants: fabrication, mechanical and in vitro biological properties. *Acta Biomater* 6:3349–3359
- [25] Matson DW, Merz MD, McClanahan ED (1992) High rate sputter deposition of wear resistant tantalum coatings. *JVST A* 10:1791–1796
- [26] Rai M, Yadav A, Gade A (2009) Silver nanoparticles as a new generation of antimicrobials. *Biotechnol Adv* 27:76–83
- [27] Knetsch MLW, Koole LH (2011) New strategies in the development of antimicrobial coatings: the example of increasing usage of silver and silver nanoparticles. *Polymer* 3:340–366
- [28] Melaiye A, Youngs WJ (2005) Silver and its application as an antimicrobial agent. *Expert Opin Ther Patents* 15:125–130
- [29] Schierholz JM, Lucas LJ, Rump A, Pulverer G (1998) Efficacy of silver-coated medical devices. *J Hosp Infect* 40:257–262
- [30] Gosheger G, Harges J, Ahrens H, Streitburger A, Buerger H, Erren M et al (2004) Silver-coated megaendoprostheses in a rabbit model—an analysis of the infection rate and toxicological side effects. *Biomater* 25:5547–5556
- [31] Tobin EJ, Bambauer R (2003) Silver coating of dialysis catheters to reduce bacterial colonization and infection. *Ther Apher Dial* 7:504–509

- [32] Gray JE, Norton PR, Alnouno R, Marolda CL, Valvano MA, Griffiths K (2003) Biological efficacy of electroless-deposited silver on plasma activated polyurethane. *Biomater* 24:2759–2765
- [33] Dowling DP, Donnelly K, McConnell ML, Eloy R, Arnaud MN (2001) Deposition of anti-bacterial silver coatings on polymeric substrates. *Thin Solid Films* 398–399:602–606
- [34] Bosetti M, Masse` A, Tobin E, Cannas M (2002) Silver coated materials for external fixation devices: in vitro biocompatibility and genotoxicity. *Biomater* 23:887–892
- [35] Noda I, Miyaji F, Ando Y, Miyamoto H, Shimazaki T, Yonekura Y et al (2009) Development of novel thermal sprayed antibacterial coating and evaluation of release properties of silver ions. *J Biomed Mater Res B* 89B:456–465
- [36] Ando Y, Miyamoto H, Noda I, Sakurai N, Akiyama T, Yonekura Y et al (2010) Calcium phosphate coating containing silver shows high antibacterial activity and low cytotoxicity and inhibits bacterial adhesion. *Mater Sci Eng C* 30:175–180
- [37] Miola M, Ferraris S, Di Nunzio S, Robotti PF, Bianchi G, Fucale G et al (2009) Surface silver-doping of biocompatible glasses to induce antibacterial properties. Part II: plasma sprayed glasscoatings. *J Mater Sci Mater Med* 20:741–749
- [38] Li B, Liu X, Meng F, Chang J, Ding C (2009) Preparation and antibacterial properties of plasma sprayed nano-titania/silver coatings. *Mater Chem Phys* 118:99–104
- [39] Li B, Liu X, Cao C, Meng F, Dong Y, Cui T et al (2008) Preparation and antibacterial effect of plasma sprayed wollastonite coatings loading silver. *Appl Surf Sci* 255:452–454
- [40] Zheng X, Chen Y, Xie Y, Ji H, Huang L, Ding C (2009) Antibacterial property and biocompatibility of plasma sprayed hydroxyapatite/silver composite coatings. *J Therm Spray Technol* 18:463
- [41] Fernández J, Gaona M, Guilemany JM (2004) Tribological study of plasma hydroxyapatite coatings. *Key Eng Mater* 254–256:383–386
- [42] Heimann RB, Vu TA (1997) Low-pressure plasma-sprayed (LPPS) bioceramic coatings with improved adhesion strength and resorption resistance. *J Therm Spray Technol* 6:145–149

- [43] Sun L, Berndt CC, Gross KA, Kucuk A (2001) Material fundamentals and clinical performance of plasma-sprayed hydroxyapatite coatings: a review. *J Biomed Mater Res* 58:570–592
- [44] Tsui YC, Doyle C, Clyne TW (1998) Plasma sprayed hydroxyapatite coatings on titanium substrates. Part 1: mechanical properties and residual stress levels. *Biomater* 19:2015–2029
- [45] Fernández J, Gaona M, Guilemany JM (2007) Effect of heat treatments on HVOF hydroxyapatite coatings. *J Therm Spray Tech* 16:220–228
- [46] Lima RS, Khor KA, Li H, Cheang P, Marple BR (2005) HVOF spraying of nanostructured hydroxyapatite for biomedical applications. *Mater Sci Eng A* 396:181–187
- [47] Khor K, Li H, Cheang P (2003) Processing–microstructure– property relations in HVOF sprayed calcium phosphate based bioceramic coatings. *Biomater* 24:2233–2243
- [48] Cho JS, Kang YC (2008) Nano-sized hydroxyapatite powders prepared by flame spray pyrolysis. *J Alloys Compd* 464:282–287
- [49] Pajares López M, Hernández Cortés P, Peregrina Palomares M, Hernández Hernández MA (1998) Vástagos cementados y no cementados en artroplastias totales de cadera por coxopatías mecánicas. *Rev Esp Cir Osteoartic* 33:59–65
- [50] Lewis G (1997) Properties of acrylic bone cement: State of the art review. *J Biomed Mater Res* 38:155–182.
- [51] Chern Lin JH, Liu ML, Ju CP (1994) Structure and properties of hydroxyapatite-bioactive glass composites plasma sprayed on Ti6Al4V. *J Mater Sci Mater Med* 5:279–283
- [52] Wheeler DL, Montfort MJ, McLoughlin SW (2001) Differential healing response of bone adjacent to porous implants coated with hydroxyapatite and 45S5 bioactive glass. *J Biomed Mater Res* 55:603–612
- [53] Floroian L, Popescu A, Servan N, Mihailescu Ion N. Polymerbioglass composite coatings: a promising alternative for advanced biomedical implants. <http://cdn.intechopen.com/pdfswm/16716.pdf>. Accessed 11 April 2015

- [54] Cai F, Miyata C, Huang X, Yang Q (2014) Microstructure, bioactivity and wear resistance of sintered composite Co-Cr-Mo/ Bioglass((R)) for medical implant applications. *Int J Surf Sci Eng* 8:264–281
- [55]. Pourhashem S, Afshar A (2014) Double layer bioglass-silica coatings on 316L stainless steel by sol-gel method. *Ceram Int* 40:993–1000
- [56] Ananth KP, Suganya S, Mangalaraj D, Ferreira JMF, Balamurugan A (2013) Electrophoretic bilayer deposition of zirconia and reinforced bioglass system on Ti6Al4V for implant applications: an in vitro investigation. *Mater Sci Eng C* 33:4160–4166
- [57] Wang DG, Chen CZ, Jin QP, Li HC, Pan YK (2014) HA/bioglass composite films deposited by pulsed laser with different substrate temperature. *Appl Phys A* 114:897–902
- [58] Sun L, Berndt CC, Khor KA, Cheang HN, Karlis A (2002) Gross, Surface characteristics and dissolution behavior of plasma-sprayed hydroxyapatite coating. *J Biomed Mater Res* 62:228–236
- [59] Formin AA, Steinhauer AB, Lyasnikov VN, Wenig SB, Zakharevich AM (2012) Nanocrystalline structure of the surface layer of plasma-sprayed hydroxyapatite coatings obtained upon preliminary induction heat treatment of metal base. *Tech Phys Lett* 38:481–483
- [60] Kurzweg H, Heimann RB, Troczynski T, Wayman ML (1998) Development of plasma-sprayed bioceramic coatings with bond coats based on titania and zirconia. *Biomater* 19:1507–1511
- [61] F1609-08 (2014) Standard Specification for calcium phosphate Coatings for Implantable Materials
- [62] ISO Standard 13779-1:2008 Implants for surgery—Hydroxyapatite— Part 1: Ceramic hydroxyapatite
- [63] ISO Standard 13779-1:2008 Implants for surgery—Hydroxyapatite— Part 2: Coatings of hydroxyapatite
- [64] ISO Standard 13779-1:2008 Implants for surgery—Hydroxyapatite— Part 3: Chemical analysis and characterization of crystallinity and phase purity

- [65] ASTM F 2068-00 Standard Specification for Femoral Prostheses— Metallic Implants
- [66] Mohseni E, Zalnezhad E, Bushroa AR (2014) Comparative investigation on the adhesion of hydroxyapatite coating on Ti–6Al–4V implant: a review paper. *Int J Adhes Adhes* 48:238–257
- [67] Kuo MC, Yen SK (2002) The process of electrochemical deposited hydroxyapatite coatings on biomedical titanium at room temperature. *Mater Sci Eng C* 20:153–160
- [68] Yoshimura M, Byrappa K (2008) Hydrothermal processing of materials: past, present and future. *J Mater Sci* 43:2085–2103.
- [69] Darr JA, Guo ZX, Raman V, Bououdina M, Rehman IU (2004) Metal organic chemical vapour deposition (MOCVD) of bone mineral like carbonated hydroxyapatite coatings. *Chem Commun* 2004:696–697
- [70] Li H, Khor KA, Cheang P (2002) Titanium dioxide reinforced hydroxyapatite coatings deposited by high velocity oxy-fuel (HVOF) spray. *Biomater* 23:85–91
- [71] Melero H, Fargas G, Garcia-Giralt N, Fernández J, Guilemany JM (2014) Mechanical performance of bioceramic coatings obtained by high-velocity oxy-fuel spray for biomedical purposes. *Surf Coat Technol* 242:92–99
- [72] Melero H, Torrell M, Fernández J, Gomes JR, Guilemany JM (2013) Tribological characterization of biocompatible HAp-TiO<sub>2</sub> coatings obtained by high velocity oxy-fuel spray. *Wear* 305:8–13
- [73] Bhadang KA, Gross KA (2004) Influence of fluorapatite on the properties of thermally sprayed hydroxyapatite coatings. *Biomater* 25:4935–4945
- [74] Gu YW, Khor KA, Pan D, Cheang P (2004) Activity of plasma sprayed yttria stabilized zirconia reinforced hydroxyapatite/Ti–6Al–4V composite coatings in simulated body fluid. *Biomater* 25:3177–3185
- [75] Fathi MH, Azam F (2007) Novel hydroxyapatite/tantalum surface coating for metallic dental implant. *Mater Lett* 61:1238–1241

- [76] Roy M, Fielding GA, Beyenal H, Bandyopadhyay A, Bose S (2012) Mechanical, in vitro antimicrobial, and biological properties of plasma-sprayed silver-doped hydroxyapatite coating. *ACS Appl Mater Interfaces* 4:1341–1349
- [77] Yonekura Y, Miyamoto H, Shimazaki T, Ando Y, Noda I, Mawatari M et al (2011) Osteoconductivity of thermal-sprayed silver-containing hydroxyapatite coating in the rat tibia. *J Bone Jt Surg* 93B:644–649
- [78] Shimazaki T, Miyamoto H, Ando Y, Noda I, Yonekura Y, Kawano S et al (2010) In vivo antibacterial and silver-releasing properties of novel thermal sprayed silver-containing hydroxyapatite coating. *J of Biomed Mater Res Part B* 92B:386–389
- [79] Balani K, Anderson R, Laha T, Andara M, Tercero J, Crumpler E et al (2007) Plasma-sprayed carbon nanotube reinforced hydroxyapatite coatings and their interaction with human osteoblasts in vitro. *Biomater* 28:618–624
- [80] Green SM, Schlegel J (2001) A polyaryletherketone biomaterial for use in medical implant applications. *Polym for the Med Ind Proc*, Brussels, 14–15 May 2001, pp 1–7
- [81] Li H, Zou X, Woo C, Ding M, Lind M, Bünnger C (2007) Experimental lumbar spine fusion with novel tantalum-coated carbon fiber implant. *J Biomed Mater Res Part B* 81B:194–200
- [82] Ma R, Tang T (2014) Current strategies to improve the bioactivity of PEEK. *Int J Mol Sci* 15:5426–5445
- [83] Roeder RK, Conrad TL (2012) Bioactive polyaryletherketone composites. In: Kurtz SM (ed) *PEEK biomaterials handbook*. William Andrew Publishing, Oxford, pp 163–179
- [84] Riner M, Roth A, Brandsberg F, Wintermantel E, Mayer J. Development of a human hip endoprosthesis stem made by injection molding of carbon fiber reinforced PEEK. <http://www.iccm-central.org/Proceedings/ICCM13proceedings/SITE/PAPERS/paper-1409.pdf>
- [85] Brydone AS, Meek D, Maclaine S (2010) Bone grafting, orthopaedic biomaterials, and the clinical need for bone engineering *Proceedings of the Institution of Mechanical Engineers, Part H. J Eng Med* 224:1329–1343
- [86] Furlong R, Osborn J (1991) Fixation of hip prostheses by hydroxyapatite ceramic coatings. *J Bone Jt Surg* 73B:741–745

- [87] Jaffe W, Scott D (1999) Total hip arthroplasty with hydroxyapatite-coated prostheses. In: Imura S, Wada M, Omori H (eds) Joint arthroplasty. Springer, Tokyo, pp 159–187
- [88] Pramanik S, Agarwak AK, Rai KN (2005) Chronology of total hip joint replacement and materials development. Trends Biomater Artif Organs 19:15–26
- [89] Cross MJ, Parish EN (2005) A hydroxyapatite-coated total knee replacement. J Bone Jt Surg Br 87B:1073–1076
- [90] Manley MTC, D'Aantonio WN, Edin JA, Geesink JA, Rudolph GT (1998) Fixation of acetabular cups without cement in total hip arthroplasty. A comparison of three different implant surfaces at a minimum duration of follow-up of five years\*. J Bone Jt Surg 80:1175–1185
- [91] Nilsson KG, Kärrholm J, Carlsson L, Dale'n T (1999) Hydroxyapatite coating versus cemented fixation of the tibial component in total knee arthroplasty: prospective randomized comparison of hydroxyapatite-coated and cemented tibial components with 5-year follow-up using radiostereometry. J Arthroplast 14:9–20
- [92] Zhang S (2011) Biological and biomedical coatings handbook, vol 2. Taylor & Francis, Boca Raton
- [93] Davis JR (2004) Introduction to thermal spray processing. In: Davis JR (ed) Handbook of thermal spray technology. ASM International, Materials Park, pp 3–13
- [94] Davis JR (2004) Thermal spray processes. In: Davis JR (ed) Handbook of thermal spray technology. ASM International, Materials Park, pp 54–76
- [95] Fernández J, Guilemany JM, Gaona M (2005) La proyección térmica en la obtención de recubrimientos biocompatibles: ventajas de la proyección térmica por alta velocidad (HVOF) sobre la proyección térmica por plasma atmosférico (APS). Biomechanics 13:16–39
- [96] Kang AS, Singh G, Chawla V (2013) Some problems associated with thermal sprayed ha coatings: a review. Int J Surf Eng Mater Technol 3:10–20
- [97] Villa M, Dosta S, Fernández J, Guilemany JM (2012) La proyección fría (CGS): Una alternativa a las tecnologías convencionales de deposición. Rev Metal 48:175–191

- [98] Champagne Victor K (2007) The cold spray materials deposition process: fundamentals and applications. Woodhead, Cambridge
- [99] Ghelichi R, Guagliano M (2009) Coating by the cold spray process: a state o the art. *Fratt Integr Strutt* 8:30–44
- [100] Singh HR, Sidhu TS, Kalsi SBS (2012) Cold spray technology: future of coating deposition processes. *Frat Integr Strutt* 22:69–84
- [101] Morgan R, Fox P, Pattison J, Sutcliffe C, O'Neill W (2004) Analysis of cold gas dynamically sprayed aluminium deposits. *Mater Lett* 58:1317–1320
- [102] Suhonen T, Varis T, Dosta S, Torrell M, Guilemany JM (2013) Residual stress development in cold sprayed Al, Cu and Ti coatings. *Acta Mater* 61:6329–6337
- [103] Champagne VK, Helfritch DJ (2014) Mainstreaming cold spray—push for applications. *Surf Eng* 30:396–403
- [104] Moridi A, Hassani-Gangaraj SM, Guagliano M, Dao M (2014) Cold spray coating: review of material systems and future perspectives. *Surf Eng* 30:369–395
- [105] Richer P et al (2005) Effect of particle geometry and substrate preparation in cold spray. ITSC 2005 “Thermal spray connects: explore its surfacing potential!” Basel, Switzerland, pp.193–199
- [106] Makinen H, Langeborn J, Vuoristo P (2007) Adhesion of cold sprayed coatings: effect of powder, substrate and heat treatment. In: Marple BR, Hyland MM, Lau Y, Lia C, Lima RS, Montavon G (eds) *Thermal spray global solutions*. ASM International, Materials Park, pp 31–36
- [107] Sakaki K, Tajima K, Li H, Shinkai S, Shimitzu Y (2004) Influence of substrate conditions and traverse speed on cold sprayed coatings. In: *International Thermal Spray Conference 2004: Advances in Technology and Application*, Osaka (Japan), pp 358–362. ASM International, Material Park
- [108] Wu J, Yang J, Fang H, Yoon S, Lee C (2006) The bond strength of Al–Si coating on mild steel by kinetic spraying deposition. *Appl Surf Sci* 252:7809–7814

- [109] Marrocco T, McCartney DG, Shipway PH, Sturgeon AJ (2006) Production of titanium deposits by cold-gas dynamic spray: numerical modeling and experimental characterization. *J Therm Spray Tech* 15:263–272
- [110] Price TS, Shipway PH, McCartney DG (2006) Effect of cold spray deposition of a titanium coating on fatigue behavior of a titanium alloy. *J Therm Spray Tech* 15:507–512.
- [111] Eason PD (2012) A structure property processing comparison of cold rolled pm copper and cold gas dynamically sprayed copper. *J Powder Metall Min* 1:101
- [112] Miguel JM, Vizcaíno S, Dosta S, Cinca N, Lorenzana C, Guilemany JM (2014) Recubrimientos de materiales compuestos metal-cerámico obtenidos por nuevas tecnologías de proyección térmica: Proyección fría (CGS) y su resistencia al desgaste. *Rev Metal* 47:390–401
- [113] Li W-Y, Zhang C, Guo X, Xu J, Li C-J, Liao H et al (2007) Ti and Ti-6Al-4V coatings by cold spraying and microstructure modification by heat treatment. *Adv Eng Mater* 9:418–423
- [114] Wong W, Rezaeian A, Yue S, Irissou E, Legoux J-G (2009) Effect of gas temperature, gas pressure, and particle characteristics on cold sprayed pure titanium coatings, thermal spray 2009. In: Marple BR, Hyland MM, Lau Y-C, Li C-J, Lima RS, Montavon G (eds) *Proceedings of the International Thermal Spray Conference*. ASM International, Materials Park, pp 231–236
- [115] Li C-J, Li W-Y (2003) Deposition characteristics of titanium coating in cold spraying. *Surf Coat Technol* 167:278–283.
- [116] Sun J, Han Y, Cui K (2008) Innovative fabrication of porous titanium coating on titanium by cold spraying and vacuum sintering. *Mater Lett* 62:3623–3625
- [117] Qiu D, Zhang M, Grøndahl L (2013) A novel composite porous coating approach for bioactive titanium-based orthopedic implants. *J Biomed Mater Res Part A* 101A:862–872
- [118] Gardon M, Latorre A, Torrell M, Dosta S, Fernández J, Guilemany JM (2013) Cold gas spray titanium coatings onto a biocompatible polymer. *Mater Lett* 106:97–99

- [119] Guilemany JM, Dosta S, Cinca N, Fernández J, Garcia I. Feasibility of cold gas spraying to produce metal coatings onto activated polymeric substrates. Thermal Spray Centre (CPT). Intellectual properties protection (iPP). Ref.1240B p 10
- [120] Al-Mangour B, Mongrain R, Irissou E, Yue S (2013) Improving the strength and corrosion resistance of 316L stainless steel for biomedical applications using cold spray. *Surf Coat Technol* 216:297–307
- [121] Steenkiste T, Gorkiewicz DW (2004) Analysis of tantalum coatings produced by the kinetic spray process. *J Therm Spray Technol* 13:265–273
- [122] Lozier A, Popoola OO, Mason JJ, Forstein M (2009) Bone fracture fixation system. US Patent 0198286 A1, August 6, 2009
- [123] Kliemann J-O, Gutzmann H, Gaertner F, Huebner H, Borchers C, Klassen T (2011) Formation of cold-sprayed ceramic titanium dioxide layers on metal surfaces. *J Therm Spray Technol* 20:292–298
- [124] Salim NT, Yamada M, Nakano H, Fukumoto M (2011) The synthesis of titanium dioxide (TiO<sub>2</sub>) powder for cold spray process. In: 3rd International Congress on Ceramics (ICC): Novel Chemical Processing Sol-Gel and Solution-Based Processing 18:032019.
- [125] Ishikawa K, Miyamoto Y, Nagayama M, Asaoka K (1997) Blast coating method: new method of coating titanium surface with hydroxyapatite at room temperature. *J Biomed Mater Res* 38:129–134
- [126] O'Hare P, Meenan BJ, Burke GA, Byrne G, Dowling D, Hunt JA (2010) Biological responses to hydroxyapatite surfaces deposited via a co-incident microblasting technique. *Biomater* 31:515–522
- [127] Gbureck U, Masten A, Probst J, Thull R (2003) Tribochemical structuring and coating of implant metal surfaces with titanium oxide and hydroxyapatite layers. *Mater Sci Eng C* 23:461–465
- [128] O'Neill L, O'Sullivan C, O'Hare P, Sexton L, Keady F, O'Donoghue J (2009) Deposition of substituted apatites onto titanium surfaces using a novel blasting process. *Surf Coat Technol* 204:484–488

- [129] O'Sullivan C, O'Hare P, O'Leary ND, Crean AM, Ryan K, Dobson ADW et al (2010) Deposition of substituted apatites with anticolonizing properties onto titanium surfaces using a novel blasting process. *J Biomed Mater Res B* 95B: 141–149
- [130] Byrne GD, O'Neill L, Twomey B, Dowling DP (2013) Comparison between shot peening and abrasive blasting processes as deposition methods for hydroxyapatite coatings onto a titanium alloy. *Surf Coat Technol* 216:224–231
- [131] Chun D-M, Ahn S-H (2011) Deposition mechanism of dry sprayed ceramic particles at room temperature using a nanoparticle deposition system. *Acta Mater* 59:2693–2703
- [132] Chun D-M, Choi J-O, Lee CS, Ahn S-H (2012) Effect of standoff distance for cold gas spraying of fine ceramic particles (5  $\mu\text{m}$ ) under low vacuum and room temperature using nanoparticle deposition system (NPDS). *Surf Coat Technol* 206: 2125–2132
- [133] Akedo J (2006) Aerosol deposition of ceramic thick films at room temperature: densification mechanism of ceramic layers. *J Am Ceram Soc* 89:1834–1839
- [134] Hahn B-D, Park D-S, Choi J-J, Ryu J, Yoon W-H, Kim K-H et al (2009) Dense nanostructured hydroxyapatite coating on titanium by aerosol deposition. *J Am Ceram Soc* 92:683–687.
- [135] Park D-S, Kim I-S, Kim H, Chou AHK, Hahn B-D, Li L-H et al (2010) Improved biocompatibility of hydroxyapatite thin film prepared by aerosol deposition. *J Biomed Mater Res B* 94B:353–358.
- [136] Zhang L, Zhang WT (2011) Numerical investigation on particle velocity in cold spraying of hydroxyapatite coating. *Adv Mater Res* 18:717–722
- [137] Singh RP (2011) Numerical evaluation, optimization and mathematical validation of cold spraying of hydroxyapatite using taguchi approach. *Inter J Eng Sci Technol* 3:7006–7015
- [138] Singh RP, Batra B (2013) Effect of cold spraying parameters and their interaction on hydroxyapatite deposition. *J Appl Fluid Mech* 6:555–561
- [139] Noorakma AW, Zuhailawati H, Aishvarya V, Dhindaw BK (2013) Hydroxyapatite-coated magnesium-based biodegradable alloy: cold spray deposition and simulated body fluid studies. *J Mater Eng Perform* 22:2997–3004

- [140] Noh JH, Kim DW, An JS, Chang HR, Kim DH, Hong KS, Chin DK (2012) Method for modifying the surface area of a bioinert material. US Patent 0009341 A1, January 12, 2012
- [141] Lee JH, Jang HL, Lee KM, Baek H-R, Jin K, Hong KS et al (2013) In vitro and in vivo evaluation of the bioactivity of hydroxyapatite-coated polyetheretherketone biocomposites created by cold spray technology. *Acta Biomater* 9:6177–6187
- [142] Chen MW, McCauley JW, Dandekar DP, Bourne NK (2006) Dynamic plasticity and failure of high-purity alumina under shock loading. *Nat Mater* 5:614–618
- [143] Mukhopadhyay A, Joshi K, Dey A, Chakraborty R, Rav A, Biswas S et al (2010) Shock deformation of coarse grain alumina above Hugoniot elastic limit. *J Mater Sci* 45:3635–3651.
- [144] Zhou X, Mohanty P (2012) Electrochemical behavior of cold sprayed hydroxyapatite/titanium composite in Hanks' solution. *Electrochim Acta* 65:134–140
- [145] Shukla V, Elliott G, Kear B, McCandlish L (2001) Hyperkinetic deposition of nanopowders by supersonic rectangular jet impingement. *Script Mater* 44:2179–2182
- [146] Zhou X (2012) Hydroxyapatite/titanium composite coating for biomedical applications. PhD thesis. University of Michigan
- [147] Choudhuri A, Mohanty PS, Karthikeyan J (2009) Bio-ceramic composite coatings by cold spray technology. In: *Proceedings of the International Thermal Spray Conference*, pp 391–96
- [148] Liu Y, Dang Z, Wang Y, Huang J, Li H (2014) Hydroxyapatite/graphene-nanosheet composite coatings deposited by vacuum cold spraying for biomedical applications: inherited nanostructures and enhanced properties. *Carbon* 67:250–259
- [149] Sanpo N, Tan M, Cheang P, Khor KA (2009) Antibacterial property of cold-sprayed HA-Ag/PEEK coating. *J Therm Spray Tech* 18:10–15
- [150] Gardon M, Melero H, Garcia-Giralt N, Dosta S, Cano IG, Guilemany JM (2014) Enhancing the bioactivity of polymeric implants by means of cold gas spray coatings, *J Biomed Mater Res Part B*

- [151] Balla VK, Bodhak S, Bose S, Bandyopadhyay A (2010) Porous tantalum structures for bone implants: fabrication, mechanical and in vitro biological properties. *Acta Biomater* 6:3349–3359
- [152] Bobyn JD, Stackpool GJ, Hacing SA, Tanzer M, Krygier JJ (1999) Characteristics of bone ingrowth and interface mechanics of a new porous tantalum biomaterial. *J Bone Jt Surg Br* 81:907–914
- [153] Zhao L, Chu PK, Zhang Y, Wu Z (2009) Antibacterial coatings on titanium implants. *J Biomed Mater Res B* 91B:470–480
- [154] Sanpo N, Hailan C, Loke K, Keng KP, Cheang P, Berndt CC, et al. (2010) Biocompatibility and antibacterial property of cold sprayed ZnO/titanium composite coating. In: Mendez-Vilas A (ed). *Science and Technology against Microbial Pathogens. Research, Development and Evaluation*. In: *Proceedings of the International Conference on Antimicrobial Research*, World Scientific pp 140-44
- [155] Tamai K, Kawate K, Kawahara I, Takakura Y, Sakaki K (2009) Inorganic antimicrobial coating for titanium alloy and its effect on bacteria. *J Orthop Sci* 14:204–209
- [156] Champagne V, Helfrich D (2013) A demonstration of the antimicrobial effectiveness of various copper surfaces. *J Biol Eng* 7:1–7
- [157] Sanpo N, Ang S, Cheang P, Khor KA (2009) Antibacterial property of cold sprayed chitosan–Cu/Al coating. *J Therm Spray Tech* 18:600–608
- [158] Sanpo N, Saraswati T, Tan Meng Lu, Cheang P (2008) Antibacterial property of cold sprayed ZnO–Al coating. In: *Proceedings of the 2008 international conference on biomedical engineering and informatics (BMEI 2008)*, vol 1, pp 488–491



# CHAPTER 2

## *MOTIVATION AND OBJECTIVES*

---



## **2.1. MOTIVATION**

The use of joint prostheses is increasing nowadays with the increase of human ageing and chronic diseases. In orthopedic terms, more and more patients will require the use of prosthesis in order to substitute a critical part of their skeleton. Even so, there are still some problems related with the current implanted prostheses and their viability once is introduced into the body. The possible causes are not always easily diagnosed. Common causes of prosthetic failure could be aseptic loosening, infection and instability. Usually, early failures are consequent to dislocation, infection or implant failure, meanwhile late failures (>5years post operation) are because of osteolysis or aseptic/mechanical loosening. Therefore, there is a continuous research in biomedical field to overcome these problematics. In response to those needs, porous titanium (Ti) and dense hydroxyapatite (HA) coatings are commonly used commercially for these applications.

Plasma spraying (PS) deposition technique is currently used for that purpose. Our research group has been investigating in this direction from many years. However, the high temperatures imply some drawbacks, as could be oxidation for metallic materials or decomposition in secondary phases for temperature sensitive materials like hydroxyapatite. For high-temperature sensitive materials, PS in vacuum conditions are used, the so-called vacuum plasma spray (VPS) process. As titanium cannot be sprayed under atmospheric conditions due to the extremely high affinity to oxygen and nitrogen, VPS uses a vacuum chamber pressure in order to achieve well inert environment; however, high cost still an inconvenience

As a new alternative, the cold spray (CS) is proposed for the production of those coatings. The industrial interest of the use of this technique in biomedical field is due to its deposition at low temperature (solid-state process), avoiding oxidation in metallic materials and decomposition in secondary phases as could be for HA. The possibility of spraying different types of materials, at low-cost, in a friendly environment, and maintaining the microstructure of the feedstock powder to the coating is a novelty for producing customized coatings.

## **2.2. OBJECTIVES OF THE THESIS**

The main objective is the obtaining of functionalized coatings, basically Ti and HA coatings, by means of CS in order to improve the osseointegration and long-term fixation. This has been achieved through an accurate evaluation and optimization of the spraying parameters.

As regards to Ti coatings, they were optimized according to the mechanical properties that ASTM standards for joint prostheses applications require. Furthermore, the development of different nanotextured surface treatments was performed on titanium coatings in order to evaluate their possible improvement in biocompatibility.

With reference to HA coatings, the understanding on the deposition process of ceramic powder in terms of CS and the effect of the different HA microstructures on their deposition was analyzed.

The biological properties of those coatings were tested statically and dynamically to evaluate cell response according to:

- The effect of surface roughness onto Ti coatings, as well as the effect of the different (crystalline and nanocrystalline) HA coatings.
- The differences between a non-coated and a HA coated Ti coating.
- The possible improvement in biocompatibility in front of the presence of nanostructured surfaces onto Ti coatings.
- The method in which HA coatings can be thermal sprayed (PS and CS).

# CHAPTER 3

## *RAW MATERIALS AND EXPERIMENTAL PROCEDURE*

---



### **3.1. RAW MATERIALS**

#### **3.1.1. Commercial pure titanium powder**

The high strength, low weight ratio and outstanding corrosion resistance inherent to titanium (Ti) and its alloys has led to a wide and diversified range of successful applications which demand high levels of reliable performance in surgery and medicine as well as in aerospace, automotive, chemical plant, power generation, oil and gas extraction, sports, and other major industries.

Unalloyed commercial pure titanium (CP-Ti) is available in four different grades, which are used based on the corrosion resistance, ductility and strength requirements of the specific application. Grade 1 has the highest formability, while grade 4 has the highest strength and moderate formability. Table 3.1 shows a brief description of Ti grades.

**Table 3.1.** Description of Ti grades [1]

<b>ASTM Grade</b>	<b>Alloy Description</b>
<b>Ti Grade 1 (G1)</b>	Lower strength, softest, unalloyed Ti grade with highest ductility, cold formability and impact toughness, with excellent resistance to mildly reducing to highly oxidizing media with or without chlorides and high weldability
<b>Ti Grade 2 (G2)</b>	Moderate strength unalloyed Ti with excellent weldability, cold formability, excellent resistance to mildly reducing to highly oxidizing media with or without chlorides.
<b>Ti Grade 3 (G3)</b>	Slightly stronger version of Ti G2 with similar corrosion resistance with good weldability and reasonable cold formability/ductility.
<b>Ti Grade 4 (G4)</b>	Much stronger, high interstitial version of Ti G2 and G3 with reasonable weldability and reduced ductility and cold formability.

CP-Ti users utilize its excellent corrosion resistance, formability and weldable characteristics in many critical applications. Ti G2 is stronger than G1 and equally corrosion-resistant against most applications. Ti G2 has numerous applications in the medical industry. Biocompatibility of Ti G2 is excellent, especially when direct contact with tissue or bone is required.

CP-Ti G2 powder (Biomed T400) from MBN Nanomaterialia S.p.A. (Italy) was chosen to perform this research. This powder is developed by a grinding process of particle size reduction based on ball milling technology. This ball milling process is performed in Ti devices and Ti milling means which ensure the requested product purity. The particle size distribution is controlled by post processing operation of powder classification in controlled environment. The Biomed T400 Titanium metal powder is developed for coatings in the biomedical field in observance of ASTM1580/1 rules.

### **3.1.2. Calcium phosphate powders**

Hydroxyapatite (HA) is the major component, and an essential ingredient, of normal bone and teeth. The osseointegration of an implant can be accelerated depending on HA phases in the coating.

The typical feedstock used for HA coatings is a fully crystalline pure HA powder. It is commonly manufactured by chemical precipitation from a mixture of a calcium-ion-containing solution and a phosphate-containing solution followed by calcination.

Depending on the process to produce HA coatings [2], new phases can appear due to higher temperatures or rapid coolings. The pure crystalline HA is very stable in the body fluid, but the dissolution rates of other HA phases formed during thermal spraying are much higher, which is in the order of amorphous phase (ACP) > tetracalcium phosphate (TTCP) > alpha tricalcium phosphate ( $\alpha$ -TCP) > oxyhydroxyapatite (OHA) > beta tricalcium phosphate ( $\beta$ -TCP) > HA [3]. Although high dissolution rates enhance biological properties due to the release of calcium and phosphate ions, higher dissolution rates can lead to coating failure. The crystallinity of a HA is desired to implant coating.

For that reason, the following crystalline and nanocrystalline HA powders were chosen in order to perform this research:

- An agglomerate nanocrystalline HA powder obtained from Medicoat AG (France).
- A sintered crystalline HA powder (Captal®30) obtained from Plasma Biotat Limited (United Kingdom).

### 3.1.3. Ti6Al4V alloy substrate

The Ti6Al4V alloy is widely used to manufacture implants. The addition of alloying elements to titanium enables it to have a wide range of properties because aluminium tends to stabilize the  $\alpha$ -phase and vanadium tends to stabilize the  $\beta$ -phase, lowering the temperature of the transformation from  $\alpha$  to  $\beta$ . The  $\alpha$ -phase promotes good weldability, excellent strength characteristics and oxidation resistance. The addition of controlled amounts of vanadium as a  $\beta$ -stabilizer causes the higher strength of beta-phase to persist below the transformation temperature which results in a two-phase system. The  $\beta$ -phase can precipitate by an ageing heat treatment. This microstructure produce local strain fields capable of absorbing deformation energy. Cracks are arrested or deterred at the particles. The mechanical properties of the CP-Ti and the Ti6Al4V alloy are given in table 3.2.

**Table 3.2.** Mechanical properties of CP-Ti (ASTM F 67) and Ti6Al4V alloy (ASTM F 136) [4]

<b>Property</b>	<b>Grade 1 (G1)</b>	<b>Grade 2 (G2)</b>	<b>Grade 3 (G3)</b>	<b>Grade 4 (G4)</b>	<b>Ti6Al4V</b>
<b>Tensile strength (MPa)</b>	240	345	450	550	860
<b>Yield Strength (MPa)</b>	170	275	380	485	795
<b>Elongation (%)</b>	24	20	18	15	10

The modulus of elasticity of these materials is about 110 GPa. This is much lower than stainless steels and cobalt-base alloys modulus (210 and 240 GPa, respectively). When compared by specific strength (strength/density) the Ti alloys exceed any other implant materials. Ti and Ti alloys, nevertheless, have poor shear strength, making them less desirable for bone screws, plates and similar applications. They also tend to gall or seize in sliding contact with itself or another metal. Different Ti6Al4V alloy substrates were obtained from TECHNALLOY S.A. (Spain):

- Ti6Al4V alloy sheet of 5 mm thickness for coating optimization.
- Ti6Al4V alloy sheet of 2 mm thickness for mechanical (Abrasion test) and biological testing of the coatings.
- Ti6Al4V alloy bars of  $\varnothing 24.5$  mm (Tensile strength test) and  $\varnothing 20$  mm (Shear strength test).

### 3.2. METHODS OF POWDER CHARACTERIZATION

Powders characteristics as particle size, chemical and phase composition, density, shape and flowability among others are very important on its good deposition onto the substrate. All these variables have been evaluated as follows:

- **Particle size:** A laser diffraction (LS) particle size analyser Beckman Coulter LS 13320 was used to study the granulometry of the feedstock powders. This equipment uses a laser with a 5 mW powder and 750 nm wavelength leading to the detection of particles with an apparent diameter between 200 nm and 2 mm. Before testing, metallic or ceramic particles are dispersed in a glass with acetone in order to avoid particle agglomerations.
- **Density:** There are three methods to measure the density:
  - Apparent density: This method is based on the standard specification ASTM B-212-09 [5]. A flask is filled until matches 25 cm<sup>3</sup>, and then the volume of the powder is weighted inside the funnel in order to obtain in a direct manner the relation of mass over the volume.
  - Vibrated density: This method is based on the standard specification ASTM B-527-93 [6]. It is introduced a known mass of powder in a graduated cylinder, and then this is introduced in an ultrasound bath during 5 minutes. Then the volume is measured and with the previous known value of the mass the density is measured.
  - Real density: This method is based on the standard specification ASTM B-962-08 [7]. The real density is measured introducing in a flask of 25 ml a known mass of the powder in consideration. After weight the flask+powder, it is introduced in the flask a liquid with high wettability (in our case, cyclohexanone). Knowing the density of the dissolvent, it can be calculate the following equation 3.1, the real density:

$$(eq. 3.1) \rho = \frac{m_p}{(25 - \frac{m_t - m_p}{\rho_{liq}})}$$

where  $m_p$  is the mass powder introduced,  $m_t$  is the total mass (powder + cyclohexanone) and  $\rho_{liq}$  is the cyclohexanone density at working temperature.

- **Flowability:** This method is based on the standard specification ASTM B-213-03 standard [8] and establish the use of a Hall powder flowmeter funnel (of small diameter) for powders with high flowability and a Carney powder flowmeter funnel (of major diameter) for powders with low flowability. In order to measure the flowability of the powder, 50 gr of powder are weight and introduced to the metallic Hall/Carney powder flowmeters funnels sealing the outlet hole. Then, the hole opens and the time that the powder needs to pass out through the hole is timed.
- **Brauner-Emmet-Teller (BET):** Particle surface area was measured with a Micrometrics, model TriStar equipment with nitrogen as the adsorptive gas.
- **Morphology:** Two scanning electron microscopes (SEM) were used to examine the top and cross section surfaces of the powders:
  - JEOL 5510 microscope equipped with an energy dispersive spectroscopy (EDS) for microanalysis.
  - ProX Phenom microscope equipped with EDS detector for microanalysis.
- **Microstructure:** Microstructural particle examinations were carried out using JEM JEOL 2100 transmission electron microscope (TEM). TEM specimens (in our case, lamellas) were obtained by focused ion beam (FIB) lift out technique.
- **Phase composition:** Phase analysis has been carried out with the well-known x-ray diffraction (XRD) technique using a Bragg Brentano  $\theta/2\theta$  Siemens D-500 diffractometer with Cu K $\alpha$  radiation. A Rietveld analysis, using the FullProf software [9], was carried out to refine the lattice parameters, to determine the crystal size and to find the percentage of the crystalline phases and amorphous phase [10]. Fourier transform infrared (FTIR) spectroscopy measurements were carried out in a Scientific Nicolet iZ10 MX, using attenuated total reflection diamond corrector and a DTG detector in a reflectance mode from 4000 to 675 cm<sup>-1</sup> with a resolution of 4 cm<sup>-1</sup>. All FTIR analysis carried out in combination with ATR, providing excellent quality data and the best possible reproducibility.

- **Dilatometry:** Also known as thermomechanical analysis, it measures the contractions or linear expansion of a solid sample depending on the temperature, which allows the analysis processes such as phase transitions and chemical reactions. The temperature range is from 25 °C up to 1600 °C with an accuracy of 0.01  $\mu\text{m}$ , using a heat rate of 5 °C/min. The equipment used was a Setaram TMA Setsys 16/18 (France).
- **Picoindenter:** In order to evaluate the compression loading mode of HA powder at different strain rates and the collapse effect of the porous structure, compression tests were carried out using a PicoIndenter PI85 nanoindenter (NanoTest, Micro Materials Ltd., UK) with a diamond flat punch of 10  $\mu\text{m}$  diameter under load control. The force–displacement curves were measured while recording the evolution in a SEM. The nominal strain rate in the elastic regime was in the order of 10 and 100  $\text{nm s}^{-1}$  considered as low and high-strain rates, respectively.

### **3.3. COATING PRODUCTION**

#### **3.3.1. Thermal spraying techniques**

This thesis is focused on the production of functionalized coatings by cold spray (CS). However, optimal hydroxyapatite coatings obtained in previous researches by Plasma Spray were sprayed again in order to be compared with the optimal HA coatings obtained by CS. More information about CS equipment is enclosed (see appendixes).

- **High pressure cold spray (HPCS):** The HPCS equipment used is a KINETICS® 4000 (Cold Gas Technology, Ampfing, Germany), with a maximum operating pressure of 40 bars, temperature of 800°C, and limited to the use of nitrogen as the propellant gas.
- **Low pressure cold spray (LPCS):** The LPCS equipment used is a low pressure Dycomet 423 (The Netherlands), with a maximum operating pressure of 10 bars, temperature of 600°C and limited to the use of air as the propellant gas.

- **Plasma spray (PS):** The equipment used for PS is A-3000 S model from PLASME TECHNIK. The plasma spraying gun is a PLASME TECHNIK F4-MB model with two powder injectors. The gun has a copper cylindrical cathode with a tip of ThO<sub>2</sub> and a circular anode cooled with water. The equipment can work up a maximum powder of 55 KW and voltages between 70-80 V.

### 3.3.2. Nanotexturing surface treatments

- **Anodic oxidation surface treatment:** The anodic anodization was performed on optimal CP-Ti coatings in a two electrode configuration using a DELTA ELEKTRONIKA SM 400-AR-4 power supply, controlled by LabVIEW. An AA304 stainless steel foil is used as auxiliary electrode. An ethylene glycol bath with 5 wt% H<sub>2</sub>O and 0.5 wt% NH<sub>4</sub>F was used. Final optimal conditions of 30V and 45 min were applied [11]. The anodic oxidation treatment was followed by thermal treatment under controlled atmosphere at 450°C during 1h.
- **Alkaline surface treatment:** According to different works [12,13], the alkaline treatment was applied on the optimal CP-Ti coating in order to improve surface biocompatibility. This treatment consists in an immersion of 3 days in 5M NaOH at 80°C. Samples were washed with distilled water and dried in an oven at 40 °C. The alkaline treatment was followed by a thermal treatment under controlled atmosphere at 600 °C during 1h [13].

## 3.4. METHODS OF COATING CHARACTERIZATION

Methods of coating characterization are divided according to: microstructural, mechanical and biological characterization.

### 3.4.1. Microstructural coating characterization

- **Optical microscopy:** Optical Microscopy (Leica DMI5000 M) was used to analyse coating structure, as well as for measure the thickness and porosity of the coatings according to ASTM F-1854 [14], in which covers stereological test methods for characterizing the coating thickness and void coating of various porous coatings adhering to non-porous substrates.

- **Confocal microscopy:** Confocal microscopy (Leica DCM3D) equipment was used to measure 2D and 3D surface topography. The surface profiles, as well as surface roughness and waviness were measured according to ISO 4287, at a magnification of 10x and an stitching of 2x2 [15].
- **Electronic microscopy:** Surface examinations were performed by field emission scanning electron microscopy (FESEM) JEOL JSM 7100F); microstructural examinations were carried out using JEM JEOL 2100 TEM. TEM specimens (in our case, lamellas) were obtained by FIB lift out technique.
- **Atomic force microscopy (AFM):** An AFM Multimode8 with Nanoscope V electronic controller (Bruker) and a SNL probe K: 0.35N/m (Bruker) was used to measure the surface nanoroughness.
- **Chemical attack:** The Kroll's reagent was used to evaluate the particle deformation from the Ti coatings, as well as the microstructure of Ti6Al4V alloy substrate.
- **X-ray photoelectron spectroscopy (XPS):** XPS measurements were performed in a PHI 5500 Multitechnique System (from Physical Electronics) with a monochromatic X-ray source (Aluminium K $\alpha$  line of 1486.6 eV energy and 350 W), placed perpendicular to the analyzer axis and calibrated using the 3d $_{5/2}$  line of Ag with a full width at half maximum (FWHM) of 0.8 eV. The analysed area was a circle of 0.8 mm diameter, and the selected resolution for the spectra was 187.85 eV of pass energy and 0.8 eV/step for the general spectra and 23.5 eV of pass energy and 0.1 eV/step for the spectra of the different elements. In-depth measurements for composition depth profiles were obtained by sputtering the surface with an Ar $^{+}$  ion source (4 keV energy). A low energy electron gun (less than 10 eV) was used in order to discharge the surface when necessary. All measurements were made in an ultra-high vacuum chamber pressure between  $5 \times 10^{-9}$  and  $2 \times 10^{-8}$  torr. All samples were measured as-received and after a sputter-cleaning (between 2-10min) to remove possible sample contamination.

- **Contact angle:** A custom made contact angle goniometer with imageJ software program has been used to the measurement of the contact angles, performing static measurements in sessile drop mode. MilliQ water and Hank's solution were used for measure 2  $\mu\text{l}$  droplet.

### 3.4.2. Mechanical coating characterization

- **Tensile strength test:** This test method covers the determination of the degree of adhesion (bonding strength) of a coating to a substrate or the cohesion strength of the coating in a tension normal to the surface. The test consists of coating one face of a substrate fixture, bonding this coating to the face of a loading fixture (Fig. 3.1a), and subjecting this assembly of coating and fixtures to a tensile load normal to the plane of the coating (Fig. 3.1b). It is adapted particularly for testing coatings applied by thermal spray. Tensile strength measurements were performed using Servosis ME-402/10 model equipment with a strain rate of 0.02 mm/s which was controlled by position until failure occurs following the ASTM F-1147-05 [16]. The tensile (adhesion/cohesion) strength was calculated applying the following formula equation 3.2:

$$\text{(eq. 3.2) Tensile strength} = \frac{\text{maximum load}}{\text{cross section area}}$$

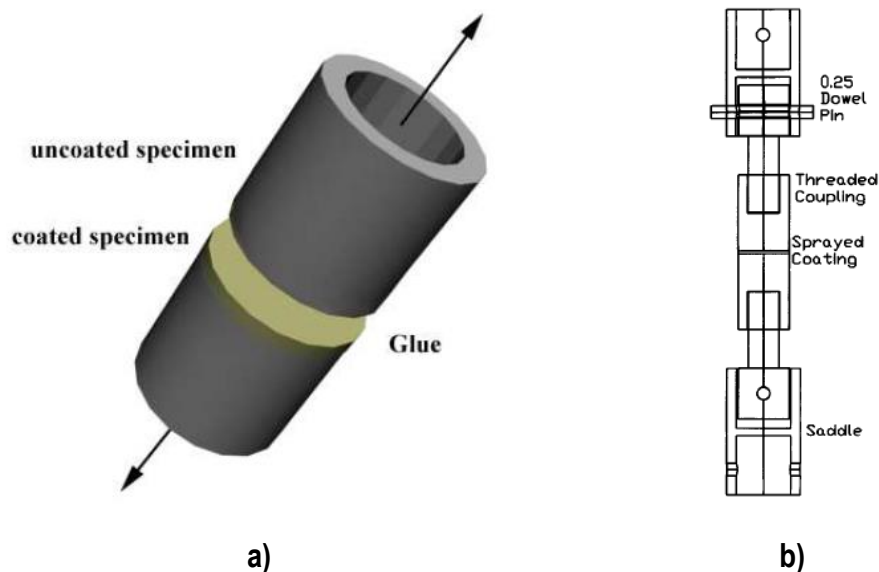


Figure 3.1. a) Specimen assembly and b) schematic set-up for the tensile strength test

- Shear strength test:** This test method covers shear testing of continuous coatings adhering to dense metal substrates at ambient temperatures. This test method consists of subjecting a specimen assembly (Fig. 3.2.a) composed of one coated and one uncoated component to a shear load (Fig. 3.2.b). The components to be tested were bonded together by use of a polymeric adhesive. Shear testing was applied following ASTM F1044 [17], by using a Shimadzu AG-IS 50KN model equipment with a constant speed of 0.25 cm/min until failure. The shear (adhesion/cohesion) strength was calculated applying the following formula equation 3.3:

$$\text{(eq. 3.3) Shear strength} = \frac{\text{maximum load}}{\text{cross section area}}$$

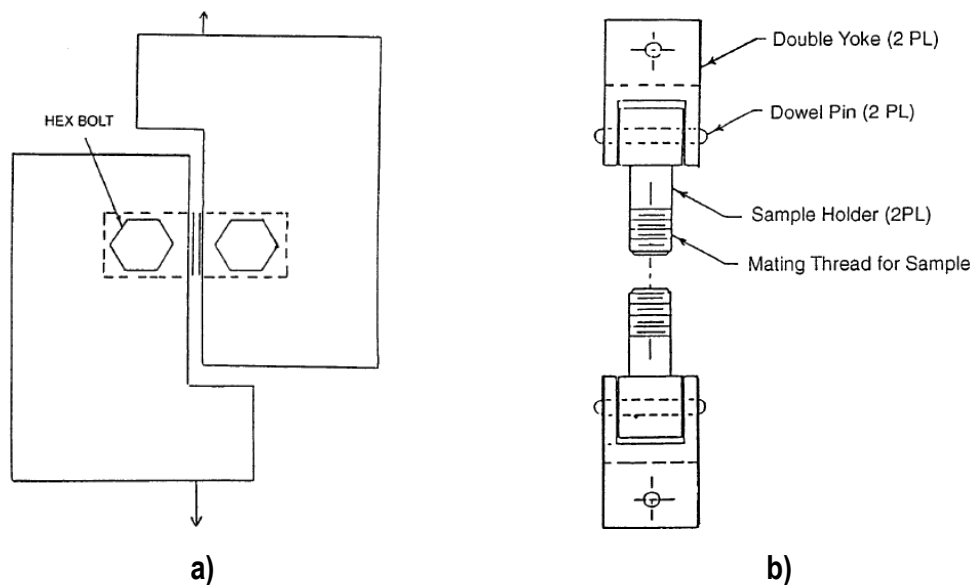


Figure 3.2. a) Shear test specimen assembly and b) Shear strength test

- Abrasive test:** This test method quantifies the abrasion resistance of metallic coatings produced by thermal spray processes on flat metallic surfaces. This test method uses a Taber abrader with H-22 Calibrade® wheels (made of vitrified clay and abrasive grain) and the 250 g mass of the abrading head without added weights (Fig. 3.3). Specimens are abraded repeatedly and cleaned ultrasonically for a set number of rotational cycles (2 to 100 cycles). The specimens are weighed after each cleaning, and the mass loss is the measure of abrasive wear to the specimen. Abrasion measurements were performed by using a 5135 model Taber rotary platform abrasion tester following the standard specification ASTM F-1978 [18].

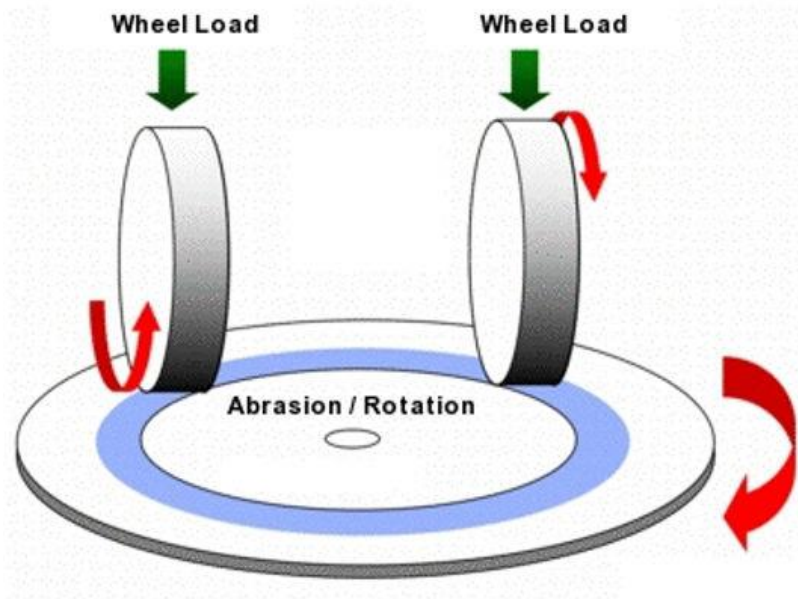


Figure 3.3. Operating schema of abrasive Taber test

- Scratch test:** The adhesion of the HA coatings with the substrate can also be measured with scratch test according to ASTM C1624-05 [19]. CSM-Revetest equipment was used for that purpose with a constant velocity of 10mm/min and a normal progressive applied force increasing from 1 to 140N (Fig. 3.4). The critical scratch load ( $L_c$ ) is the adhesive cause of coating failure.

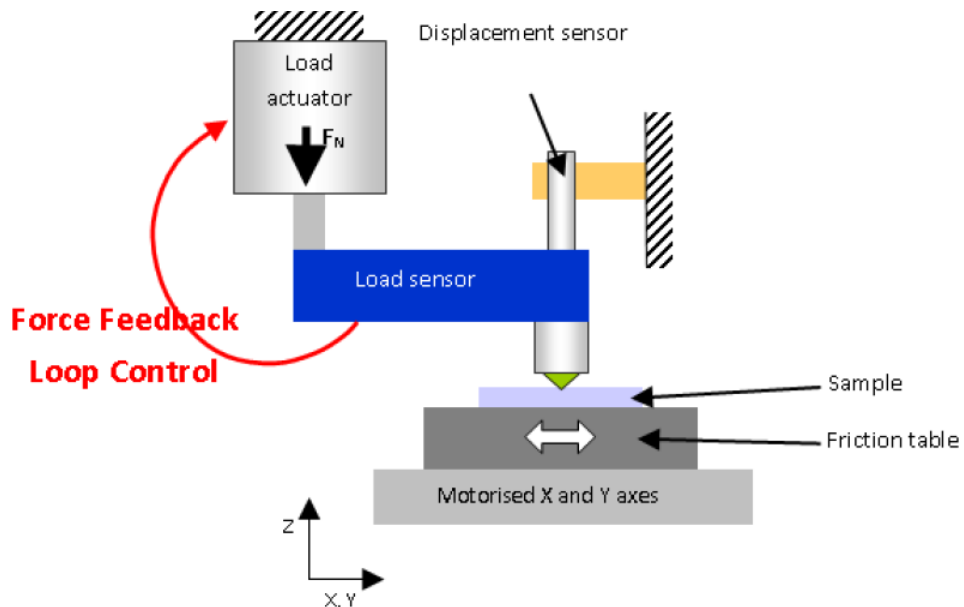


Figure 3.4. Schema of scratch test

### 3.4.3. Biological coating characterization

#### 3.4.3.1. Static Testing

- **Cell culture:** Human osteoblastic cells (HOB) have been obtained from knee trabecular bone after prosthesis replacement following the protocol described by Nàcher et al. [20]. The study has been approved by the of Parc de Salut Mar Ethics Committee. Briefly, trabecular bone was dissected into 1-2 mm pieces that were washed in phosphate-buffered solution (PBS) and placed into a 15 cm diameter Petri dish containing 15 ml Dulbecco's modified Eagle's medium (DMEM) supplemented with 10% Fetal Bovine Serum (FBS), penicillin (100 UI/ml), streptomycin (100 UI/mL), ascorbic acid (100 mg/ml) (Invitrogen) and fungisone (0.4%) (Gibco). The explants were incubated at 37 °C in a humidified atmosphere of 5% CO<sub>2</sub>, changing the medium once a week until cell confluence. Finally, cells were changed into new 75 cm<sup>2</sup> flasks until the suitable number has been reached. A maximum of a third subculture has been used in the experiments. For materials testing, samples were overnight sterilized in ethanol 70°, washed in PBS and placed on a 48-well polystyrene culture plate (Nunc A/S). Each material was seeded with 100.000 cells and cultured with DMEM supplemented with 10% FBS and ascorbic acid; for mineralization assays β-glycerophosphate (5 mM) was also added. Samples were tested at 1, 7 and 14 days of culture, except for mineralization assays that were performed at 28 days. Each test contained two replicas of each sample and they were tested together with a positive and negative control. The tests were carried out three times in order to ensure reproducibility. Results were normalized by control well (without material) within each experiment.
- **Cell viability/proliferation tests:** Cell proliferation has been tested using the MTS assay CellTiter 96® AQueous One Solution Cell Proliferation assay (Promega) in order to calculate cell quantification. According to its respective protocol, 50 µl of MTS were added in each sample cultured with 250 µl of supplemented medium, incubating for 1-4 hours (depending on the sample) and then recording the absorbance at 490nm using a scanning multi-well spectrophotometer.

LIVE/DEAD Viability/Cytotoxicity assay kit for mammalian cells (Invitrogen) was performed in order to characterize qualitatively cell viability, attachment and distribution. It discriminates live from dead cells by simultaneously staining with green-fluorescent calcein-AM (live cells) and red-fluorescent ethidium homodimer-1 (dead cells). Live/Dead assay was performed by adding 300  $\mu$ l of a solution at 4  $\mu$ M EthD-1 and 2  $\mu$ M of calcein AM in PBS, per sample and incubated for 30-45 min at room temperature. Depending on the surface roughness, samples have been observed in Olympus BX61 motorized microscope (low roughness) or with a Confocal TCS SP5 Upright from Leica Microsystems (high roughness). Images from Olympus BX61 motorized microscope were processed directly by its own software MicroSuite™. The images taken with the Confocal TCS SP5 Upright microscope were processed by Fiji image processing package based on ImageJ software.

- **Cell differentiation test:** Osteoblastic cell differentiation levels were evaluated through alkaline phosphatase (ALP) activity, using the Abcam's Alkaline Phosphatase assay kit. This assay uses p-nitrophenyl phosphate (pNPP) as a phosphatase substrate which turns yellow when dephosphorylated (it turns to p-nitrophenol) by ALP. The resulting absorbance was measured at 405 nm using a scanning multi-well spectrophotometer.
- **Cell mineralization test:** The cells attached to the samples were washed with PBS and fixed with 10% formamide during 10 min. The samples were washed with PBS and stained with 300  $\mu$ l of 40 mM/l alizarin red solution, pH 4.2 (Sigma-Aldrich) per well at room temperature during 10 min under gentle shaking. The unincorporated dye was removed and samples were washed carefully with PBS to remove excess stain. Then, mineralization was quantified by dissolving the precipitated alizarin red with 10% cetylpyridinium chloride solution at room temperature during 30 min on gentle shaking. 100  $\mu$ l of the stained solutions were quantified at 550 nm using a scanning multi-well spectrophotometer.
- **Cell morphology:** Phalloidin-Tetramethylrhodamine B isothiocyanate (Sigma-Aldrich) was used for determining the structure of the cytoskeleton of cells seeded onto the

materials. Cells were cleaned with PBS several times and fixed 10 min in 3.7% formaldehyde (Probus) solution in PBS. Then, cells were washed extensively again in PBS and permeabilized with 0.1% TRITON® X-100 (Sigma-Aldrich) in PBS 5 min and gently rinsed with PBS. After that, cells were washed again in PBS and immersed in phalloidin (protected from the light) 40 min at room temperature. Cells were observed with a Leica Confocal TCS SP5 Upright microscope and images were processed by Fiji image processing package; furthermore, cells were observed in JEOL JSM 7100F FESEM; thus, cells were fixed using the following protocol:

- Samples should be immersed in 3.7% formaldehyde (Probus) solution in PBS (1 h at room temperature).
- Samples were washed extensively with PBS.
- The dehydration of the samples was done with the % solvent and times of table 4.5 at room temperature.

**Table 3.3.** Dehydration process of samples with different % of ethanol

% ethanol	Time	% ethanol	Time
50%	10 min (x1)	90%	10 min (x1)
70%	10 min (x1)	96%	10 min (x3)
80%	10 min (x1)	100%	10 min (x3)

- Then samples were critical point dried and observed by FESEM.

### 3.4.3.2. Dynamic testing

- **Lysozyme protein:** Lysozyme proteins were cultivated and provided by the Adult Stem Cell Group, BioMediTech (University of Tampere, Tampere, Finland) and grown according standard procedures.
- **Human mesenchymal stem cells derived from adipose tissue (AD-MSC) culture:** AD-MSC were cultivated and provided by the Adult Stem Cell Group, BioMediTech (University of Tampere, Tampere, Finland) and grown according standard procedures. The cells were washed with PBS and the medium was replaced and dispersed in a cultivation bottle by a cell scraper, resulting in approximately 0.1 million cells per mL concentration in cell culture medium.

- **Multi-Parametric Surface Plasmon Resonance (MP-SPR):** A first attempt was done to calculate the real-time interactions of lysozyme proteins and AD-MSC with plasma sprayed hydroxyapatite surfaces. A MP-SPR Navi™ 200 instrument (BioNavis Ltd., Tampere, Finland) was used for that purpose. SPR is an established method for biomolecular interaction analysis (Fig. 3.5). It is popular due to its sensitivity and its real-time label-free principle. Multi-Parametric Surface Plasmon Resonance (MP-SPR) is based on SPR theory, however its advantageous optical setup measures a full SPR curve which enables new insight into interactions. For instance, it provides measurements of small molecules, lipids and biomaterials without bulk effect. MP-SPR widens the application range of traditional SPR from small molecules up to nanoparticles and even living cells [21]. Measurements can be performed even in complex media such as serum. Measurements were performed in angular scan measurement mode and at temperatures of 20°C and 21°C, respectively. Measurements were performed on a sensor slide, typically a gold-coated glass slide that is placed between the prism and flow-cell with and without PS HA coating.
  - For lysozyme protein (0.2 mg/mL) interaction, a running buffer was 0.15 M NaCl, flow rate 30  $\mu$ L/min and measurement was done with 670 nm laser wavelength.
  - For AD-MSC cells, MP-SPR measurements were done simultaneously with 670 and 980 nm wavelengths using a steady-state cuvette. AD-MSC suspension was injected to the cuvette and the interaction was monitored until the cell attachment seemed to reach a plateau value.

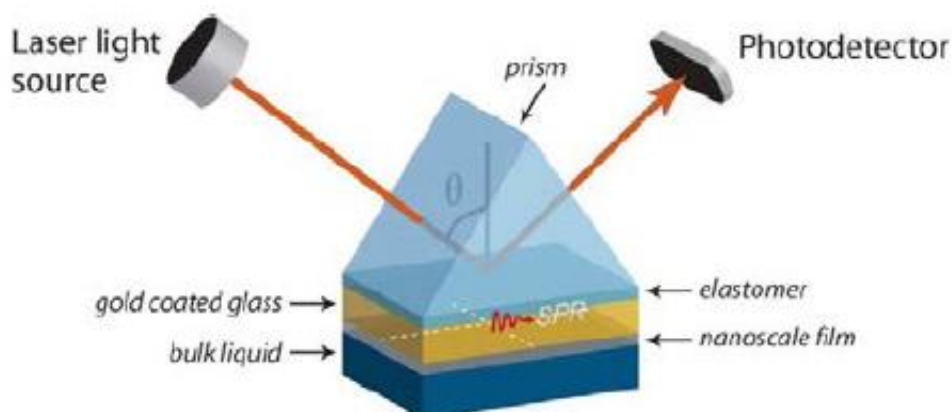


Figure 3.5. Schema of MP-SPR equipment.

---

### **3.5. REFERENCES**

- [1] Titanium alloy guide: <http://www.rtiintl.com/Titanium/RTI-Titanium-Alloy-Guide.pdf>. Accessed 11 April 2016
- [2] Sadat-Shojai M, Khorasani M-T, Dinpanah-Khoshdargi E, Jamshidi A (2013) Synthesis methods for nanosized hydroxyapatite with diverse structures. *Acta Biomater* 9:7591–7621.
- [3] Sun L, Berndt CC, Gross KA, Kucuk A (2001) Material fundamentals and clinical performance of plasma-sprayed hydroxyapatite coatings: A review. *J Biomed Mater Res* 58:570–592.
- [4] Oldani C, Dominguez A (2012) Titanium as a Biomaterial for Implants. *Recent Advances in Arthroplasty*
- [5] ASTM B-212-09 - Standard Test Method for Apparent density of Free-Flowing Metal Powders using the Hall Flowmeter Funnel.
- [6] ASTM B-527-93 - Standard Test Method for Determination of Tap Density of Metallic Powders and Compounds.
- [7] ASTM B-962-08 Standard Test Methods for Density of Compacted or Sintered Powder Metallurgy (PM) Products Using Archimedes' Principle
- [8] ASTM B-213-03 - Standard Test Method for Flow Rate of Metal Powders.
- [9] Rodriguez-Carvajal J, Introduction to the Program FULLPROF: Refinement of Crystal and Magnetic Structures from Powder and Single Crystal Data
- [10] Alcobé X (2013) El método de rietveld en el caso de muestras multifásicas. Análisis cuantitativo. Aspectos prácticos y ejemplos. XIII Escuela sobre el Metodo Rietvld, Universidad Jaume I Castellón
- [11] Santiveri, C. (2016). Master dissertation (University of Barcelona). Anodizing of titanium coatings with different roughnesses, 1-67.
- [12] Nishiguchi S, Kato H, Neo M, et al (2001) Alkali- and heat-treated porous titanium for orthopedic implants. *J Biomed Mater Res* 54:198–208.

---

[13] Wei M, Kim H-M, Kokubo T, Evans JH (2002) Optimising the bioactivity of alkaline-treated titanium alloy. *Mater Sci Eng C* 20:125–134.

[14] ASTM F-1854-98 - Standard Test Method for Stereological Evaluation of Porous Coatings on Medical Implants.

[15] UNE-EN ISO 4287:1999 Especificación geométrica de productos (GPS). Calidad superficial: Método del perfil. Términos, definiciones y parámetros del estado superficial.

[16] ASTM C-633-01 - Standard Test Method for Adhesion or Cohesion Strength of Thermal Spray Coatings.

[17] ASTM 1044-99 - Standard Test Method for Shear Testing of Calcium Phosphate Coatings and Metallic Coatings.

[18] ASTM 1978-00 - Standard Test Method for Measuring Abrasion Resistance of Metallic Thermal Spray Coatings by Using the Taber Abraser.

[19] ASTM C1624-05 - Standard Test Method for Adhesion Strength and Mechanical Failure Modes of Ceramic Coatings by Quantitative Single Point Scratch Testing

[20] Nàcher M, Aubia J, Serrano S, et al (1994) Effect of cyclosporine A on normal human osteoblasts in vitro. *Bone Miner* 26:231–243.

[21] Vilardell AM, Cinca N, Jokinen A, et al (2016) Real-Time Protein and Cell Binding Measurements on Hydroxyapatite Coatings. *J Funct Biomater* 7:23.



# CHAPTER 4

## *RESULTS AND DISCUSSION*

---



## 4.1. FEEDSTOCK POWDERS AND SUBSTRATE

In chapter 3: *Raw materials and experimental procedure*, the reasons of the election of those materials were already discussed; thus, this subchapter exposes the results and the discussion of the characterization of the powders and the substrate selected for the present research. It is divided in the following parts:

- 4.1.1. Commercial pure titanium (CP-Ti) powder
- 4.1.2. Hydroxyapatite (HA) powders
- 4.1.3. Ti6Al4V alloy substrate

### 4.1.1. COMMERCIAL PURE TITANIUM POWDER

#### 4.1.1.1. Particle size distribution and flowability

Particle size and flowability are two parameters of great importance in thermal spray. Figure 4.1 shows the particle size distribution of the CP-Ti grade 2 powder in which both, differential (continuous line) and accumulative (dashed line) volume percentages are plotted. As it could be observed, particles show a broad gaussian distribution where the  $\bar{\phi}_{\text{mean}}$  is 170.1  $\mu\text{m}$ , being the  $\phi_{10}=96.3 \mu\text{m}$  and  $\phi_{90}=254.7 \mu\text{m}$ . This coarse powder was chosen in order to obtain rough titanium coatings (enclosed in 4.2.1. *Highly rough titanium coatings*).

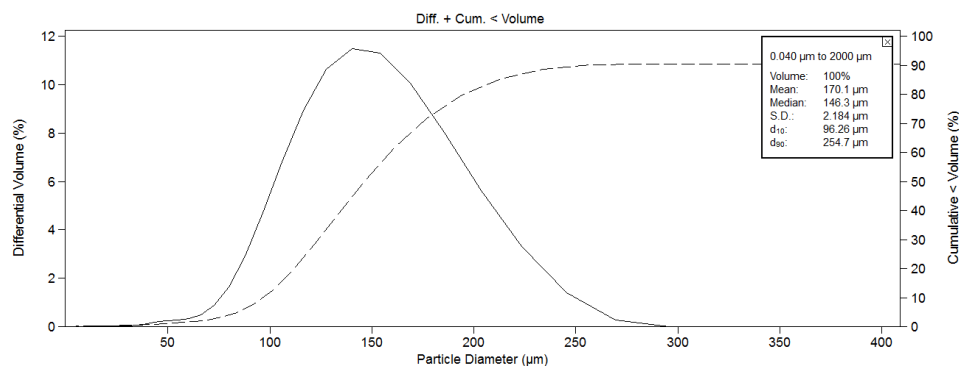


**Figure 4.1.** Particle size distribution for as-received CP-Ti powder

The flowability of a powder (i.e., their capability in flowing through the powder feeder and injection system, usually measured by the Hall flowmeter) is extremely important in all thermal spray processes. Poor flowability results in fluctuations in powder feed rate and thus in inhomogeneous coating structures [1]. CP-Ti powder shows good flowability indicating that no problems might be expected when spraying. CP-Ti powder flows through Carney and Hall

powder flowmeter funnels indicating a good flowability of the powder with a time of 9 s/50g and 47s/50g respectively.

#### 4.1.1.2. Particle morphology

CP-Ti powder presents the typical morphology obtained by attrition milling of metallic materials. The particles present an irregular morphology with angular shapes (Fig. 4.2a). At higher magnification, a nanotopography morphology consisting in surface asperities can be distinguished, which depends on the powder processing route (Fig 4.2b). Figure 4.2c and d show the scanning electron microscope (SEM) micrographs of the cross section area of the CP-Ti particles at different magnifications, showing its dense and compact microstructure.

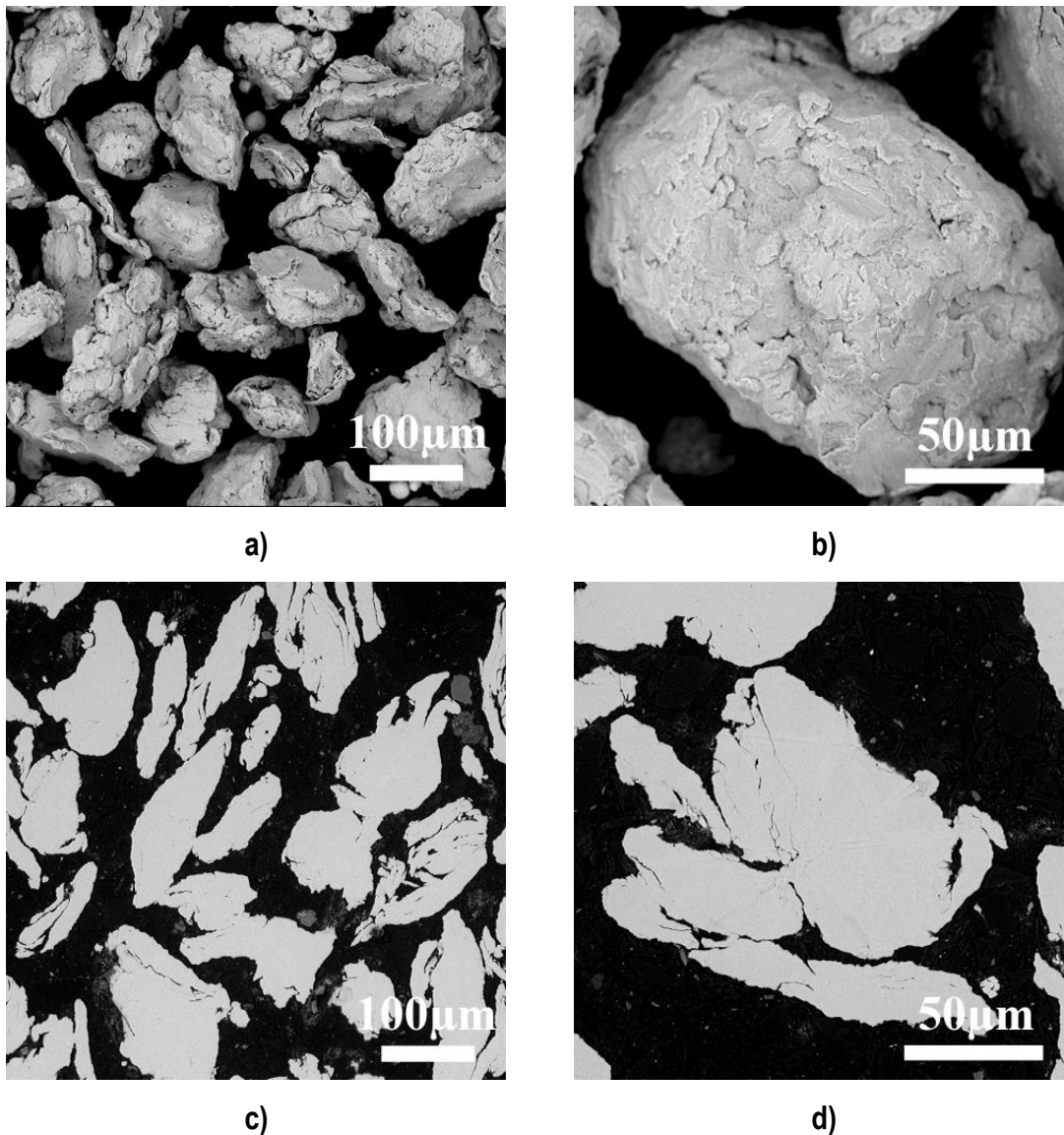


**Figure 4.2.** SEM micrographs of a-b) surface morphology and c-d) the cross section areas at different magnifications of CP-Ti feedstock powder

#### 4.1.1.3. Particle microstructure

In order to examine the features within the CP-Ti particle, a thin lamella was obtained by focused ion beam (FIB) lift-out technique (Fig. 4.3). Figure 4.4 shows the transmission electron microscope (TEM) micrographs of the lamella from a CP-Ti particle. The feedstock particles are featured by ultra-fine grained (UFG) regions indicated by dashed circles in figure 4.4 (corresponding ring Selected Area Electron Diffraction –SAED- patterns), as well as regions with grains of some tens of nanometres (dashed square). Studies reveal that significantly smaller grain size of the material can induce favourable biological responses. Exceptional improvements were seen in surface topography, wettability and in the homogeneity of the oxide layer [2]. Moreover, according to some works in the literature, UFG titanium (Ti) offers higher biocompatibility than simply CP-Ti grade 2, and also adequate mechanical behaviour. Nelson Elias et al. [3] found that an UFG Ti obtained by severe plastic deformation had a strength matching that of the Ti6Al4V alloy, commonly used in high strength structural implants, without toxic alloying elements, such as aluminum and vanadium that, by dissolving away from the implant, may be harmful to human health. The overall enhancement in mechanical and biological performance means that this material can be used in most biomedical applications of the conventional Ti6Al4V alloy.

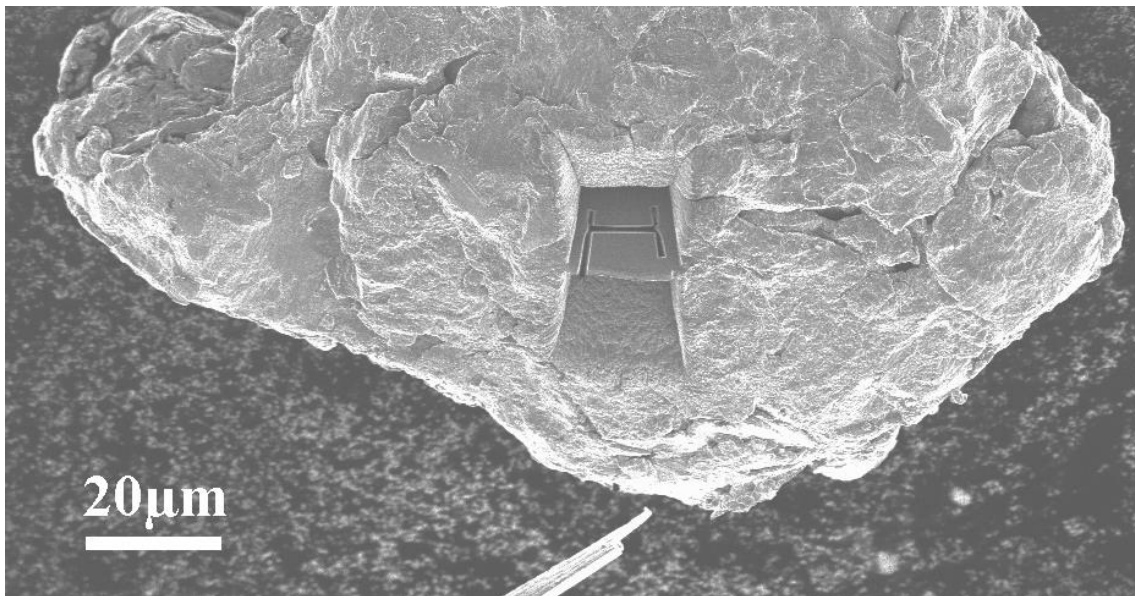


**Figure 4.3** SEM micrograph from the FIB preparation lamella of a CP-Ti particle

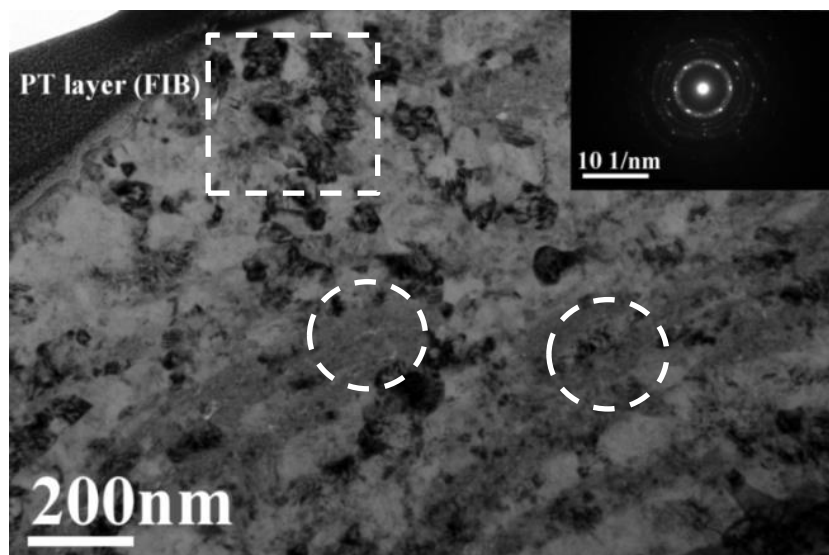


**Figure 4.4.** TEM features of CP-Ti particle at different magnifications. Circles indicate nanocrystalline regions (ring SAED pattern) while the square indicates grains of some tens of nanometres.

#### 4.1.1.4. Phase composition: X-ray diffraction analysis

Figure 4.5 shows the x-ray diffraction (XRD) pattern of the CP-Ti powder. No other elements except Ti were found. By using the FullProf software, a fitting procedure was applied in order to calculate the crystallite size according to de Scherrer equation (see appendixes). The average of the crystallite size of CP-Ti powder was calculated to be about 21 nm, matching with the results observed by TEM in figure 4.4.

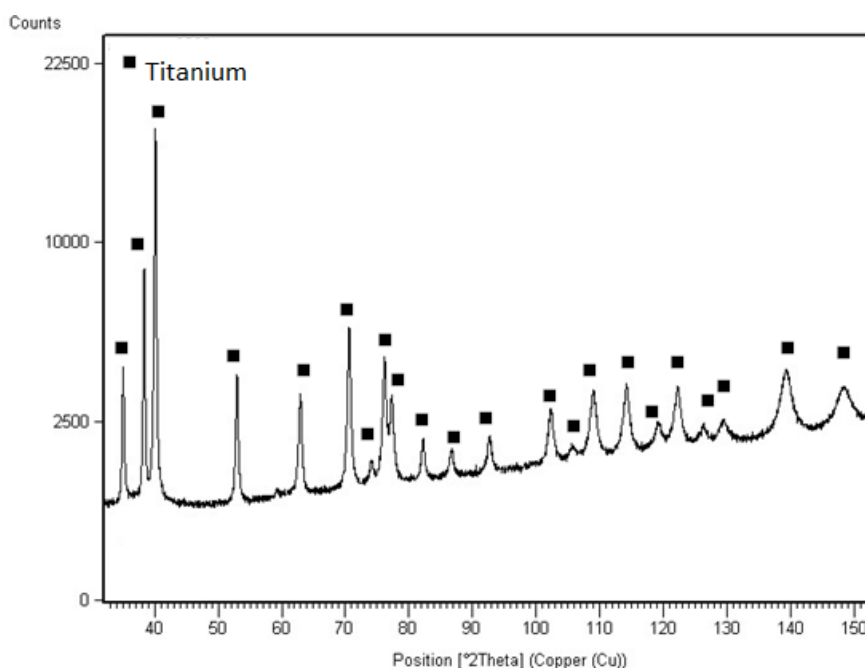


**Figure 4.5.** XRD of CP-Ti powder

## 4.1.2. HYDROXYAPATITE POWDERS

### 4.1.2.1. Particle size distribution

#### Sintered HA powder

Figure 4.6a shows the particle size distribution of the sintered HA as-received powder with  $\bar{\phi}_{\text{mean}}$  of 28.2  $\mu\text{m}$ , being the  $\phi_{10}$ =16.4  $\mu\text{m}$  and  $\phi_{90}$ =52.8  $\mu\text{m}$ . A tail of submicron particles up to 10  $\mu\text{m}$  and a tail of coarse particles from 60  $\mu\text{m}$  to 140  $\mu\text{m}$  can be observed in volume percentage. Figure 4.6b shows the differential number percentage of particles versus particle diameter percentage, where it can be clearly observed that there is a high amount of particles under 1  $\mu\text{m}$  particle size.

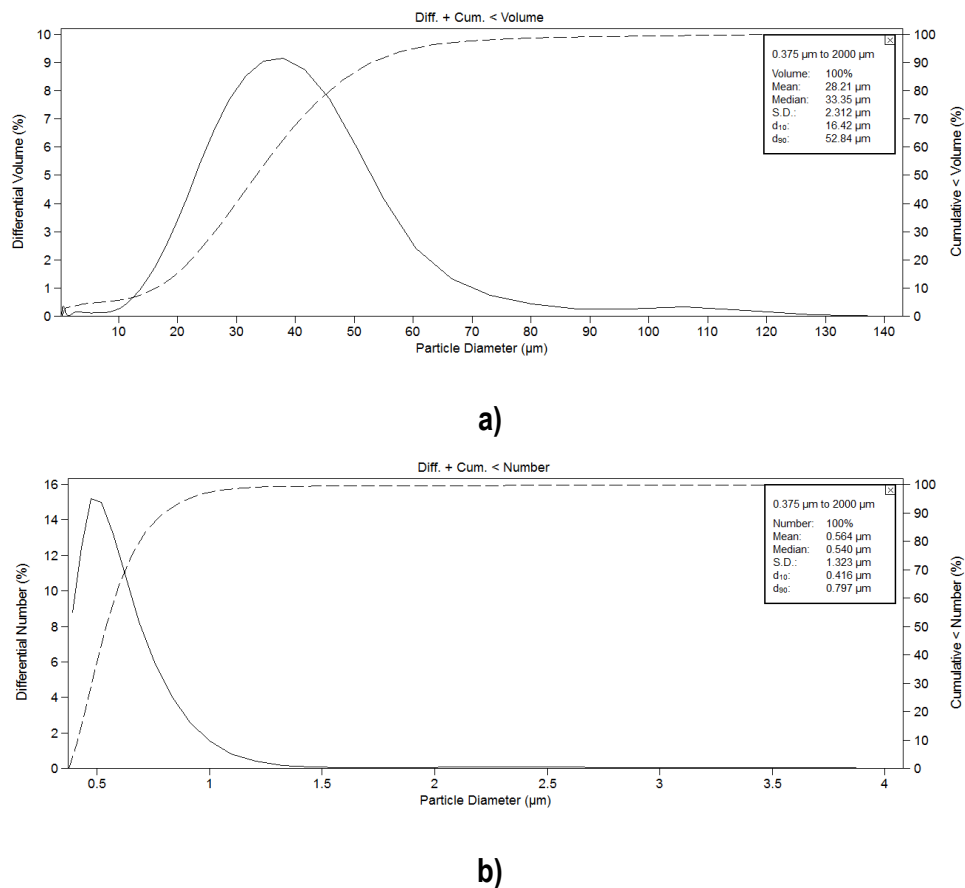


**Figure 4.6.** Particle size distribution of the as-received sintered HA powder graphed with a) differential volume and b) differential number percentages as a Y axis versus particle diameter

As it was observed that sintered HA powder has a bad flowability, it was sieved in order to eliminate the cue of fine HA particles. As it was hard to separate the fine particles from the as-received powder with a dry-sieving procedure, the sieving was performed in wet

conditions. The suspension of the wet-sieving was formulated by taking 20 wt. % of dry powder with 40 wt. % distilled water and 40 wt.%ethanol [4,5]. Figure 4.7 shows the particle size distribution of sintered HA powder after wet-sieving between 40-20 $\mu\text{m}$  size diameter. Either in differential volume (Fig. 4.7a) or differential number (Fig. 4.7b), the percentages of sintered HA particles show narrower peaks, in comparison with the as-received sintered HA powder. After the wet-sieving, fine and coarse particles were removed from the as-received feedstock powder, offering this time  $\bar{\phi}_{\text{mean}} = 32.8 \mu\text{m}$ , being the  $\phi_{10} = 26.4 \mu\text{m}$  and  $\phi_{90} = 40.2 \mu\text{m}$  in differential volume percentage.

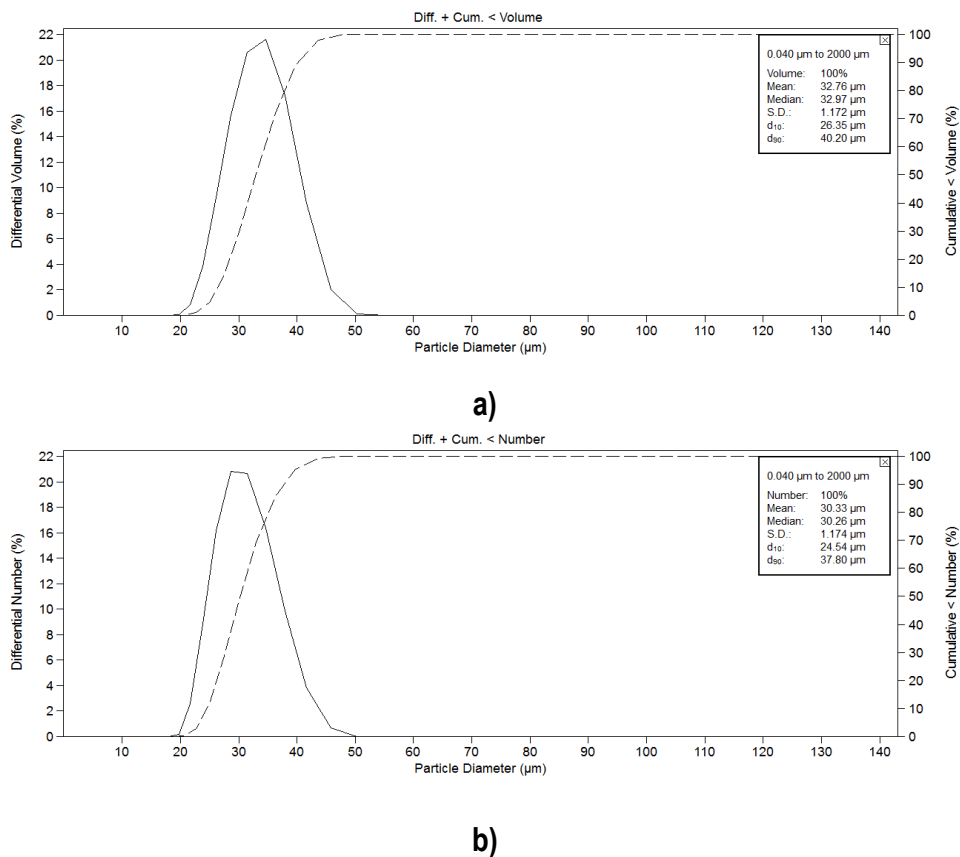


**Figure 4.7.** Particle size distribution of the as-received sintered HA powder after wet-sieving graphed with a) differential volume and b) differential number percentages as a Y axis versus particle diameter

### Agglomerate HA powder

Figure 4.8 shows the particle size distribution of the as-received agglomerate HA powder in which both, differential (continuous line) and accumulative (dashed line) volume percentages are plotted. As it could be observed, the particles show a broad distribution where the  $\bar{\phi}_{\text{mean}}$  is

33.0  $\mu\text{m}$ , being the  $\text{Ø}_{10}$ =22.7  $\mu\text{m}$  and  $\text{Ø}_{90}$ =56.4  $\mu\text{m}$ . It could be observed a tail of fine particles up to 15  $\mu\text{m}$  and a coarse tail of coarse particles from 80  $\mu\text{m}$  to 140 $\mu\text{m}$ .

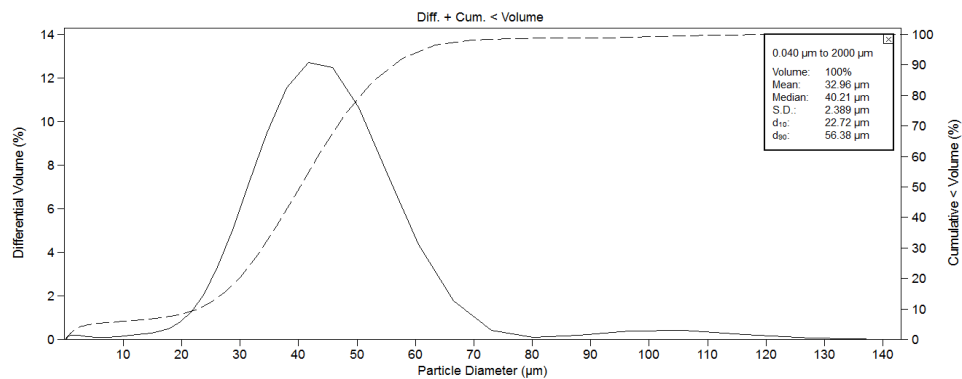


**Figure 4.8.** Particle size distribution of the as-received agglomerate HA powder graphed with differential volume as a Y axis versus particle diameter

The agglomerate HA powder was dry-sieved between 63-40  $\mu\text{m}$  and 40-20  $\mu\text{m}$  in order to achieve a narrowest particle size distribution and a more homogeneous particle velocity (Fig. 4.9). Despite the presence of a fine tail of particles, the agglomerate HA powder was not wet sieved due to its good flowability. The respective diameters for both range size fractions are:  $\text{Ø}_{\text{mean}}$  is 36.4  $\mu\text{m}$ , being the  $\text{Ø}_{10}$ =28.7  $\mu\text{m}$  and  $\text{Ø}_{90}$ =57.2  $\mu\text{m}$  for the 60-40  $\mu\text{m}$  particle size fraction and  $\text{Ø}_{\text{mean}}$  is 24.5  $\mu\text{m}$ , being the  $\text{Ø}_{10}$ =16.9  $\mu\text{m}$  and  $\text{Ø}_{90}$ =40.7  $\mu\text{m}$  for the 40-20  $\mu\text{m}$  particle size fraction.

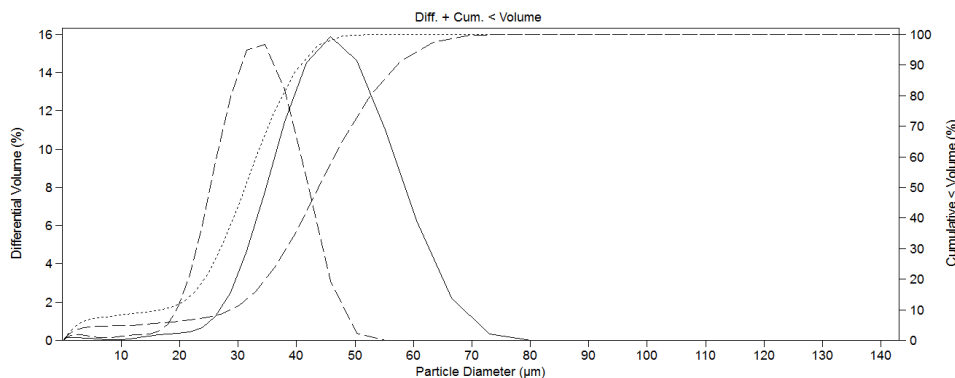


**Figure 4.9.** Particle size distribution of the agglomerate HA powder after dry-sieving between 63-40  $\mu\text{m}$  and 40-20  $\mu\text{m}$  graphed with differential volume as a Y axis versus particle diameter

#### 4.1.2.2. Flowability

The flowability of the HA powders was tested before and after the sievings (Table 4.1). The as-received sintered HA powder does not flow in any of both, Carney and Hall powder flowmeter funnels, however, after the sieving process between 40-20  $\mu\text{m}$  particle size

diameter, an improvement of flowability was observed due to the removal of the fine and coarse particles. On the other hand, the as-received agglomerate HA powder has better flowability than the as-received sintered HA powder. Even so, an improvement of flowability after sieving between 63-40  $\mu\text{m}$  was observed.

**Table 4.1.** Flowability of HA powders before and after the sieving with Carney and Hall funnels

	<b>Carney powder flowmeter funnel</b>	<b>Hall powder flowmeter funnel</b>
	<i>Flow Rate 3 Avg. (s/50 g)</i>	<i>Flow Rate 3 Avg. (s/50 g)</i>
<b>Sintered HA as-received</b>	Does not flow	Does not flow
<b>Sintered HA (40-20 <math>\mu\text{m}</math>)</b>	22"	2'32"
<b>Agglomerate HA as-received</b>	1'05"	19'49"
<b>Agglomerate HA (63-40 <math>\mu\text{m}</math>)</b>	1'00"	6'45"
<b>Agglomerate HA (40-20 <math>\mu\text{m}</math>)</b>	1'39"	Does not flow

#### 4.1.2.3. Particle morphology

##### Sintered HA powder

The micrographs in figure 4.10a display the morphology of the sintered HA powder; the magnified structure shows better the grain and porous morphology (Fig. 4.10b); these sintered HA particles are formed by small crystalline grains. Figure 4.10c shows the cross section area of sintered HA particles showing its intern and interconnected porosity (Fig. 4.10d).

The powder microstructure also affects the mechanism of particle deposition. It should be said that the use of dense and spherical particles for spraying would result in much better flowability in thermal spray, inducing more regular powder feed rate. The use of different porous HA powders in the present research (sintered and agglomerate HA powders), will allow the understanding of ceramic feedstock powders by CS, in terms of particle microstructure and deposition mechanism onto a substrate.

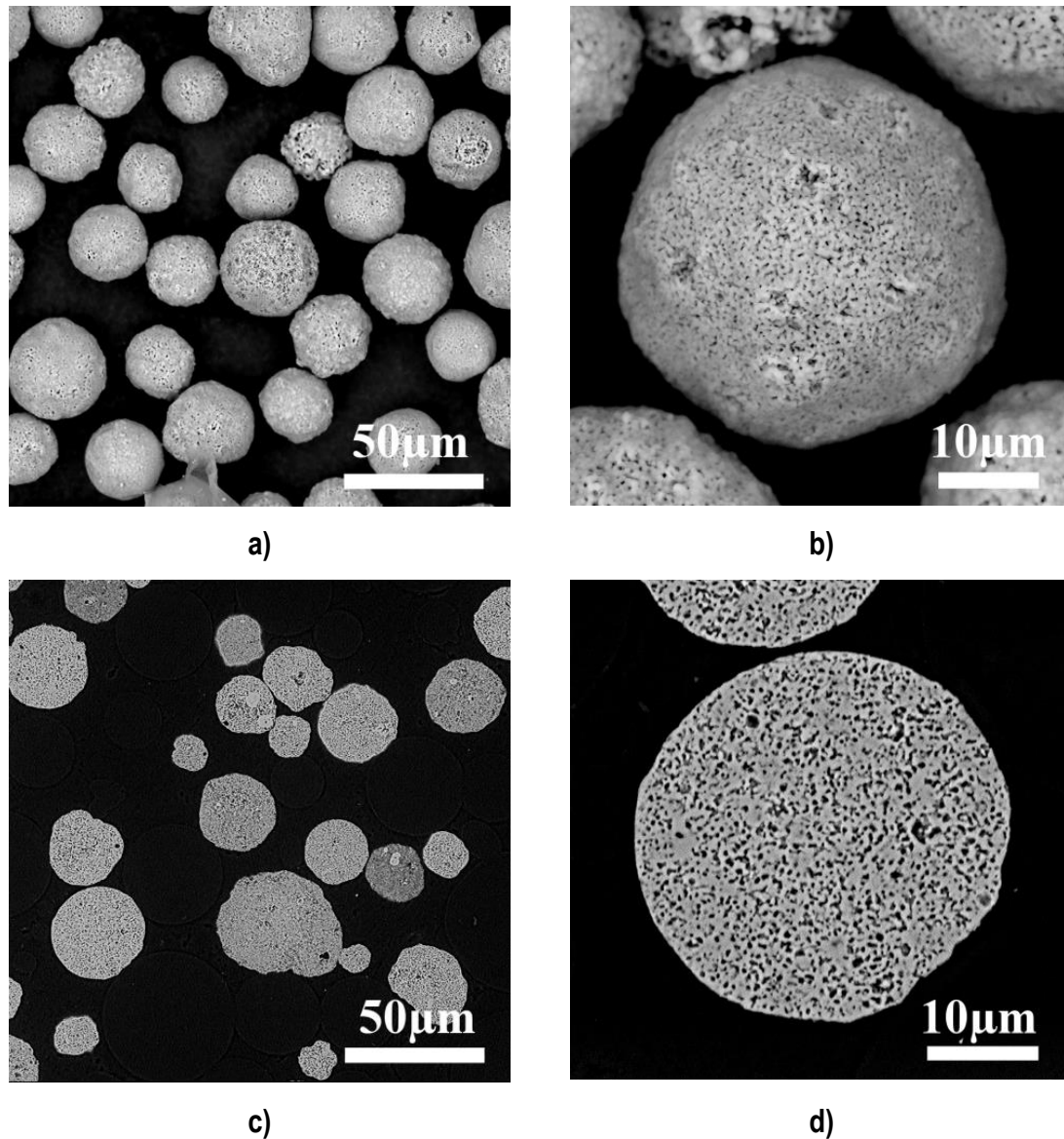


**Figure 4.10.** SEM micrographs of a-b) surface morphology and c-d) cross section areas at different magnifications of sintered HA powder

### **Agglomerate HA powder**

The SEM micrographs in figure 4.11a-b display the morphology of the agglomerate HA particles at different magnifications; the spherical particle morphology appears to be composed of very fine agglomerates (zoom in fig. 4.11b). The cross section area is shown in figure 4.11c showing the non-homogeneous interconnected porosity microstructure of the particle (Fig. 4.11d).

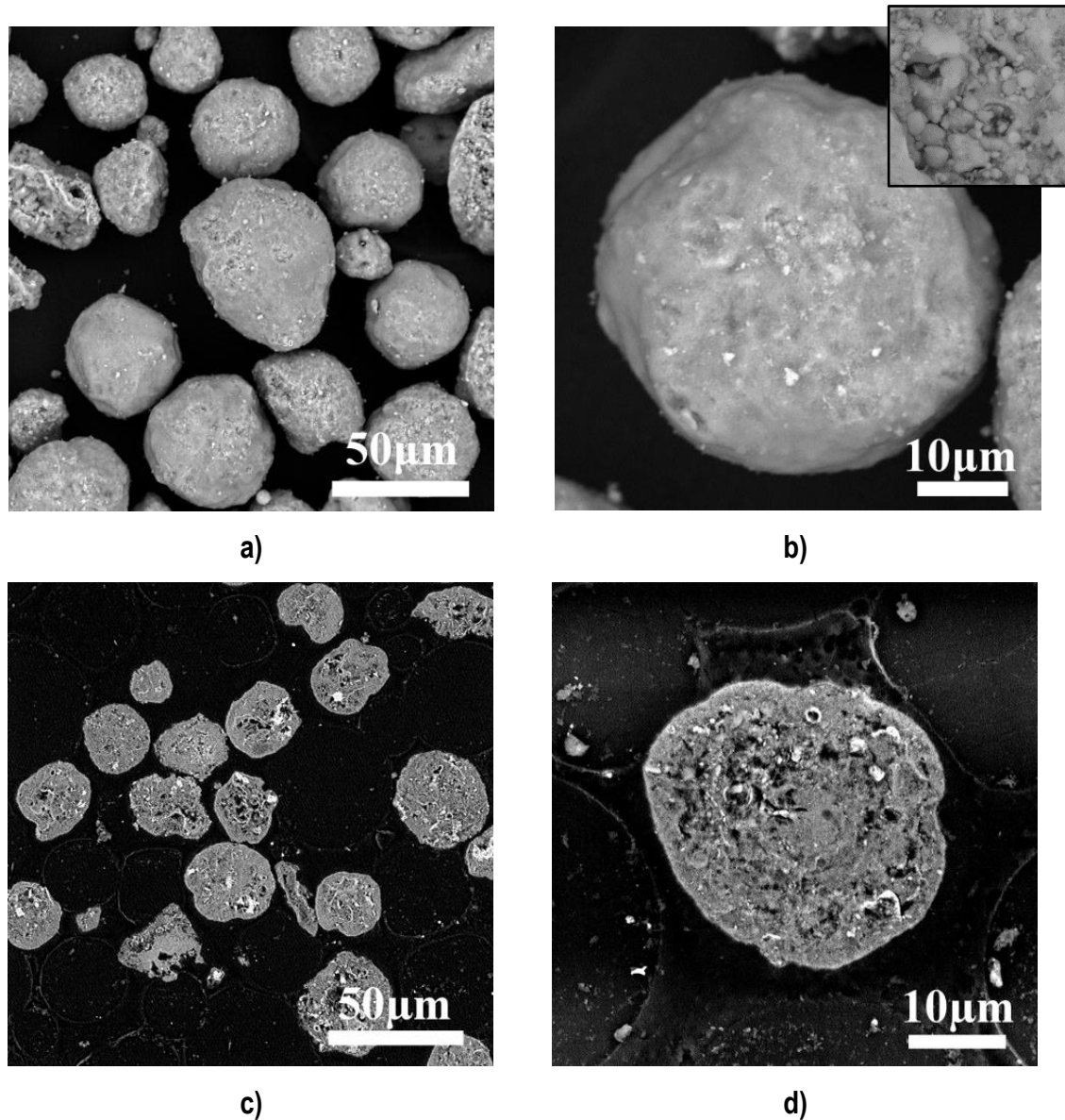


**Figure 4.11.** SEM micrographs of a-b) surface morphology and c-d) cross section areas at different magnifications of agglomerate HA powder

#### 4.1.2.4. General features of hydroxyapatite particles

The free surface areas were measured by Brauner-Emmett-Teller (BET) method and have values of 1.39 m<sup>2</sup>/g for sintered HA and 88.61m<sup>2</sup>/g for agglomerate HA powders. The HA feedstock powder densities were measured according to their respective American Society for Testing Materials (ASTM) standard specifications [6,7,8] and are shown in table 4.2.

**Table 4.2.** Density values of HA powders

	$\rho_{\text{Apparent}} \text{ (g/cm}^3\text{)}$	$\rho_{\text{vibrated}} \text{ (g/cm}^3\text{)}$	$\rho_{\text{real}} \text{ (g/cm}^3\text{)}$
<b>Sintered HA</b>	1.036	1.26	3.001
<b>Agglomerate HA</b>	0.469	0.473	0.485

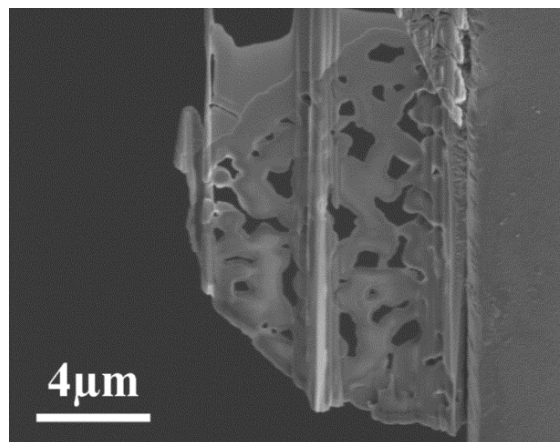
The higher BET and the low density of the agglomerate HA powder match with the morphology of the particle and its microstructure, indicating the higher porosity in comparison with the sintered HA powder.

An energy dispersive spectroscopy (EDS) analysis for the two powders indicated a Ca/P ratio of 1.87 and 1.76 for the sintered HA and agglomerate HA powders respectively. Considering that a stoichiometric HA has a Ca/P ratio of 1.67, this indicates that they could directly bond to bone in contrast to calcium phosphates that have lower ratio of Ca/P than 1.4 [9]. The large value of the sintered HA powder is related to the sintering process [10]. This would indicate that the phase stability of calcium rich HA was disrupted when sintered at high temperatures.

#### 4.1.2.5. Particle microstructure

##### Sintered HA powder

The particle microstructure was evaluated in terms of TEM. In order to examine the features within the particle, a thin lamella was obtained by FIB lift-out technique (Fig. 4.12). The interconnected porous structure could be well observed through FIB along preparation time. No pore size extension was observed as result of the process preparation.

**Figure 4.12.** FIB preparation lamella of a sintered HA particle

The grain structure of sintered HA powder consists in small equiaxed grains, with an average grain size diameter of 0.5–2  $\mu\text{m}$ , illustrated in the TEM micrograph in figure 4.13a. Some dense parts were seen with triple boundary points. The SAED pattern of a single grain is presented, showing a monocrystalline structure (Fig. 4.13a). The grain boundaries are well delineated by curved original flaws with a wavy nature. No amorphous secondary phases were observed at any of the triple points investigated, but rather Moiré fringes in addition to lattice fringes, resulting from the overlap of crystalline regions (Fig. 4.13b). Some grains are connected by necks (Fig. 4.13c). It is also illustrated in the magnification of one of these neck-grain interfaces (Fig. 4.13d); it shows a bubble-like structure, which might come from some damage resulting from irradiation. More likely, the SAED indicates that most grains have a single-crystal structure.

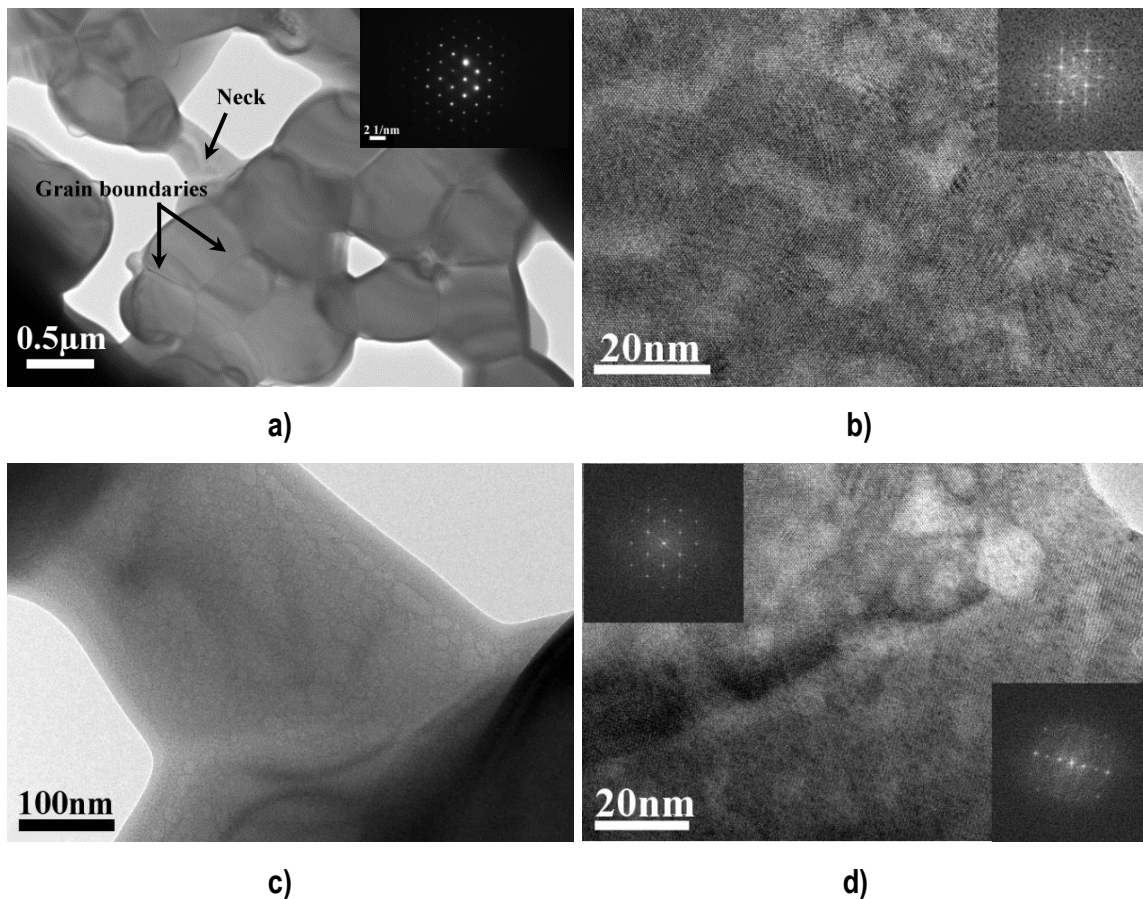


**Figure 4.13.** a-b) TEM micrograph of the sintered HA particle and SAED pattern, b) neck morphology and, detailed features of the c) neck and d) neck-grain interface structure

### Agglomerate HA powder

The agglomerate HA particle shows different kind of porosity in comparison with the sintered HA particle due to the different methods of powder production. Figure 4.14 shows the lamella of the agglomerate HA article obtained by FIB lift-out technique showing a porous texture.

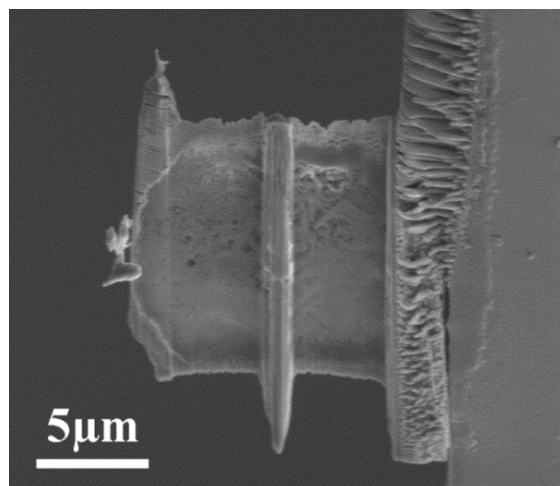


**Figure 4.14.** FIB preparation lamella of a agglomerate HA particle

The TEM micrographs actually reveal a structure consisting of a needle-like morphology (Fig. 4.15a) whose electron diffraction exhibits a ring pattern denoting its nanocrystalline nature (Fig. 4.15b). At higher magnification, particle superposition becomes apparent, leading to the observation of Moiré fringes (Fig. 4.15c). It is, however, quite obvious the analogy with other works reporting these morphologies as a result of the reaction between calcium hydroxide and ortho-phosphoric acid:  $5\text{Ca}(\text{OH})_2 + 3\text{H}_3\text{PO}_4 \rightarrow \text{Ca}_5(\text{PO}_4)_3(\text{OH}) + 9\text{H}_2\text{O}$  [11]. Upon heating the as-supplied powder at temperatures above 800°C, the structure completely changed from needle-like to spheroidal, as shown in figure 4.15d [12].

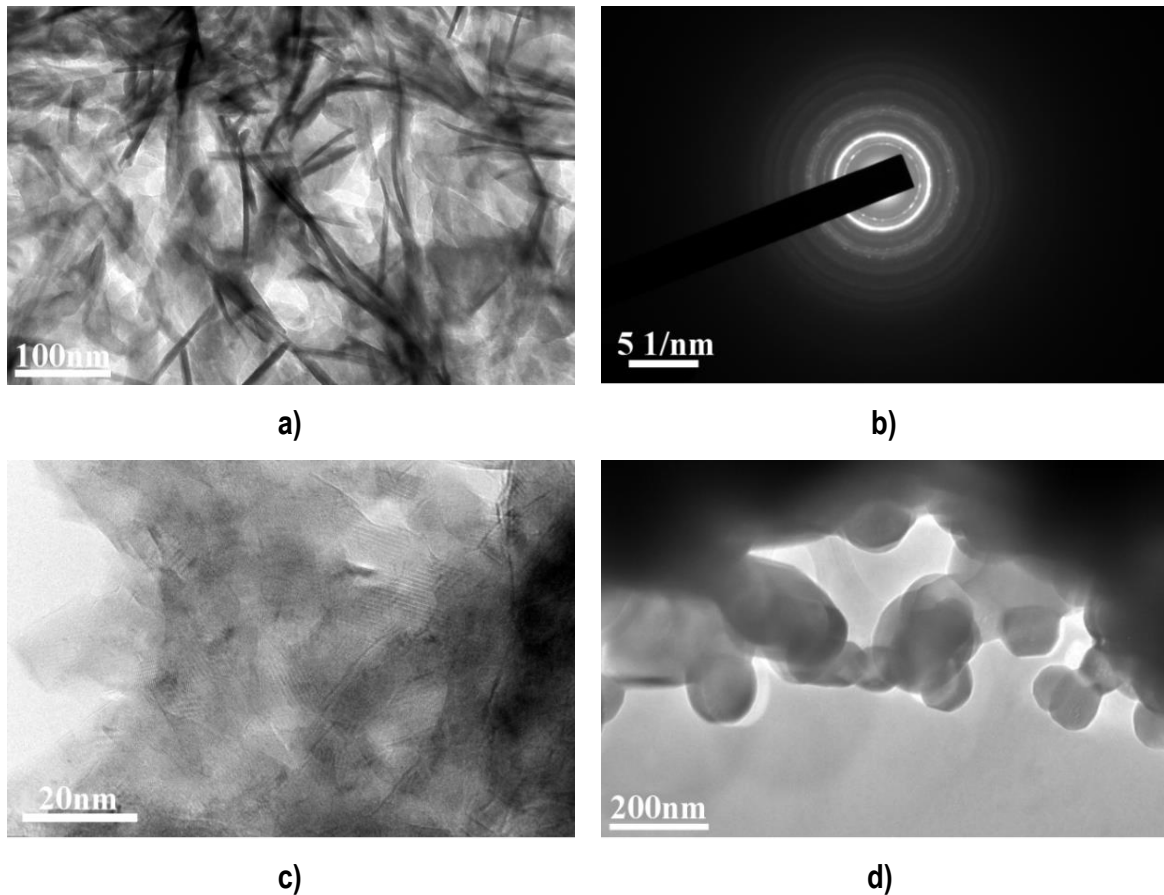


**Figure 4.15.** a-b) TEM micrographs and SAED pattern of HA-particle and c) TEM micrographs of HA-particle upon heating above 800°C

#### 4.1.2.6. Phase composition: X-ray diffraction analysis

##### Sintered HA powder

Figure 4.16 shows the XRD of the sintered HA powder with very narrow peaks indicating its high crystallinity. It has been well identified according to the 9–432 pattern corresponding to a hexagonal P63/m lattice.

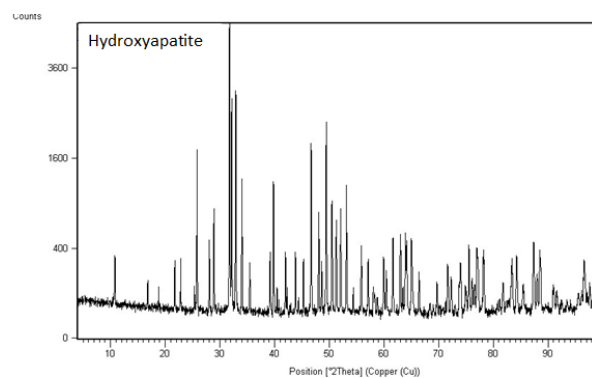


**Figure 4.16.** XRD of the sintered HA powder

However, a slight shift is observed between the pattern from the database and our pattern; this is because of some differences in the cell parameters. The 9-432 joint committee on powder diffraction standards (JCPDS) pattern has  $a=b=9.418$  Å and  $c=6.884$  Å. Table 4.3 shows a list with the most intense peaks, their  $2\theta$  values and the calculated “a” and “c” parameters according to the following equation 4.1:

$$\text{(eq. 4.1)} \quad \frac{1}{d_{hkl}^2} = \left[ \frac{4}{3} (h^2 + k^2 - hk) + l^2 \left( \frac{a}{c} \right)^2 \right] \frac{a^2}{a^2}$$

**Table 4.3.** Calculated parameters of most intense peaks of sintered HA

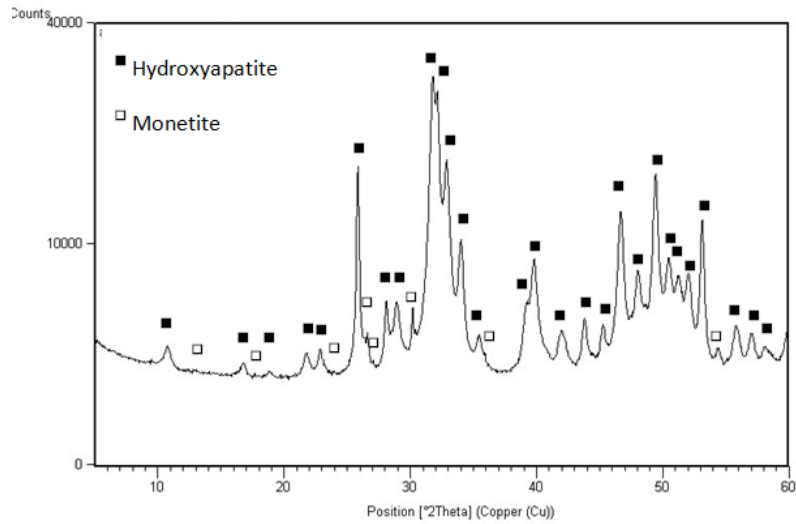
<b>h k l</b>	<b>2θ</b>	<b>a</b>	<b>c</b>
<b>0 0 2</b>	25.84		
<b>2 1 1</b>	31.77	9.416	6.888
<b>1 1 2</b>	32.17		

As mentioned before in the TEM micrographs, the SAED pattern indicates that most grains have a single-crystal structure, leading to a submicrometric average size for the HA phase to be about 1-2µm.

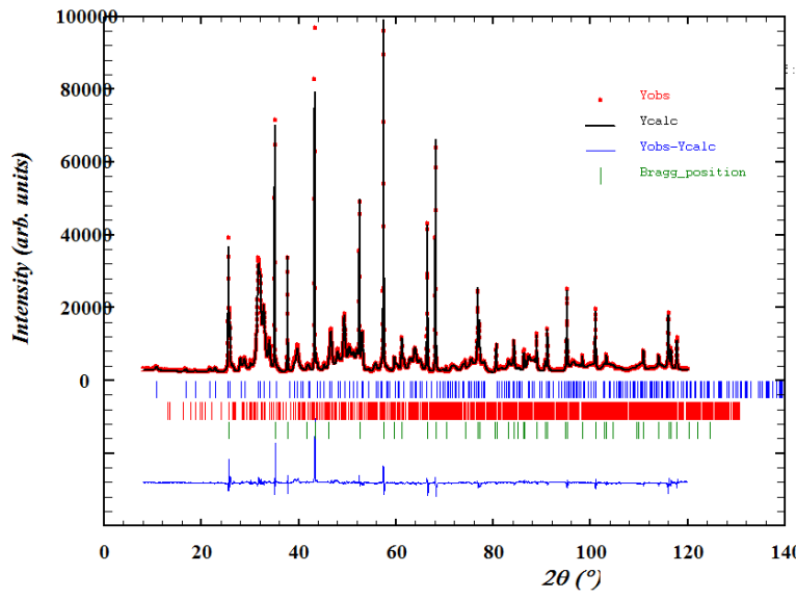
### **Agglomerate HA powder**

Figure 4.17a shows the XRD pattern of the agglomerate HA powder with broad peaks, more likely as a consequence of the very small crystallite size. The identification revealed the presence of the 9-432 JCPDS HA syn. pattern corresponding to a hexagonal P63m/lattice, as well as the 9-080 JCPDS pattern, which corresponds to the monetite phase, a calcium hydroxide phosphate with triclinic lattice.

By using the FullProf software and Rietveld procedure (see appendixes), the XRD pattern was refined (Fig. 4.17b) and the content of the HA phase was found to be 88.65 %, the monetite phase 3.78 % and the amorphous phase 7.56 %. Table 4.4 shows that the refined lattice dimensions are very similar to the pattern ones. A final crystal value of 13.8 nm was found for the HA phase. According to the fitted parameters, an average crystal size for the monetite was calculated to be about 63 nm.



a)



b)

Figure 4.17. a) XRD and b) Rietveld analysis of agglomerate HA powder

Table 4.4. Outcomes of Rietveld's Method

	Hydroxyapatite	9-432 pattern	Monetite	9-0080 pattern
a (A)	9.4286	9.4180	6.9047	6.9060
b (A)	9.4286	9.4180	6.6416	8.5770
c (A)	6.8920	6.8840	7.0014	6.6340
α (°)	90	90	96.423	93.990
β (°)	90	90	103.873	91.500
γ (°)	120	120	88.514	127.60

## 4.1.2.7. Phase transformation: Fourier transform infrared spectroscopy

## Sintered and agglomerate HA powder

The fourier transform infrared spectroscopy (FTIR) spectrum of sintered (Fig. 4.18) and agglomerate HA (Fig. 4.19) powders contain characteristic phosphate, carbonate and hydroxyl bands as presented in table 4.5. Theoretically, there are four vibrational modes present for phosphate ions,  $\nu_1$ ,  $\nu_2$ ,  $\nu_3$  and  $\nu_4$ . The phosphate  $\nu_1$  band is present at 961-962  $\text{cm}^{-1}$  corresponding to non-degenerate symmetric P-O stretching, whereas the  $\nu_3$  region between 1190-976  $\text{cm}^{-1}$  corresponds to anti-symmetric P-O stretching and the  $\nu_4$  bands at 560, 598 and 629  $\text{cm}^{-1}$  corresponding to triply degenerated O-P-O bending for sintered HA and 560, 600 and 629 for agglomerate HA.  $\nu_2$  is not found in FTIR spectrum because of its wave number ( $\text{cm}^{-1}$ ) is below the minimum of data spectrum [13]. Theoretically, carbonate ions have four vibrational modes, in which three of them can be observed in the infrared spectrum and two in Raman spectrum. Carbonate bands  $\nu_3$  and  $\nu_2$  are located in the region of 1650-1300  $\text{cm}^{-1}$  and at 875  $\text{cm}^{-1}$  respectively, but for sintered HA it was not found a  $\nu_2$  band. Despite not distinguished by XRD, the presence of carbonate ions may come from a reaction between carbon dioxide in air and the high pH precursor solution in powder production [14]. Finally, the sharp band at 3569  $\text{cm}^{-1}$  corresponds to the stretching mode of hydroxyl vibrations.

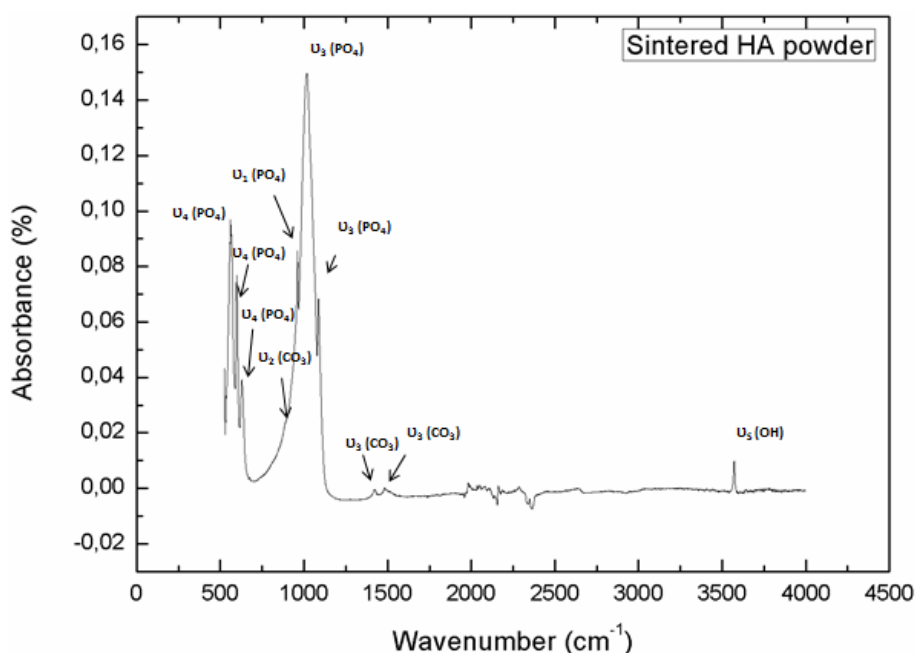


Figure 4.18. FTIR spectrum of sintered HA powder

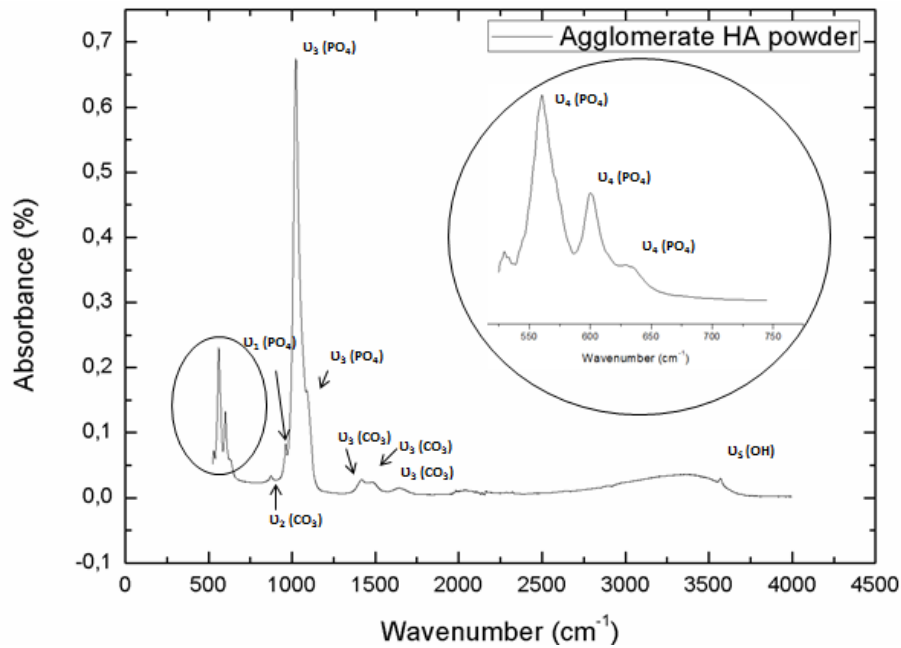


Figure 4.19. FTIR spectrum of agglomerate HA powder

Table 4.5. Infrared band positions for sintered and agglomerate HA powders

	Sintered HA powder	Agglomerate HA powder
<b>Hydroxyl stretch</b>	3571	3569
<b>Carbonate <math>\nu_3</math></b>		1650-1300
- (m)	-	1641
- (m)	1483	1448
- (m)	1420	1417
- (m)	-	-
<b>Phosphate <math>\nu_3</math></b>	1190-976	1190-976
- (vs)	1087	1088
- (vs)	1016	1023
<b>Phosphate <math>\nu_1</math> (m)</b>	961	962
<b>Carbonate <math>\nu_2</math> (ms)</b>	-	875
<b>Phosphate <math>\nu_4</math></b>	660-520	660-520
- (m)	629	629
- (vs)	598	600
- (vs)	560	560

### 4.1.3. Ti6Al4V ALLOY SUBSTRATE

The Ti6Al4V alloy substrates have  $\alpha+\beta$  biphasic microstructure, in which consist in ~70% of  $\alpha$ -phase (hexagonal close packed –HCP-) and ~30% of  $\beta$ -phase (body centred cubic -BCC). Figure 4.20 shows optical micrograph, the light regions are the  $\alpha$ -phase and dark regions the  $\beta$ -phase [15]. This microstructure is typical from mill-annealed structure. This structure

presents a good combination of resistance, toughness, ductility and fatigue resistance. These structures are the result from a hot deformation of the material in the range of temperatures in which  $\alpha$  and  $\beta$  are stable (600°C, 2h) [16].

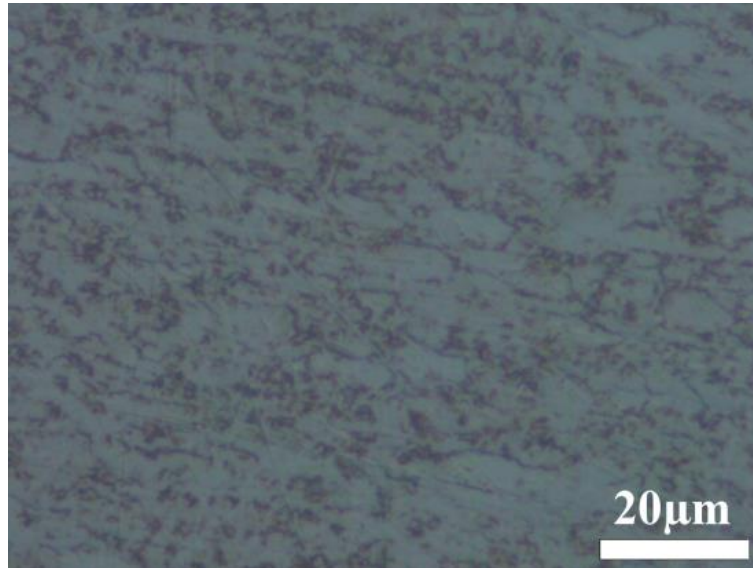


**Figure 4.20.** Optical microscope micrograph of mill-annealed Ti6Al4V alloy

## **4.2. COATINGS**

This subchapter exposes the results and discussion of the coatings production and characterization from the powders analysed in the previous subchapter. The parts that compound this subchapter are:

- 4.2.1. Highly rough titanium coatings
- 4.2.2. Nanotexturing surface treatments on highly rough titanium coating
- 4.2.3. Hydroxyapatite coatings
- 4.2.4. Biological properties of the coatings

All parts include an introduction explaining the novelty of each part.

The three first parts include the production of those coatings, mainly by cold spray (CS) and their functionalization by posterior surface treatments that affect the surface composition and topography at the nanoscale as well. Some mechanical properties are included as well to evaluate if the system accomplishes the medical standards.

The biological characterization of the coatings is not included in each part; it is included as the fourth part of this subchapter. The reason is because the in vitro testing was analyzed in terms of comparative results among the different coatings. For that reason, it was preferred not to expose the results in an individual form. All in vitro results were performed comparing coatings to see which have better biological properties.

### **4.2.1. HIGHLY ROUGH TITANIUM COATINGS**

#### **4.2.1.1. Introduction**

Titanium is one of the metals that has been quite largely studied for its deposition by CS due to its potential in aeronautical and aerospace industry [17] as well as anodic protection in corrosive environments [18] and in dimensional restoration and repair fields. These applications mainly require the formation of dense coatings. This has been quite easy from the beginning for ideal materials with relatively low melting points, high densities, low mechanical strength and low heat capacities such as zinc and copper; for others, more expertise and development has been needed. In the Ti case, it has been influenced by: (i) its high strength to weight ratio but relative low deformability due to its hexagonal close-packed crystal structure, (ii) the noticeable flow stress rate sensitivity and strain hardening at high strain rates, (iii) low thermal softening sensitivity and, (iv) the disruption of oxide layers to promote metallurgical contacts [19]. Dense coatings could be achieved with small sized particles (16  $\mu\text{m}$ ) using helium gas [20]. Nevertheless, this is still quite a handicap when using nitrogen whatever the particle size is. Actually, it has been mostly observed the formation of a gradual increasing porosity from the inner part of the coatings to the outer part due to the lower tamping effect of the top-layer [21].

However, a CS porous Ti coating could be quite useful in biomedical applications [22], to be compared to the existing porous metallic plasma spray coatings e.g. titanium and tantalum. In this case, the final application would demand for a different microstructure. The strategy here used for such purpose has been employing large sized irregular particles. Van Steenkiste et al. [23] used a new nozzle configuration to be able to successfully deposit aluminum particles in the range between 63 and 106  $\mu\text{m}$ , but in their case to obtain dense coatings. Using coarse particles to produce porous coatings is easier than using small particles due to their lower velocities and wider gaps to be filled between the deposited particles during spraying.

In addition, large dimensions involve lower cooling rates as well as lower strain-rates and thus lower strain-rate hardening. All these facts, considering also the low thermal diffusivity of Ti which facilitates the local retention of interfacial heating, may favor the occurrence of shear instabilities and therefore better bonding at the contact points; the formation of adiabatic shear instabilities has been reported to be the mostly accepted bonding mechanism in CS [24]. Moreover, in this particular case, two other key points must further be considered. One is that because of the irregular shape of the feedstock, particles accelerate more easily due to an increased drag force acting on the particle and second, also due to the particle morphology, it may promote non-uniform contact points upon impact and even not being able to well remove the oxide layers [25]. Actually, CSIRO/Australia, for example, reported that irregular Ti powders, despite less common, were better for CS than the spherical ones [26].

Direct comparison just with these reported studies is difficult since here coarse particles are used; larger particle diameters result in higher kinetic energies but their velocities are much slowed down. For a particle to stick, all of its kinetic energy must be transformed into heat and strain energy of the coating and substrate requiring an inelastic collision process such as plastic deformation for the particle and the substrate [23]. If the incident particle velocity is too low, the yield strength of the particle and/or substrate material would not be exceeded and the particle would not stick, whereas if the velocity is too high then the particle might not be able to transfer all of its kinetic energy via its plastic deformation, and the particle could bounce off [23,27]. Due to the relatively broad particle distribution used in the present case, particles acquire different a wide range of velocities; if the particles reach a given velocity, called “critical velocity” (see appendixes), they can bind to the surface and create a coating. This velocity is clearly dependent on both sprayed material and substrate properties. Those particles with a velocity smaller than critical velocity, would not contribute or only a few to coating formation [23]. Contrary, particles with much higher velocities would erode or bounce off the substrate.

So, this part of the subchapter is focused on the development of highly rough and porous CP-Ti coatings by CS according to the ASTM standard specifications for joint prosthesis.

#### 4.2.1.2. Spraying conditions

A factorial design  $3^2$  was used to understand the influence of the main parameters on coating production: Gas temperature and gas pressure. Three temperatures (200-800°C) and three pressures (10-40 bars) were chosen, while parameters such as spraying distance, powder feeding rate and traverse speed were kept constant in order to better understand the effect of the chosen parameters. A total of 9 samples (sample 1 to sample 9) were obtained in the factorial design  $3^2$  (Fig. 4.21).

---

*As highly rough titanium coatings were protected by an intellectual property [22], spraying conditions were expressed in terms of  $T_{x(number)}$  (temperature) and  $P_{x(number)}$  (pressure).*

---

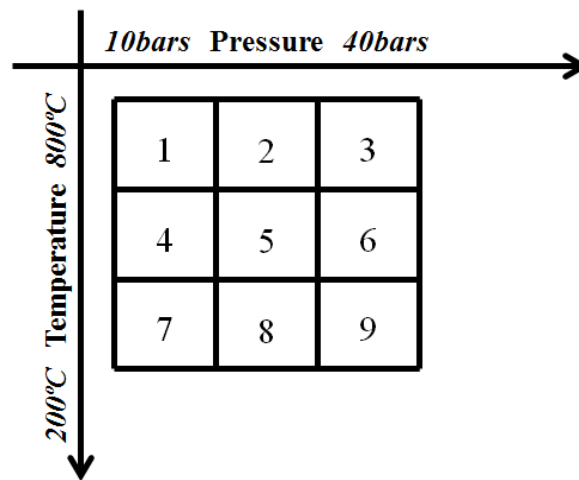


Figure 4.21. Factorial design  $3^2$  of CS CP-Ti coatings (Samples 1 to 9)

#### 4.2.1.3. Coating characterization

##### a) Correlation of spraying parameters with bonding features

The CP-Ti coarse particles were sprayed onto Ti6Al4V alloy substrates in order to achieve high roughness. According to the factorial design (Fig. 4.21), particles were named from sample 1 to sample 9. Figure 4.22 displays the respective cross section micrographs of the samples according to the factorial design. It could be observed that for all spraying parameters deposition was achieved. In all cases, except for sample 7 (Fig. 4.22g), cross section areas show partial descohesion at the interface substrate-coating, affecting the

mechanical reliability properties, due to the much lower or higher particle velocities in comparison with the critical velocity (see appendixes).

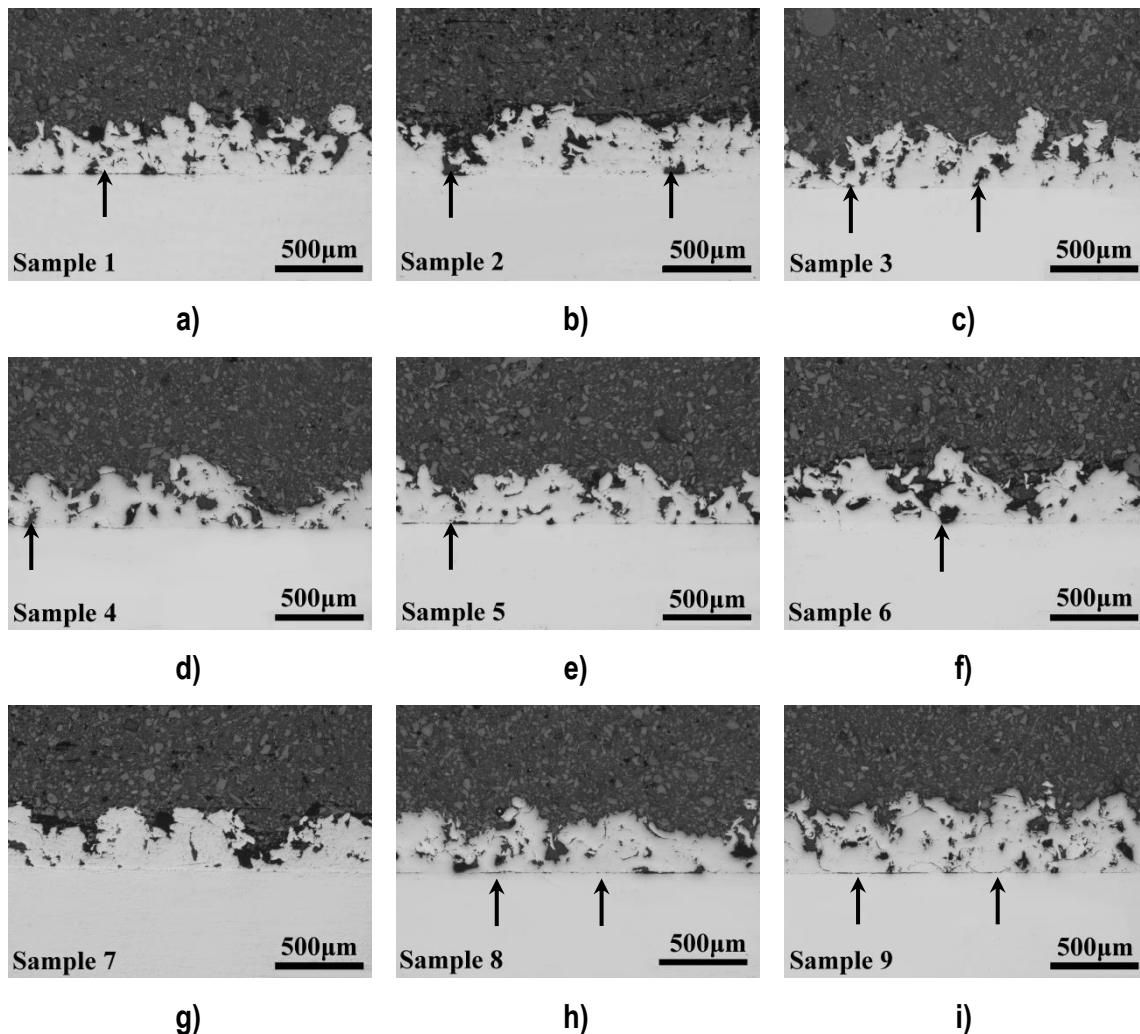


**Figure 4.22.** Optical micrographs of the cross-sections areas of CS CP-Ti coatings according to  $3^2$  factorial design from figure 4.21

During the impact with the substrate, particles undergo plastic deformation and adhere to the surface. In CS, the kinetic energy of the particles, supplied by the expansion of the gas, is converted into plastic deformation energy allowing bonding between particles. Binder et al [27] studied the influence of gas temperature (nitrogen) for titanium deposition and observed that the parameter settings of  $T=600^{\circ}\text{C}$  and  $p=4\text{MPa}$  with spherical feedstock particles ( $\text{Ø}_{50}$  of  $33.5\ \mu\text{m}$ ) are hardly deformed, but increasing gas temperature up to  $1000^{\circ}\text{C}$ , flattening ratios increase. Particle temperatures and velocities are increased with process gas temperature for an obtaining of higher thermal softening and therefore splat ductility. General results show that by increasing the propelling gas temperature and pressure the porosity level

in the coating decreases [28] whereas the deposition efficiency increases, also increasing the coating thickness [29]. Nevertheless, most of the studies undergone at moment are done with spherical particles, but a few with irregular ones. Patisson et al [30] found that irregular Ti particles accelerated and decelerated more rapidly than spherical particles and hipotized that is due to the greater drag force experienced. Cinca et al [25] exposes that irregular particle morphology seems to play a role in stress distribution and a non-uniform contact at the substrate interface. Therefore, it cannot be compared in the same terms.

Three CS CP-Ti coatings were chosen to be compared along this study: sample 1 (CS CP-Ti coating obtained with lowest energetic conditions –LEc–), sample 7 (CS CP-Ti coating that shows good interface between coating-substrate and with intermedium energetic conditions –IEc–) and sample 9 (CS CP-Ti coating obtained with highest energetic conditions–HEc–). Table 4.6 shows the thickness and porosity of those coatings. As mentioned before, results show that by increasing the gas pressure, the porosity (with a pore size between 50-100 $\mu$ m), level in the coating decreases, whereas particle deposition increases with the increasing coating thickness.

**Table 4.6.** Thickness and porosity values of CS CP-Ti coatings

<b>Samples</b>	<b>Thickness (<math>\mu</math>m)</b>	<b>Porosity (%)</b>
<b>Sample 1</b>	294 $\pm$ 74	15
<b>Sample 7</b>	297 $\pm$ 74	12
<b>Sample 9</b>	353 $\pm$ 73	8

#### b) Particle deformation and interfaces

The three CS CP-Ti coating microstructures (sample 1, sample 7 and sample 9) were etched in order to observe particle-particle interfaces (Fig. 4.23). Through detail evaluation of etched sections, it was observed that coatings obtained at high energetic conditions (HEc) display less porosity and higher tamping effect than coatings at less energetic conditions (LEc). Contrary, coating thickness increases with the energetic conditions, as many particles reach the critical velocity and acquire higher flattening to deposit onto the substrate.

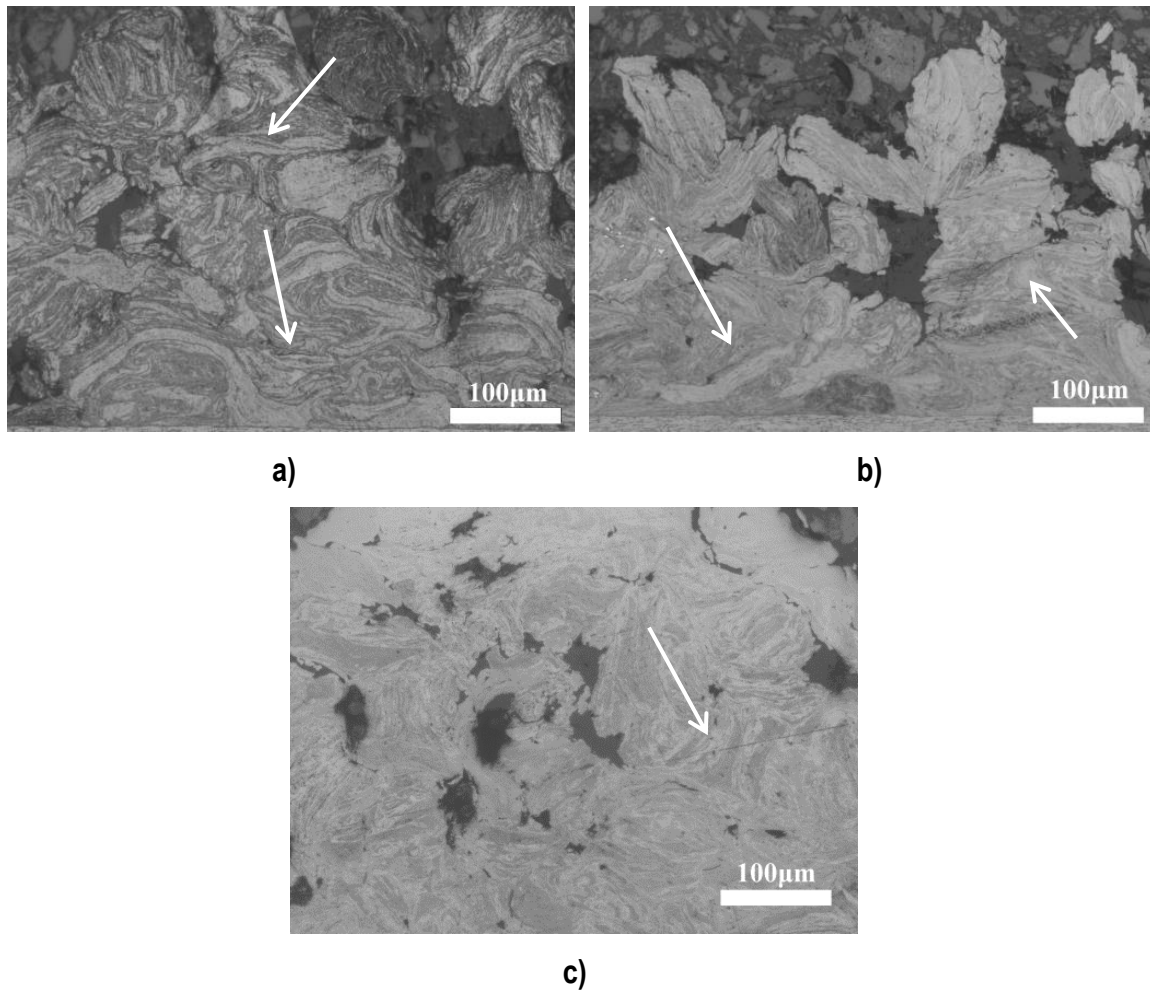


**Figure 4.23.** Optical micrographs of the CS CP-Ti coatings etched cross sections of a) sample 1, b) sample 7 and c) sample 9

The main bonding mechanism reported in CS coatings involves a metallurgical bonding when thermal softening dominates over work hardening during lateral flow upon impact of the particles at high strain rates; due to the very short impact time, the process is considered to be adiabatic and the deformation is highly localized. This has been extensively simulated for spherical particle shapes but irregular particles impose a further condition that is highly important for the so called critical velocity, this is that the velocity above which particles are more prone to attach is different from the spherical ones [19]. As presented in figure 4.23, softened viscous flow at the interfaces (marked by arrows) results in significant enlargement of the adiabatic shear instability (ASI) region. Bae et al. [19] reported different bonding features and associated mechanisms in CS Ti coatings with spherical Ti particles with a mean size of 22  $\mu\text{m}$ . The bonding features and mechanisms of kinetic sprayed CS CP-Ti coatings were associated with its unique material properties and high strain rate characteristics. The enhanced thermal boost-up zone (impact zone) due to thermally accelerated adiabatic shear

instabilities (ASIs) by powder preheating resulted in improved coating properties. ASIs (of the impacting particle and/or substrate) is considered one of the dominant mechanism for successful bonding in CS. Relatively low deformations and resultant low particle temperatures were obtained from particles at 650 m/s particle velocity. Bae et al. [19] found that there is a highly localized temperature increase at the interface because of the relatively low thermal diffusivity of Ti. This means that heat evolved locally by deformation tends to accumulate rather than disperse.

From what has been here observed at the analysed structures, the ability of the particles to bond despite their relatively low deformation, might be explained by their high interfacial temperatures resulting from friction and adiabatic impacting processes as suggested by Li et al. [31]. Coarse particles adhere one to the other, being able to build up porous coatings and the good particle cohesion at the contact points is illustrated by the continuous interfaces at figure 4.23.

#### c) Microstructure features

The TEM features of the CS CP-Ti coating resulted in a combination of: (i) nanocrystalline regions and grains of about 100 nm indicated by white arrows (Fig. 4.24a) and (ii) polygonal grains larger than 200nm (Fig. 4.24b). Both regions coexist within the titanium particle cores, as well as at particle-particle boundaries. Figure 4.24c shows a transition from a nanocrystalline areas to a coarse grain region at one side of the interface (dashed circles), while at the other side, some fine grains of medium size can be observed; another boundary (Fig. 4.24d) shows more uniform grain sizes in a polycrystalline region. Neither elongated grains nor dislocations or twins were specially observed. Most grain boundaries appear to be high angle. Also, there was no sign of any oxide film at any examined interparticle boundary.

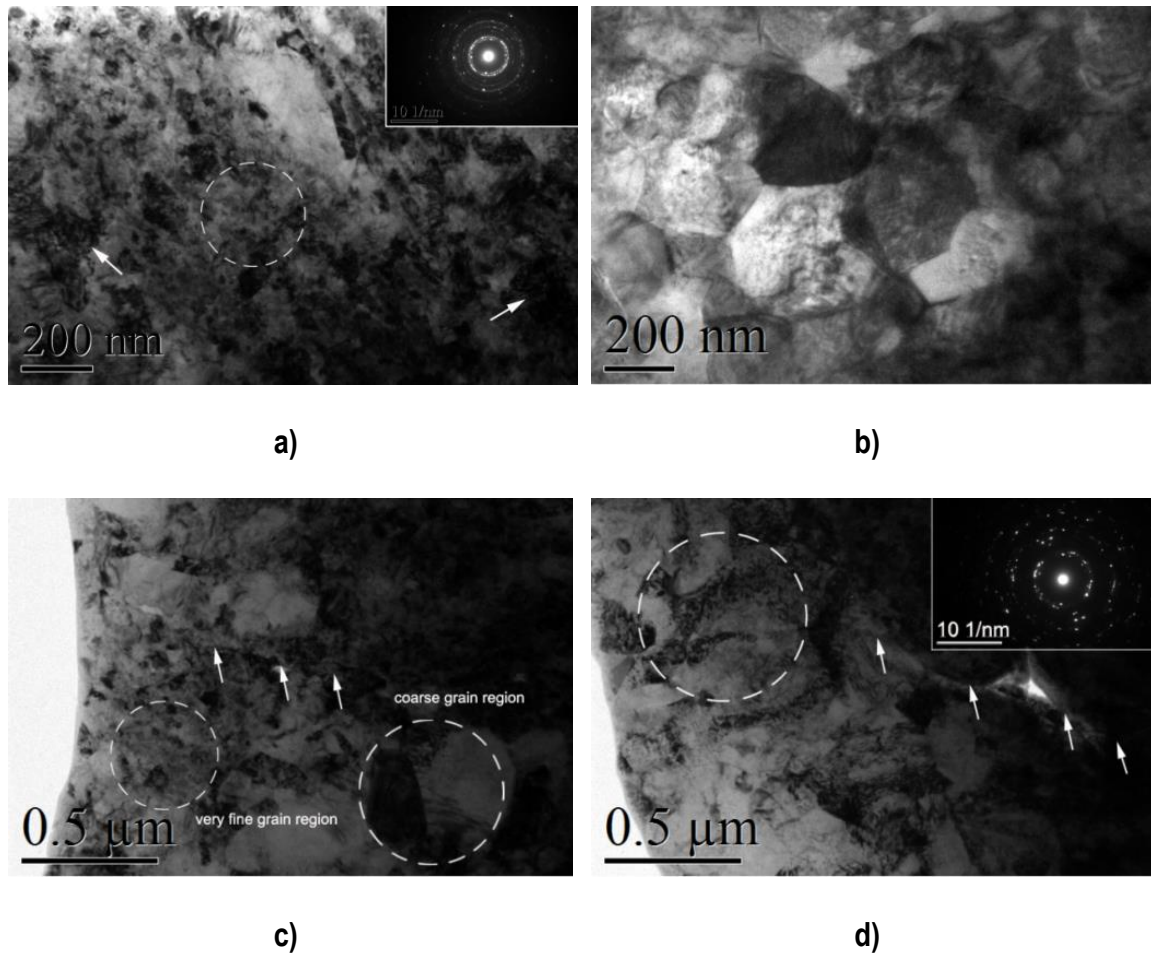


**Figure 4.24.** TEM features of the CS CP-Ti coating .a) Nanocrystalline regions (dashed circle) and grains of about 100 nm (white arrows), b) coarse grains up to 200nm, c) detail of a particle-particle boundary (white arrows) with different grain sizes at both sides and d) another boundary (white arrows) with the corresponding SAED pattern (area from circle).

As mentioned before, there is a highly localized temperature increase at the interface because of the relatively low thermal diffusivity of Ti. This means that heat evolved locally by deformation tends to accumulate rather than disperse. Because of this, King et al. [32] and Cinca et al. [25] observed much grain refinement at the interfaces. By spraying a feedstock below 50 μm, they also noticed much more heterogeneities. Their coatings presented not only equiaxed and elongated subgrains, but also poorly defined grain boundaries. These authors report that the presence of elongated grains occurs due to a high level of strain energy that has remained unrelieved by dislocation rearrangement processes, whereas the formation of polygonal subgrains is attributed to high strain and strain rates [33]. It appears that, at the levels of strain developed in their coatings, it is enough to result in such feature diversification. In our case, the grain morphology observed in the feedstock was also

observed in the coating. Only some few areas of coarser grains have been noticed; considering that these have been found both in the particle core and boundary, it may be reasonable to think that they are also present in the initial powder structure since such grain coarsening would be more unlikely. The presence of such fine grained structure affects in the CS process because the feedstock then possesses much higher strength than a conventional micrograin sized powder. In biomedical applications, the reduction of grain size has been found to slightly promote better osseointegration in severe plastic deformation (SPD) processing of dental implants [2].

#### d) Surface features

##### ➤ Top surface morphology

Figure 4.25a shows the top surface of sample 7 of CS CP-Ti coating, where the irregular morphology of the particles is clearly visible. In comparison with the first particles that arrive to the substrate, these are less deformed because the non-presence of further impinging particles show less plastic deformation but provide high roughness.

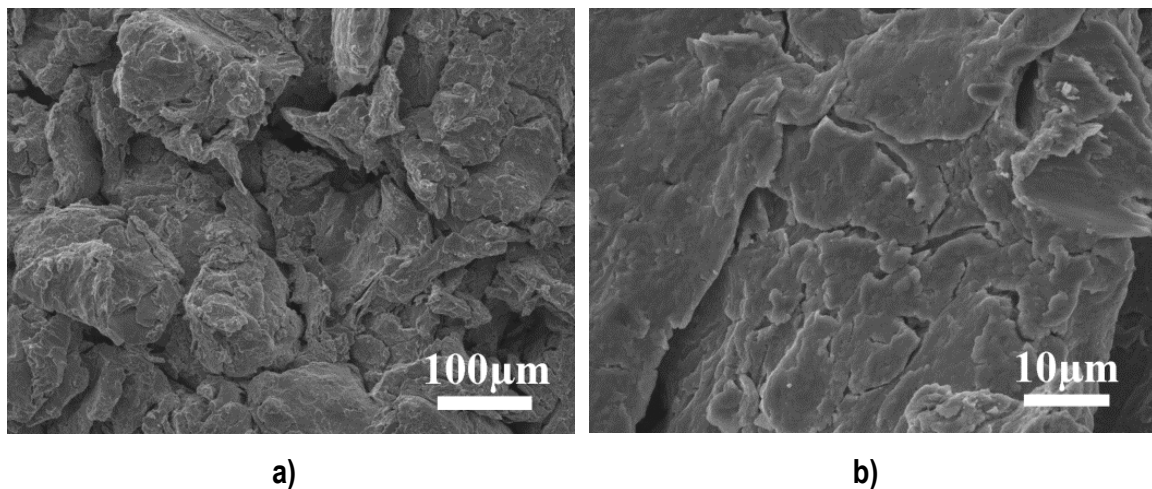


**Figure 4.25.** SEM micrographs of top surface of CS CP-Ti coating at different magnifications

The use of irregular particles may have also some influence at the submicron topography level because of the small asperities of the as-produced particle topography (Fig. 4.25b)

##### ➤ Surface topography parameters

The use of different topographical roughness scales affects different cellular behaviour aspects such as cell adhesion, proliferation, differentiation, morphology, orientation and

mechanical fixation. The surface roughness can be divided into three levels depending on the scale of the features: macro-, micro and nano-size topologies.

The macro level is defined for topographical features as being in the range of millimetres to tens of microns. Numerous reports have shown that the early fixation and the long-term mechanical stability of the prosthesis can be improved by a high roughness profile compared to smooth surfaces [34]. The high roughness results in mechanical interlocking between the implant surface and bone on growth, but at the same time may be an increase in peri-implantitis as well as an increase in ionic leakage [35]. The microtopography for dental implants is defined for surface roughness as being in the range of 1-10  $\mu\text{m}$ . This range of roughness maximizes the interlocking between mineralized bone and the surface of the implant [36], but a value for joint prosthesis is not officially established yet, although it seems that companies tend to produce coatings with a profile roughness above  $R_a > 15 \mu\text{m}$  [37]. The surface profiles in the nanometre range play an important role in the adsorption of proteins, adhesion of osteoblastic cells and thus the rate of osseointegration [38].

The most common techniques to produce surface roughness are [39]:

- Roughening of implants by thermal spraying
- Roughening of implants by grit blasting (GB)
- Roughening of implants by acid-etching
- Roughening of implants by anodic oxidation\*
- Roughening of implants by alkaline treatment \*

Roughening of implants by GB induces a surface roughness of  $R_a \sim 1\text{-}2 \mu\text{m}$  [39,40]; roughening implants by acid etching with strong acids such as HCl,  $\text{H}_2\text{SO}_4$ ,  $\text{HNO}_3$  and H produce micro pits on titanium surface with sizes ranging from 0.5 to  $2 \mu\text{m}$  in diameter [39]. Nanoporous surfaces can be produced by anodic oxidation process. The result of roughening by anodic oxidation treatment is to thicken the oxide layer to more than 1000 nm on titanium. Another approach is the performance of an alkaline treatment on titanium surface, leading to a nanoporous surface structure with an average pore size of 150–200 nm [41].

---

\* These treatments also results in composition change

When osteoblasts cells are seeded on smooth surfaces they assume a flat morphology; If they are seeded under rough surfaces where distances between rough peaks are longer than cell size, the surface is perceived as smooth; if distance between peaks is shorter than cell size, cells are unable to flat and extend and force to the cell to assume earlier osteoblastic morphology [42]. However, there are still several poorly described surface analyses and there is no consensus on 'smooth' and 'rough' surfaces. If the surface topography is measured, only a few studies characterize the surface topography more than in the height direction. A high surface energy and high topography of Ti substrates show that both micron-scale and submicron scale structural features are necessary [43]. It will be shown that the obtaining of CP-Ti coatings by CS combines global-roughness with a value of  $R_a=40.2\mu\text{m}$  and microroughness with values of  $R_a=10\mu\text{m}$  (sample 7).

The  $R_a$  and  $R_z$  profile roughness parameters were measured as a requirement for technical specifications in metal coatings for implant prosthesis [37]. Figure 4.26 and table 4.7 show the  $R_a$  and  $R_z$  profile roughness values from all samples reaching minimum values of  $R_a=27.8\mu\text{m}$  and  $R_z=151.9\mu\text{m}$  and maximum values of  $R_a=40.7\mu\text{m}$  and  $R_z=235.7\mu\text{m}$ . Surface measurements show that sample 7 presents one of the highest roughness values.

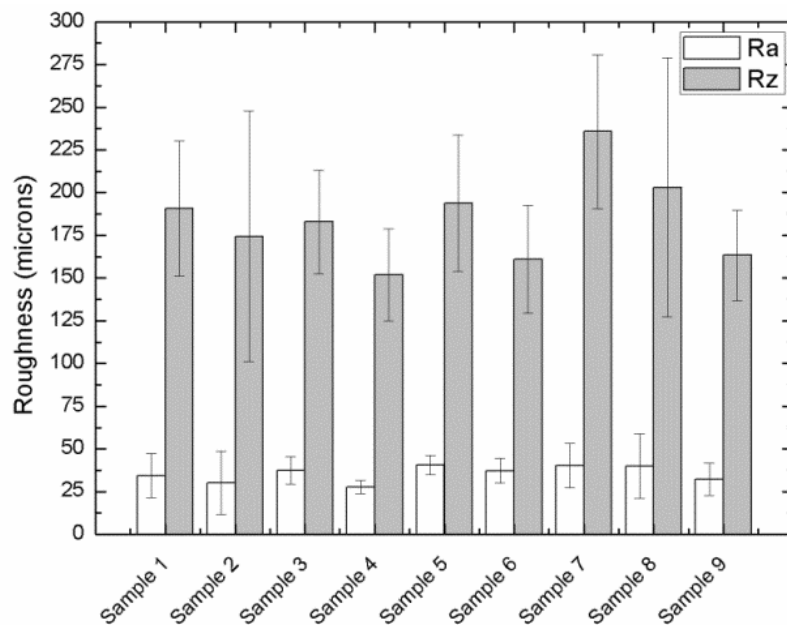


Figure 4.26. Statistical results of profile topography values of CS CP-Ti coatings

**Table 4.7.** Profile topography of CS CP-Ti coatings

	<b>Ra (<math>\mu\text{m}</math>)</b>	<b>Rz (<math>\mu\text{m}</math>)</b>		<b>Ra (<math>\mu\text{m}</math>)</b>	<b>Rz (<math>\mu\text{m}</math>)</b>
<b>Sample 1</b>	34 $\pm$ 1	190 $\pm$ 4	<b>Sample 6</b>	37 $\pm$ 7	160 $\pm$ 3
<b>Sample 2</b>	30 $\pm$ 2	174 $\pm$ 7	<b>Sample 7</b>	40 $\pm$ 2	235 $\pm$ 4
<b>Sample 3</b>	37 $\pm$ 8	182 $\pm$ 3	<b>Sample 8</b>	39 $\pm$ 2	203 $\pm$ 8
<b>Sample 4</b>	27 $\pm$ 3	151 $\pm$ 3	<b>Sample 9</b>	32 $\pm$ 9	163 $\pm$ 3
<b>Sample 5</b>	40 $\pm$ 5	193 $\pm$ 4			

Rønold et al. [44] found a way to determine an ideal roughness value from sand blasting (SB) for optimal clinical performance. The study showed that the increasing roughness does not always cause an increased in bone fixation. Higher tensile strength was obtained by SB than SB plus acid etching the surface. A Sa roughness parameter value between 3.62 and 3.90  $\mu\text{m}$  was obtained for SB surfaces. Conforto et al. [45] compared three surface roughnesses for dental and hip prostheses application, one obtained by sand-blasted large grit acid-etched (SLA) (Two-level roughness: submicron porosity superimposed on a 20-50  $\mu\text{m}$ ) and two by plasma spray (70-100  $\mu\text{m}$  and 200-250  $\mu\text{m}$ ) in which structural and mechanical properties differ.

However, in all cases, the spraying conditions did not much affect Ra and Rz roughness parameters and the selection of an optimum was based on the tensile strength values, as presented afterwards in the mechanical properties section; however, the one that is showed in the cross section better bonding interface is sample 7. Lima et al. [46] reported that the relative deposition efficiency, microhardness and elastic modulus of CP-Ti by CS increase when roughness decreases. Basically roughness tends to decrease when gun temperature increases and when spray distance decreases. But at highest temperatures, particles will also have the highest velocities of impact, having a high degree of flattening and establishing many points of contact between particles. An increase of spraying energetic conditions will influence coating microstructure. Karthikeyan et al. [47] reported a reduction of porosity with the increase of pressure and a decrease of traverse speed. In comparison with vacuum plasma spray (VPS), high roughness values were obtained with a Ra=100  $\mu\text{m}$  and a pore diameter of 100  $\mu\text{m}$  with a coating thickness between 260-300  $\mu\text{m}$  [48]. Another manner to obtain porous coatings would be changing the spraying angle [27]. CS perpendicular impacts lead to very dense and thigh bonded microstructures with negligible porosities whereas using

impact angles of  $70^\circ$  the coating microstructure shows defects and a higher porosity. Moreover, the decreasing of impact angle produces low flattening ratios.

As said before, the height-descriptive two-dimensional parameters (profiles)  $R_a$ ,  $R_q$ ,  $R_z$  and  $R_t$  are by no comparison the most commonly used parameters; sometimes, their three-dimensional counterparts  $S_a$ ,  $S_q$ ,  $S_z$  and  $S_t$  appear. This is slightly surprising because modern implant surfaces are often modified with different techniques such as blasting and etching, where the etching will leave high frequency components in addition to the longer wavelengths produced by the blasting technique. Height-descriptive parameters, in combination with spatial, hybrid or functional parameters, preferably in three-dimensions, would provide a much better characterization for all modern implant surfaces.

It must be emphasized that depending on how materials are manufactured, different surfaces topographies can be produced. The term “surface” (S) is understood as a group of irregularities, regular or irregular spaces that tend to form characteristic patterns or textures along its extension. This surface texture, called profile (P) is mainly divided in two different components: Roughness (R) and waviness (W), but depending on its frequency (wave length) it could also provide microroughness and form (Fig. 4.27).

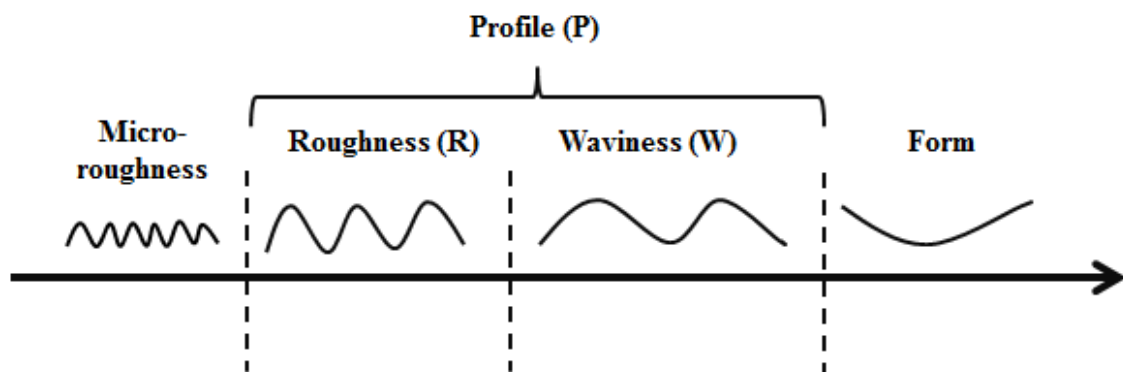
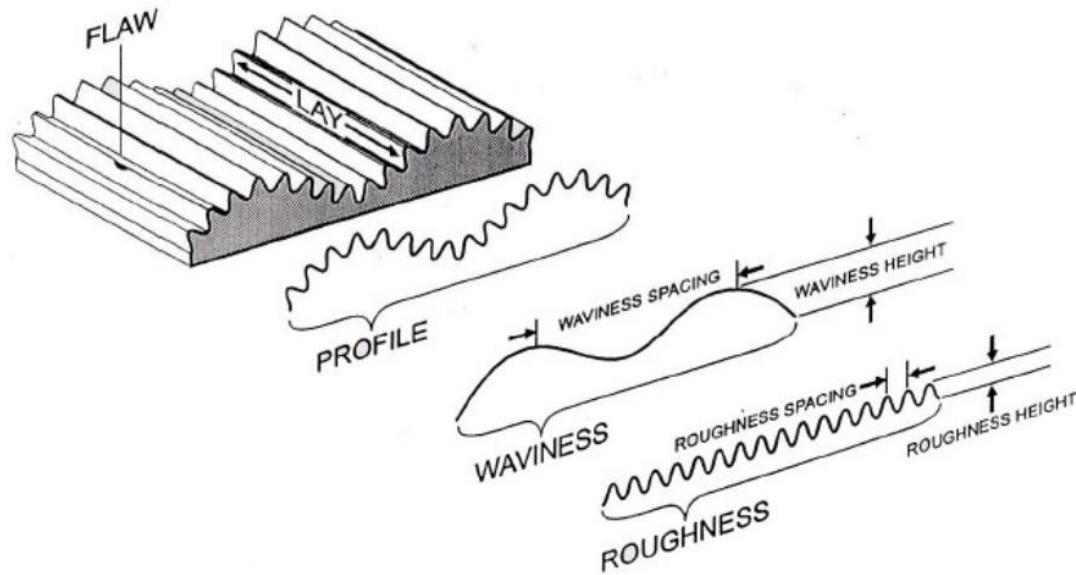


Figure 4.27. Schema of the different divisions of surface texture

Figure 4.28 shows an example of how a surface profile is divided in waviness and roughness



**Figure 4.28.** Example of surface profile divided in surface waviness and surface roughness

SB surface treatments were performed onto Ti6Al4V alloy substrates in order to compare the roughness values with the ones obtained from CS CP-Ti coating (Sample 7). Table 4.8 and figure 4.29 show the profile values together with the 2D roughness and waviness. The SB produces a less rough and less complex surface than the CP-Ti CS coating. Both samples show a microroughness with a distance between peaks on the order of tens of microns. Even so, from the 2D roughness, it was observed that the SB surface manifests more narrow ridges and groves,  $Rz \approx 20 \mu\text{m}$ , in comparison with the CS CP-Ti coating ( $Rz \approx 60 \mu\text{m}$ ). As the CS CP-Ti coating was produced by irregular coarse particles, it could be observed a major contribution of the waviness in comparison with the SB surface.

**Table 4.8.** 2D Surface topography values of SB and CS CP-Ti coating

	2D Profile ( $\mu\text{m}$ )		2D Roughness ( $\mu\text{m}$ )		2D Waviness ( $\mu\text{m}$ )	
	Ra $\pm$ SD	Rz $\pm$ SD	Ra $\pm$ SD	Rz $\pm$ SD	Wa $\pm$ SD	Wz $\pm$ SD
<b>SB</b>	4 $\pm$ 1	38 $\pm$ 5	3 $\pm$ 0.3	23 $\pm$ 6	2 $\pm$ 0.3	3 $\pm$ 0
<b>CP-Ti</b>	40 $\pm$ 13	236 $\pm$ 45	12 $\pm$ 01	68 $\pm$ 8	11 $\pm$ 3	22 $\pm$ 3

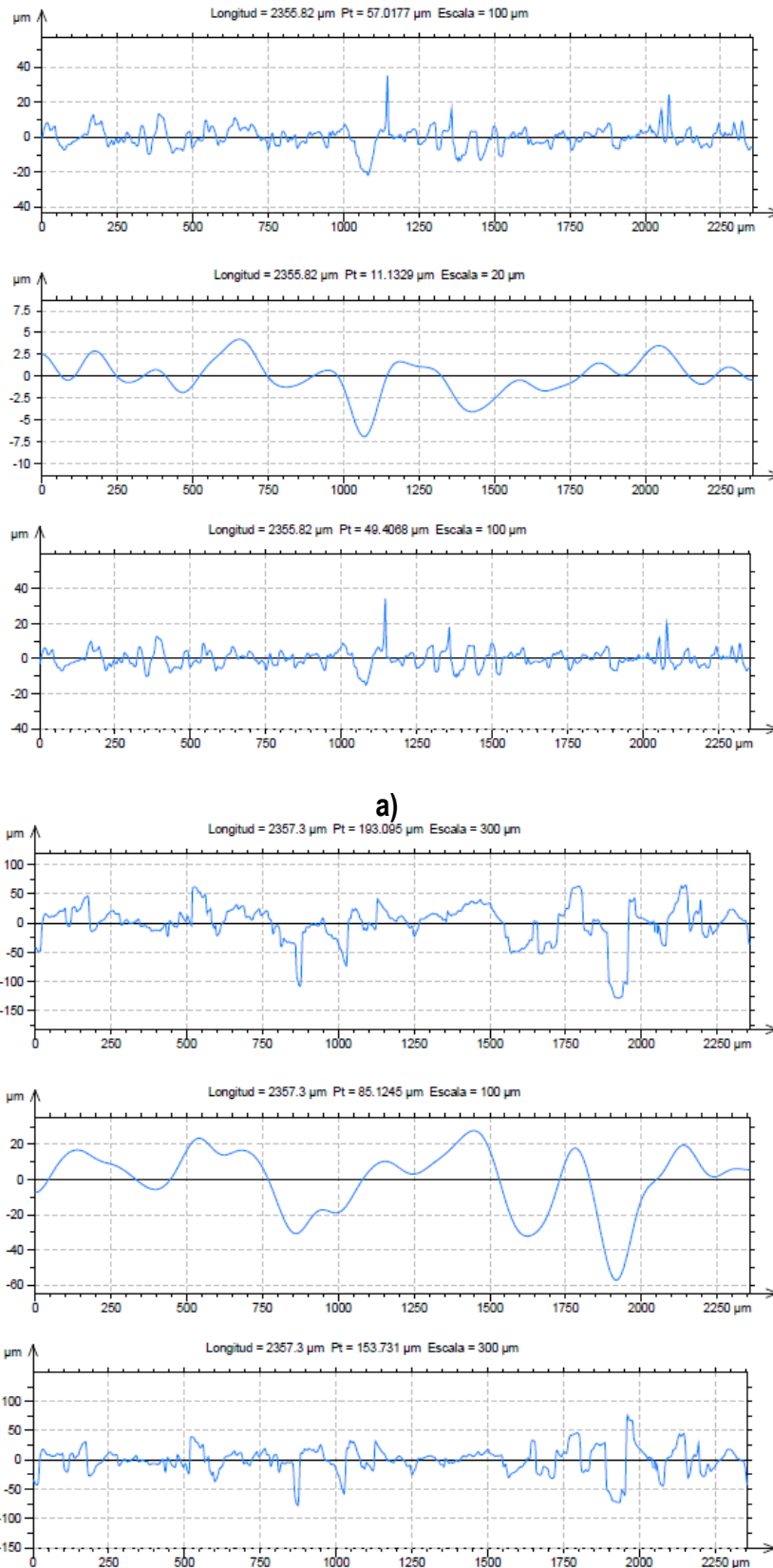


Figure 4.29. 2D Surface profiles of a) SB and b) CS CP-Ti coating ordered by: 2D Profile, waviness and roughness (Top to down)

The combination between roughness and waviness profiles leads to high increase of the surface area. The 3D parameters such as Sdr (developed surface) and Spr (projected surface) are the ones related with that increase. Spr is defined as the projected area of the developed area (Sdr) on a plane, while Sdr is defined as the total area of all small triangles that would compound a mesh that covers all the surface texture at the resolution of a measurement (Fig. 4.30).

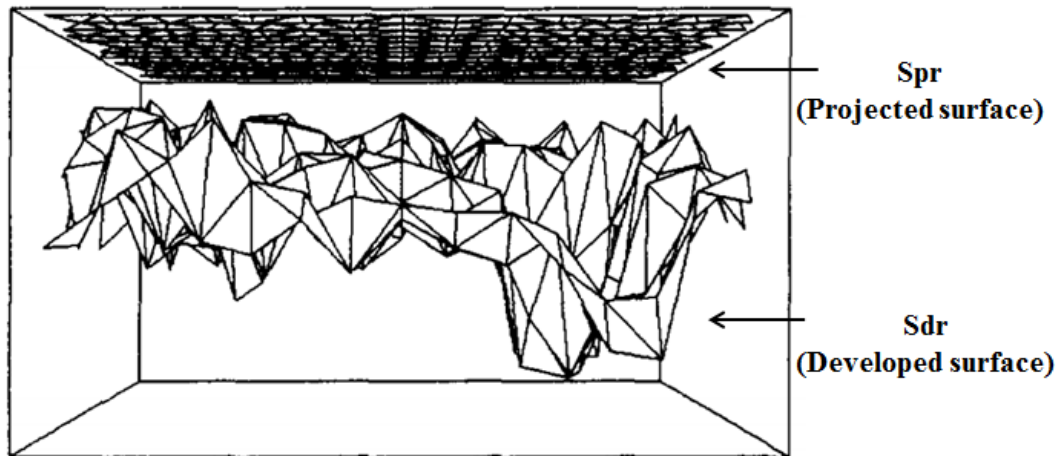


Figure 4.30. Example of the developed (Sdr) and projected (Spr) surface

The 3D Sa and Sz parameters are shown in table 4.9, together with Sdr and Spr values, so that the increase of roughness is compared with the increase of surface area. It is shown that the surface area corresponding to the CS CP-Ti coating increases  $\sim x2,7$  times in comparison with a #240 grinded Ti6Al4V alloy substrate and  $\sim x1.8$  in comparison with a SB surface.

Table 4.9. 3D Surface topography values of SB and CS CP-Ti coating

	3D Profile		Sdr	Spr
	Sa $\pm$ SD( $\mu$ m)	Sz $\pm$ SD( $\mu$ m)	Sdr $\pm$ SD( $\mu$ m <sup>2</sup> )	Spr ( $\mu$ m <sup>2</sup> )
<b>SB</b>	16 $\pm$ 1	256 $\pm$ 2	61 $\cdot$ 10 <sup>5</sup> $\pm$ 2 $\cdot$ 10 <sup>5</sup>	42 $\cdot$ 10 <sup>5</sup>
<b>CP-Ti</b>	50 $\pm$ 0.3	357 $\pm$ 34	111 $\cdot$ 10 <sup>5</sup> $\pm$ 3 $\cdot$ 10 <sup>5</sup>	

Figure 4.31 shows the 3D roughness and waviness surfaces from SB surface and CS CP-Ti coating.

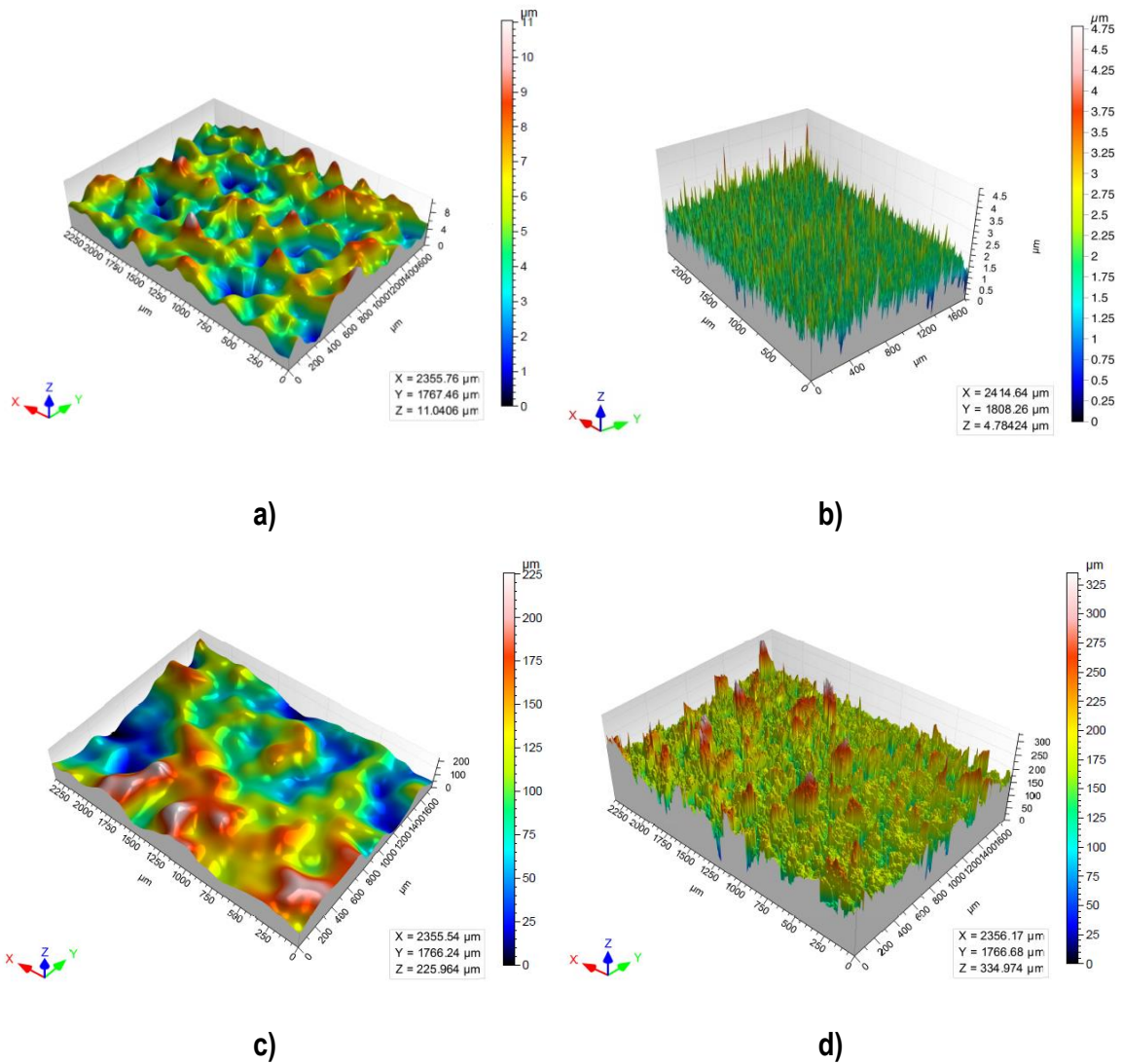


Figure 4.31. 3D waviness and roughness topographies of a-b) SB and c-d) CS CP-Ti coating

➤ Surface composition

Two x-ray photoelectron spectroscopy (XPS) analysis were performed; the first of the as-sprayed CS CP-Ti coating and the second after 2 minutes of sputter cleaning by Ar<sup>+</sup> ions. Table 4.10 shows the identified XPS element values and figure 4.32a shows both XPS spectrums.

Table 4.10. XPS element percentage of CS CP-Ti coating (IEc-sample 7)

	Ti2p	O1s	C1s
As-received (%)	22.3	45.0	32.7
Sputter cleaning – 2min- (%)	69.3	18.0	12.7

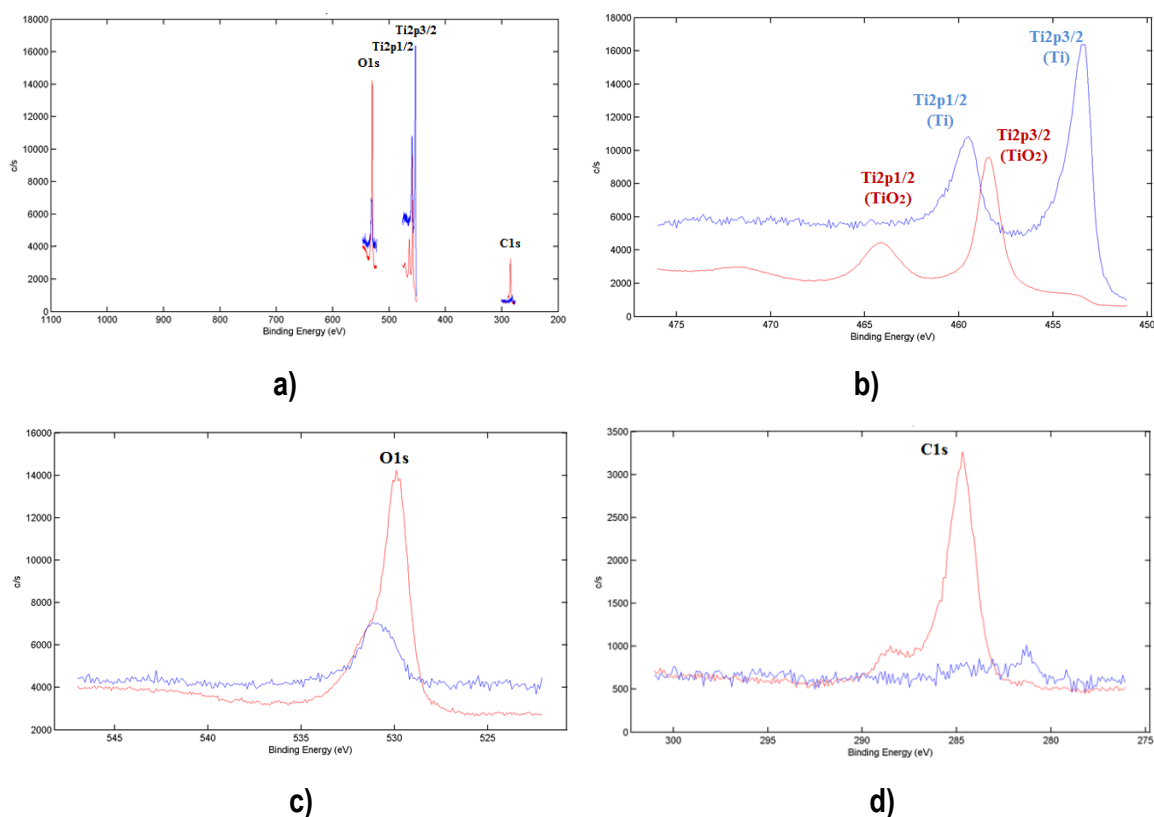


**Figure 4.32.** a) High-resolution survey XPS spectra of as-sprayed CS CP-Ti coating (red line) and after 2 min of sputter cleaning with  $\text{Ar}^+$  ions (blue line), and magnification of b) Ti, c) O and d) C XPS peaks

The following elements were identified from both XPS spectrums: C, O and Ti. As expected from surface contamination, after 2 min of sputter cleaning, the O and C percentages decrease as well as Ti increase (Fig. 4.32c-d). In addition, and as expected from an atmospheric oxidation of titanium, a thin  $\text{TiO}_2$  layer (2–10 nm) appears after the CS process [49]. The main Ti peaks (Ti  $2p_{1/2}$  and Ti  $2p_{3/2}$ ), which appear at 464.16eV and 458.42eV (native  $\text{TiO}_2$  layer) for the as-sprayed coating, shift to 459.53eV and 453.4eV (Ti (0)) respectively after the sputter cleaning surface (Fig. 4.32b) [50,51]. Table 4.11 shows the quantification of oxide phases from the Ti peaks before and after the sputter cleaning.

This native oxide layer was attributed to the titanium atmospheric oxidation due to the small thickness found. On the other hand, the decrease of C after the sputter cleaning was attributed to surface contamination.

**Table 11.** Deconvolution of Ti peaks of the XPS spectrums before and after sputter cleaning by Ar<sup>+</sup> ions of the as-received CS CP-Ti coating

	TiO	Ti <sub>2</sub> O <sub>3</sub>	TiO <sub>2</sub>
<b>As-received (%)</b>			
E <sub>peak</sub>	454.15	456.43	458.36
Quantification	9%	11%	80%
E <sub>peak</sub>	459.84	461.31	464.04
Quantification	11%	5%	84%
<b>Sputter cleaning -2min-</b>			
E <sub>peak</sub>	453.47	454.95	457.39
Quantification	67%	24%	9%
E <sub>peak</sub>	459.49	460.74	463.13
Quantification	75%	19%	6%

➤ Surface wettability

The effect of surface energy, water contact angle or wettability has to be considered as it affects protein adsorption, cell adhesion, proliferation and osteoblastic differentiation. Those functions increase by a decrease in the water contact angle or an increase in surface energy [52]. Many basic and applied investigations deal with the influence of surface roughness on wettability. One main conclusion is that roughness increases the water contact angle if its value on the unroughned surface of the same material is >90° and decreases it if the angle is <90° [53]. Contrary, dynamic contact angle experiments show that the microstructured surfaces are extremely hydrophobic but shift to total wettability once wetted during the first immersion cycle. One possible explanation may be the hierarchical structure of the used samples (microetched surfaces), in which results in a better surface wettability. So, it was said that roughness induces metastable hydrophobicity, suggesting that a pre-immersion in aqueous liquid should be taken into account before the implant contacts the host issue [54]. In addition, the combination of micro/nano-textured (acid etching followed by anodic oxidation treatment) surface was reported that yields dramatically smaller distilled water contact angles (16.22°) [55].

Figure 4.33 shows the contact angle of MilliQ water onto SB surface (Fig 4.33a) and CS CP-Ti coating (Fig. 4.33b). The contact angle was measured with Hank's solution droplet too, but no significant differences between both liquids were found. On the SB surface, both liquids show hydrophilic behaviour. MilliQ water droplets show contact angles of 32.7° and 32.2°

while with Hank's solution a 34.2° and 32.1°. On the other hand, CS CP-Ti coating shows superhydrophilic behaviour without showing a contact angle of 0° for both liquids.

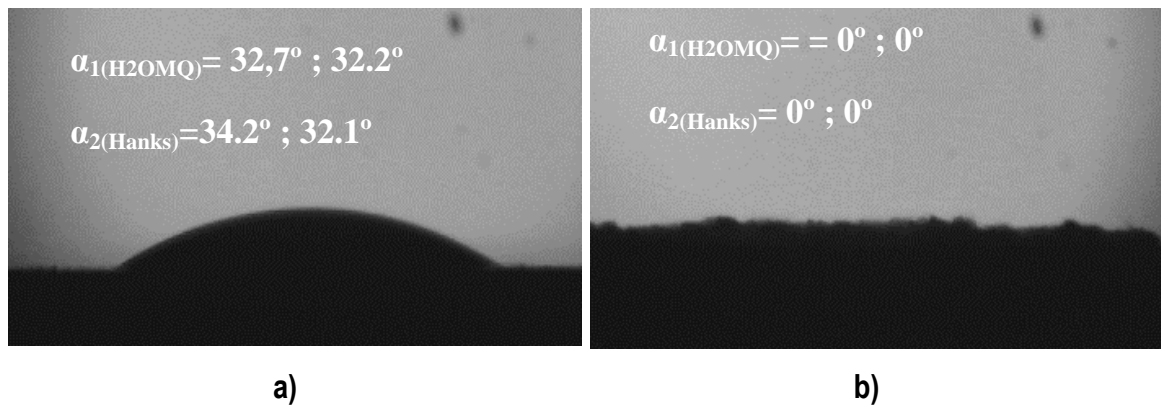


Figure 4.33. Contact angles of MilliQ water droplets for a) SB and b) CS CP-Ti coating

#### 4.2.1.4. Mechanical characterization

##### a) Tensile strength test

The spraying conditions of samples 1, 7 and 9 (LEc, IEC and HEc), were sprayed in order to test and compare the tensile strength values. The standard test method for adhesion was applied following American Society for Testing Materials ASTM C-633 [56] for the evaluation of coating adherence. Table 4.12 shows the tensile strength values obtained for each sample together with the type of failure mode (adhesive or cohesive), while figure 4.34 shows the respective graph.

Table 4.12. Tensile strength results of CS CP-Ti coatings

	Tensile strength (MPa)					
	Sample 1	Failure mode	Sample 7	Failure mode	Sample 9	Failure mode
Test 1	15.5	Adhesive	36.2	Cohesive	24.2	Adhesive
Test 2	43.4	50%Adhesive 50%Cohesive	37.0	Cohesive	40.7	Cohesive
Test 3	32.0	Adhesive	39.4	66.6%Adh 33.3%Coh	26.4	50%Adhesive 50%Cohesive
Test 4	12.3	Adhesive	46.0	Glue	S/N	-
Mean±SD	26±2		40±5		23±9	

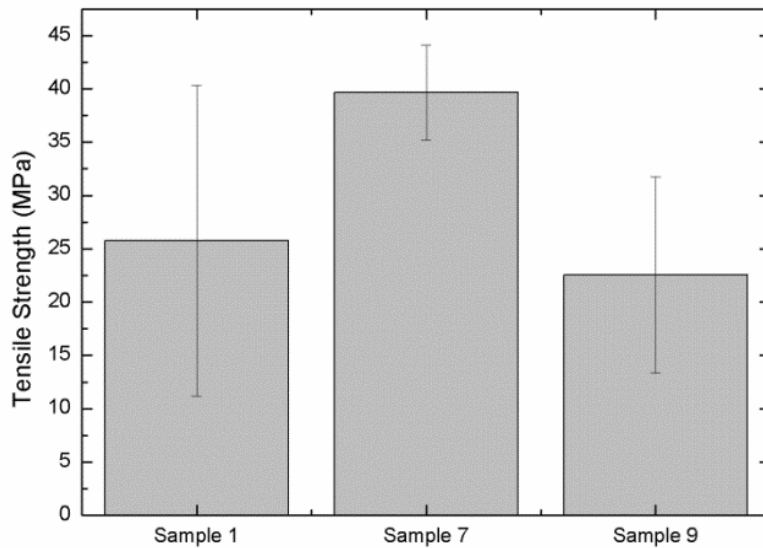


**Figure 4.34.** Tensile strength values of CS CP-Ti coatings

It can be observed that the coating that exhibited the best coating-substrate interface in figure 4.22 (IEc, sample 7), shows the highest tensile strength, also with the lowest scattering of the measured values. According to the ASTM standard specifications for hip (F-2068 [57]), knee (F-2083 [58]) and shoulder (F1378 [59]) joint prosthesis, the coating overcomes the minimum value required (20MPa).

The coating failure mode was mainly cohesive, indicating a good bonding adherence at the substrate-coating interface. However, the low values and the broad high scattering of sample 1 (LEc) and sample 9 (HEc) are produced due to the partial decohesion at the interface, leading to a low reliability. Non well-bonded particles influence much on the decrease of mechanical properties as shear and tensile strengths than lower process gas temperatures. The failure modes of samples 1 and 9 were mostly adhesive. Figure 4.35 shows the fracture surfaces of CS CP-Ti coatings after the tensile strength test.

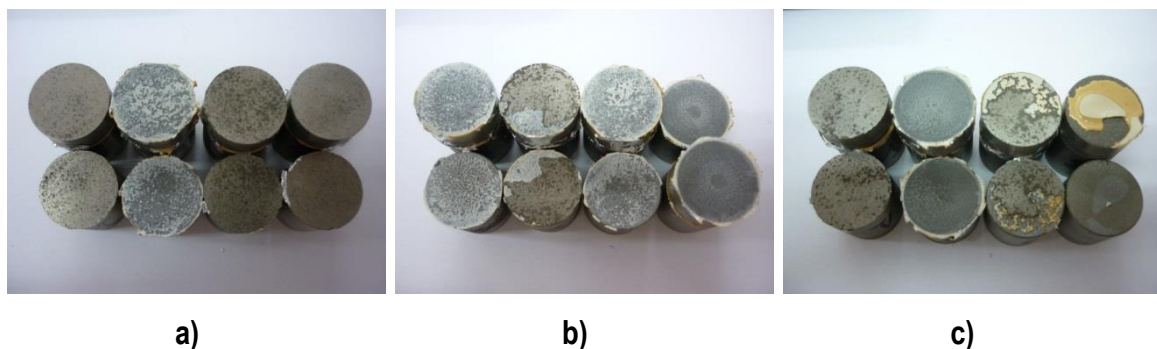


**Figure 4.35.** Tensile strength fracture surface of CS CP-Ti coatings a) sample 1, b) sample 7 and c) sample 9

Sample 7 was selected as optimal conditions, achieving a mean tensile strength of  $40\pm 5$ MPa with an adhesive failure. Wong et al. [29] reported that the adhesion of the coatings to the substrate improves as the inlet gas temperature was increased to  $500^{\circ}\text{C}$  with a gas pressure of 30bars. However, low temperatures ( $300^{\circ}\text{C}$ ) showed a wide gap between the substrate and the CS CP-Ti coating suggesting that the initial contact between the powder and the substrate did not allow sufficient plastic deformation, thus leading to a weak coating bond. As a consequence of low gas temperature, coatings show porous microstructure and particles light deformation.

Compared to other thermal spray techniques, VPS achieves tensile strength values  $>40$ MPa with a porosity between 20-60% [60]. VPS Ti coatings values of  $9957\pm 1452$  PSI ( $68.7\pm 10$ MPa) were obtained with a porosity of 34% by Bio-Coat company et al. [61]. By CS, dense Ti+HA coatings obtained by CS with irregular  $-90+22$   $\mu\text{m}$  Ti particles, are able to achieve a tensile strength of 60MPa [62]. The increase of particle size (present research -  $150+90$   $\mu\text{m}$ ) leads a decrease in tensile strength but an increase in roughness. However, tensile strength values obtained using coarse particles fulfils with the ASTM standards with much cost effective technology compared to VPS. Both of them exceed the value of 20MPa according standard specifications ASTM F-2068 [57], ASTM F-2083 [58], ASTM F1378 [59] (Femoral, total knee and shoulder prostheses respectively).

Other approaches to produce porous Ti coatings on titanium fabricated by CS involve the use of magnesium particles as a porogen element. Mg+Ti powders were sprayed followed by vacuum sintering was obtained with a tensile-strength up to 42MPa [63].

#### b) Fracture surface

A bending test, which consists on deforming the test material at the midpoint causing a concave surface or a bend to form without the occurrence of the fracture, was performed to determine the ductility or resistance to fracture of the CS CP-Ti coating (according to [64]), but no fracture was observed after severe bending (Fig. 4.36).

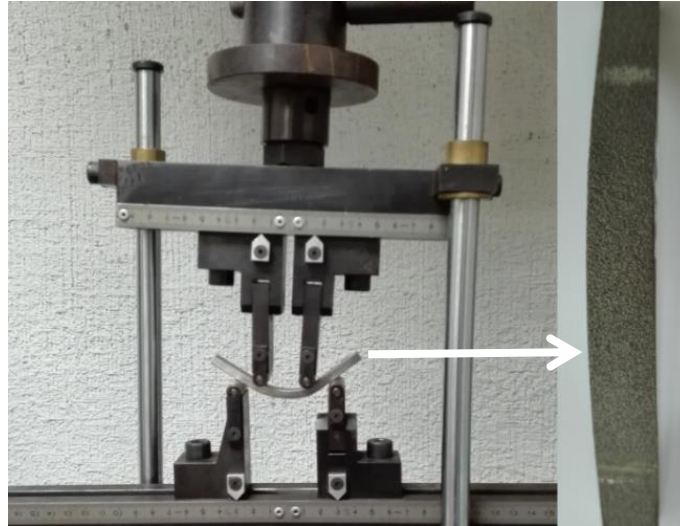


**Figure 4.36.** a) Bending test of CS CP-Ti coating sample (left) and b) bended CS CP-Ti coating sample

Even so, those samples were fractured on purpose to analyse the fracture surface. Figure 4.37a shows a general view of the surface fracture section of the Ti coating. It appears that the coating has mainly failed at particle-particle interfaces through decohesion. Further magnification reveals the presence of particles which have been deposited with quite extensive deformation (Fig. 4.37b). The interfaces appear to be quite smooth but in some regions, such as in figure 4.37c, some features indicating ductile fracture (white arrow) can be observed, due to a high level of material flow at interfaces when shear stresses take place upon impact. No other extensive features were found. Metallurgical bonding might be formed owing to the high particle surface temperature during impact enhancing coating cohesion. Some authors have attributed this to melting [31,65]. Here, considering the reduced velocities for the large particle sizes, the occurrence of melting is less probable. However, further studies would be necessary to clarify this.

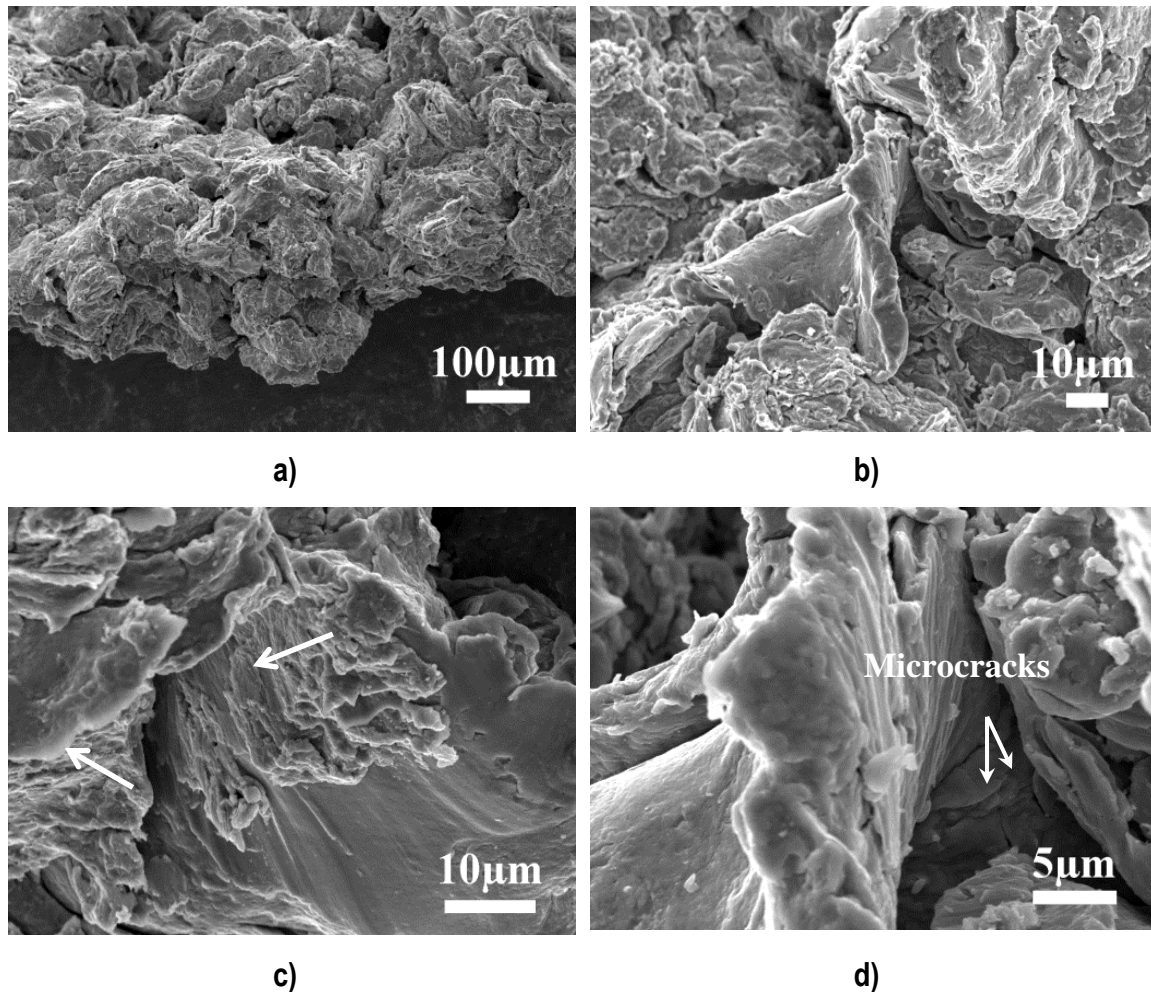


**Figure 4.37.** Fracture surface of the CS CP-Ti coating (sample 7): a) General view, b) higher magnification showing deformed particles and c-d) details of ductile fracture

Furthermore, some microcracks on the fracture surface were found (Fig. 4.37d), probably coming from the native surface oxide layer of titanium.

### c) Shear strength test

The optimal spraying conditions (sample 7) of CS CP-Ti coating that overcome the ASTM standard specifications [57,58,59] for tensile strength test were evaluated also by shear strength test (ASTM F-1044 [66]), according with the same standard specifications [57,58]. From the five specimens tested, a mean value of  $39 \pm 2$  MPa was obtained (Table 4.13), overcoming the minimum requisite of the ASTM standards (20 MPa).

Usually, mechanical adhesion in tension differs significantly from mechanical adhesion in shear, but here, both are equally important and a must-have requisite. For example, a high interface roughness may improve the shear bond strength, whereas the tensile mechanical

bond strength primarily depends on vertical anchorage in the surface profile. The values obtained for the CS porous Ti coating indicate that it surpasses the standard specifications for femoral prostheses as well as total knee implants.

**Table 4.13.** Shear strength of optimal CS CP-Ti coating (IEc-sample 7)

	Rupture load (N)	Shear strength (MPa)
<b>Test 1</b>	10.7	37.4
<b>Test 2</b>	11.61	40.7
<b>Test 3</b>	11.66	40.9
<b>Test 4</b>	10.4	36.4
<b>Test 5</b>	11.6	40.7
<b>Mean±SD</b>	11±1	39±2

A low scattering of the values was found due to the good bonding strength between the coating and the substrate. The fracture type was cohesive. Figure 4.38 shows CS CP-Ti coating surface with some shear broken peaks can be observed, while the opposite surface shows some adhered remains coming from top of the asperities of the rough CS CP-Ti coating.

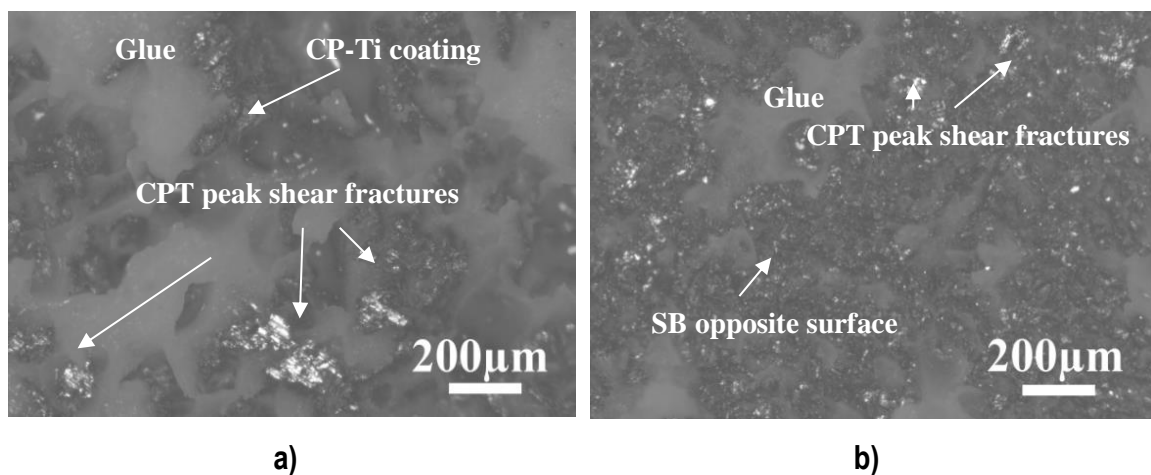


**Figure 4.38.** a) Coated and b) not coated CS CP-Ti coating (sample 7) after shear strength test

Similar results were obtained by VPS with values of  $5932 \pm 240$  Psi ( $40.90 \pm 1.65$ MPa) [61]. Nishiguchi et al. [67] produced porous titanium implants by plasma-spray with different preparation (as manufactured; with AW-glass ceramic coating; with alkaline treatment) which were inserted into bilateral femoral of a dog; after 4 weeks, shear strength tests showed 10.8,

12.7 and 15 MPa respectively, and an increase of it at 12 weeks of 16.0-16.7MPa due to bone ingrowth. Aebli et al. [68], studied the osseointegration of Ti and HA coated implants by VPS and it was found that shear strength values were very similar up to 4 weeks. At 1 week, implants reached shear strength values of  $0.29\pm 0.17$  MPa (Ti) and  $0.17\pm 0.09$  MPa (HA) and  $10.05\pm 1.49$ MPa (Ti) and  $10.43\pm 2.73$ MPa (HA) at 4 weeks. By contrast, with Ti/HA coatings by CS with a volume fraction of 10% HA, a value closer to 40MPa was obtained [69].

#### d) Abrasion test

The optimal spraying CS CP-Ti coating (IEc-sample 7) was tested by abrasion test; six specimens were tested according to ASTM standard F-1978 [70] resulting in a mean loss mass of  $37\pm 4$ mg/100cycles, without surpassing the limit established by the ASTM standard F-2068 (65mg/100cycles) [57] (Table 4.14).

**Table 4.14.** Loss mass each 100 cycles of optimal CS CP-Ti coating (IEc-sample 7)

	<b>Initial Weight (g)</b>	<b>Final Weight (g)</b>	<b><math>\Delta W</math> (mg)</b>
<b>Test 1</b>	99.4448	99.4111	33.7
<b>Test 2</b>	100.3132	100.2754	37.8
<b>Test 3</b>	99.7437	99.7067	37.0
<b>Test 4</b>	100.1292	100.0891	40.1
<b>Test 5</b>	99.4202	99.3896	30.6
<b>Test 6</b>	100.2950	100.2517	43.3
<b>Mean<math>\pm</math>SD</b>			<b>37<math>\pm</math>5</b>

Figure 4.39 shows SEM micrographs of the wear track after the Taber abrasion test. They reveal an abrasive wear mechanism as observed with the scratch wear scars on the top asperities of the coating. Plowing is more likely observed rather than wedge formation or cutting, also typical for abrasive wear of ductile materials.

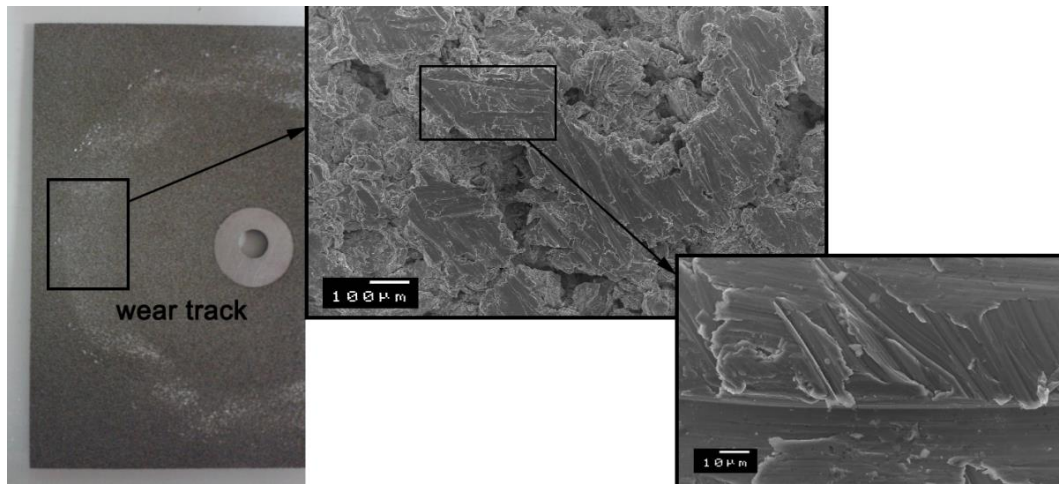


**Figure 4.39.** Top surface of optimal CS CP-Ti coating (IEc-sample 7) after abrasion test

The taber abraser test is used to measure low-stress abrasive wear resistance of materials and coatings where two- and three- body abrasive wear can be assessed with this method [71]. In comparison with other methods, taber wear shows purely abrasive wear, whereas the ball-on-disc test offers a complex blend of wear mechanisms and provides the coefficient of friction useful for analysing a wear loss measurement [72]. According to the corresponding standards, the CS coatings also prove to be feasible for biomedical applications. The loss mass obtained from CP-Ti by CS coatings is similar to CP-Ti by VPS coatings resulting in a  $37\pm 5$  mg and  $31\pm 12$ mg respectively [61].

Top wear surface reveals a ductile wear; scratching is produced on the top of the asperities and would progressively promote levelling of those asperities reducing the surface roughness although in view of the obtained results this would occur at very slow rates. In this case of plastic flow or deformation, wear tends to deform plastically the surface area and without having a high mass loss. The wear track surface reveals an abrasive wear mechanism. Two-body abrasion occurs when the asperity of the wheel contacts the CS CP-Ti coating surface. None a particle detachment between both surfaces is severely perceived [73].

## **4.2.2. NANOTEXTURING SURFACE TREATMENTS ON HIGHLY ROUGH TITANIUM COATING**

### **4.2.2.1. Introduction**

Cell-surface interactions play a crucial role for biomaterial application in orthopaedics. The progressive application of nanostructured surfaces in medicine has gained increasing interest to improve the cytocompatibility and osteointegration of orthopaedic implants [74]. The immature bone is characterized by an average inorganic grain size of 10–50 nm whereas mature bone has an average inorganic grain size of 20–50 nm (2–5 nm in diameter) [75]. Different methods are purposed to generate nanostructured surfaces such as: laser treatment [76], SLA [77], anodic oxidation [78] and alkaline treatment [79] among others. In addition, some studies have shown that implants with micro-nano-textured surfaces possess stronger interfacial bonding strengths [80].

This part of the subchapter is focused on the development of nanotextured surface treatments; especially anodic oxidation and alkaline surface treatments onto the optimal highly rough CS CP-Ti coating (IEc-sample 7). The novelty is to reproduce those nano-scale surfaces onto the highly rough CS CP-Ti coating and compare how affects those nanofeatures to cell response (results enclosed in the part: *4.2.4. Biological properties of the coatings*).

### **4.2.2.2. Nanotexturing by anodic oxidation**

#### **a) Introduction**

The achievement of porous surfaces by thermal spraying is a versatile system that offers an off-the-shelf solution for various problems, including aseptic loosening, infections, periprosthetic fractures, and instability. However, to improve the performance of the coating, the presence of a TiO<sub>2</sub> surface layer has been thought to be suitable due to its promising antibacterial properties apart from the improvement of cell response. Normally, the anodic oxidation treatment is performed for dental applications, but it might be a good alternative to produce hierarchical surfaces.

At present, it is obvious that infections associated with indwelling medical devices remain a significant clinical challenge. In vitro studies have already shown that surface features at the

nanometer scale stimulate and control several molecular and cellular events on the tissue/implant interface, which can be observed by differences in cell morphology, orientation and proliferation. In this way, bacteria adhesion is not affected by high roughness but rather by nanometer sized topographies, which may be useful for reducing bacteria adhesion. Actually, micro and nanoscale surface modification by anodic oxidation usually increase bone ingrowth and reduce fibrous tissue, which may extend the longevity of fixation, limiting pathways for particle migration, and impeding the progression of osteolysis and aseptic loosening of arthroplasty components.

The controlled formation of the oxide layer through anodic oxidation treatment enables the formation of an optimum oxide morphology containing highly ordered pore arrays or self-ordered tubular shapes. The formation of TiO<sub>2</sub> Nanotubes (NTs) represents a unique combination of shape and functionality where, in the ideal case, materials' properties can be directly influenced by the 1D-nanoscale nature of the geometry [81]. The obtaining of TiO<sub>2</sub> NTs surface improves biocompatibility and bioactivity; moreover, it acts as barrier against the corrosion of the titanium, thus improving its corrosion resistance [78].

In the present part, the surface topography of the optimal highly rough CS CP-Ti coating (IEc-sample 7) was characterized after its functionalization by anodic oxidation with the obtaining of a TiO<sub>2</sub> NTs layer.

#### b) Functionalization by anodic oxidation

On the basis of producing a TiO<sub>2</sub> NTs layer, the initiation and growth of porous TiO<sub>2</sub> are essentially following the scheme in figure 4.40. In the very early stages a compact titanium oxide layer grows up (Fig. 4.40a). During the formation of this layer in the initial phase of polarization the current drops strongly (according to a high- field law). However, due to the presence of F<sup>-</sup> ions, dissolution and breakdown of the barrier oxide film occurs randomly on the surface (Fig. 4.40b) and the current starts increasing again. The breakdown sites act as seeds to the growth of a disordered worm-like structure underneath the remaining compact layer (Fig. 4.40c). The effective surface area increases and therefore the measured current increases. About the transition from irregular to regular pores, it can be speculated that the different pores compete for the total available current. Only if the current in a pore is sufficiently high it will “survive”; thus under a critical value the pore growth is “shut down”.

After this natural selection process a self-organized situation is established. This process occurs underneath the initial barrier layer (Fig. 40d). With increasing anodic oxidation time (exposure to electrolyte) it is possible to dissolve the remnants of the compact barrier (Fig. 40e) [82].

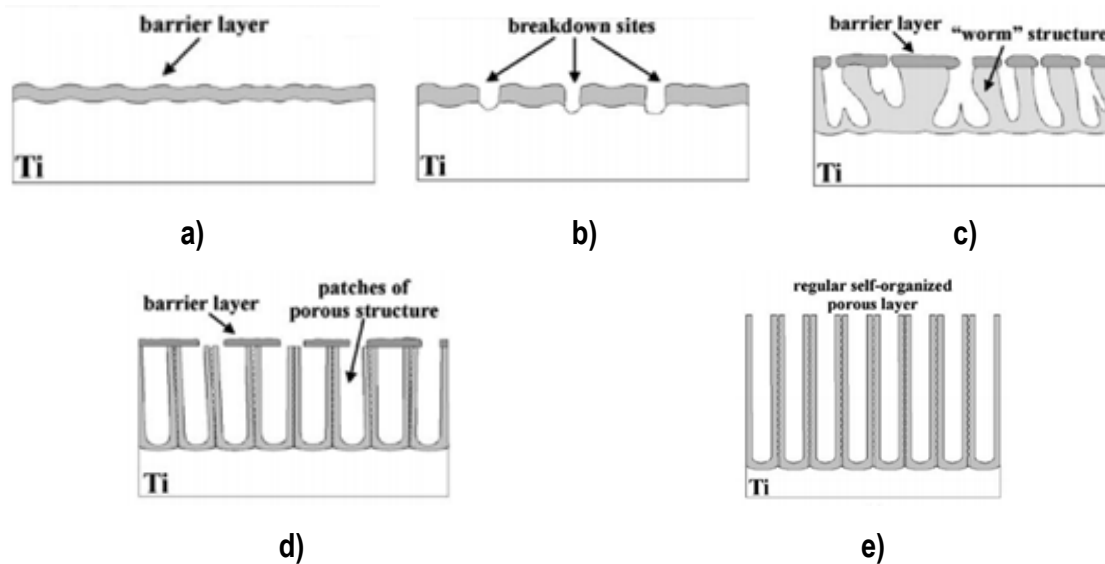


**Figure 4.40.** Schematic representation of the  $\text{TiO}_2$  NTs arrays formation: a) compact layer growth to the maximum thickness, b) breakdown of the barrier film, c) growth of the pores resulting in a worm-like structure, d) more ordered structure partially covered with the thin layer, and e) regular self-organized porous  $\text{TiO}_2$  structure [82]

#### c) Surface features of titanium oxide nanotube layer onto cold gas commercial pure titanium coating

##### ➤ Top surface morphology

A first optimization of  $\text{TiO}_2$  NTs anodic oxidation was performed on smooth Ti foils [83,84], and the optimal conditions were readjusted to anodize rough CS CP-Ti coatings. Thus, two different voltages were applied to anodize the rough CS CP-Ti coating: 30V and 40V at three different immersion times: 30 min, 45 min and 60 min. At 30V, a NT oxide layer after all different times was observed, but with some differences. After 30min, the  $\text{TiO}_2$  NTs oxide layer shows oxide remnants on the surface provinent from the oxide barrier layer. The increase of immersion time from 30 min up to 45 min leads to a cleaner surface, although still the presence of a few remnants. After 60min,  $\text{TiO}_2$  NTs oxide layer shows a surface free from oxide remanents, but the corners and edges of  $\text{TiO}_2$  NTs starts to be etching and destroyed. Higher voltages of 40V were tried, but after a short time (30 min) the result still the

same as 30V during 60 min. By the time, the optimal to anodize rough CS CP-Ti coatings were found to be at 30V during 45 min, although, further optimization is required due to the presence of a few oxide remnants onto the TiO<sub>2</sub> NTs layer from the oxide compact layer formed during the first seconds of the anodic oxidation treatment.

Figure 4.41 shows the as-sprayed CS CP-Ti coating morphology after being anodized at 30V during 30min (Fig. 4.41a-b) and 45 min (Fig. 4.41c-d). After 30min, it could be observed the formation of the TiO<sub>2</sub> NTs oxide layer onto the CS CP-Ti coating, but with a lot of surface remnants from the oxide barrier layer (Fig. 4.41a marked with arrows). Contrary, for 45min, the TiO<sub>2</sub> NTs oxide layer shows a cleaner surface although still de presence of a few oxides (dashed circle in fig. 4.41c). A compact TiO<sub>2</sub> NT oxide layer with a pore diameter between 50-100 nm was produced after the anodic oxidation treatment.

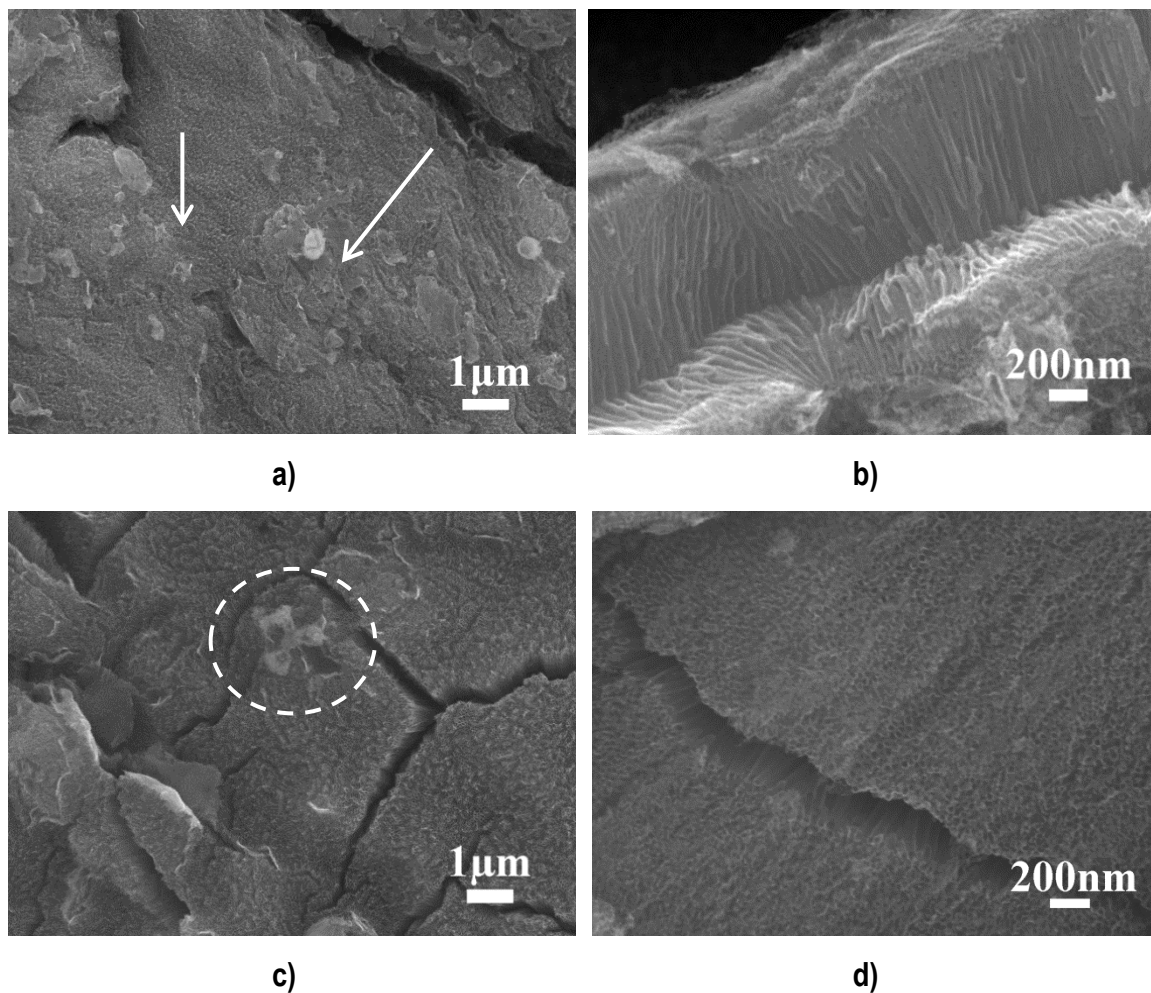


**Figure 4.41.** Field Emission Scanning Electron Microscopy (FESEM) images of anodized CS CP-Ti coating at 30V for a-b) 30 min and c-d) 45 min at different magnifications

In order to determinate the thickness of the TiO<sub>2</sub> NTs layer, the FIB technique was used to remove part of the TiO<sub>2</sub> NTs layer with gallium ions in order to observe the cross section of the TiO<sub>2</sub> NTs oxide layer (Fig. 4.42a). The TiO<sub>2</sub> NTs layer shows a thickness value of  $2.4 \pm 0.3 \mu\text{m}$  was found (Fig. 4.42b).

The morphology of the TiO<sub>2</sub> layers (particularly the pore diameter and length) is affected by the electrochemical conditions used (applied potential, electrolyte composition, pH, and anodizing time. Ghicov et al [85] used as electrolytes 1M (NH<sub>4</sub>)H<sub>2</sub>PO<sub>4</sub> and 1M H<sub>3</sub>PO<sub>4</sub> with small amounts of fluoride ions. For H<sub>3</sub>PO<sub>4</sub> a length of 500nm NT was form, but with (NH<sub>4</sub>) H<sub>2</sub>PO<sub>4</sub> a length up to 4 $\mu\text{m}$  was able to obtain. The difference of thickness is mainly attributed to pH dependence of the oxide dissolution rate, that is, the dissolution rate at low pH (H<sub>3</sub>PO<sub>4</sub>) is much higher than high pH ((NH<sub>4</sub>) H<sub>2</sub>PO<sub>4</sub>) [85].

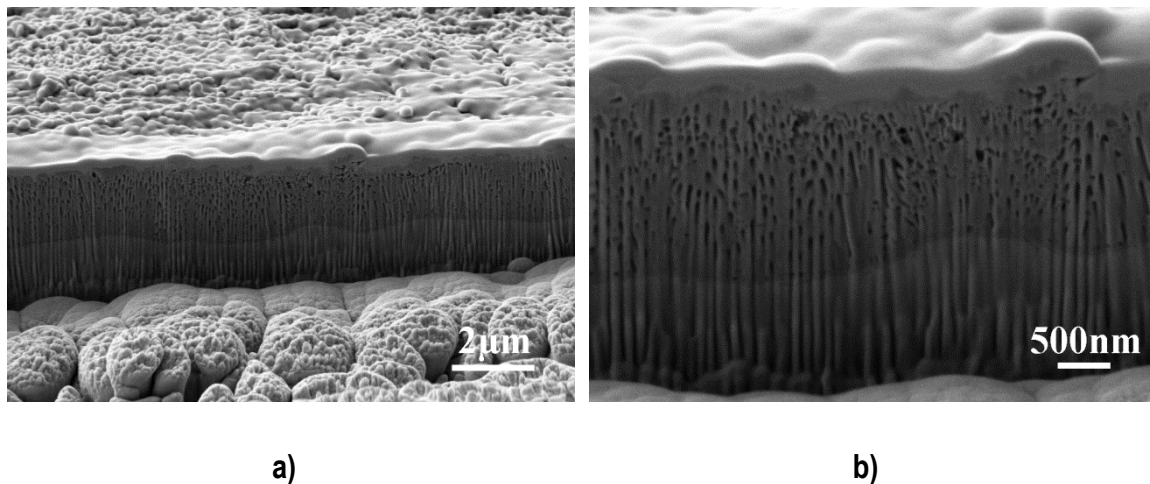


**Figure 4.42.** SEM micrographs of a FIB cut by gallium ions of NTs layer onto CS CP-Ti coating at different magnifications

The anodic oxidation approach has been mainly applied for the surface modification of Ti implants in order to improve the bioactivity and osteoproduction; this is, for example, unalloyed titanium, tantalum and niobium can stimulate the growth of new bone onto the surface of the biomaterial and spontaneously bind to living bone cells, if they have been previously subjected to a surface treatment. Xie et al. [86] performed an anodic oxidation onto VPS Ti coatings deposited on Ti6Al4V substrates, and found higher cell adhesion quantity (about 30% more) on the hierarchical structure than that on the as-sprayed VPS coatings.

The anodic oxidation on Ti surfaces has been investigated in the biomedical field in terms of their antibacterial properties [87,88], drug delivery [89,90] systems and cell viability [91,92], due to their simple fabrication and also their appropriate biological response.

Several studies have revealed considerable impact of TiO<sub>2</sub> NTs surfaces on osteoblast differentiation [91] as well on proliferation and subsequent mineralization of extracellular matrix [92], which makes such surfaces ideal for their use in orthopaedic applications.

➤ Surface composition

In order to analyze the oxide layer, an XPS study was performed. The anodic oxidized surface was tested as-received and after 5 min of sputter cleaning by Ar<sup>+</sup> ions. Table 4.15 shows the percentage elements identified by XPS

**Table 4.15.** XPS element percentage of TiO<sub>2</sub> NTs layer onto CS CP-Ti coating (IEc-sample 7)

	Ti2p	O1s	C1s	F1s
<b>As-received (%)</b>	21.38	45.7	26.53	6.40
<b>Sputter cleaning-5min- (%)</b>	36.83	50.44	4.82	7.91

It could be observed that after the sputter cleaning, carbon percentage (probably provided by sample manipulations) show an important decrease. Contrary, oxygen content does not decrease, in comparison with the XPS of as-sprayed CP-Ti coating in which it was detected the native oxide layer of Ti (Fig.4.32), due to the presence of titanium oxide. It also was detected a small amount of fluor contamination from the electrolyde.

Figure 4.43 shows the XPS spectrums of TiO<sub>2</sub> NTs layer onto CS CP-Ti coating (IEc-sample 7)

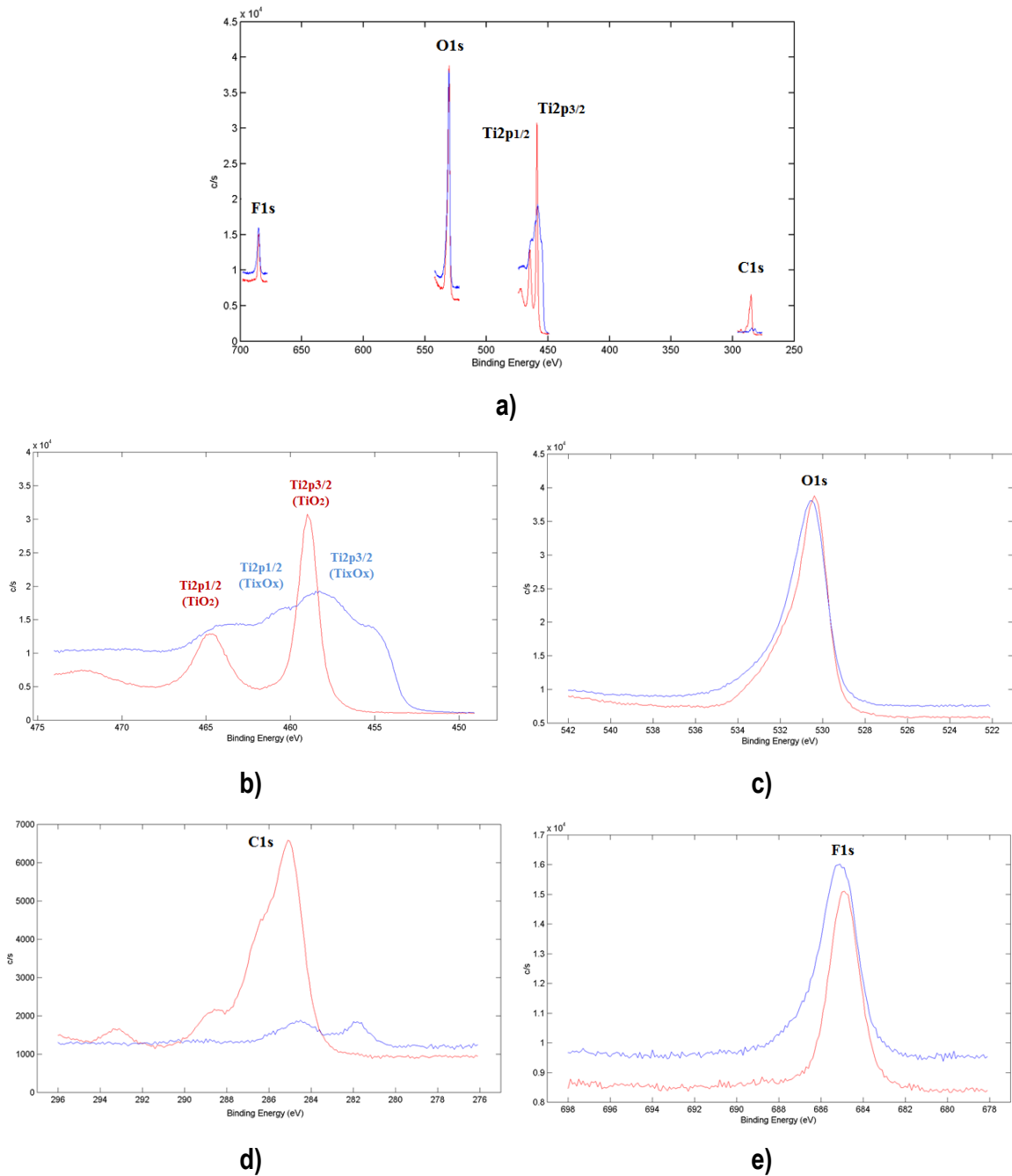


**Figure 4.43.** a) High-resolution survey XPS spectra of as-sprayed (red) and 5min of sputter-cleaned with argon ions (blue) of TiO<sub>2</sub> NTs layer onto CS CP-Ti CS coating, and magnification of XPS spectra of b) Ti, c) O, d) C and e) F peaks

Table 4.16 shows the percentage of the different kinds of titanium oxides found in TiO<sub>2</sub> NTs oxide layer. As expected from the titanium, the XPS of the as-received sample shows the formation of the native oxide Ti layer, mainly composed of TiO<sub>2</sub>. However, the XPS after being sputter cleaned shows the presence of TiO, Ti<sub>2</sub>O<sub>3</sub> and TiO<sub>2</sub> suboxides, resulting from the top surface remnants of the compact oxide layer created at a short time during the anodic oxidation treatment.

**Table 4.16.** Deconvolution of Ti peaks of the XPS spectrums before and after sputter cleaning by Ar<sup>+</sup> ions of the as received TiO<sub>2</sub> NTs layer onto CS CP-Ti coating

	TiO	Ti <sub>2</sub> O <sub>3</sub>	TiO <sub>2</sub>
<b>As-received (%)</b>			
E <sub>peak</sub>	457.20	457.99	458.99
Quantification	11%	5%	84%
E <sub>peak</sub>	460.49	462.08	464.70
Quantification	11%	5%	84%
<b>Sputter cleaning-5min-(%)</b>			
E <sub>peak</sub>	454.71	456.64	458.52
Quantification	25%	23%	52%
E <sub>peak</sub>	460.85	462.44	464.09
Quantification	38%	17%	45%

Titanium oxide is known to have varying stoichiometries and the common compounds are Ti<sub>3</sub>O to Ti<sub>2</sub>O, Ti<sub>3</sub>O<sub>2</sub>, TiO, Ti<sub>2</sub>O<sub>3</sub>, Ti<sub>3</sub>O<sub>5</sub> and TiO<sub>2</sub>. This is a consequence of the fact that titanium exists in many different stable oxidation states and that oxygen is highly soluble in titanium. The most stable titanium oxide is TiO<sub>2</sub>, with Ti in the preferred oxidation state of +IV. Ti oxides, in particular TiO<sub>2</sub>, are thermodynamically very stable and the Gibbs free energy of formation is highly negative for a variety of oxidation media, such as water or oxygen containing organic molecules [93]. According to Mor et al. [94], the amorphous oxide layer consist of TiO and Ti<sub>2</sub>O<sub>3</sub> in the intermediate layer, and TiO<sub>2</sub> in the outer layer. The XPS suggests that insufficient oxidation takes places during anodization of pure Ti and the anodized NTs consist of not only titania but also other forms such as TiO and Ti<sub>2</sub>O<sub>3</sub> [95]. Even so, first attempts were suitable to prove the capability of TiO<sub>2</sub> NTs layer onto CS CP-Ti coating and also to prove its biological cell response (results enclosed in the part: 4.2.2. *Biological properties of the coatings*).

Figure 4.44 shows the XRD of the TiO<sub>2</sub> NTs layer on CS CP-Ti coating (IEc-sample 7) before and after perform the thermal treatment at 450°C during 1h. By annealing, amorphous TiO<sub>2</sub> NTs layer change to crystalline form and become more hydrophilic (due to the obtaining of anatasa phase), resulting in an encouraging effect on cell behavior [52]. It is demonstrated that TiO<sub>2</sub> NTs are stable up to 580 °C [96]. After that, the formation of rutile lead to eventually protrusions emerging from the metal at 550-580°C and are considered to be the principal cause of TiO<sub>2</sub> NTs collapse [97]. Before the thermal treatment, the formation of amorphous

oxide layer could be observed (Fig. 4.44a). After the thermal treatment, the transformation of the amorphous oxide layer to crystalline TiO<sub>2</sub> anatase oxide layer has been identified (Fig. 4.44b).

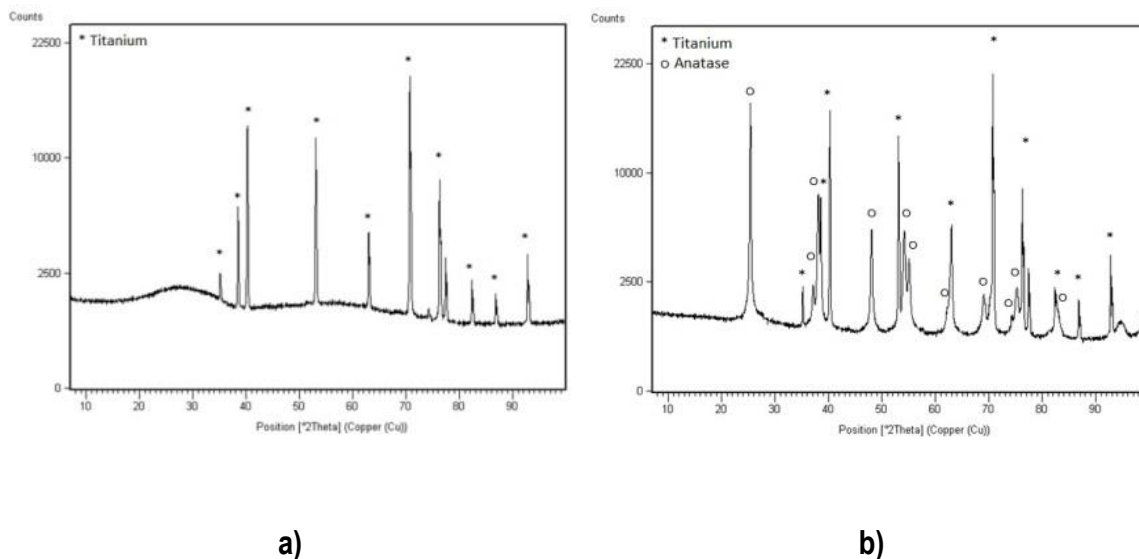


**Figure 4.44.** XRD of the TiO<sub>2</sub> NTs layer onto CS CP-Ti coating a) before and b) after the thermal treatment at 450°C during 1h

Also it should be said that the thermal treatment also plays another important role [96]. The presence of fluorine could also alter the properties of the surface in biomedical field; however, it is already report a proportional decrease of fluorine content following the heat treatment of the film with the annealing temperature.

#### ➤ Surface wettability

The wettability of TiO<sub>2</sub> NTs layer onto CS CP-Ti coating was measured with MilliQ water and Hank's solution. Although TiO<sub>2</sub> anatase induces surface hydrophilicity, no differences were perceived in comparison with the already obtained superhydrophilic by CS CP-Ti coatings. It is reported that TiO<sub>2</sub> NTs CP-Ti sheet obtains contact angle values <11° in comparison with the 54° value of the CP-Ti sheet [98].

A considerable number of studies have indicated that cells tend to attach better to hydrophilic surfaces than to hydrophobic ones [99]. However, some other works argue that cells adhere better on intermediate hydrophobic surfaces with contact angles of around 70° [100,101].

Therefore, it is evident that to analyze the biocompatibility of samples, this needs to be clarified; thus, the morphology and the wettability of the oxide layer must be analyzed (*results*

enclosed in the part: *Biological properties of the coatings*). Surface wettability also plays an important role in bacteria attachment depending on the NT pore diameter. According to Zhiqiang et al. [102], who performed in vitro testing with bone marrow mesenchymal stem cells (BMSCs) and *Staphylococcus aureus* bacteria, the hydrophilicity of the TNTs increased with ascending anatase pore diameter, then decreasing the bacteria adhesion.

➤ Surface topography parameters

Regarding surface topography, the measurements were performed by confocal microscope to measure 2D surface roughness and waviness and 3D surface, meanwhile Atomic Force Microscopy (AFM) was used to measure the surface nanoroughness.

Tables 4.17-4.18 and figure 4.45 show the 2D and 3D measurements of the surface profile, roughness and waviness.

**Table 4.17.** 2D Topography values of TiO<sub>2</sub> NTs layer onto CS CP-Ti coating

	2D Profile (μm)		2D Roughness (μm)		2D Waviness(μm)	
	Ra±SD	Rz±SD	Ra±SD	Rz±SD	Wa±SD	Wz±SD
<b>CP-Ti+NTs</b>	28±1.8	143±1.2	10±1.7	48±3.0	13±5.6	27±8.6

**Table 4.18.** 3D surface parameters of TiO<sub>2</sub> NTs layer onto CS CP-Ti coating

	3D Profile (μm)		Sdar (μm <sup>2</sup> )	Spar (μm <sup>2</sup> )
	Sa±SD	Sz±SD	Sdr±SD	Spr±SD
<b>CP-Ti+ NTs</b>	50±1.5	349±12.2	106·10 <sup>5</sup> ±24.2·10 <sup>5</sup>	42·10 <sup>5</sup>

The measurements obtained from TiO<sub>2</sub> NTs layer onto CS CP-Ti coating do not have significant differences in comparison with the as-sprayed CS CP-Ti coating. The surface topography profiles have similar profile patterns before and after the anodic oxidation treatment. For that reason, atomic force microscope (AFM) results were performed in order to compared those ones with the alkaline treatment and HA coatings.

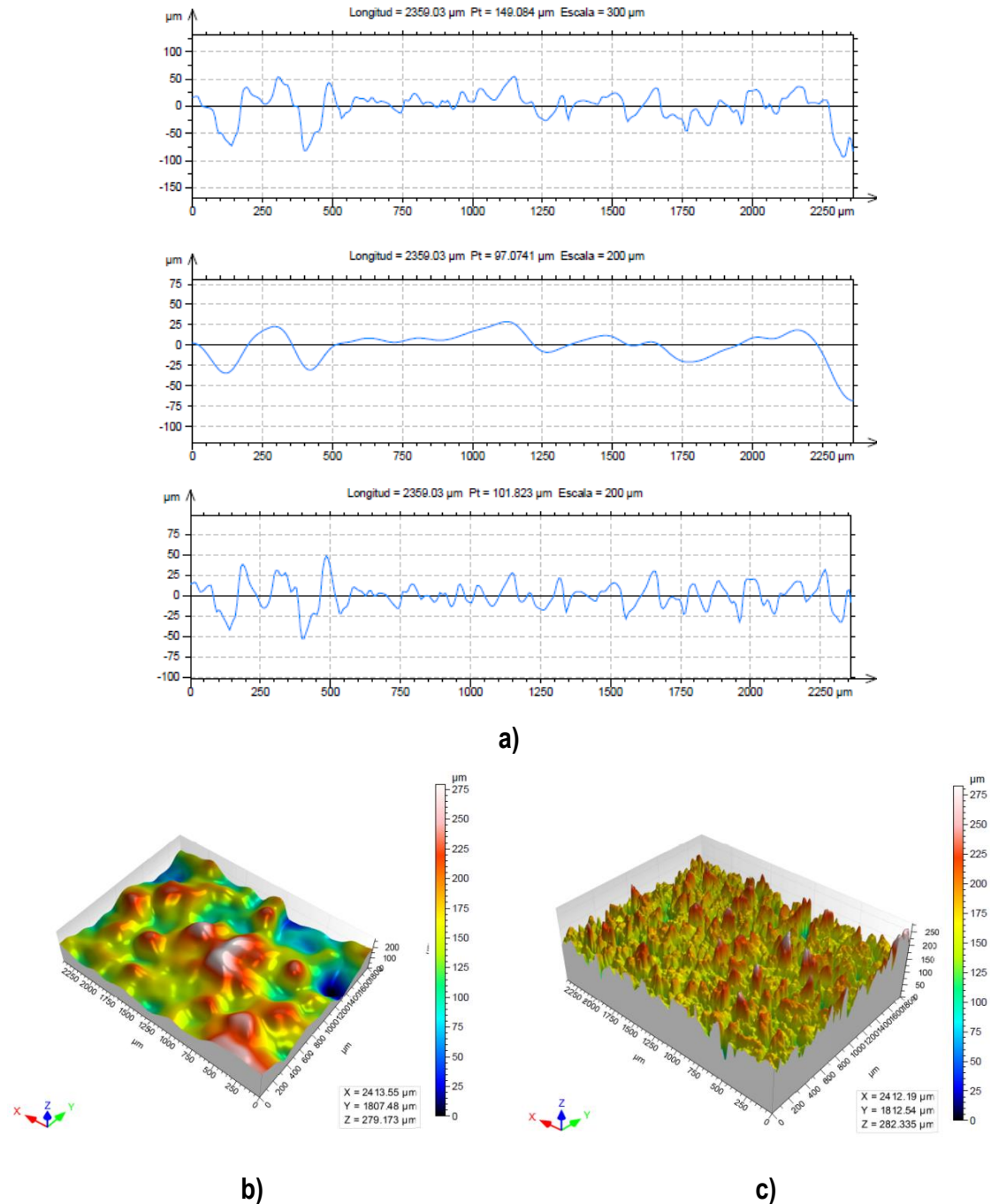


**Figure 4.45.** a) 2D Surface profile, waviness and roughness, and 3D surface b) waviness and c) roughness topographies of NTs layer onto CS CP-Ti coating

Figure 4.46 shows the 2D and 3D top surface topography micrographs of the TiO<sub>2</sub> NTs layer onto CS C-PTi coating. The TiO<sub>2</sub> NTs layer produce nanotopography onto the high micro roughness of CS CP-Ti coating with a mean value of Ra=36.8±4.6 nm. Brammer et al. [98] reported different surface roughness (Ra) for different NT diameter produced onto a 0.25 mm thick CP-Ti sheet: Ø30nm (Ra= 13.0nm), Ø50nm (Ra= 12.7nm), Ø70nm (Ra= 13.5nm) and Ø100nm (Ra= 13.2nm).

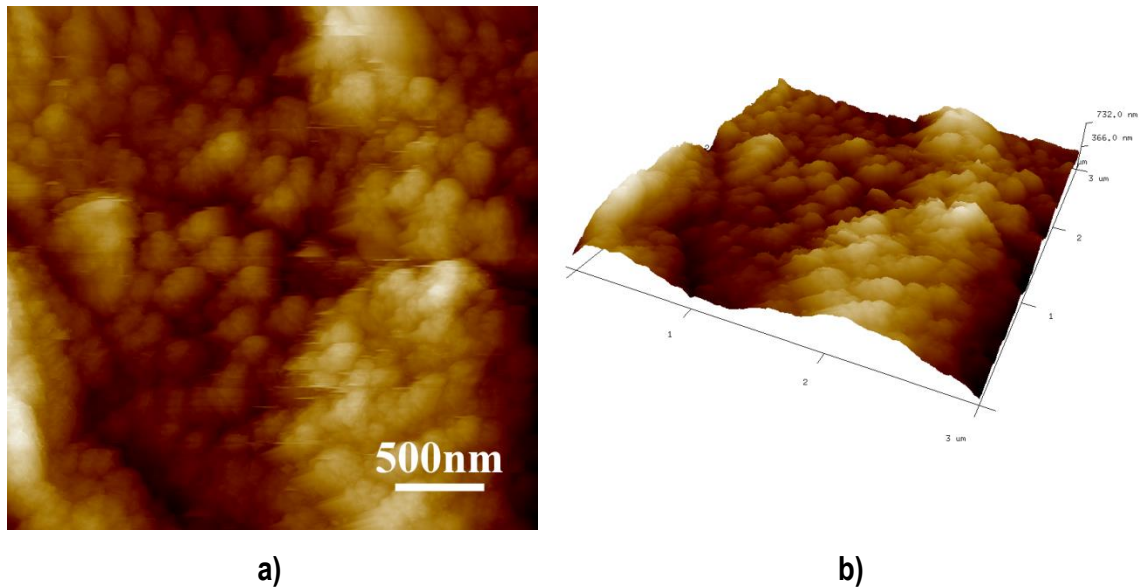


Figure 4.46. a) 2D and b) 3D AFM micrographs of  $\text{TiO}_2$  NTs layer onto CS CP-Ti coating

#### 4.2.2.3. Nanotexturing by alkaline surface treatment

##### a) Introduction

The obtaining of sodium titanate hydrogel on titanium as a result of an alkaline treatment has become much more popular than pure titanium in dental and orthopaedic applications owing to its higher corrosion resistance and higher bioactivity since it induces apatite formation in Simulated Body Fluids (SBF) [79].

Alkaline treatments have already been studied during these last decades onto smooth [104] and microrough surfaces (e.g. Ti sandblasted or acid etched substrates [103]) and a lot of studies were performed at different process parameters such as: immersion in NaOH at different times and temperatures [79,104,105,106,107] mainly on smooth Ti surfaces, but also on rough [108] and porous [109] CP-Ti coatings.

##### b) Functionalization by alkaline treatment

The optimal alkaline treatment conditions extracted from the literature was performed onto the highly rough CS CP-Ti coating (IEc-sample 7). The optimal alkaline treatment for Ti was an immersion of 3 days in 5M NaOH solution at 80°C [79,106].

As mentioned previously, the cell activity is sensitive to nanotopography but also to the crystallinity. After the immersion of titanium in alkaline solution, authors mention [105] that an “amorphous/microcrystalline” sodium titanate hydrogel structure is deposited onto the pure Ti

surface, revealing a porous network structure. The gel layer as-formed is, however, mechanically unstable; for that reason it is normally heat treated to transform the gel layer into a more mechanically stable layer. It was found that between 400-500°C the gel layer was deshydrated and at 600°C it was fairly densified and converted into crystalline sodium titanate [110]. The present study is focused on the alkaline treatment followed by a heat treatment at 600°C during 1h. Higher temperatures (700°C) of sodium titanate hydrogel starts showing a needlelike porous surface topography structure [79].

Some authors just studied the characterization and biological response of the sodium titanate layer [106], but others study the alkaline treatment (thermal treatment+immersion in SBF) in order to analyze the precipitated layer of apatite (Fig. 4.47). This part is focused on the characterization of the sodium titanate hydrogel layer, while its biological characterization is enclosed in 4.2.4. *Biological properties of the coatings*).

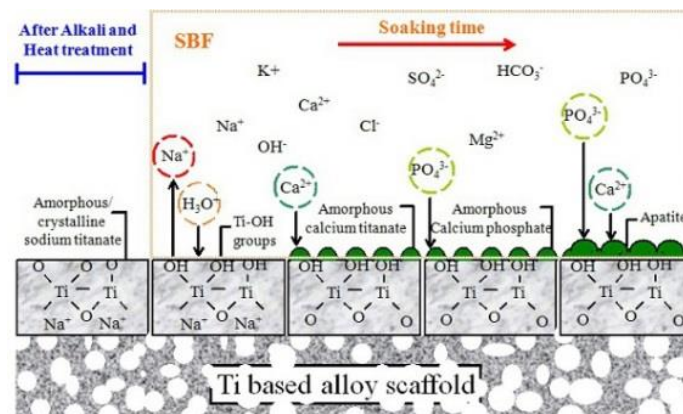


Figure 4.47. Schema of alkaline treatment followed by heat treatment and immersion in SBF [111]

### c) Surface features of alkaline treatment onto cold gas commercial pure titanium coatings

#### ➤ Top surface morphology

Figure 4.48 shows SEM micrographs of the alkaline treated CS CP-Ti coating (IEc-sample 7) before and after the thermal treatment. Both samples show nanoscale featured surfaces that consist in a porous structure of <100nm size. However, after the thermal treatment, the surface morphology differs from each other leading to a more refined structure. It is reported that at higher temperatures, the immersion in alkaline treatment lead to a more homogeneously small distributed porous surface structure [79], this could be explain the change in morphology of alkaline treated samples after the performed thermal treatment at

600°C during 1h. The morphology obtained of the sodium titanate layer onto the highly rough CS CP-Ti coating, is the same than onto the smooth surface, as reported in [79]. The topography of titanium substrate seems to not affect the morphology of the sodium titanate layer before and after the thermal treatment.

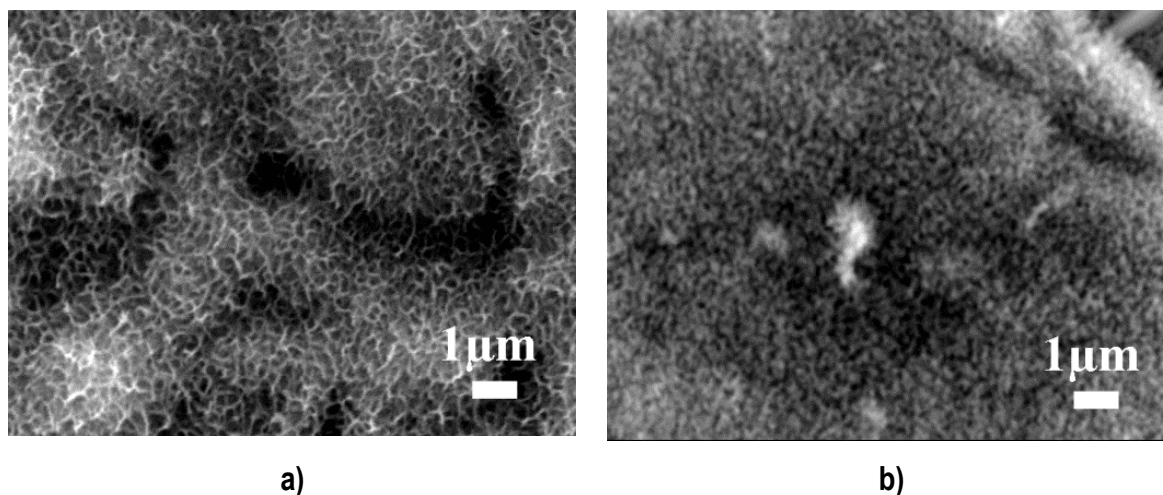


**Figure 4.48.** FESEM images of alkaline treatment onto CS CP-Ti coating (IEC-sample 7) a) before and b) after the thermal treatment at 600°C during 1h

➤ Surface composition

Two XPS were performed onto alkaline treated CS CP-Ti coating (IEC-sample 7) after the thermal treatment in order to analyze the obtained layer; the first was performed on the as-received sample and the second and the third after 2 min and 10 min of sputter cleaning by Ar<sup>+</sup> ions. Table 4.19 shows the percentage of the main identified elements from XPS spectrums while figure 4.49 shows both XPS spectrums.

**Table 4.19.** XPS element percentage of alkaline treated CS CP-Ti coating (IEC-sample 7) after thermal treatment

	Ti2p	O1s	C1s	Na1s
<b>As-received (%)</b>	9.5	65.7	11.5	13.4
<b>Sputter cleaning -2min-(%)</b>	14.9	66.2	4.3	14.6
<b>Sputter-cleaning-10min-(%)</b>	21.96	64.71	1.34	11.9

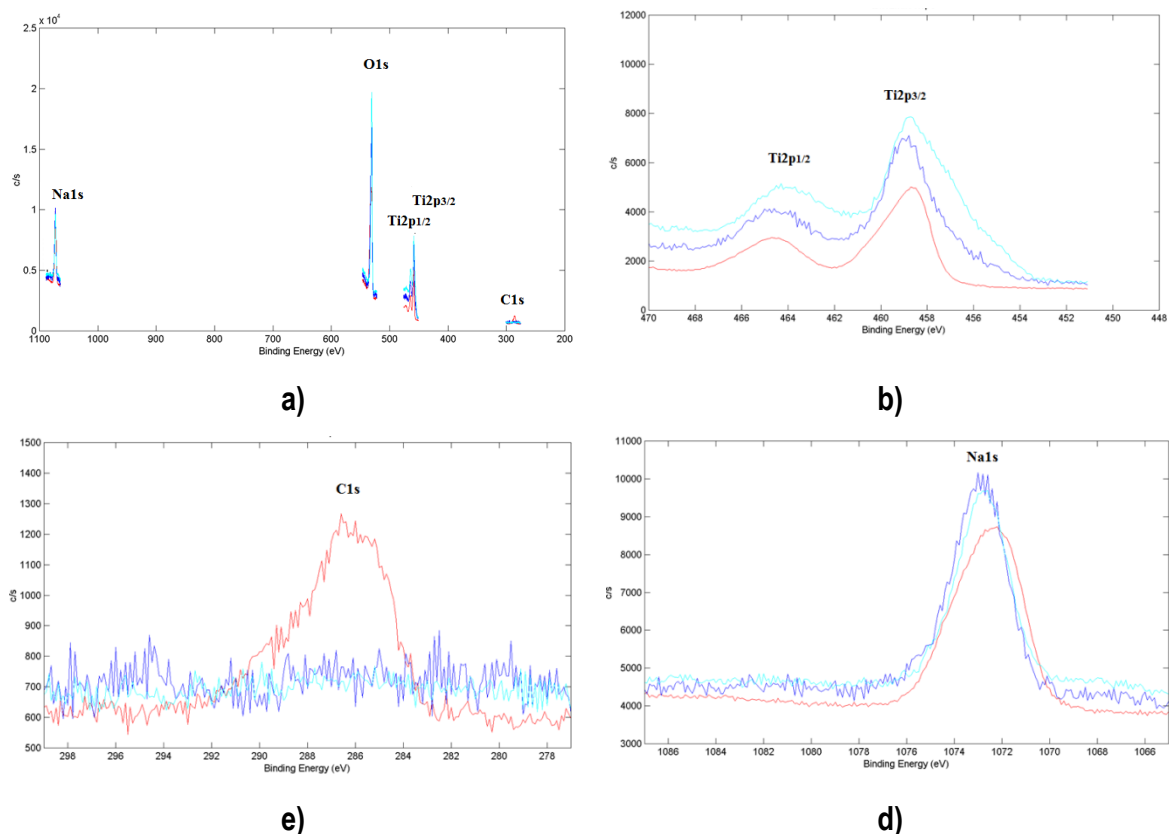


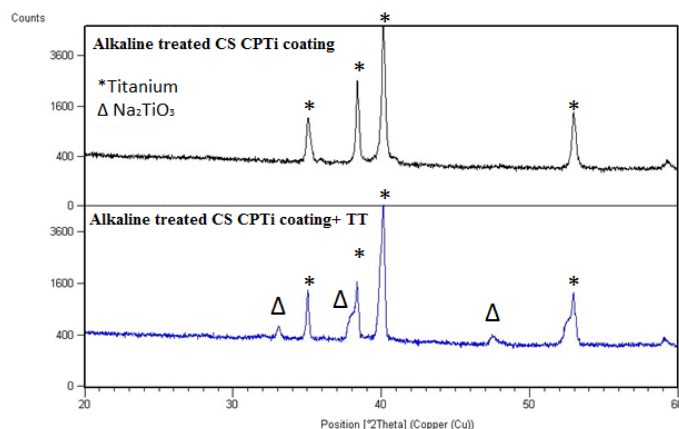
**Figure 4.49.** a) High-resolution survey XPS spectra of as-sprayed (red line) and after 2min (blue line) and 10min (cyan line) of sputter cleaning by Ar<sup>+</sup> ions of alkaline treatment CS CP-Ti coating, and magnification of XPS spectra of b) Ti, c) O, d) C and e) Na peaks

The main elements detected by XPS were Ti, O, C and Na, indicating this last element the possible presence of sodium titanate hydrogen layer. Therefore, due to immersion an oxide layer it was formed. Table 4.20 shows the deconvolution of Ti peaks, in which mostly predominates TiO<sub>2</sub> phase.

**Table 4.20.** Deconvolution of Ti peaks of the XPS spectrum corresponding to the alkaline treated CS CP-Ti coating after thermal treatment

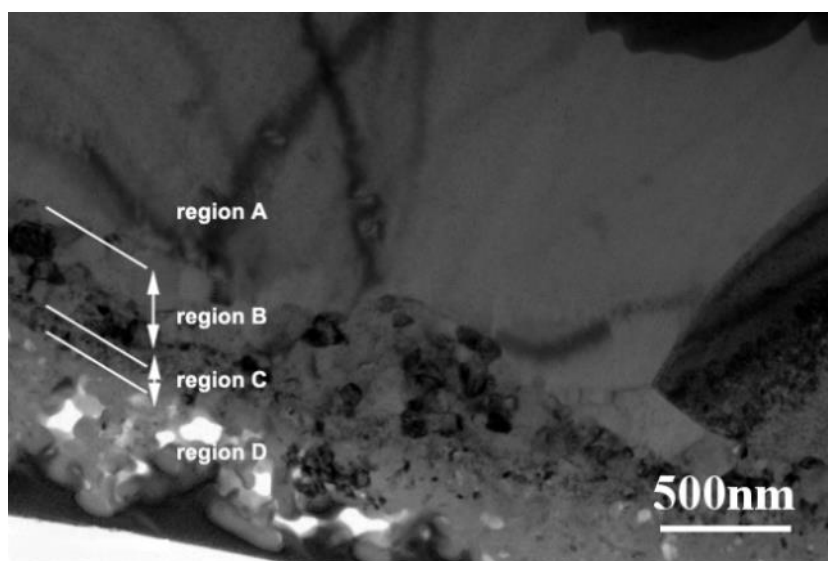
	Ti <sub>2</sub> O <sub>3</sub>	TiO <sub>2</sub>
<b>As-received (%)</b>		
E <sub>peak</sub>	457.51	458.70
Quantification	10%	90%
<b>Sputter-cleaned-2min-</b>		
E <sub>peak</sub>	456.26	458.87
Quantification	18%	82%
<b>Sputter-cleaned-10min-</b>		
E <sub>peak</sub>	455.86	458.53
Quantification	26%	74%

Figure 4.50 shows the XRD of alkaline treated CS CP-Ti coating before and after the thermal treatment. Before the thermal treatment, the presence of sodium titanate layer was hardly identified. Normally, samples immersed in alkaline solutions with a concentration  $>5\text{M}$  (with or without thermal treatment at  $600^\circ\text{C}$  during 1h) used to start showing sodium titanate peaks of low intensity between  $25\text{-}35$  and  $47\text{-}49$  in  $2\Theta$  on XRD pattern [79, 109]. After thermal treatment, sodium titanate peaks starts acquiring intensity [79].



**Figure 4.50.** XRD of alkaline treated CS CP-Ti coating (lec-sample 7) a) before and b) after the thermal treatment of  $600^\circ\text{C}$  at 1h

A thin lamella of the alkaline treated CS CP-Ti coating was obtained by FIB lift-out technique to analyse its microstructure. TEM reveals four different regions within the surface (Fig. 4.51). Each region is clearly distinguished from each other due to the grain size, as well as the sodium titanate layer nanocoating thickness of  $\sim 500\text{nm}$ .



**Figure 4.51.** TEM micrograph of FIB lamella indicating the 4 different regions

Figure 4.52 shows the SAED patterns of the regions A (zone 2) and B (zone 1) from figure 4.51. The region A belongs to the CS CP-Ti coating, where each coarse grain presents a monocrystalline SAED pattern. Although it was previously observed a UFG microstructure within the CP-Ti feedstock powder and coating, a coarse grain structure was observed after the thermal treatment, due to the grain growth; it is already reported that the growth CP-Ti exponents are high when compared to that of other metals and alloy [112]; followed by a growth rate decrease. This drop in the growth rate arises because as the grain size increases, the grain boundary area per unit of volume decreases, as does the interfacial energy per unit volume.

The Region B consists in a layer located between the regions A and C, and its structure is composed by small grains (~50-100nm); the polycrystalline nanostructure of region B (zone 1) was identified as a TiO<sub>2</sub> anatase coming from the alkaline treatment.

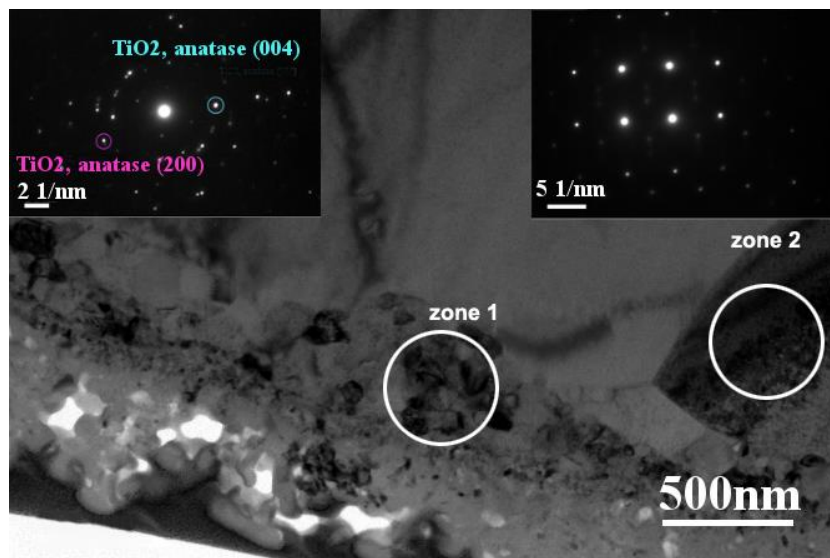


**Figure 4.52.** TEM features of the alkaline treated CS CP-Ti coating (IEc-sample 7). Zone 1) Nanocrystalline TiO<sub>2</sub> anatase region, and zone 2) microcrystalline region with the corresponding SAED pattern (area from circle)

Figure 4.53 shows regions C (zone 2) and D (zone 1). The region C consists in a polycrystalline structure composed by nanograins <25nm. The spots of its SAED pattern have been identified as and TiO<sub>2</sub> anatase, although it was perceived the presence of a structure similar of apatite (probably some Ca impurities from the NaOH feedstock). In addition, region D (zone 1) belongs to the porous sodium titanate layer. The spots have been mostly identified as Na<sub>2</sub>TiO<sub>3</sub>. However, it is still visible the presense of like-apatite pattern observed

in region C. The porous sodium titanate layer is composed by a polycrystalline structure with small grains of a size of  $\sim 100\text{nm}$ . This micrograph confirms the polycrystalline structure of the sodium titanate layer, as lot of reports identified it as a “microcrystalline or amorphous” layer [79,105,110].

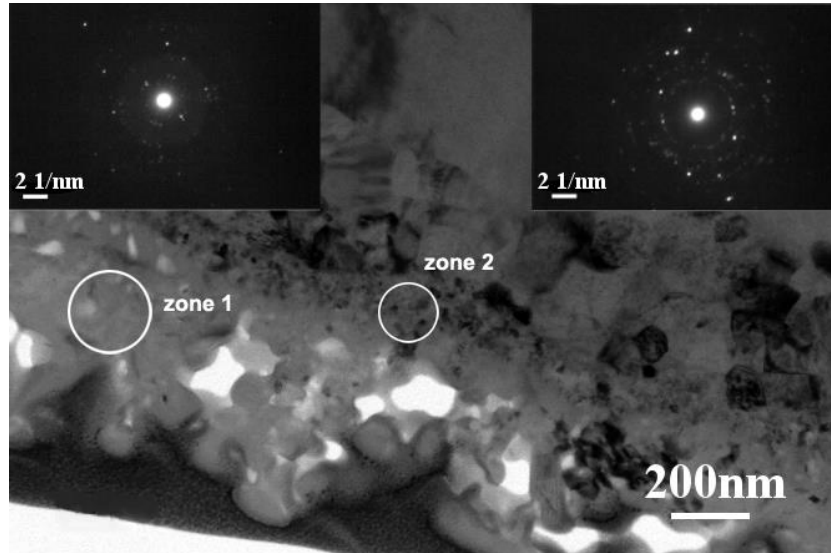


**Figure 4.53.** TEM features of the alkaline treated CS CP-Ti coating. Zone 1) Nanocrystalline region from sodium titanate layer, and zone 2) nanocrystalline diffusion oxide titanium region, with the corresponding SAED patterns (area from circle)

Figure 4.54 shows a high resolution TEM micrograph of region D, in which could be observed the  $\text{Na}_2\text{TiO}_3$  nanocrystals with a rectangular morphology and approximate size of  $80 \times 20\text{nm}$ .

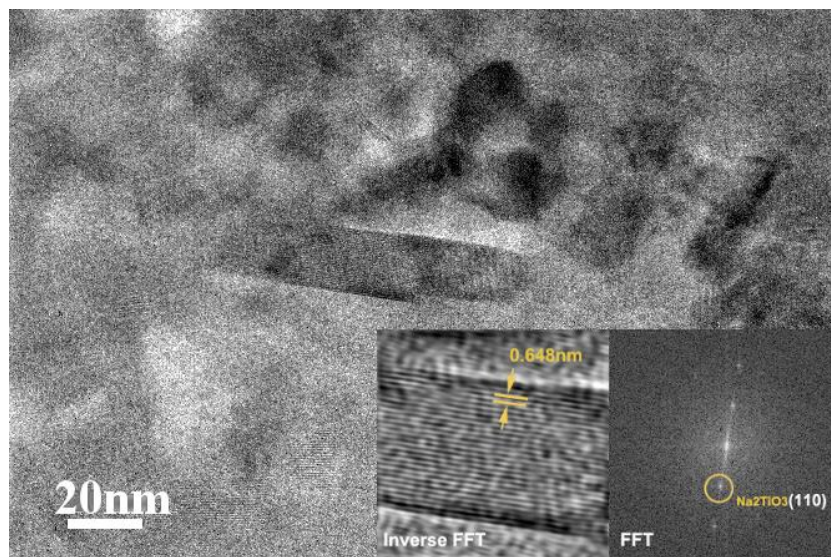


**Figure 4.54.** TEM features of the alkaline treated CS CP-Ti coating (IEc-sample 7). Region D from figure 4.53 patterns

➤ Surface wettability

The alkaline surface treatment is already reported to enhance hydrophilicity in titanium [113,114]. Moreover, the TiO<sub>2</sub> anatase produced after the NaOH immersion could help in that purpose. The wettability of alkaline treatment CS CP-Ti coating was measured with MilliQ water and Hank's solution and a contact angle of 0° was obtained in both cases.

➤ Surface topography parameters

Regarding surface topography, tables 4.21-22 show the 2D and 3D measurements of the surface profile, roughness and waviness. In comparison with the as-received CS CP-Ti coating, both, roughness and waviness topographies show a slight decrease, although the microughness is maintained.

**Table 4.21.** 2D Surface topography values of alkaline treated CS CP-Ti coating

	2D Profile (µm)		2D Roughness (µm)		2D Waviness (µm)	
	Ra±SD	Rz±SD	Ra±SD	Rz±SD	Wa±SD	Wz±SD
<b>CP-Ti+NaOH</b>	26±2	134±16	9±0.1	57±13	10±0.1	22±3.5

**Table 4.22.** 3D surface parameters of alkaline treated CS CP-Ti coating

	3D Profile (µm)		Sdar (µm <sup>2</sup> )	Spar (µm <sup>2</sup> )
	Sa±SD	Sz±SD	Sdr±SD	Spr±SD
<b>CP-Ti+ NaOH</b>	42±5	328±17	88·10 <sup>5</sup> ±1·10 <sup>5</sup>	42·10 <sup>5</sup>

Figure 4.55 shows the topography of the 2D and 3D measurements of the surface profile, roughness and waviness.

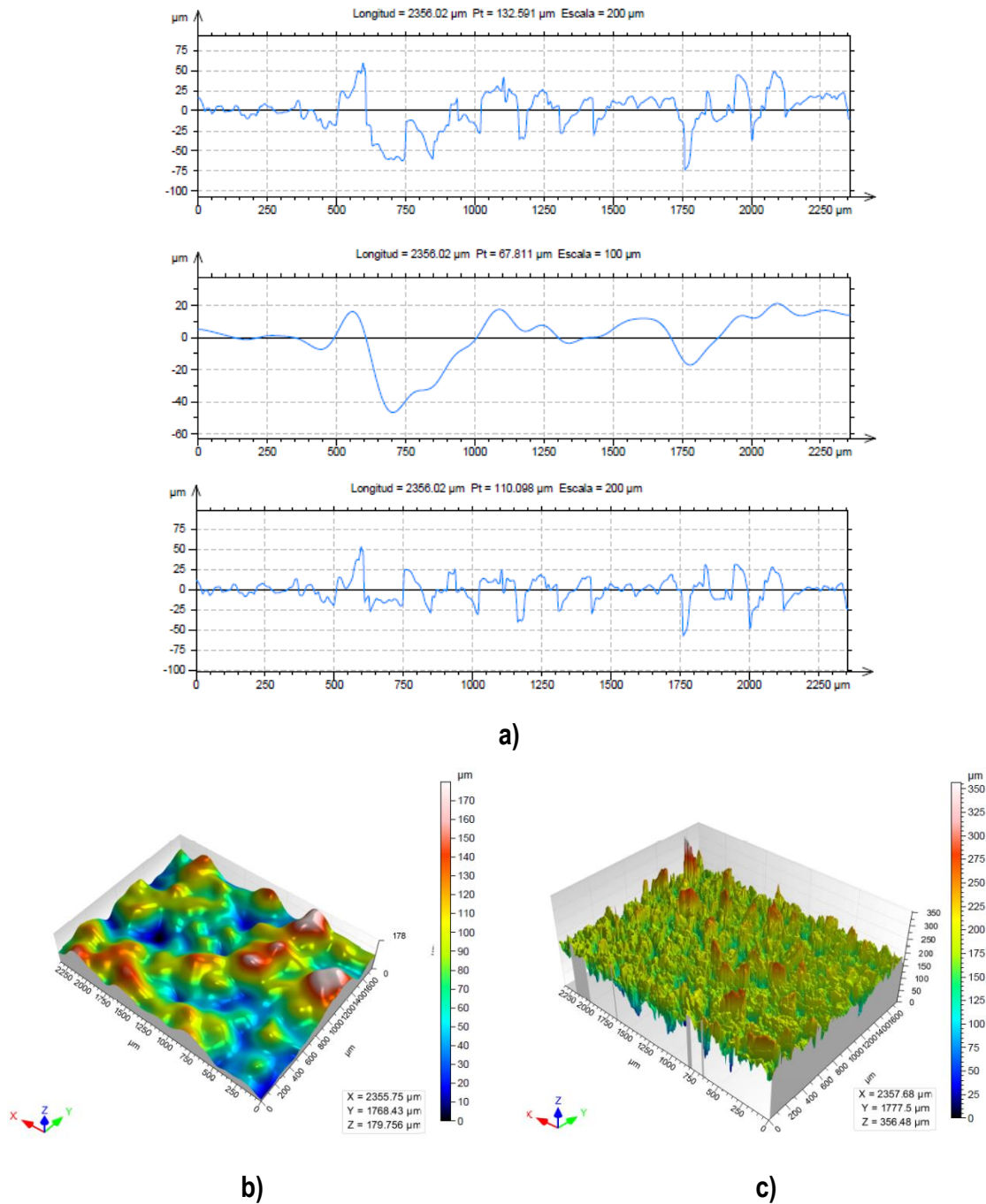
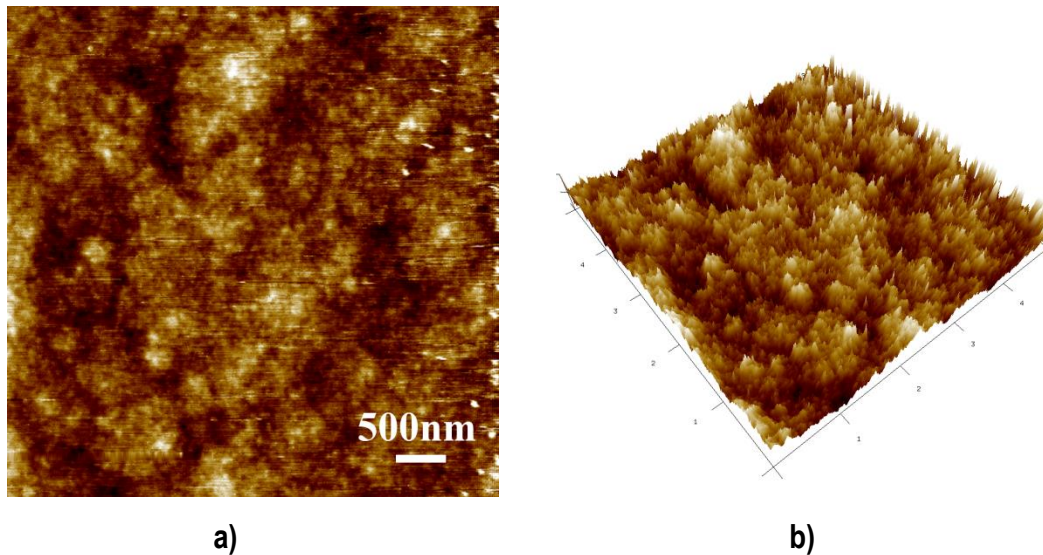


Figure 4.55. a) 2D surface profiles and b-c) 3D surface waviness and roughness topographies

As no significant surface topographic differences were perceived in confocal microscopy between CS CP-Ti coating before and after the nanotexturization by alkaline treatment, AFM measurements were performed in order to analyze the nanotopography. Figure 4.56 shows the 2D and 3D surface topographies of alkaline treated CS CP-Ti coatings (IEc-sample 7). The  $R_a$  parameter was calculated to be  $1.2 \pm 0.2$  nm. In comparison with the anodic oxidation treatment ( $R_a = 36.8 \pm 4.6$  nm), small nanofeatures were found.



**Figure 4.56.** AFM micrographs of a) 2D and b) 3D topographies of alkaline treated CS CP-Ti coating (IEc-sample 7)

## 4.2.3. HYROXYAPATITE COATINGS

### 4.2.3.1. Introduction

Although the deposition of ceramics has not been much investigated by CS, their solid bonding phenomena has also been reported in other deposition techniques at room temperature such as aerosol deposition (AD), sometimes known as vacuum cold spray (VCS) and nanoparticle deposition systems (NPDS) [115, 116, 117, 118, 119], in which HA coatings have also been actually produced by this technology [120,121]. In AD, the impinged particles fracture on the substrate in analogy to the plastic deformation of a metallic particle. Then, the newly formed surface bonds to the substrate surface. This phenomenon is called room-temperature impact consolidation (RTIC) [115] (Fig. 4.57a). It resembles the dynamic fragmentation simulated by Park et al. [122] where an alumina particle undergoes shock-induced plasticity and is finally fragmented in order to release the energy that the material cannot accommodate. These authors indicate that the film growth process is a competition between particle plasticity and fracture+erosion. The suggested ceramic deposition mechanism in NPDS is analogue: first, submicron particles strike the substrate and fragmentation and packing of the particles occurs. The fractured nanoparticles stick together with few bonding sites due to a low packing density, which results in weak bonding. Subsequent submicron particles strike the accumulated nanoparticles and shock compaction

of the nanoparticles occurs. The nanoparticles are consolidated at high heat energy and pressure [115,123].

CS is, however, different from AD and NPDS mainly in that the latter two, use submicrometer feedstock particles while usually particles  $<50 \mu\text{m}$  are used in CS. A careful reading of the few articles published about CS of ceramics indicates that the actual bonding mechanism is highly dependent on the microstructure of the feedstock powder and the relative particle–substrate hardness ratio, but the actual mechanism is not yet well clarified. This would explain why some authors observe the embedment of the ceramic particles into very soft and ductile substrates (Fig. 4.57b), whereas others, such as Yamada et al. [124] support a chemical bonding (Fig. 4.57c) rather than anchoring. It appears that for dense powders, the effective deposition is either possible on soft substrates, where the embedment is possible but the posterior coating built-up is hardly likely [125,126] or, on harder substrates through particle fragmentation [122]. On soft substrates, only if substrate material is brought to the surface and is available to bind other particles, a second layer or parts of it are likely to be attached to the coating upon impact. On harder substrates, it is thought that the optimal particle state for a successful substrate attachment is that in which the Hugoniot Elastic Limit (HEL) of the ceramic is reached [122]. The HEL of high-performance ceramics under plane shock wave propagation has generally been attributed to the generation and propagation of microcracks, plastic deformation, and possible phase transformations [127]. If, as result of the spraying parameters, the shock loading pressure exceeds the HEL value, the plastic-fracture ratio decreases. Due to this increased fracture, the elastic rebound forces make that only small remnants of the brittle particle remain in the bonding zones. Most authors agree that the HEL for a ceramic provides a threshold below which the material retains some cohesion and has finite spall strength and above which the material has zero spall strength and becomes a confined powder, except for the work presented by Longy & Cagnoux (1990), who reported that cohesion can be maintained above HEL [128].

For porous or granular powders, the mechanisms may change since yielding threshold is known to decrease with decreasing density. Notice that Klieman et al. [126] as well as Yamada et al. [124] sprayed  $\text{TiO}_2$  onto stainless steel, achieving the second ones much thicker deposits; although the spraying tested conditions are slightly different for both studies, it is obvious that the intrinsic porosity of the powder used by the second group of authors is

much more favourable for crack nucleation and, therefore, fragmentation and porous collapse. In addition, the nanoscaled primary particles configuring the porous powder seem to be also important to explain the chemical bonding mechanism.

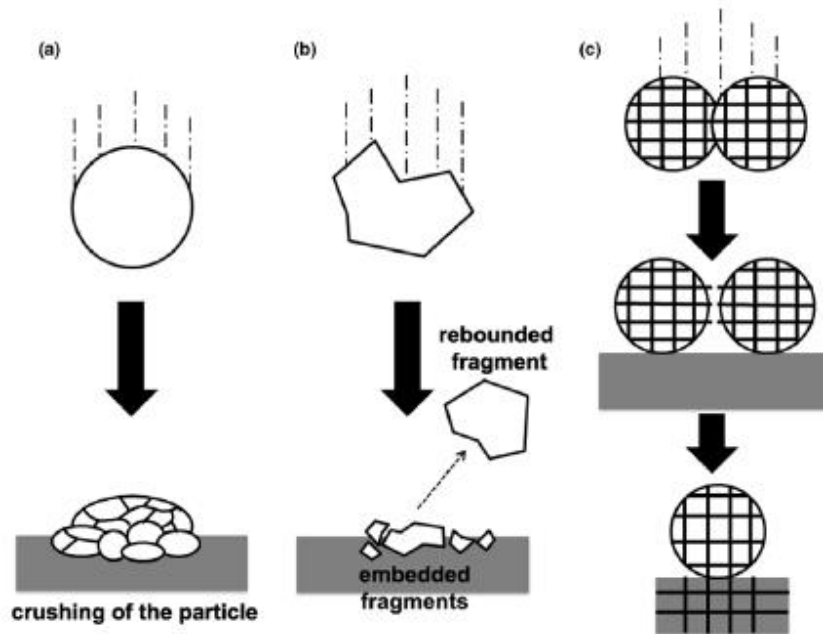


**Figure 4.57.** Suggested bonding mechanisms of ceramic particles in low-temperature deposition processes: a) room-temperature impact consolidation (RTIC), b) embedment or mechanical anchoring, c) chemical bonding

The micrographs presented in the present chapter also seem to reveal the importance of the primary porous structure. In any of the substrates, their attachment leads to slight scattering of fragments around the central part, similar to the jets of metal splats, which has been commonly associated to adiabatic shearing instabilities when the material flows. However, it is obvious that the term “plastic flow” in ceramics cannot be understood as in metals due to the constraining conditions imposed by the surrounding material.

This part of the subchapter is focusing on the development of HA coatings by CS. Two powders with different microstructured were sprayed and their mechanism of deposition were analyzed, as well as their microstructural properties.

### 4.2.3.2. Spraying conditions

---

*As hydroxyapatite coatings were protected by an intellectual property [129], spraying conditions were expressed in terms of  $T_{x(number)}$  (temperature),  $P_{x(number)}$  (pressure),  $D_{x(number)}$  (distance) and  $FR_{x(number)}$  (Feeding rate).*

---

#### a) Splat characterization

##### Sintered HA powder

Sintered HA feedstock powder started to be optimized by High Pressure Cold Spray (HPCS) equipment. The influence of spraying parameters of as-received sintered HA particles was evaluated by a wipe test consisting of a fast movement of the substrate through the spray jet. Wipe tests were performed with a  $3^3$  factorial design experiment, with three different pressures, temperatures and distances as variable parameters (Fig. 4.58a). From the different combination of parameters it was found that the combinations that had more splats deposited were the ones marked in figure 4.58a in red colour. Those conditions were sprayed again but with intermedium pressures and distances in other to accurate better the spraying conditions (Fig. 4.58b). Suitable spraying conditions were found in figure 4.58b (marked in red colour).

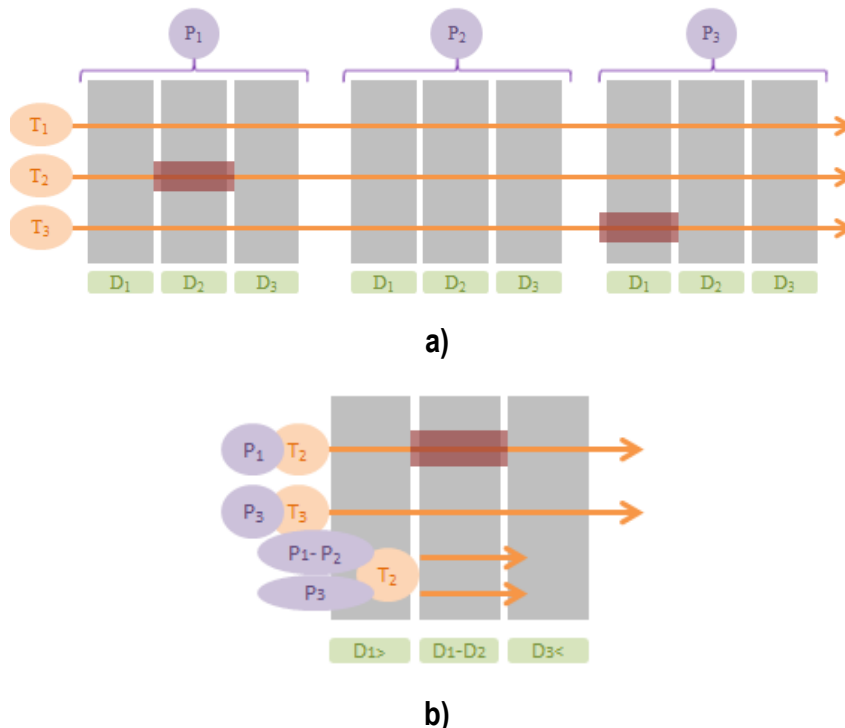
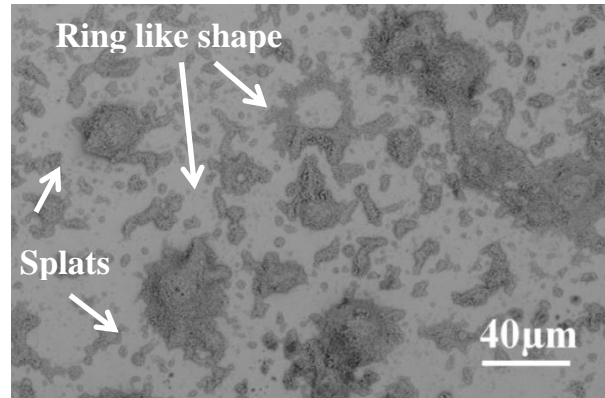


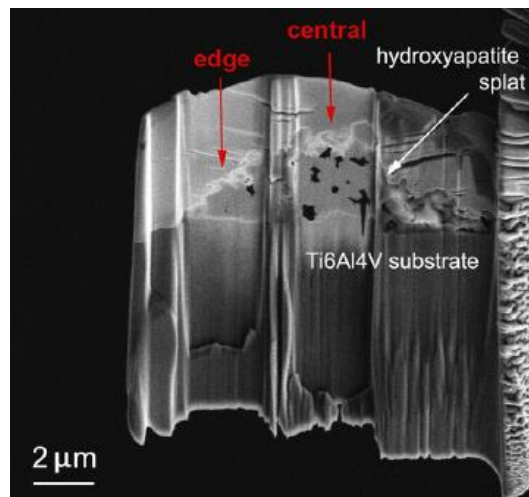
Figure 4.58. a-b) Schema of spraying conditions for wipe test

Figure 4.59 shows the splat morphologies of the sintered HA powder onto the polished Ti6Al4V alloy substrate from the suitable spraying conditions obtained in figure 4.58b. Top view morphology of sintered HA splats consists of a mixture of attached splats with fragments scattered around as well as ring-like shape HA remnants resulting from the bounce off of some of the particles. Near the fractured particles, slight substrate deformation was observed.



**Figure 4.59.** Top view morphology of several HA single particle impacts on Ti6Al4V alloy substrate

The particle microstructure was evaluated in terms of TEM. In order to examine the features within the particle, a thin lamella of a 12 μm particle size was obtained by FIB lift-out technique and compared to the initial feedstock structure. Figure 4.60 shows the FIB lamella of an approximately 12 μm sintered HA splat onto the Ti6Al4V alloy.



**Figure 4.60.** FIB preparation of a sintered HA splat on Ti6Al4V alloy substrate

Figure 4.61a shows the TEM micrograph of the corresponding central part, where the porous structure is still visible; the porous size distribution has changed because of the impact from that of the original particle (Fig. 4.12a) since no more necks can be distinguished. This indicates that these narrow neck areas, if present, can act as damage initiation points under

high-impact loading stresses. The appearance of contrast areas compared to figure 4.12a may be attributed to strained effects and also dislocation entanglement at grain boundaries. However, the grains still keep dimensions of the same order as those in feedstock. The structure keeps some pre-existing curved flaws and no extense intergranular cracking is noticed.

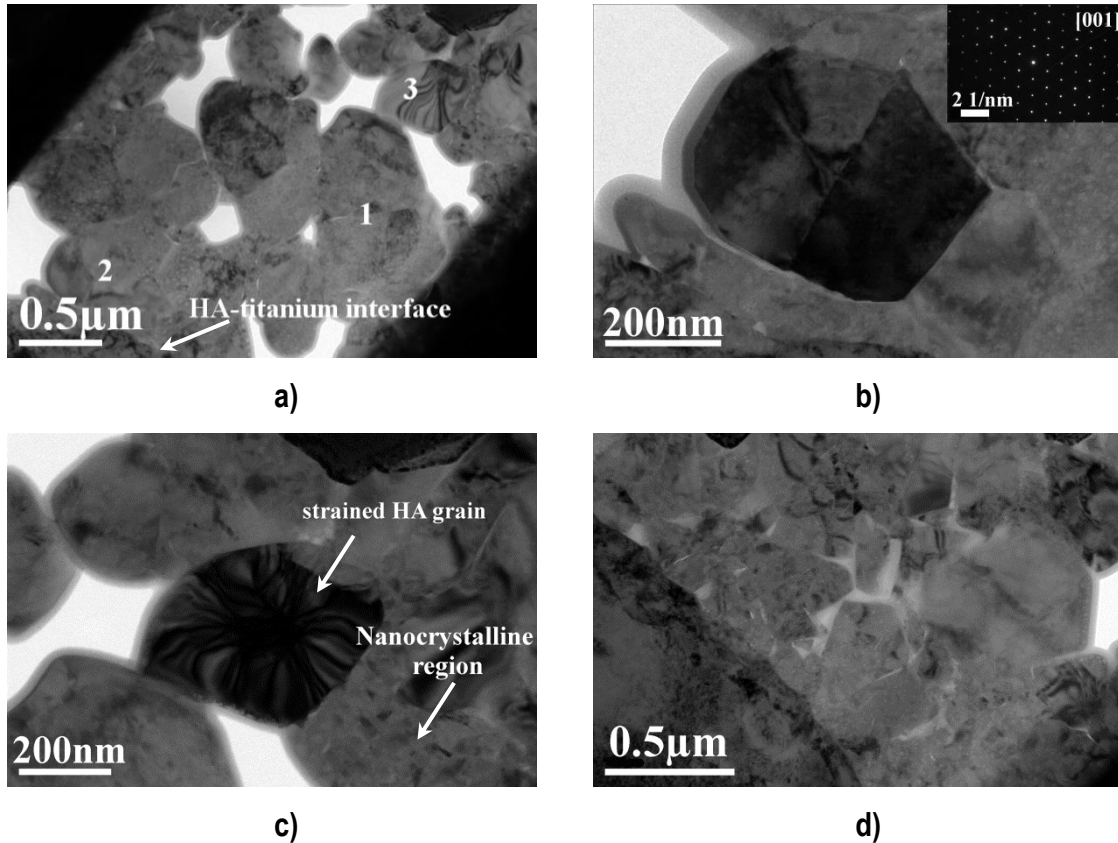


**Figure 4.61.** Optical micrographs of the top surfaces of the CS HA-rough Ti coatings from the sintered feedstock powder onto a) #240 grinded, b) SB surfaces and c) CS CP-Ti coating; d-e) Cross section of CS CP-Ti coating in bright and dark field

No large cracks were observed at all. Figure 4.61b exhibits a singular grain oriented along the [001] zone axis with a particular straight internal feature; its observation by HRTEM as well as its electron diffraction indicates that the whole grain is obtained in the same zone axis without any sign of misorientation. Therefore, there is no shear or twisting, just a plastic deformation feature in a single favourable oriented plane. Highly strained grains and fine grain areas are also characteristic of the complex structure resulting from impact figure 4.61c. More likely, SAED indicates that most grains have a single-crystal structure, except for specific regions such as that indicated in figure 4.61c, which appears to be highly polycrystalline and consists of randomly oriented crystallites less than 50 nm in size, with an average of ~20 nm. The

edge part of the splat appears to be more compact than the central part (Fig. 4.61d) and grains seem to be more cracked and slightly crushed; in some of them, extinction contours can be observed.

The crushing and pore collapsing observed in figure 4.61d which has some similarities to the well-reported macroscopic examples of shock loading of rocks [130], this may be explained by the shock loading under high-strain rates occurring in microsized CS ceramic particles; this leads to strain localization and the typically shear band formation in inelastic solids. As assumed from the previous sections, strain localization in granular materials may not be the same as in fully dense materials. In granular materials, it can also take place normal to the principal compressive stress, forming so called compaction or dilation bands [131]. Curran et al. [132] developed a micromechanical model for a granular material under high-strain rate deformation, with competition between dilatation and pore compaction.

At the microscale level, the propagation of the shock wave may proceed through microfracturing due to tensile and compressive stresses, as well as local shearing and twisting of grains, due to hydrostatic stress component [133], which would explain the contrast at the strained areas. The mechanism of fracturing might be well expected considering that, under the shock pressures given in CS, the stress state in particles upon impact is much above the HEL limit of the material [134]. Here, the presence of pores makes that the deformation occurs most likely first by fracture of the sintered necks between the grains. Grain boundaries of initial HA particles are the weak sites that easily induce intergranular microcrack formation, behaving as damage initiation points. Damage can further proceed in transgranular mode by shear and/or twist fracture at single or multiple planes in favourable oriented grains [132].

With the increased strain rates up to the levels occurring in CS, slip is more difficult, and associated crack initiation may be suppressed, with a commensurate rise in strength, as observed from the force versus displacement curves at the flat punch tests. However, some cells and networks of dislocations were observed, which could be responsible for the work hardening of the material during dynamic deformation and become a competitive mechanism.

The particle–substrate interface is rather smooth with no noticeable detachment (Fig.4.62). In addition, SAED pattern of the HA side shows a ring pattern typical of a polycrystalline area as

well as the titanium side. From the high resolution TEM image of the interface, many Moirée patterns can be observed, indicating overlapping of the fine grains.

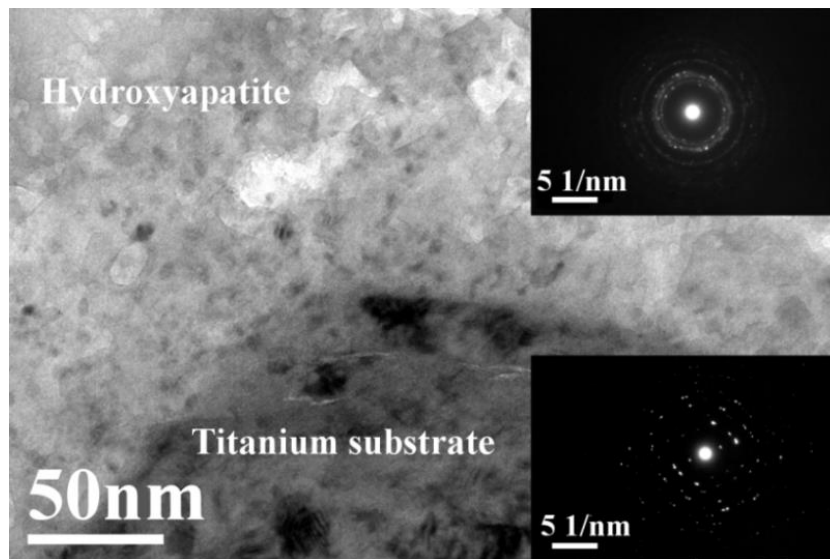


**Figure 4.62.** a) HA-Ti alloy interface showing the fine-grain size at both sides of the interface, as well as the corresponding SAED patterns

Figure 4.63 is the general structure of a 7  $\mu\text{m}$  splat showing some single-crystal regions (label 1 with corresponding SAED at inset 1) and some polycrystalline areas (labels 2 and 3 with corresponding SAED at inset 2 and 3). The presence of both single crystal and fine-grain structures in the two investigated particles might be indicative of heterogeneous stress distribution upon particle impact.

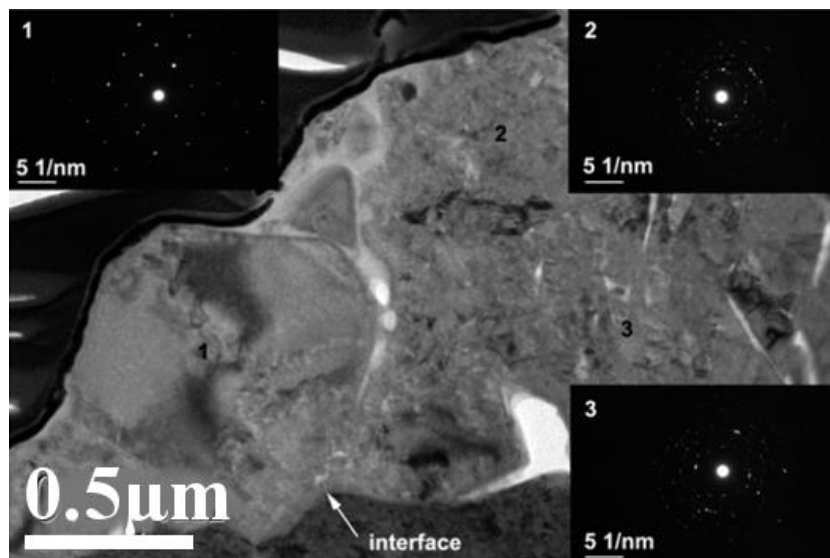


**Figure 4.63.** TEM micrograph of a 7  $\mu\text{m}$  HA splat onto Ti6Al4V alloy substrate (inset SAED patterns)

Then, the impact mechanism of the 12  $\mu\text{m}$  HA splat seems to have occurred by: (i) slight void collapse, (ii) dynamic fragmentation proceeding by cracking and crushing and (iii) reduction in crystal size by plastic deformation mechanisms. In view of the microstructure of the 7  $\mu\text{m}$  splat, a denser structure is visible with predominance of very fine-grain regions, without the presence of plastic deformation features.

Figure 4.64 presents the compressive stress-strain loading curves of a single sintered HA particle for an about two 15  $\mu\text{m}$  at low and high-strain rates. Although the high-strain rate is very much lower than that typically occurring during CS ( $10^6 \text{ s}^{-1}$ ), it has been proved to be enough to show the collapse of the particle (Fig. 4.64a), whereas at low strain rate, the progressive cracking is observed by the several load drops during the indentation; the first significant drop corresponds to the occurrence of the crack indicated by an arrow in the inset of figure 4.64b. At the end of the curve, just before the collapse, it can be observed how this upper right part becomes to be detached. By contrast, the insets in figure 4.64a indicate that the particles maintains intact until it cannot withstand the high load and collapses.

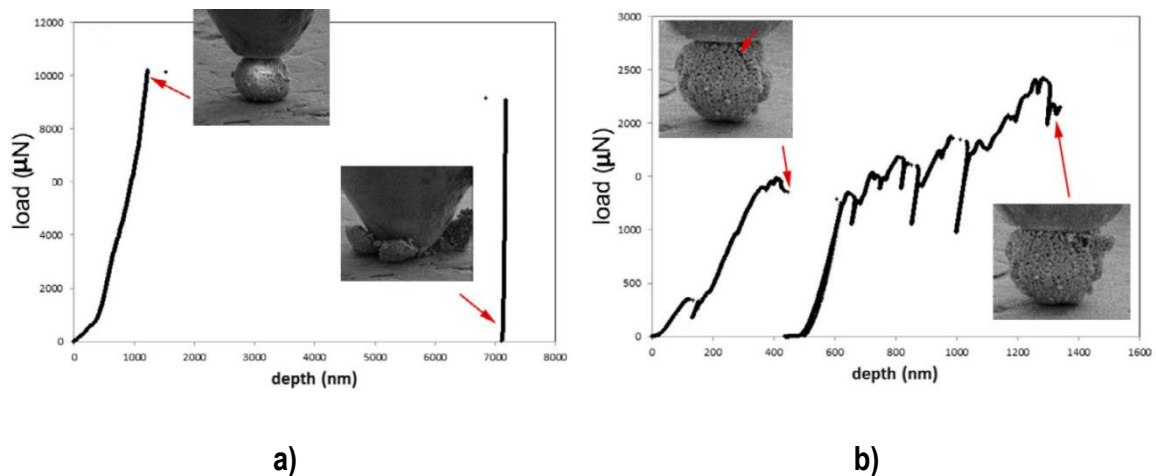


**Figure 4.64.** Loading compressive curves for a single sintered HA particle at a) high and b) low strain rate

Although no temperature measurements on the particles can be undergone, depending on the local temperature rise upon impact, also recrystallization mechanisms might be involved, which would explain the grain refinement observed in figure 4.63 for the 7  $\mu\text{m}$  splat on Ti6Al4V alloy substrate. In this case, if this is the actual mechanism or it is purely given by shock-induced plastic deformation through strong rotation of a local region at boundaries through the formation of low-angle grain boundaries, would involve precise control of the kinetic energy and particle temperature. The differences observed for the 7 and 12  $\mu\text{m}$  splats

appear to indicate how important the particle size effect is, as already predicted by the simulation work of Singh et al. [135]. The fact that the coarser HA splat on titanium alloy possessed still some porosity and that the extent of fine-grain areas is low means that it required higher shear stress for deformation mechanisms. In both cases, however, small and large splats, the coexistence of single-crystalline areas and polycrystalline areas rather than uniform reduction in crystallite size as in AD, might be indicative of a non-uniform stress distribution upon impact when increasing particle size, with predominant grain refinement in smaller particles, as well as the pore distribution with respect to the direction of load application.

The decrease in particle size increases particle velocity and, therefore, higher extends of heat release upon impact which, joined with the low titanium thermal diffusivities may lead to the formation of new nuclei as a result of strong localized heating. Considering that gas temperature was below 400°C, the local temperature rise upon impact should be high to induce ceramic recrystallization [134]. This is also worth noting at the interface, which shows grain refinement also for the 12 µm splat.

#### **Agglomerate HA powder**

Figure 4.65a shows a general view of the wipe test on the Ti6Al4V substrate and figure 4.65b is a magnification of a single deposited particle. This wipe test was performed with the same optimal conditions from the wipe test of sintered HA powder in order to compare particle deposition. A quite high particle deposition is observed and the absence of craters is an indication that upon the high shock pressure of the process and, given the hardness of the substrate and the agglomerated nature of the feedstock, the particles are more prone to spread over the surface rather than bouncing off leaving craters. This behaviour is somehow different from what was observed within the previous study with the sintered feedstock powder where, when the particles did not properly bond, they left ring-shape morphologies with the central part of the splat bounced off. That performance was well in agreement to the stress distribution simulations usually carried out in CS which indicate that upon impact tensile stresses may be developed at the centre bottom of the splats resulting in detachment [136]. Similar ceramic particle behaviour was found in the AD method. The AD method is based on shock-loading compaction due to the impact of ultrafine ceramic particles onto a surface. First, particles are mixed with a gas to generate an aerosol. During the impact onto

the substrate, part of the particles kinetic energy is converted into thermal energy causing increase in temperature at the point-of-impact and promoting bonding between the substrate and the particles and also between multiple particles. The result is a process that yields an acceptable consolidation at room temperature without the need for a thermal treatment. This process is called room temperature impact consolidation (RTIC) [118].

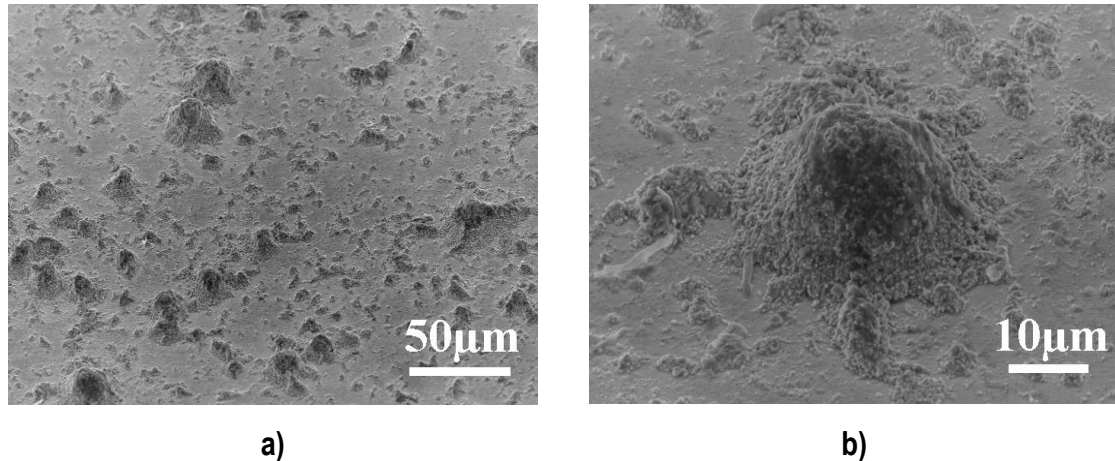


**Figure 4.65.** a-b) Wipe test of agglomerate HA on the Ti6Al4V substrate at different magnifications

The morphology of CS HA bonded particles, either coming from a sintered or an agglomerate feedstock seem to be quite similar (Fig. 4.59 and 4.65) but further insight into the microstructure reveals the differences [137]. The nature of the powder made already foresee that its deposition would be quite different from that of sintered particles, i.e by pore collapsing and crushing. Therefore, the powder processing route is really important to be considered. A FIB-splat lamella was prepared from agglomerate HA splat (Fig. 4.66a). In general, at low magnification, a random orientation of the small crystallites was observed all over the splat (Fig. 4.66b). At certain zones, more in the upper side of the prepared FIB-splat lamella, the needle-like morphology can still be observed (Fig. 4.66c). In other more inner regions (Fig. 4.66d), however, Moirée fringes are also observed but without observing such needle-like structure; rather, crystallite overlapping appears to be more significant. Figure 4.66e shows the region near the interface with the substrate, where such overlapping is visible. It must be said that all along the interface, a good adhesion was observed, similar to what was reported by Yao et al. for TiO<sub>2</sub> [138]. It seems that the impact has produced compaction of nanocrystalline grains within the particle, preserving the nanoscale nature. This is slightly different from the room-temperature impact consolidation (RTIC) mechanism reported for AD [118] because it would first require fracturing of submicrometer particles.

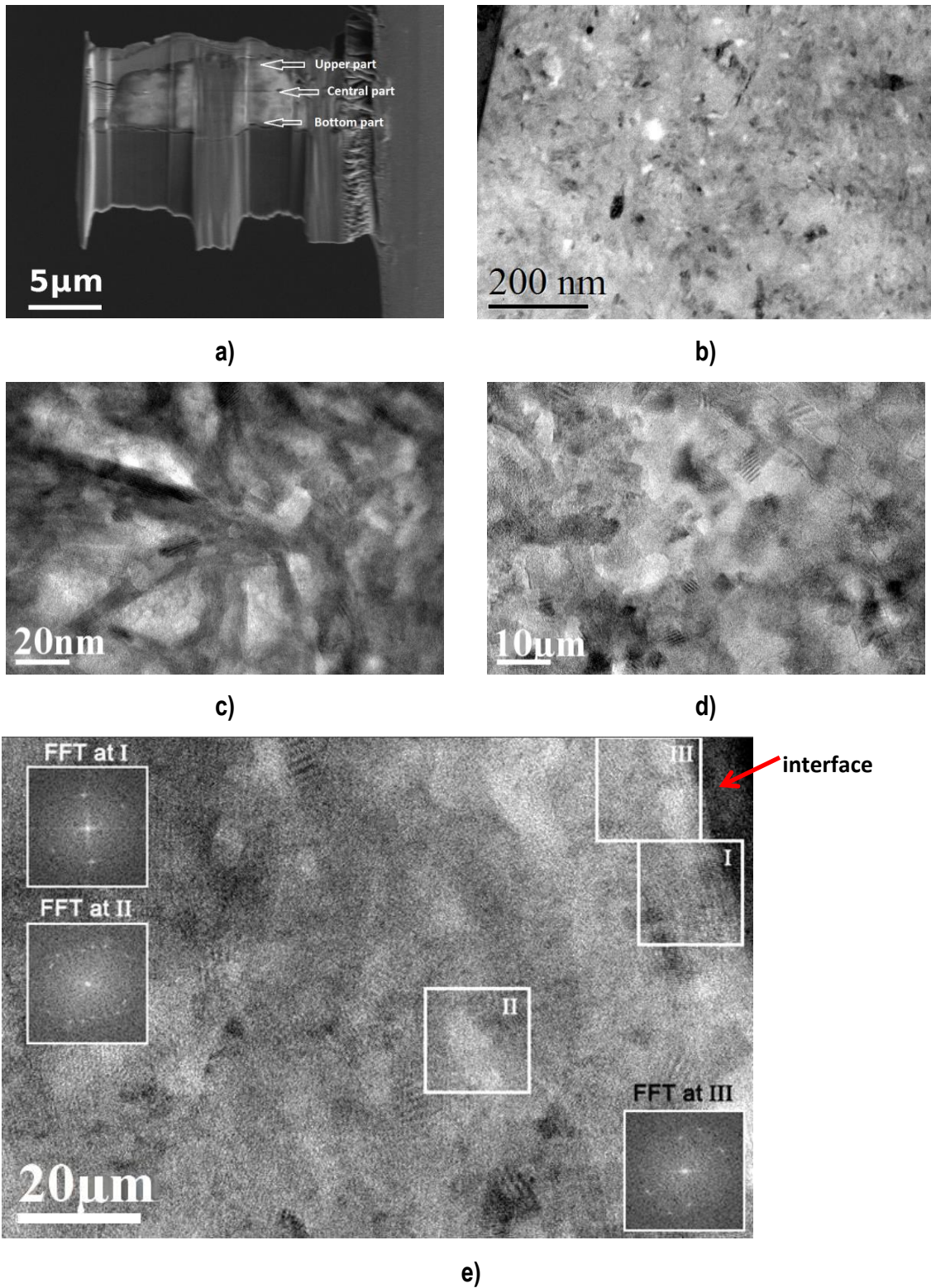


**Figure 4.66.** a) FIB preparation of HA splat on Ti6Al4V alloy. b) General TEM micrograph representative of the whole splat, c) upper, d) central and e) bottom part of the HA splat onto Ti6Al4V

b) Hydroxapatite coatings**Sintered HA powder**

The best spraying conditions selected from the wipe test were optimized according to traverse speed and feeding rate parameters until obtain a HA layer [129]. Different trials were performed with spraying conditions to build-up a coating but no significant differences were perceived. As analyzed before, the impact mechanisms of sintered HA occurred by: (i) slight void collapse, (ii) dynamic fragmentation proceeding by cracking and crushing and (iii) reduction in crystal size by plastic deformation mechanisms, thus leading to a bad adherence between ceramic-ceramic particles. For that reason, different surface activation was performed on Ti6Al4V alloy substrates in order to analyse the influence of the substrate in HA deposition. Figure 4.67 shows sintered HA deposition with the optimal spraying conditions onto #240 grinded and SB surfaces and highly rough CP-Ti coating (IEc-sample 7)

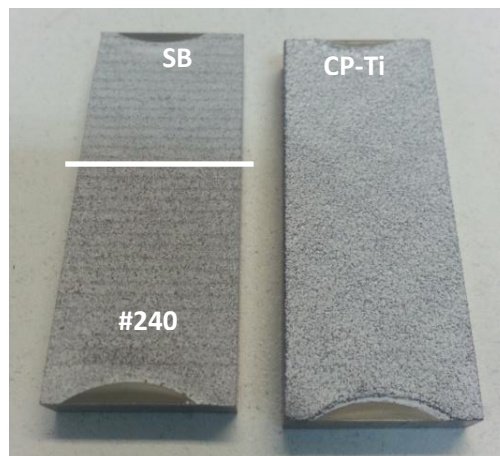


**Figure 4.67.** Sintered HA powder deposited onto SB and #240 grinded surfaces and CS CP-Ti coating

It was observed that the increase of surface roughness leads to a more uniform sintered HA coating deposition along the substrate. Figure 4.68a-b-c shows the top surface area of sintered HA coatings from figure 4.67. For the #240 grinded surface, some gaps of Ti6Al4V alloy substrate were observed, as well as for SB surface. On the other hand, sintered HA coating was able to achieve a full deposited HA area along the CS CP-Ti coating. Figures 4.68d and e show the cross section area of sintered HA deposited coating onto CS CP-Ti coatings, and it was observed that HA fills roughnes valleys of the high roughness along al the rough surface.

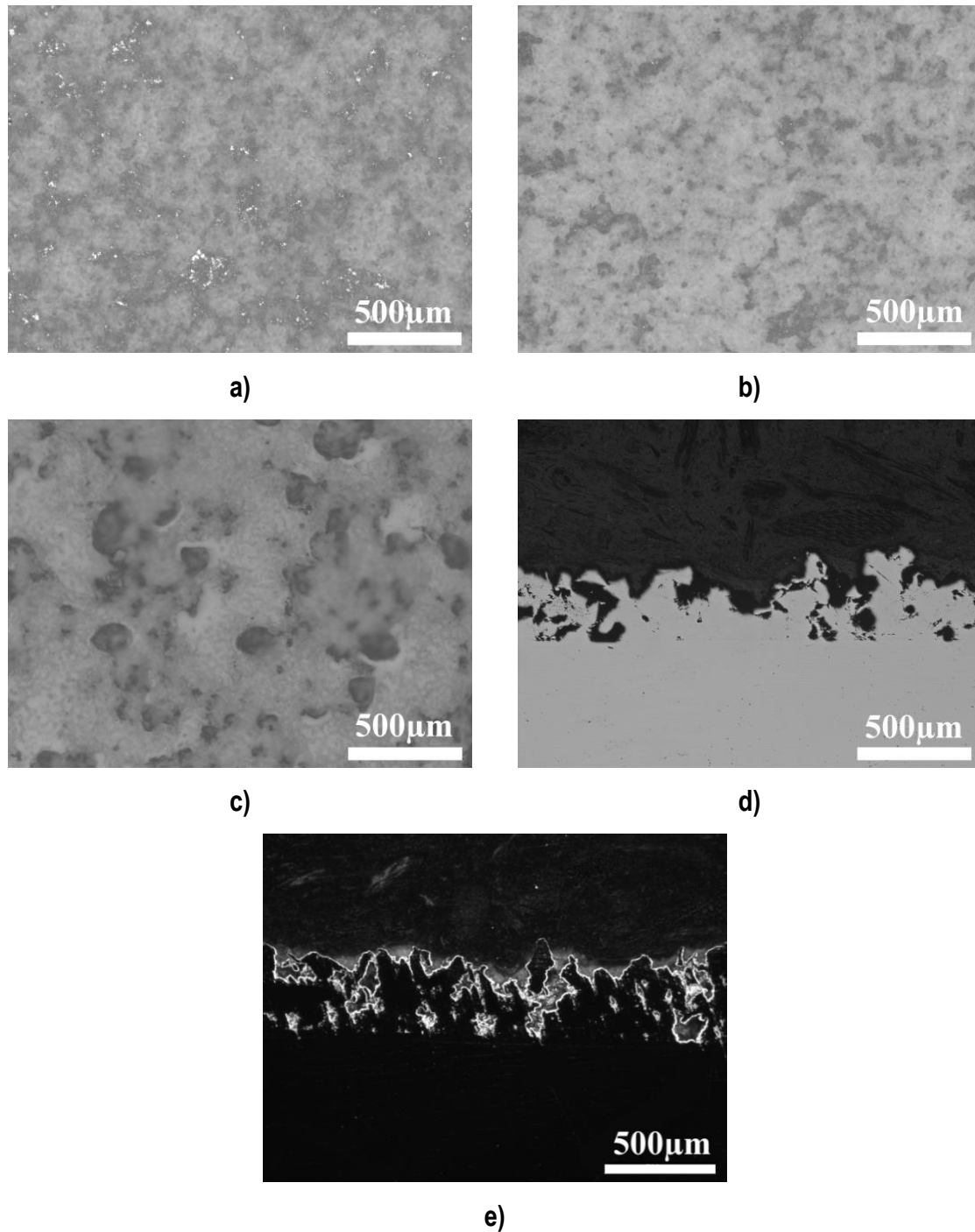


**Figure 4.68.** Top surfaces of the CS HA-rough Ti coatings from the sintered feedstock powder onto a) #240 grinded, b) SB surfaces and c) CS CP-Ti coating; d-e) Cross section of CS CP-Ti coating in bright and dark field

Moreover, analogous HA spraying conditions obtained by HPCS were also used for the Low Pressure CS (LPCS) equipment onto the same previous surfaces (Fig. 4.68). Even so, HPCS shows higher HA deposition along surface, although the differences are not significant.

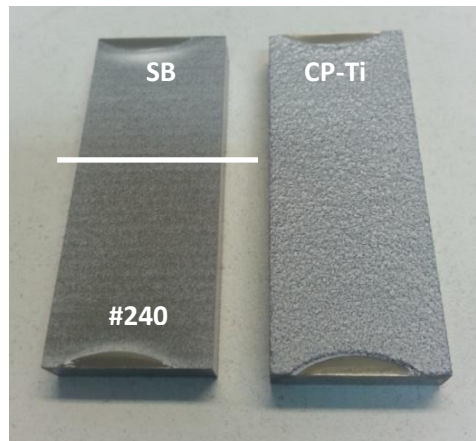


**Figure 4.69.** Sintered HA powder deposited onto SB surface, #240 grinded and CS CP-Ti coating surfaces by LPCS

### Agglomerate HA powder

The same optimal conditions found for the sintered HA powder were sprayed also with the agglomerate HA powder with HPCS and LPCS. Figure 4.70 shows the top surface view of the coatings. As could be observed, agglomerate HA powder doesn't deposit properly onto low roughness surfaces but on high ones. Therefore, on CS CP-Ti coatings, agglomerate HA particle is able to achieve thick coatings. A main difference between HPCS and LPCS is already shown in figure 4.69: the feeding rate (see appendixes). As LPCS has a constant feeding rate deposition, it is able to obtain homogeneous agglomerate HA coatings; on the other hand the feeding rate of HPCS leads to heterogeneous agglomerate HA deposition.

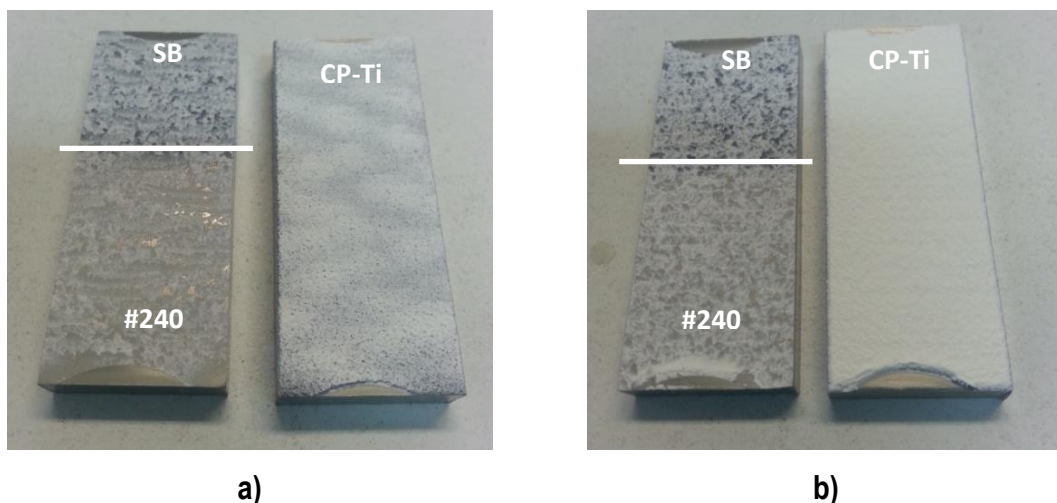


**Figure 4.70.** Agglomerate HA powder deposited onto SB, #240 grinded surfaces and CS CP-Ti coating by a) HPCS and b) LPCS

The cross section area of agglomerated HA by LPCS onto CS CP-Ti coating is already shown in figure 4.71. It could be observed a good bonding between HA and CS CP-Ti coating with a thickness of  $\sim 400\mu\text{m}$ .

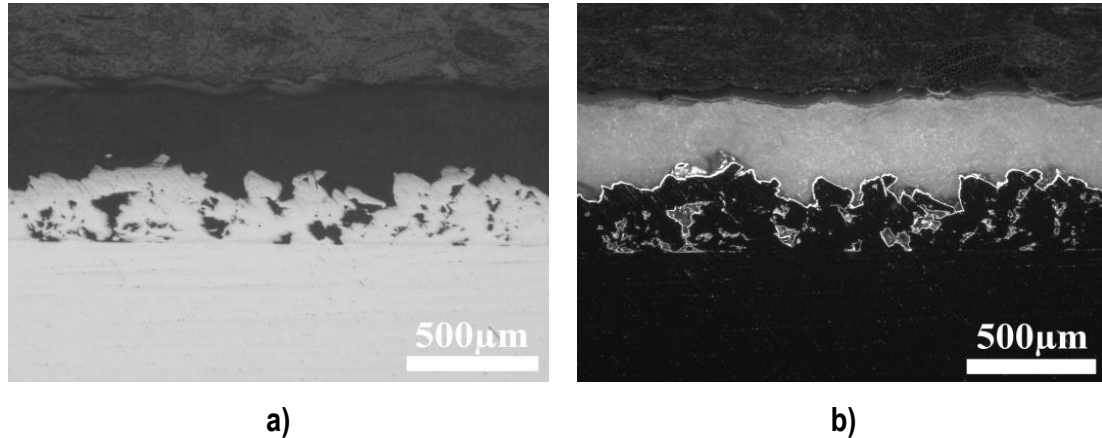


**Figure 4.71.** Optical micrographs of the cross section of the CS HA-rough Ti coatings from the agglomerated HA feedstock powder a) bright field and b) dark field.

The agglomerate HA powder is able to grow up a layer due to its particle deposition mechanism. Figure 4.72 shows the factorial design in order to evaluate the influence of Temperature (T) and Feeding Rate (FR). Four different temperatures and three feeding rates were chosen maintaining the other spraying parameters from the optimal ones found for sintered HA coating.

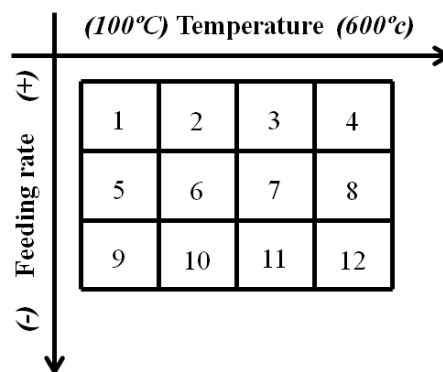


**Figure 4.72.** Factorial design of the agglomerate HA powder

Figure 4.73 shows the cross section areas of agglomerate HA coatings for each condition of the factorial design (Fig. 4.72), while table 4.23 summarizes its thicknesses. All sprayed conditions shown densified agglomerate HA coating. The cross-section areas show good coating interface between coating and rough surface without any type of defect such cracks

and voids. The agglomerate HA feedstock powder results in dense ceramic coatings onto CS CP-Ti coating with any defect at its interface; as higher is the feeding rate, higher is the thickness. Also it was observed that at low feeding rates, the increase of temperature does not affect HA thickness but yes at high feeding rates, leading to thick HA coatings while increase the temperature.

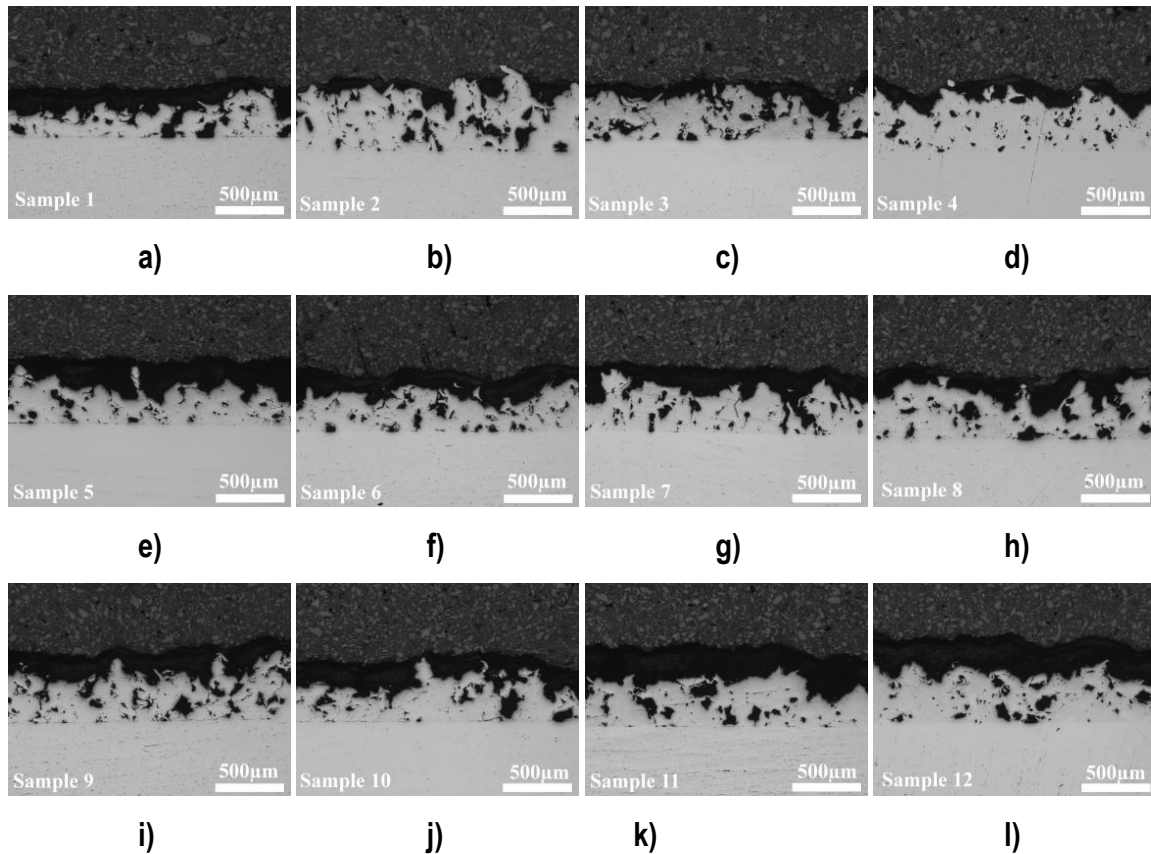


**Figure 4.73.** Cross-sections of the agglomerate HA coatings onto highly rough CS CP-Ti coating according to figure 4.72

**Table 4.23.** Thicknesses of the agglomerate HA coatings onto highly rough CS CP-Ti coating

Agglomerate HA coating thickness ( $\mu\text{m}$ ) of Samples 1 to 12					
<b>Sample 1</b>	122 $\pm$ 34	<b>Sample 2</b>	93 $\pm$ 32	<b>Sample 3</b>	83 $\pm$ 20
<b>Sample 4</b>	112 $\pm$ 39	<b>Sample 5</b>	182 $\pm$ 54	<b>Sample 6</b>	154 $\pm$ 49
<b>Sample 7</b>	179 $\pm$ 54	<b>Sample 8</b>	145 $\pm$ 50	<b>Sample 9</b>	167 $\pm$ 49
<b>Sample 10</b>	16 $\pm$ 57	<b>Sample 11</b>	241 $\pm$ 70	<b>Sample 12</b>	248 $\pm$ 59

HA coatings are well recognized for its rapid fixation and long term stability; for that, it is just necessary a coating thickness around 50  $\mu\text{m}$ . Current commercial prosthesis components

include already a rough metallic coating with a very thin bioactive HA layer to enhance cell response by combining the roughness coming from the Ti coating and the bioactivity of HA coating, showing promising results. Companies such as Eurocoating and Furlong are working on that direction showing good in vivo results and doctors actually feel more reliable having a rough surface because this gives a better feeling of mechanical anchoring afterwards for this cementless prosthesis. HA ceramic-coated femoral components in young patients followed up for 17 to 25 years have been demonstrated to have 100% survival gives excellent long-term results [139]. So, in order to optimize agglomerate HA coatings to a layer with a  $\sim 50\mu\text{m}$  thickness, the traverse speed was increased up for sample 5 (the one that had a highest deposition rate according to the respective feeding rate) until reach a coating thickness of  $50\mu\text{m}$ .

Figure 4.74a shows the top surface area of agglomerate HA coating with a  $45\pm 20$  thickness. It could be observed agglomerated HA was deposited along all CS CP-Ti coatings. Figure 4.74b shows the respective cross section area.

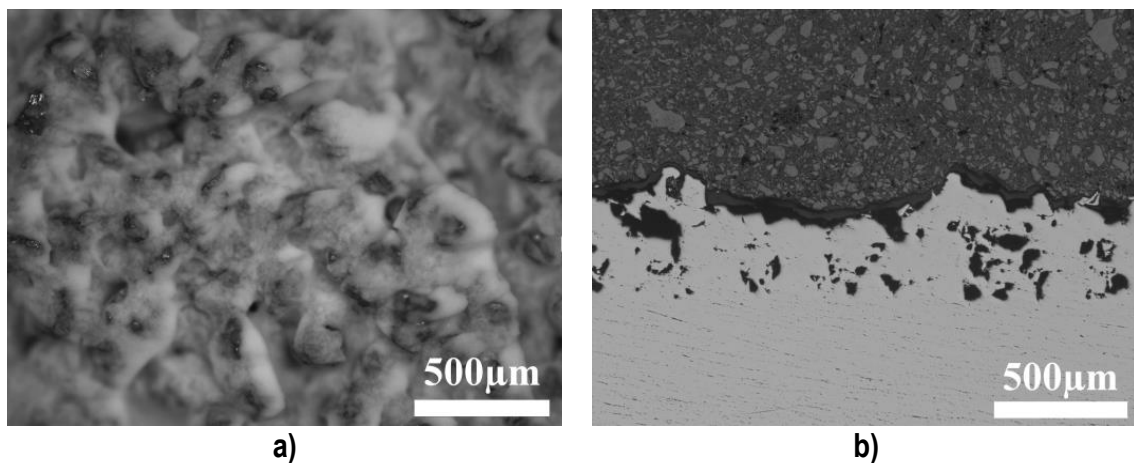


Figure 4.74. a) Top surface area and b) cross section area of  $\sim 50\mu\text{m}$  thickness agglomerate HA coating

### 4.2.3.3. Coating characterization

#### a) Surface features

##### ➤ Top surface morphology

Figure 4.75 shows the top surface areas of the optimal CS sintered and agglomerate HA coatings. During the CS process, sintered HA particles impact onto the surface and fracture in small subgrains in which feedstock powders is composed (Fig. 4.75a). Sintered HA top

surface area shows well-defined subgrain morphology along the CS CP-Ti coatings (Fig. 4.75b). On the other hand figure 4.75c shows a surface covered by the fine agglomerates in which is composed the agglomerate HA feedstock powder (Fig. 4.75d); in comparison with the as-sprayed CS CP-Ti coating, the deposition of the both HA powders cover the nanoasperities coming from the irregularities of the CP-Ti powder, as well the peaks and the valleys of CS CP-Ti coating.

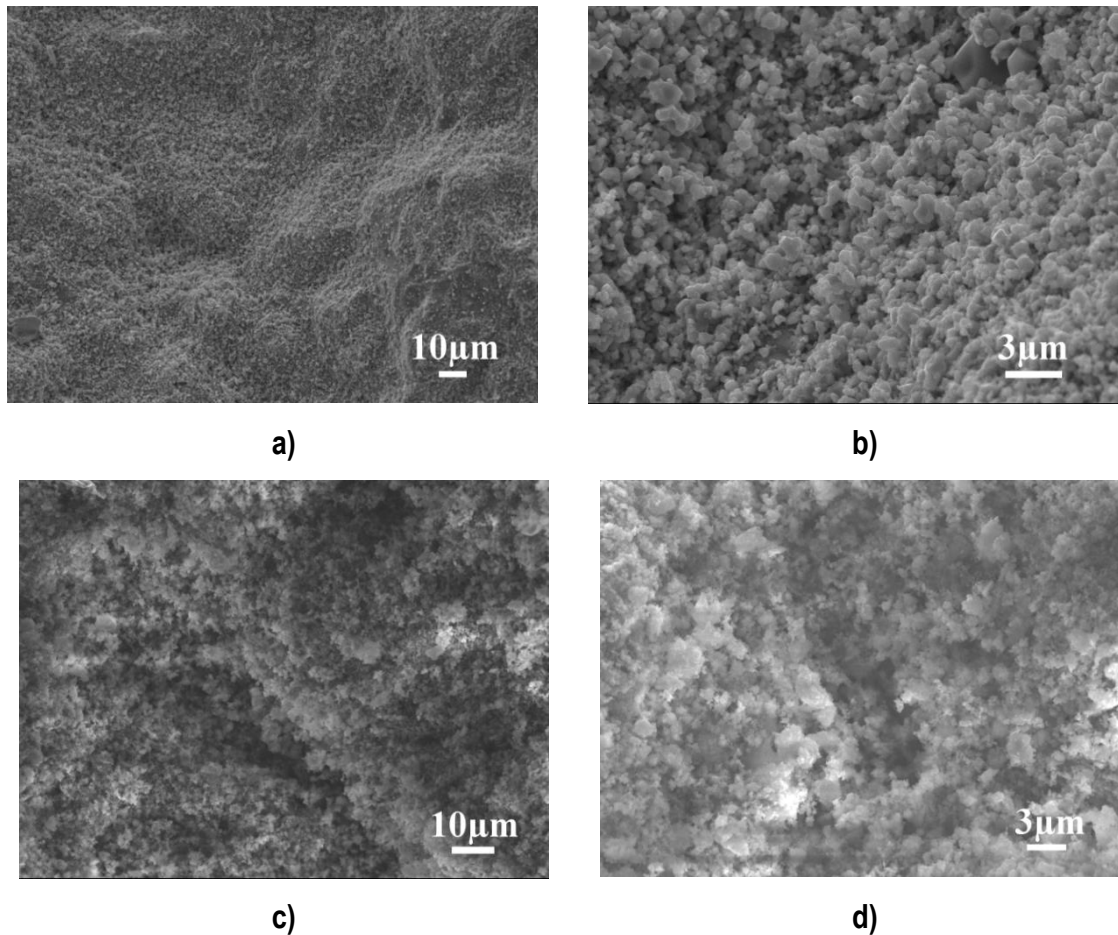


**Figure 4.75.** FESEM micrographs of the top surface areas of a-b) sintered, c-d) agglomerate HA coatings at different magnifications

The surface morphology of CS sintered HA coatings is significantly different from that obtained with the same powder but by conventional spraying, i.e. PS, thus shows have a significant lower amount of unmelted submicron size particles, due to the high temperature of the plasma jet (Fig. 4.76a). The PS HA coatings predominantly consist of well flattened lamellae. The average diameter of the splats is between 20-30 μm. It should be mentioned that in those cases that is used high spray power level, microcracks are more likely to appear in splats [140]. The unmelted particles break up into submicrograins in which feedstock

powder is composed and adheres on the coating which is detected by FESEM (marked with arrow fig. 4.76b)

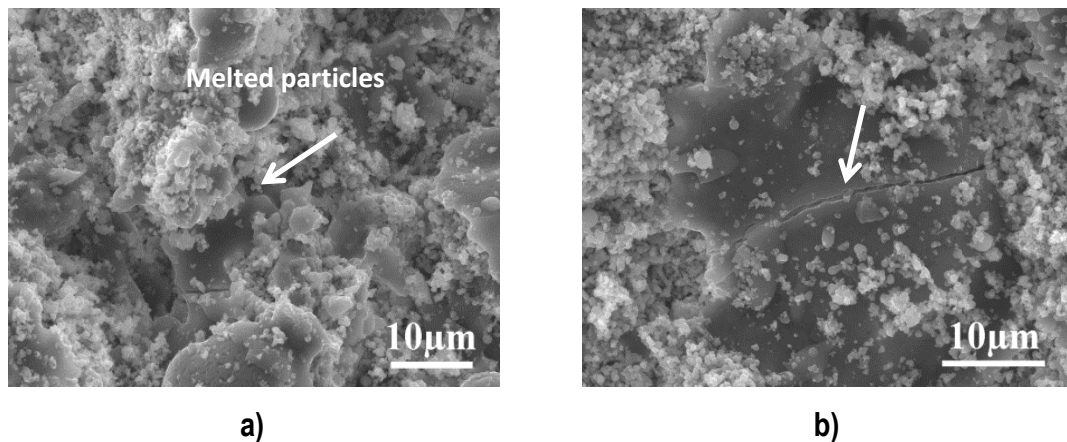


**Figure 4.76.** FESEM micrographs of the top surface areas of a-b) PS HA at different magnifications

#### ➤ Surface wettability

Measurements of the contact angle were performed with MilliQ water and Hanks solution for all surfaces but no significant differences were perceived. Figure 4.77 shows the contact angle of MilliQ water droplet onto HA coatings. A higher contact angle was measured onto PS HA coating with values of  $\alpha_1 = 32.4 \pm 6.9^\circ$  and  $\alpha_2 = 29.8 \pm 5.3^\circ$ , followed by CS HA with values of  $0^\circ$  for both angles. All HA surfaces show hydrophilic behaviour, specially the coatings sprayed with CS due to the CP-Ti rough titanium bondcoat.

The wettability of a coating not only depends on surface topography, also depends on surface microstructure and composition. It is already reported [141] a decrease of the water contact angle with time due to the absorption of the liquid drop through the microscopic pores of the HA coatings. In addition, zeta potential of composite HA (HA/CaO-P<sub>2</sub>O<sub>5</sub>) coatings presented a higher net negative charge than HA coatings indicating an increase of surface hydrophobicity. Previous works in dense ceramics [142] have shown that for similar conditions the net negative surface charge for  $\beta$ -TCP is higher than for HA, thus could explain the different angles obtained from a HA coating obtained by PS and CS, as PS technique, due to the higher temperatures, leads to the formation of secondary HA phases.

Even so, PS HA coatings are reported to be hydrophilic, and contact angles are reported to be  $57.4 \pm 3.2^\circ$  [39]. On the other hand, CS HA shows superhydrophilic behaviour in which my

come between the combination of high roughness provided by CS CP-Ti coatings and the HA coating porosity.

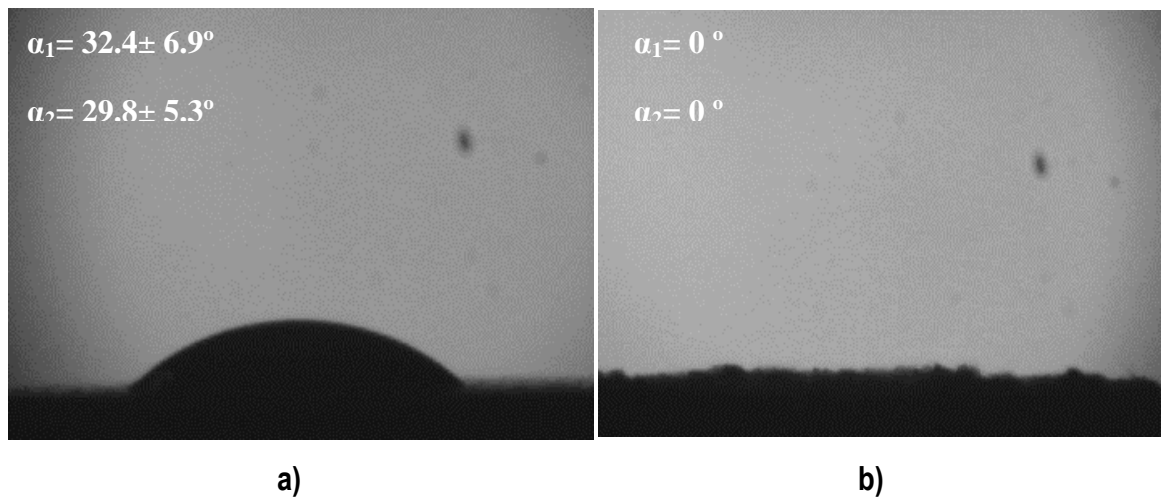


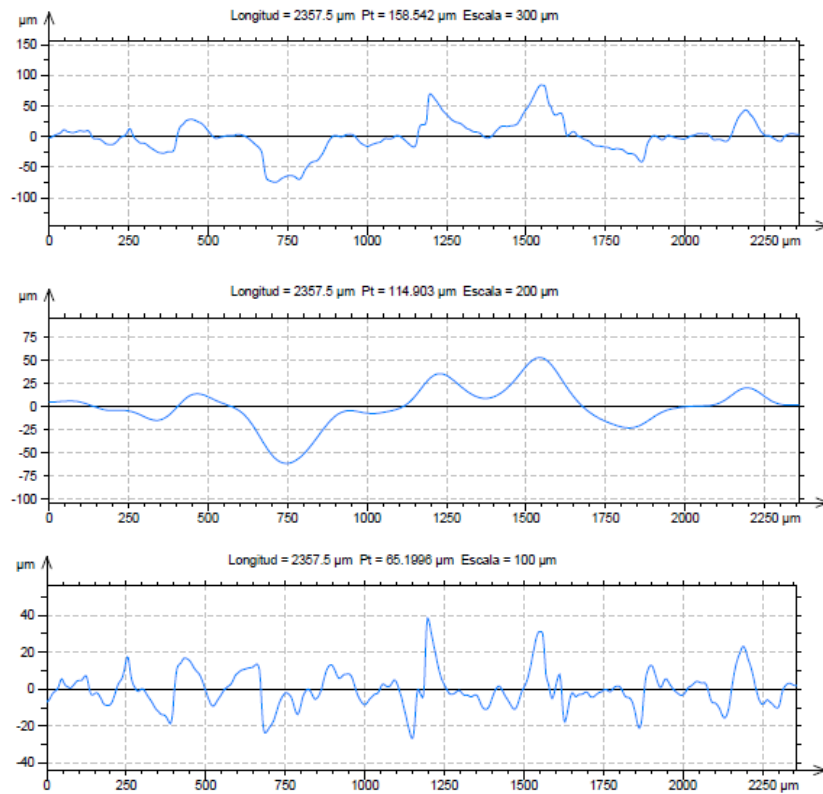
**Figure 4.77.** Contact angles of MilliQ water and Hanks solution droplets for a) PS and b) CS HA coatings

➤ Surface topography parameters

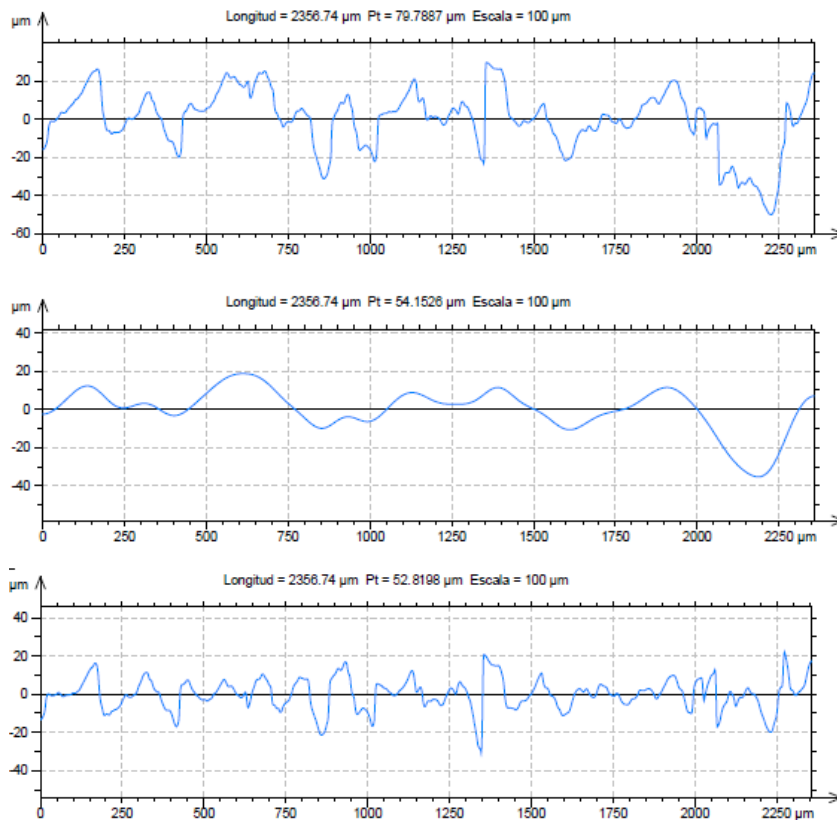
The surface topography of HA coatings shows less roughness than the CS CP-Ti coating, as it deposits along the peaks and valleys of the surface roughness, but they still preserve the good microroughness from the CS CP-Ti coating due to the thin HA thicknesses. Table 4.24 shows the surface topography values of HA coatings while figure 4.78 and 4.79 their respective profiles. On the other hand, conventional PS HA coatings differ very much from surface topography than CS HA coating deposit onto CS CP-Ti coating, as PS HA is sprayed normally onto SB Ti6AlV alloy substrate.

**Table 4.24.** 2D Surface topography of optimal sintered and agglomerate HA coatings

	2D Profile ( $\mu\text{m}$ )		2D Roughness ( $\mu\text{m}$ )		2D Waviness ( $\mu\text{m}$ )	
	Ra $\pm$ SD	Rz $\pm$ SD	Ra $\pm$ SD	Rz $\pm$ SD	Wa $\pm$ SD	Wz $\pm$ SD
<b>Sintered HA</b>	21 $\pm$ 7	117 $\pm$ 43	6 $\pm$ 2	28 $\pm$ 12	6 $\pm$ 2	27 $\pm$ 3
<b>AgglomerateHA</b>	15 $\pm$ 4	87 $\pm$ 20	4 $\pm$ 2	21 $\pm$ 9	6 $\pm$ 4	13 $\pm$ 4
<b>PS HA</b>	4 $\pm$ 1	23 $\pm$ 7	3 $\pm$ 0.3	17 $\pm$ 3	2 $\pm$ 0.3	16 $\pm$ 1



a)



b)

Figure 4.78. 2D Surface profiles of a) sintered and b) agglomerate CS HA coatings ordered by: 2D Profile, waviness and roughness (Top to down)

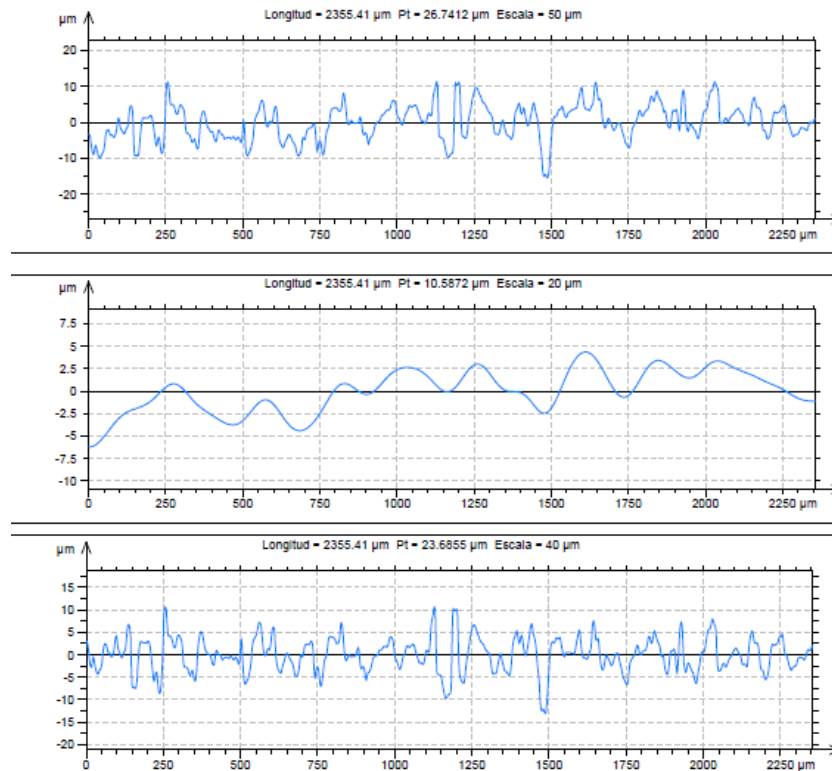


**Figure 4.79.** 2D Surface profiles of PS HA coating ordered by: 2D Profile, waviness and roughness (Top to down)

Regarding the 3D surface topography, the same happens as the 2D topography: surface area decreases with the deposited HA layer. Table 4.25 shows the 3D topography measurements. The HA layer decreases the surface roughness values, but more for the agglomerate HA powder due to the facility that it has for compacting and grow up a HA coating (Fig 4.80).

**Table 4.25.** 3D surface parameters of sintered and agglomerate HA coatings

	3D Profile (μm)		Sdr (μm <sup>2</sup> )	Spr (μm <sup>2</sup> )
	Sa±SD	Sz±SD	Sdr±SD	Spr±SD
<b>Sintered HA</b>	42±2	255±28	59·10 <sup>5</sup> ±2·10 <sup>5</sup>	42·10 <sup>5</sup>
<b>Agglomerate HA</b>	37±6	269±9	59·10 <sup>5</sup> ±1·10 <sup>5</sup>	
<b>PS HA</b>	13±5	72±4	49·10 <sup>5</sup> ±7·10 <sup>4</sup>	

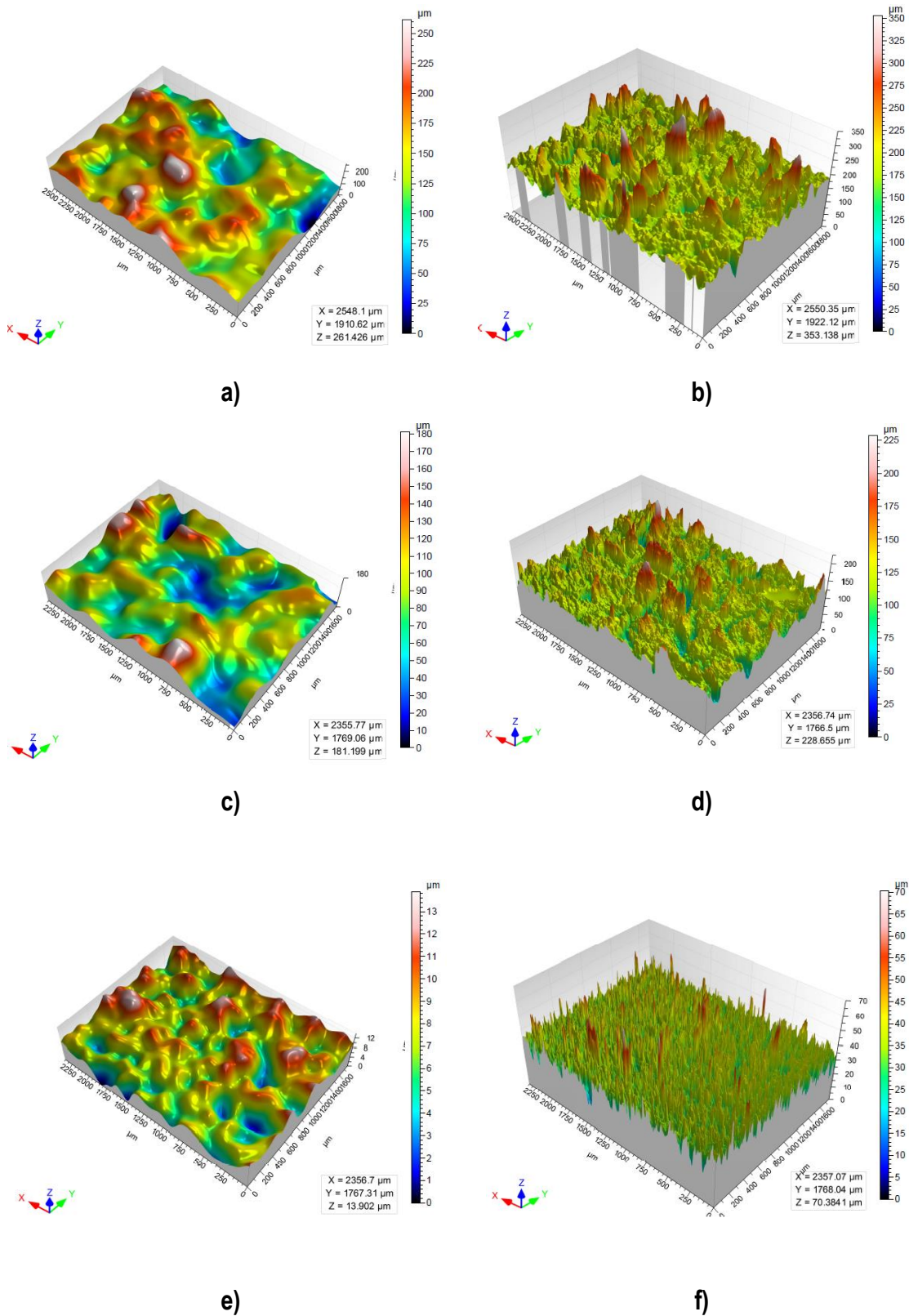
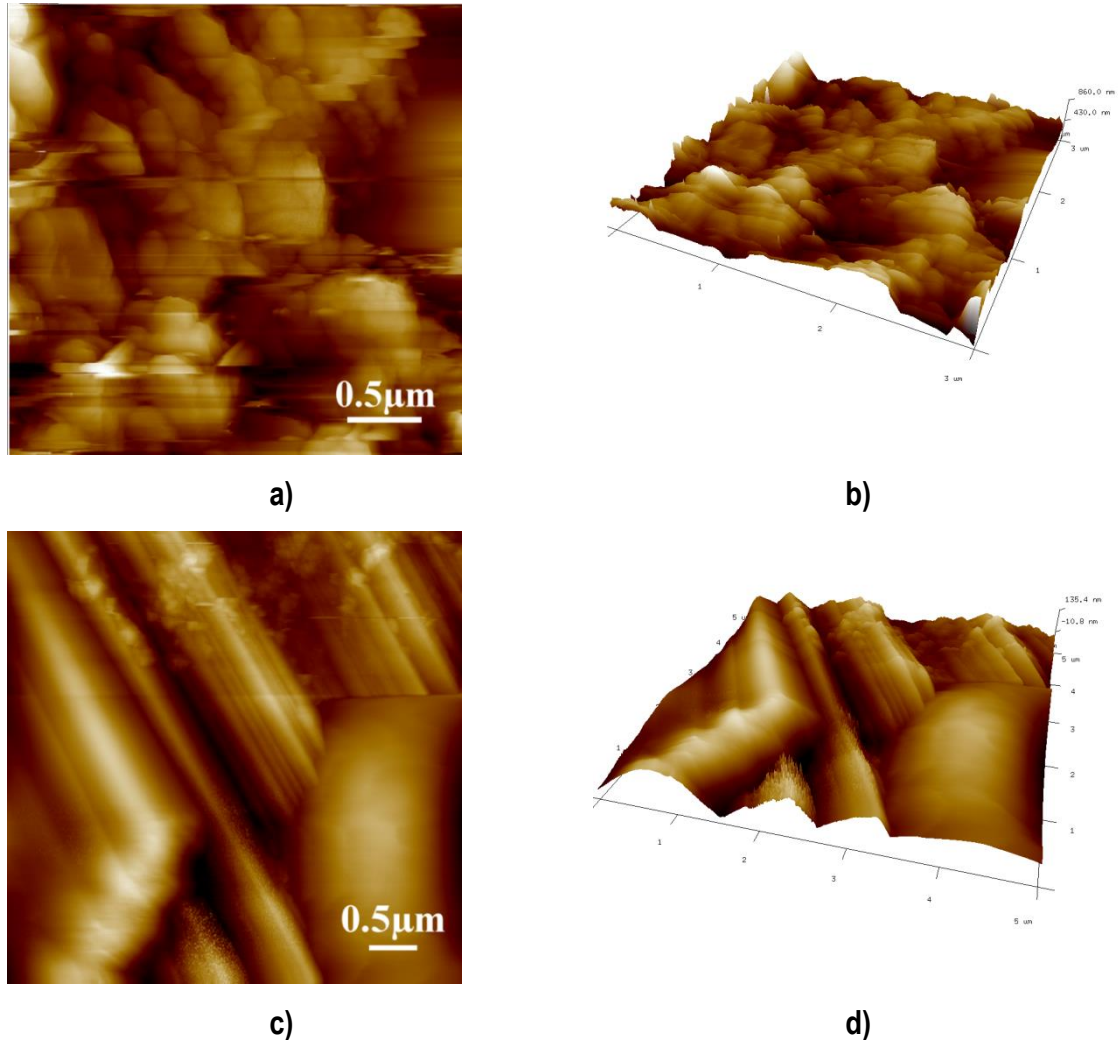


Figure 4.80. 3D waviness and roughness of a-b) sintered and c-d) agglomerate CS HA coatings and e-f) PS HA coating

Figure 4.81 shows the AFM surface nanotopography of both HA coatings. Minimal differences were observed regarding the nanoroughness. The sintered HA surface shows a

nanoroughness of  $R_a=58.2\text{nm}$  while agglomerate HA coating of  $R_a=39.1\text{nm}$ . That difference could be induced by the differences surface morphologies, in which sintered HA coating leads to a surface composed by small subgrains while agglomerate HA coating by fine agglomerates.



**Figure 4.81.** 2D and 3D AFM micrographs of the optimal a-b) sintered and c-d) agglomerate HA coatings

➤ Phase composition: X-ray diffraction analysis

**Sintered HA powder**

The XRD of the resulting CS sintered HA coating shows very broad peaks which are indicative of the reduced grain size upon particles impact (Fig. 4.82), compared to the narrow peaks in figure 4.16. In order to confirm the TEM results, a Rietveld refinement was also here performed, leading to an average of 22.6 nm of crystallite size for the HA. This confirms that TEM and XRD analysis lead to results of the same order of magnitude.

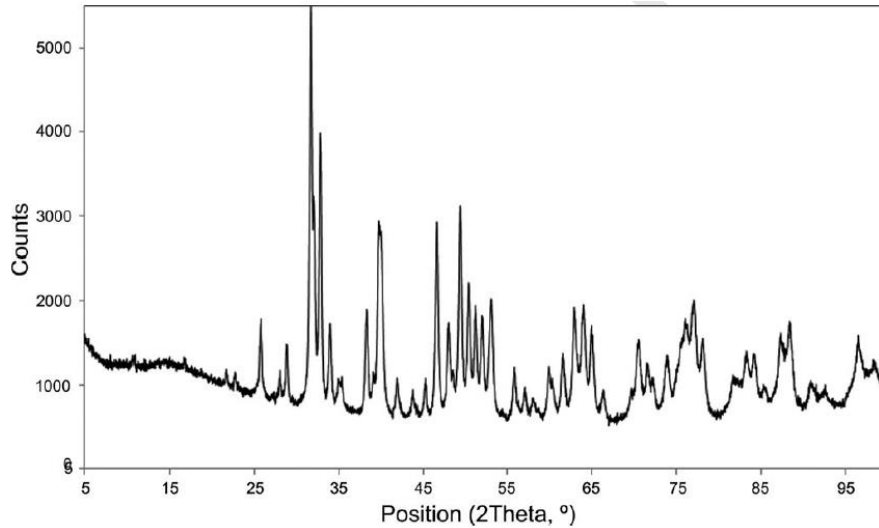


Figure 4.82. XRD of sintered HA coating

### Agglomerate HA powder

Figure 4.83a shows the XRD pattern of the agglomerate HA coating deposited by CS. Both XRD patterns maintain similar peak broadness. By using the FullProf software, the XRD pattern was refined (Fig.4.83b) and the content of the HA was found to be 86.58%, monetite phase 2.07% and amorphous phase 11.34%. It could be observed that “the heating effect” did not result in any microstructural and compositional change. Also, a final value of 11 nm was found for the HA phase. Not significant changes were perceived in comparison with feedstock powder.

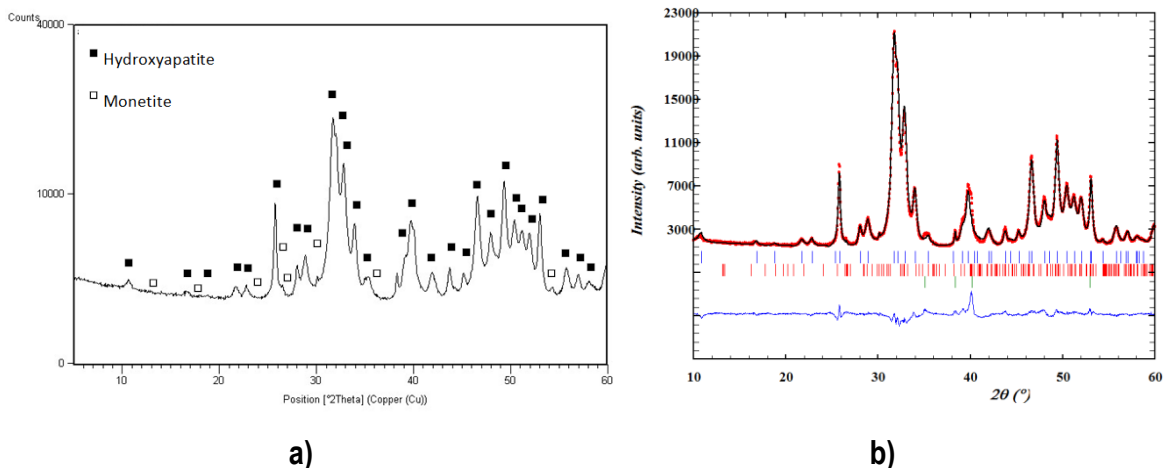
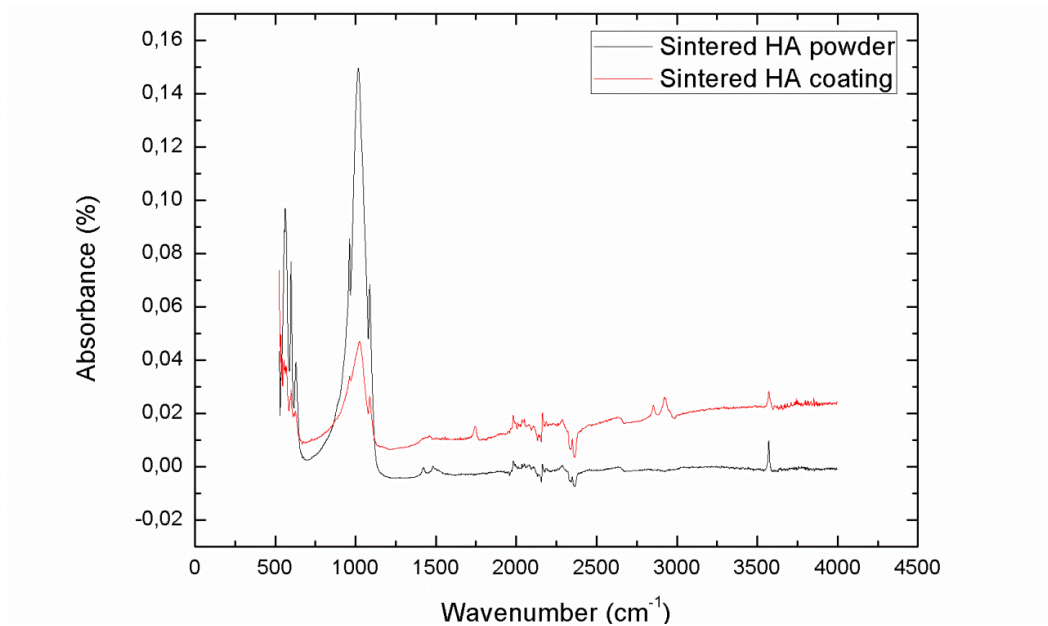


Figure 4.83. a) XRD and b) Rietveld analysis of agglomerate HA coating

➤ Phase transformation: Fourier transform infrared spectroscopy

Figures 4.84 and 4.85 show the FTIR spectra of the sintered and agglomerate HA feedstock and coatings. Both FTIRs contain the same characteristic phosphate, carbonate and hydroxyl bands as the FTIR spectrum of HA powders, which were already discussed. The unique difference between both spectra is the intensity of the peaks, which are less intense in the HA coatings because of the surface roughness. Actually, the main sampling problem in FTIR characterization of biomaterials is that nearly all solid materials are too opaque in their normal forms for direct transmission analysis in the mid-infrared region. This problem can be solved by reducing the optical density of samples to a suitable level by employing various sampling techniques but, since these procedures can alter the nature of the sample and are time consuming. For that, an attenuated total reflection diamond corrector was employed; however, it is limited in some applications due to stringent surface requirements. This confirms from the compositional point of view, that the feedstock composition is preserved after spraying.



**Figure 4.84.** FTIR spectrum of the sintered HA powder and the CS sintered HA-rough Ti coating.

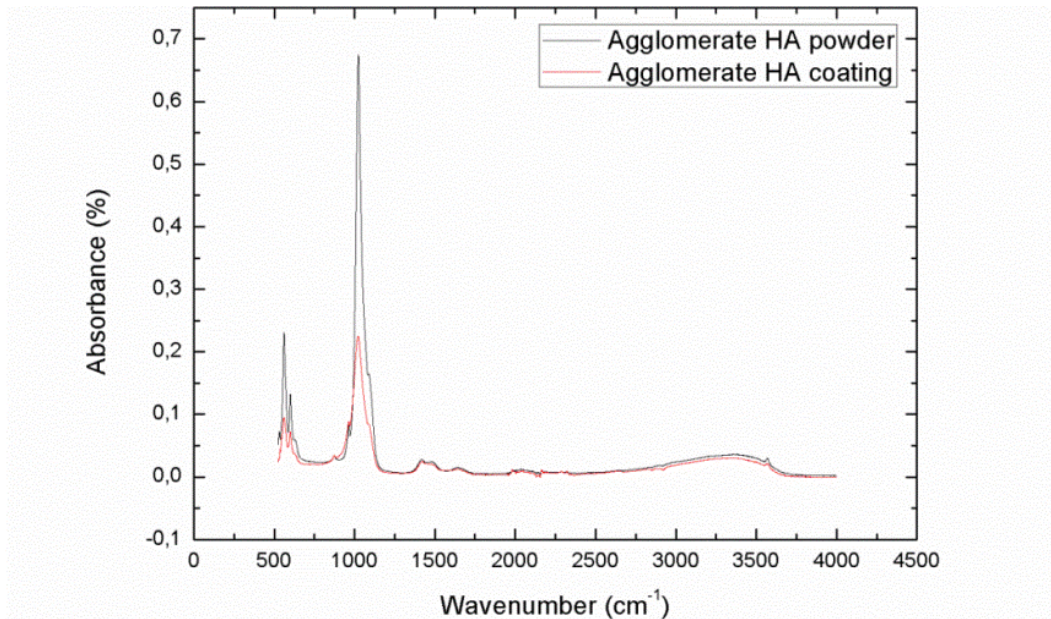
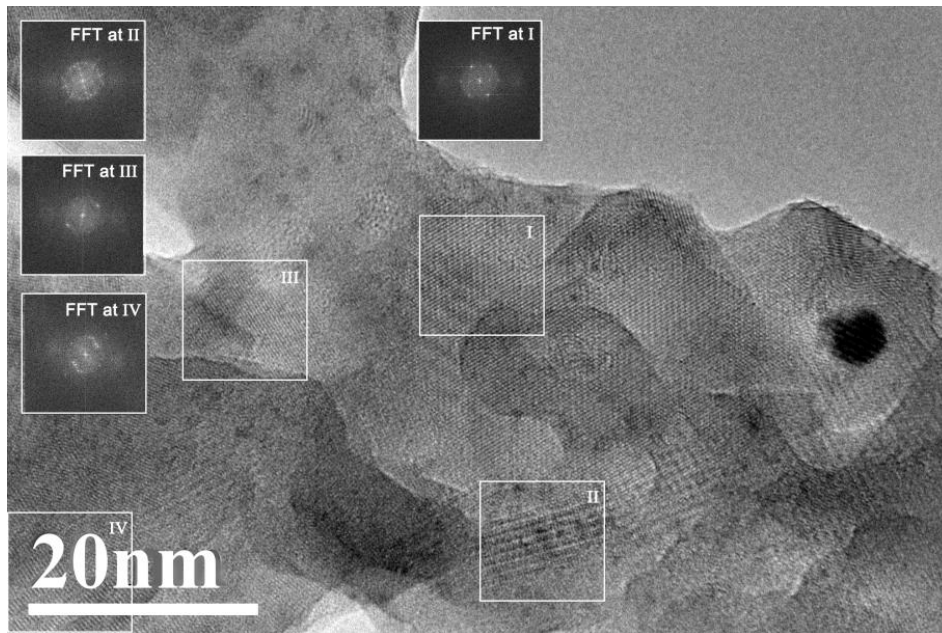


Figure 4.85. FTIR spectrum of the agglomerate HA powder and the CS agglomerate HA-rough Ti coating.

#### b) Coating microstructure

##### **Agglomerate HA powder**

The compacity of the coating and the interaction with the substrate were analyzed also by TEM. Several micrographs of different zones are shown in figures 4.86 and 4.87 showing the upper and bottom part of the section respectively. Moiré patterns were observed as in the splat but the upper side (Fig. 4.86 and 4.87) exhibiting an effective consolidation. This must be due to the tamping effect produced by continuous impact of incoming particles onto the already adhered ones. Particle-particle boundaries are difficult to be recognized as well as in figure 4.87. This might be explained by the shock compaction of nanosized particles [115]. Mamalis et al. [143] related this shock compaction to the fracture of particles, filling the interstices, cleaning the surfaces and heating of the particle surfaces which lead to either partial surface melting and welding or solid-state diffusion bonding.



**Figure 4.86.** TEM micrograph of the upper part of agglomerate HA coating

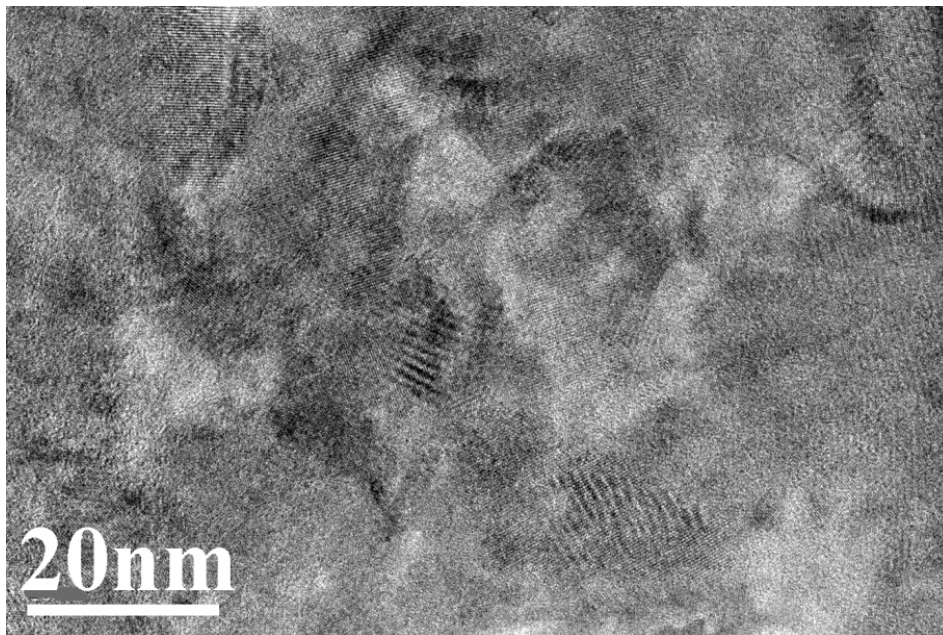


**Figure 4.87.** TEM micrograph of the bottom part of agglomerate HA coating

This thermal effect is well included in the energy balance upon particle impact. The bonding mechanisms of metal particles within a coating deposited by CS are known to be predominantly by plastic deformation at high strain rates. The heat generated upon the impact may promote dynamic recrystallization or melting in shear bands, which are occurring at the interfacial regions, i.e. particle-substrate or particle-particle interfaces. Since it has been proved that not enough heat is produced to be able to melt the impinging particle [144], the

only heat considered for energetic considerations is that of adiabatic heating, dissipated locally at the interface via plastic deformation. A proper energy balance may be then the following: (eq. 4.2)  $E_{\text{kinetic}} = E_{\text{plastic}} + E_{\text{thermal}}$ , where Dewar et al. [145], were able to calculate the particle-substrate interface temperature assuming that none of the kinetic energy that is converted to heat is lost to the environment, to the rest of the bulk splat, or to the substrate. Obviously, this is an approximation since all the physical and thermal properties of the splat are assumed to be constant.

For the impact of a ceramic particle at low-temperature deposition systems, fragmentation phenomenon has also to be included through a failure model. The Johnson-Holmquist model contains a strength model and a failure model that was used by Chun et al. [115] to simulate the impact of an alumina particle by NPDS; this model uses the normalized stress and pressure values from the strength and pressure components of the Hugoniot elastic limit ( $\sigma_{\text{HEL}}$ ,  $P_{\text{HEL}}$ ). In this case, the kinetic energy is transformed into thermal and fragmentation energies: (eq. 4.3)  $E_{\text{kinetic}} = E_{\text{fracture}} + E_{\text{thermal}} = \frac{1}{2}P(V_{00} - V_0)$ , where  $V_{00}$  and  $V_0$  are the specific volumes of the porous and solid material respectively. As already commented previously, the fracturing depends on the shock intensity and therefore to the impact conditions and, on the powder initial density.

If we consider a sintered particle, it is obvious that  $E_{\text{fracture}}$  can be significant and the gaps of the initial pores can be more or less effectively filled depending on the impact conditions; this can also result in the presence of plastic deformation mechanism. According to the simulations of Akedo et al. [117], the maximum rising impact pressure was almost the same as the experimental fracture toughness of the starting particle and enough to destroy the particle.

In the present case, however, the feedstock is not sintered and, therefore,  $E_{\text{fracture}}$  is assumed to be low and most of the kinetic energy is transformed into thermal energy. The particle density is 3,001 g/cm<sup>3</sup> for the sintered particles in [137] and, as said before, 0,55 g/cm<sup>3</sup> for the agglomerated particles of the present work; therefore, for the same particle size, the lower mass of the agglomerated particles leads to lower kinetic energy. Then, the temperature rise is obviously not high enough to produce sintering since the structure of figures 4.86 and 4.87 is far different from that of figure 4.15d but it leads to a consolidation that keeps the nanocrystallites with good cohesion.

c) Mechanical properties➤ Scratch test

Scratch testing was carried out to assess the adhesion of the CS HA layers deposited onto Ti6Al4V alloy substrates. The adherence of optimal the sintered and agglomerate HA layers were tested by scratch test. Moreover, thick agglomerate HA coating obtained by the decreasing traverse speed of the gun, was tested in order to evaluate the influence of thickness in mechanical properties. Table 4.26 shows de data of the chosen samples.

**Table 4.26.** Data of the CS HA coatings chosen for the scratch test

	Sintered HA coating	Agglomerate HA coating	Agglomerate thick HA coating
<b>Substrate</b>	Ti6Al4V alloy		
<b>Top layer</b>	Sintered/Agglomerate HA		
<b>Thickness of the top layer [<math>\mu\text{m}</math>]</b>	30	145 $\pm$ 50	362 $\pm$ 52
<b>Intermediate layer</b>	CS CP-Ti coating		
<b>Thickness intermediate layer [<math>\mu\text{m}</math>]</b>	297 $\pm$ 74		

Progressive loading tests have been performed on the samples. LC (Critical Load) is the normal load at which the first adhesion failure (first detachment of the coating) appears on the test track. Figure 4.88 illustrates the event on each sample and table 4.27 the critical load values.

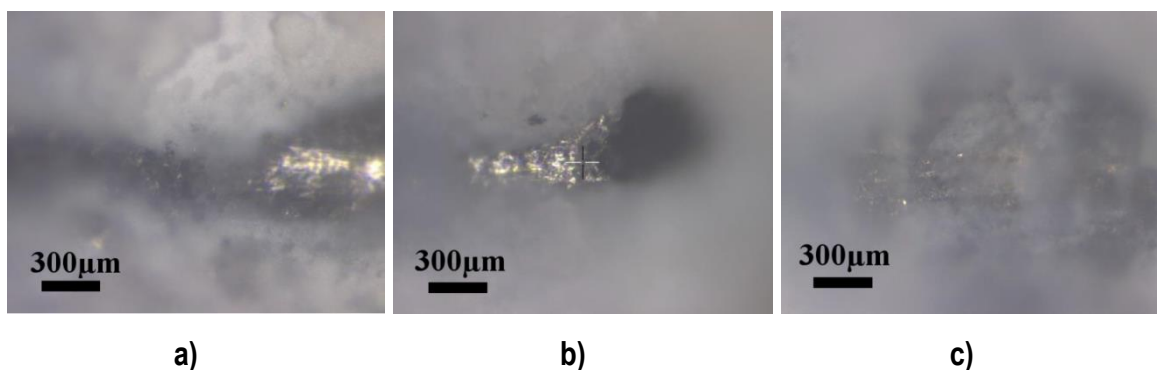


**Figure 4.88.** LC event for the a) sintered HA coating, b) agglomerate HA coating and c) thick agglomerate HA coating

Table 4.27. LC values of scratch test

	Critical Load (N)		
	Sintered	Agglomerate	Agglomerate
	HA coating	HA coating	thick HA coating
<b>Test 1</b>	1.01	1.01	55.13
<b>Test 2</b>	1.93	1.56	62.87
<b>Test 3</b>	1.01	1.01	42.54
<b>Mean±SD</b>	<b>1.3±0.5</b>	<b>1.2±0.3</b>	<b>53.5±10.3</b>

In order to better visualize the impact of low loads on the samples, some tests at 0.9N were performed on both agglomerate HA coatings (Fig. 4.89b and 4.89c). The test was not carried out on the sintered HA coating because as one can see (Fig. 4.89a), that its surface is very irregular and rough. Besides, its top layer is thinner than the other two samples, which means that we would have observed a similar effect of failure on it.

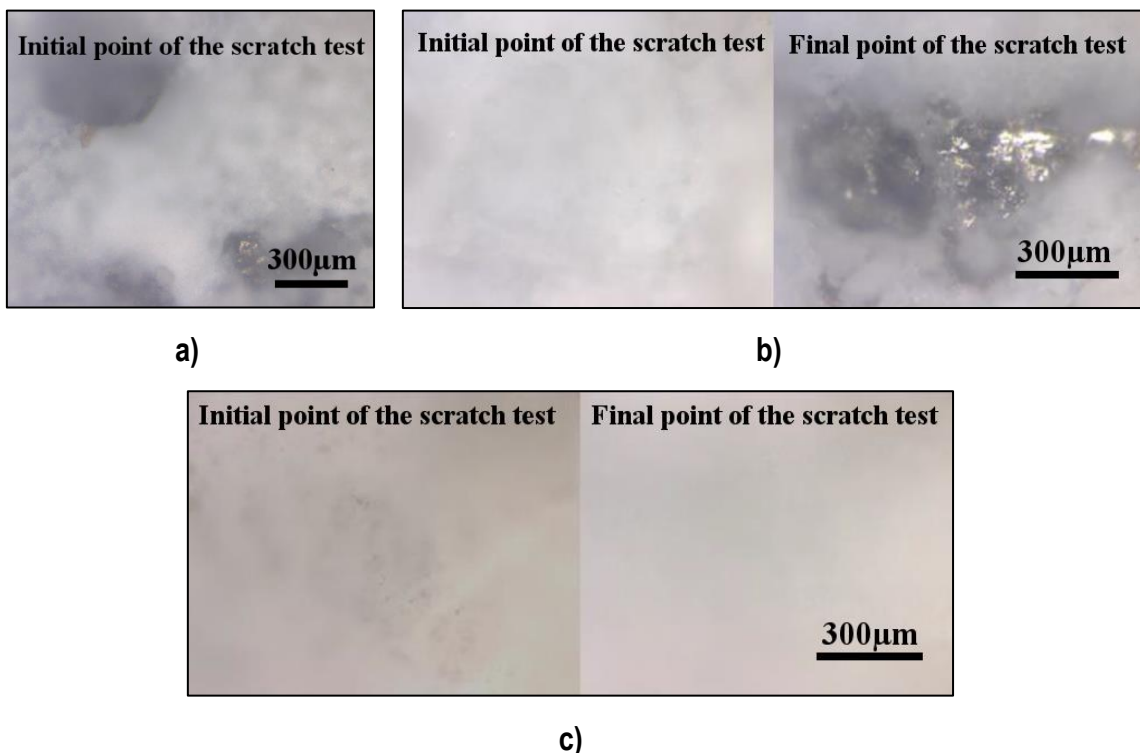


**Figure 4.89.** a) Initial top surface area of the sintered HA coating before being tested, and initial and final point of the scratch test of b) agglomerate and c) agglomerate thick HA coatings

Figure 4.90 shows an overview of the entire scratch of each sample. It is indicated with a white line the critical load.

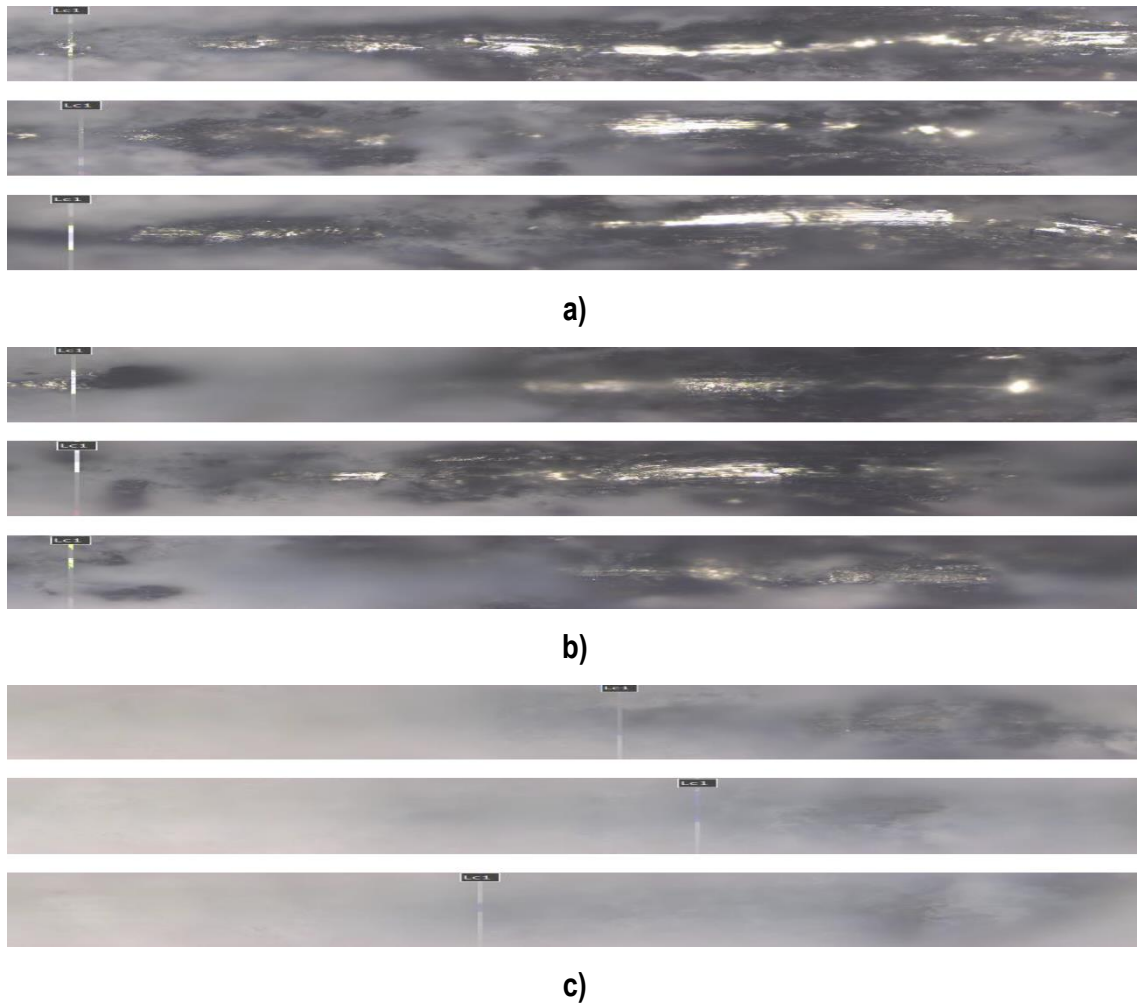


**Figure 4.90.** Scratch view of the entire load for a) sintered, b) agglomerate and c) agglomerate thick CS HA coatings

HA thin coatings removed rapidly but not HA thick coating. HA coatings produced by electrochemical deposition (ECD), for example, show at the beginning of the scratch (<2N), some detachments of the coating, whereas after exceeding a certain load (>2N), any scrap off was observed [146]. Due to the porous morphology of the HA layer prepared by ECD, the damage was reported to be mainly restrained within the coating and only in the contact area, without any delamination phenomenon. It may be qualified of a rigid-plastic behaviour as a snow-like, and the sudden decrease of the friction coefficient at about 1.1 mm of the end of the scratch was due to the flattening of the coating leading to a smooth and sliding surface as particularly shown. However, no coating thickness was provided in this research. HA coatings with thicknesses in the range of 50 to 100  $\mu\text{m}$ , were also produced by suspension plasma spraying. The adhesion of the soaked coatings to the substrate was characterized by the critical load in the scratch test and was about 10 to 12 N [147]. HA coatings obtained by ion

beam assisted deposition (IBAD) and a following post-treatment (first annealed at 500 °C for 2 h and then immersed in deionised water for 72 h at room temperature) showed that the adhesive strength of IBAD coatings is nearly twice that of ion beam sputtered coatings (IBSD). Critical loads for the coatings prepared by IBSD and IBAD at a load speed of 2000 gf/min were determined to be 6.5N and 10.3N, respectively [148].

All methods for depositing HA have shown low critical loads by scratch test. It should be pointed that in the present research, the critical load increased by the increase of thickness, probably because of the tamping effect and the compaction of HA particles during the spraying. However, other research show contrary results; Fernandez-Pradas et al. [149] obtained HA coatings (from 170 nm up to 1.5 µm) by KrF laser ablation and it was observed that coatings failed under the scratch test by spallating laterally from the diamond tip and the failure load increased as thickness decreased, until only plastic deformation and cohesive failure for the thinnest coating is observed. The highest critical load (5.7N) was obtained on a thickness of 0.17µm.

#### **4.2.3.4. Build-up of agglomerate hydroxyapatite coating**

As mentioned in *b) Hydroxyapatite coatings*, direct deposition of HA onto Ti6Al4V alloy substrate did not provide suitable deposition and coating build up; however, through the deposition of a CS CP-Ti rough bond coat, the surface was activated enough to promote the building up of agglomerate HA coating. Initial attempts on using HPSCS were not successful at all, showing inhomogeneous agglomerate HA coatings, due to the punctual-rotator feeding system. Therefore, due to the characteristics of the agglomerate HA powder, the constant feeding system and the assumption that not much large shock pressures would be suitable for this particular structure of the feedstock, LPCS was attempted. The results obtained were incredibly successful.

According to the optimal spraying conditions used for the agglomerate HA powder by LPCS, the traverse speed was decreased and the number of layers increased to build up thick HA coating.

Figure 4.91a shows agglomerate HA coatings from 1 to 4 layers. It was observed an evolution of the progressive builds up of the coating with thickness values of 1.2, 0.7, 0.3 and 0.25 mm respectively. In addition, the production of such thick coatings, they can be detached and be used as bulk materials. The first spraying layers contribute more than the following ones as

they fill the roughness valleys of CS CP-Ti coating. Even so, once the roughness valleys are filled, the coating still build up with the same thickness  $\sim 0.25\text{mm}$  as the surface roughness is decreased. Figure 4.91b shows agglomerate HA coatings up to 9 layers with a thickness of  $\sim 5\text{mm}$ .

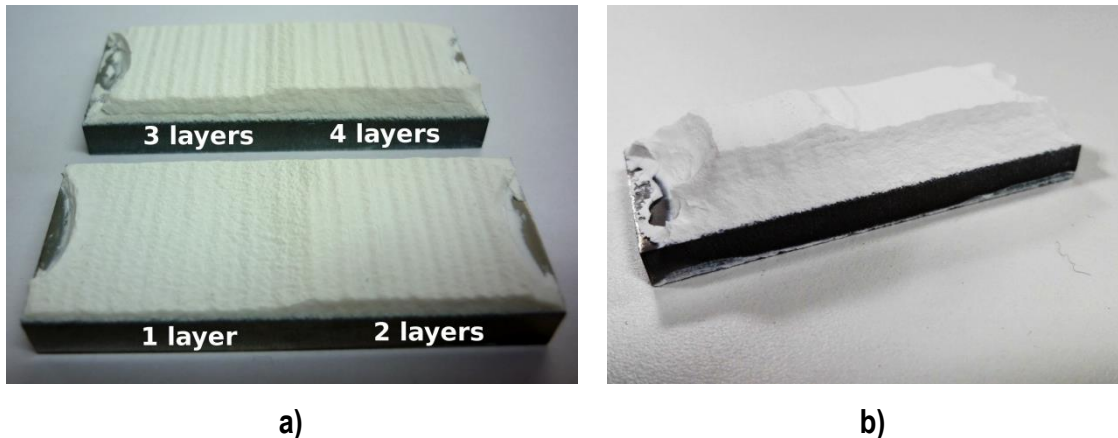


**Figure 4.91.** a) Macrograph of LPCS HA coatings from 1-4 layers up to b) 9 layers

The use of a nanoagglomerate feedstock has overcome such handicap but another key point has been proved to be necessary to build up a coating with noticeable thickness, this is the surface activation by considerable roughening achieved by the presence of the titanium rough coating. The valleys on the surface could thus be filled and serve as further contact points for proper build up.

Mainly due to feeding problems, the low pressure system was observed to be more suitable than the high pressure. The LPCS was originally created as a portable system for industrial environment. Two fundamental aspects that distinguish LPCS from HPCS are: (i) The use of low pressure gas (0.5-1 MPa instead of 2.5-3 MPa) and (ii) radial injection of the powder instead of axial injection (in most cases) [150].

The build up process appears to be a result of a compaction mechanism of the deposited ceramic particles, as also presented previously for the VCS [151], AD [117] or NPDS [152] techniques, but they mainly use sub-micron sized particles and the spraying system is slightly different. The use of micron sized ceramic particles but with nanoagglomerate structure is highly advantageous in CS compared to others such as sintered powders. For porous-sintered particles, the deposition mechanism has been mainly explained by the collapse of the porous structure and the reduction of crystallite size by fracture or plastic deformation

[137]. Dense ceramic layers of  $\alpha$ - $\text{Al}_2\text{O}_3$  and PZT with thickness of 1–100  $\mu\text{m}$  were successfully formed on glass, plastic, and metal substrates with agglomerate and submicronic feedstock powder [117].  $\text{TiO}_2$  particles of a size of 25nm and 200nm were successfully deposited by VCS. Apparently dense coatings consist of particles stacked as agglomerates that build up together with the number of spray passes. In comparison with CS, the specimen in VCS is placed in a vacuum tank coupled to a vacuum pump with a pressure that is substantially less than the atmospheric pressure. The vacuum tank allows for gas recovery and for powder overspray collection. These authors achieved a coating thickness of  $\sim 40\mu\text{m}$  with 12 layers with a 25nm particle size [151]. However some attempts are being performed with HA coatings by CS obtaining thickness values up to  $60\pm 10\mu\text{m}$  [153]. Therefore other CS attempts were performed using  $\text{TiO}_2$  agglomerate, achieving 100  $\mu\text{m}$  coating thickness. Contrary, the suggested main factor of the particle adhesion is a chemical bonding and not a mechanical bonding [154]. In the present study, HA powder is being able to reach  $\sim 5$  mm after 9 layers without delamination.

The production of build-up coatings was surprising but further thermal treatments should be performed with the aim to increase their structural strength in case that it may be used for bone graft.

Figure 4.92a shows a dilatometry of the agglomerate HA powder, which was performed with the aim to know the most suitable temperature to produce a thermal treatment. Pure crystalline HA powders, such as sintered HA powder (Fig. 4.92b), used to have one peak between the range of 1000°C and 1200°C, in which this temperature is associated to the sinterization temperature and phase transformations take place [155]. The presence of a second peak, as the case of agglomerate HA powder, could appear as the presence of other elements [156] or amorphous phase [157]. As mentioned previously, HA coating has a content of 86.58% HA, 2.07% of monetite phase and 11.34% of amorphous phase, which mostly consists of a dehydroxylated calcium phosphate. When heated, the crystallization of hydroxyl-rich areas produces HA, followed by diffusion of hydroxyl ions, thus increasing the amount of crystalline phase. Hydroxyl-deficient amorphous areas crystallize to oxyapatite at 700°C [157].

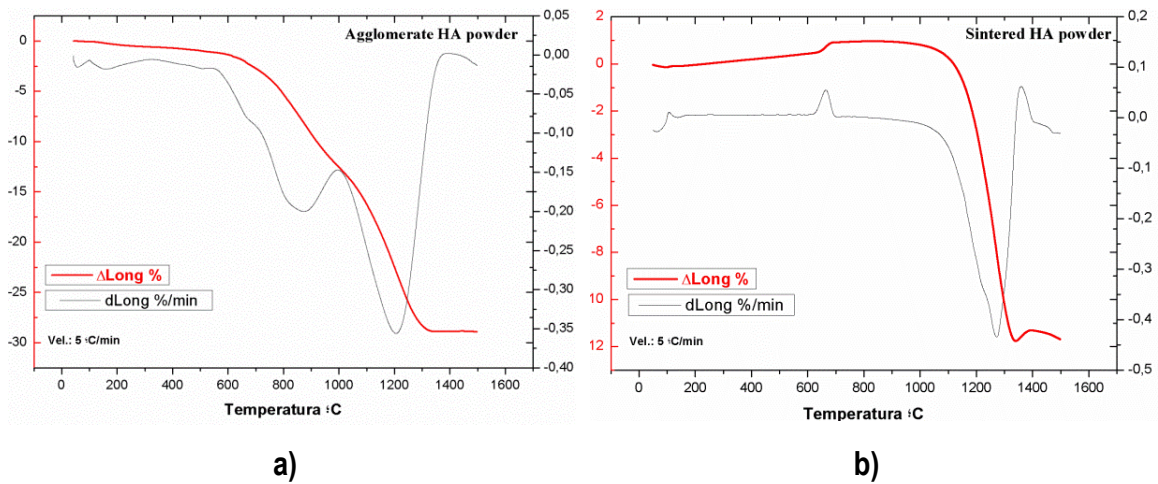
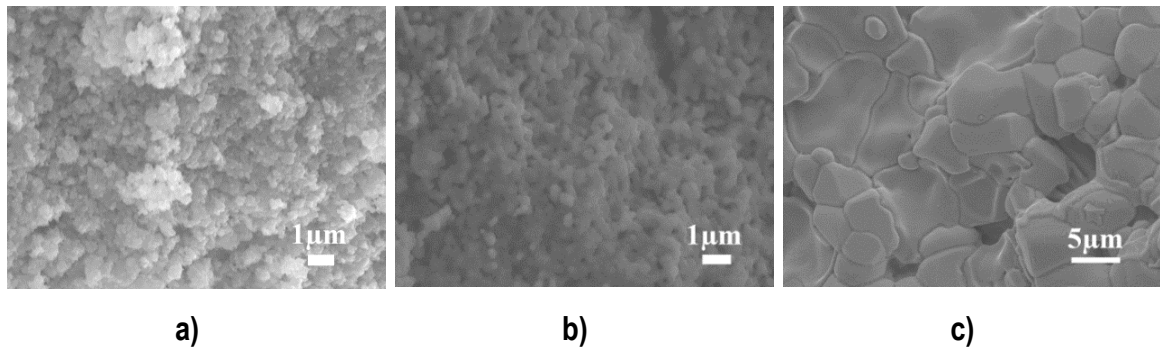


Figure 4.92. Dilatometry of a) agglomerate and b) sintered HA powders

Two different thermal treatments were performed in order to analyze their microstructure. The first thermal treatment consists in increase the temperature up to 1000°C at 5°C/min, while the second thermal treatment up to 1400°C.

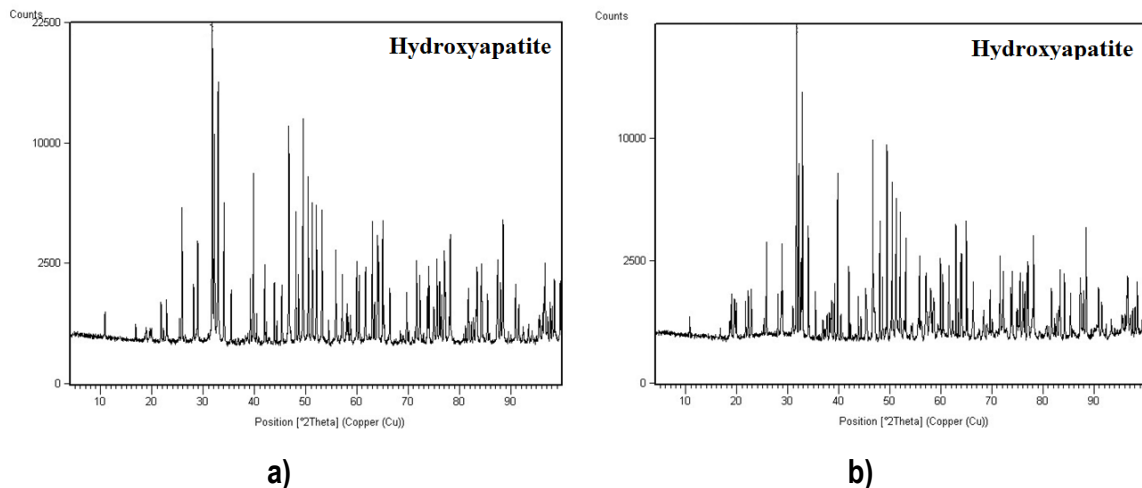
Grain boundary diffusion and lattice diffusion from the grain boundary to the neck are the most important densifying mechanism in polycrystalline ceramics. Diffusion from the grain boundaries to the pores permits neck growth as well as shrinkage (densification) [158]. The surface treatments were performed by increasing the temperature up to 1000°C (1<sup>st</sup> thermal treatment) and 1400°C (2<sup>nd</sup> thermal treatment) at 5°C/min (temperatures after the two peaks plotted in the dilatometry fig. 4.92a), which is the heat rate that were performed the dilatometries.

Figure 4.93 shows the top surface of HA bulk after both thermal treatments at 1000°C (Fig. 4.93b) and at 1400°C (Fig. 4.93b). In comparison with the as-sprayed agglomerated HA surface (Fig 4.93a), ffter the thermal treatment at 1000°C, submicron grains start coalesce and reduce pore size. At 1400°C sinterization occurs and it is observed a dense structure with big grains between 5-10  $\mu\text{m}$ .



**Figure 4.93.** FESEM micrographs of the top surface agglomerate HA bulks a) as-received and after a thermal treatment at b) 1000°C and c) 1400°C

The XRDs from HA bulks after a thermal treatment at 1000°C (Fig. 4.94a) and 1400°C (Fig. 4.94b) show narrower peaks than XRD from the as-sprayed HA bulk, indicating the growth of crystal size from a nanocrystalline to crystalline within the HA bulk.



**Figure 4.94.** XRD from the agglomerate HA bulks after a thermal treatment at a) 1000°C and b) 1400°C

Bone grafts proved to be successful in humans and animals, especially orthopaedic cases like intrabony defect repairs, maxillofacial surgery, jaw bone restoration and augmenting mandibular ridge. It eliminates the need for patients to undergo painful autograft bone grafting procedures [159]. B-OstIN is made by wet chemical methods and thereafter converted into porous mass (60-70% porosity with pores size between 100-300  $\mu\text{m}$ ) through ceramic processing routes. B-OstIN is most osteoconductive material which helps in bone bonding within 3 months [160]. Some bone grafts used to be composed by mineral-collagen composite matrix in order to enhance biological response. Ossigen® has the mineral particles are dispersed within collagen fibers forming a three-dimensional porous matrix consist of 80%

bone mineral and 20% collagen by dry weight with a 100-400  $\mu\text{m}$  optimal pore size for tissue regeneration [161]. Those commercial grafts are commercialized by blocks.

HA bulks by CS could be a good and economic process to build up customized grafts with the desired composition, shape and microstructure. However, more studies should be performed for future perspectives.

#### **4.2.4. BIOLOGICAL PROPERTIES OF THE COATING**

This fourth part is destined to the biological characterization of the coatings already obtained. In vitro tests were analyzed in terms of comparative results among the different coatings. This part is divided in the following comparisons:

All parts include an introduction explaining the novelty of each part.

- In vitro comparison between low roughness sand blasted surface and highly rough commercial pure titanium coating by cold spray
- In vitro comparison of different nanotextured treatments onto highly rough commercial pure titanium coating by cold spray
- In vitro comparison between highly rough commercial pure titanium coating and hydroxiapatite coatings by cold spray.
- In vitro comparison of hydroxyapatite coatings obtained by plasma spray and cold spray.
- In vitro dynamic testing of cell attachment onto hydroxyapatite surface

##### **4.2.4.1. In vitro comparison between low roughness sand blasted and highly rough commercial pure titanium coating by cold spray**

###### **a) Introduction**

Titanium and titanium alloys require a surface treatment in order to become bioactive and thus, being osteoproduktive materials [162]. In this way, the formation of a fibrous soft tissue capsule can be avoided, enabling better biomechanical fixation [163]. Therefore, the implant surface is a key parameter which has been addressed by many authors and still attracts the interest day by day with the aim to enhance osseointegration and promote faster fixation [164,165].

As commented in previous sections, the titanium surface modification can involve topography as well as compositional changes, thus modifying the wettability performance and the final biological properties [54,166,167]. Mekayarajjanonh et al. [168] actually reported a number of studies supporting the relationship among surface factors, including surface preparation, roughness, surface energy, wettability, and cell adhesion to biomaterial surfaces (Fig. 4.95) .

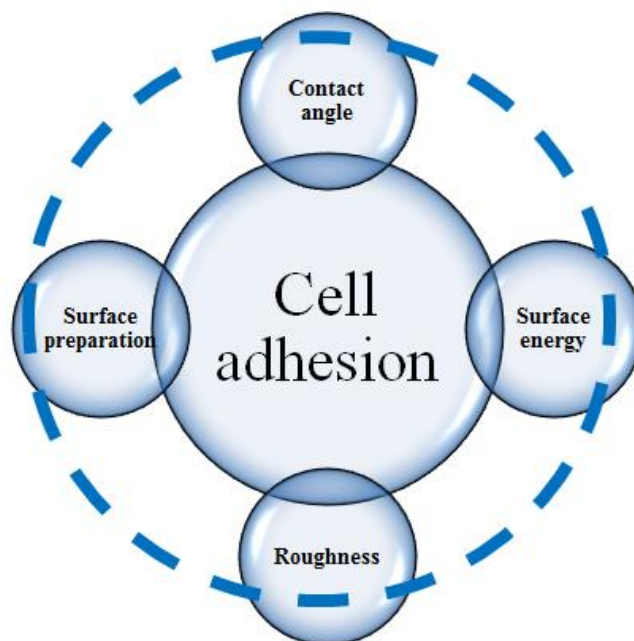


**Figure 4.95.** Relationship among surface properties with cell adhesion

Previous studies have described the increasing of surface roughness of a metallic orthopaedic implant as an improvement in bone formation around it [169]. Surface roughness seems to have a direct effect on human osteoblast (HOB) attachment and subsequent cell proliferation and differentiation. Osteoblast-like cells adhere more readily and appear more differentiated on rougher surfaces, with regards to morphology, extracellular matrix production and alkaline phosphatase (ALP) activity [169]. However, other studies support findings that when the roughness level is greater than the cell dimensions it does not enhance cell response [170]. Figure 4.96 shows how surface topography modulates osteoblast cell morphology. When osteoblast are cultured on smooth surface ( $R_a < 2 \mu\text{m}$ ), those assume a flat morphology. If they are cultured on surface with  $R_a > 2 \mu\text{m}$ , but with distances between peaks longer than the length of the cells, the surface is also perceived as smooth. On the other hand, if  $R_a > 2 \mu\text{m}$  and the peaks density is high, cells are unable expand and achieve flat morphology. Cells anchor on the surface with their extensions and the multiple surface peaks, and are forced to assume a more osteoblastic morphology. However, the ideal

topography is the one that shares both, the micro- and nano-topography. It is reported that microstructured substrates can affect cell morphology and cytoskeletal structure, while nanostructured surfaces can influence cell functions, including proliferation, differentiation and alignment [171].

### The surface topography modulates the morphology of osteoblast cells

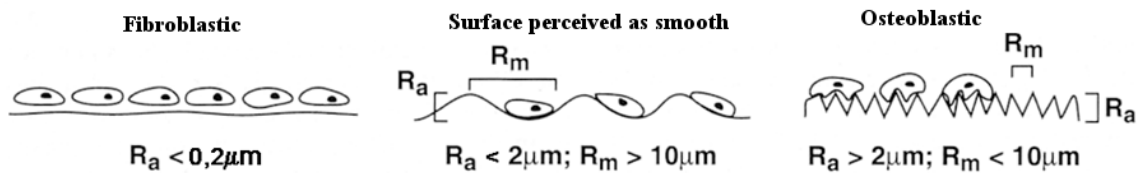


Figure 4.96. The effect of roughness on osteoblast morphology

The stability of the integrated implants can be achieved by direct bonding of the tissue to the surface (ongrowth), which has successfully been achieved using micro-rough surfaces such as SB and etched, as well as PS Ti coatings [48] or VPS [48,172]. The problem is that the roughness is highly related to the implant application, where the criteria is not the same, for example, whenever a titanium surface treatment for a dental implant or for a joint prosthesis is concerned; even dealing with the same application, the range of what is considered rough and smooth is not very clear, it still some concern and controversy regarding surface roughness [173]. It is not well defined/established a lower and a higher roughness regarding a specific application. Even so, in dental implants it is consider macro-topographic profile when the roughness is  $>10\mu\text{m}$  and a microtopographic profile between 1-10  $\mu\text{m}$  [174]. On the other hand, joint prostheses have not a defined value; it has been observed that companies specification/requirements have roughness ( $R_a$ ) values  $>15\mu\text{m}$  (e.g VPS Ti roughness  $R_t$  values  $> 100 \mu\text{m}$ ) [37,60].

Concerning the use of titanium surface treatments for joint prosthesis, a lot of studies are focused on the biological properties induced by micro- and nano- rough surfaces. Actually, given the specific requirements for the different titanium surface implants, from now on, the cited reports just concern joint prosthesis, in order to avoid much of the works regarding titanium which focus on dental implants. Wu et al. [175] found that osteoblast responded most favourably to surface that are smooth at microscopic length scales and rough at macroscopic length scales, whereas bacteria were more effective on surface that contain roughness at microscopic length scales. In that case [175], 4 different titanium surface treatments were

evaluated, in which PS surface ( $R_a = 33 \mu\text{m}$ ) ended with better results summarized in a higher osteoblast viability and proliferation and less area fraction with bacteria in comparison with polished, satin and SB surface ( $R_a = 0.006 \mu\text{m}$ ,  $0.830 \mu\text{m}$ ,  $11 \mu\text{m}$  respectively).

Actually, highly rough CP-Ti coatings are produced by VPS and are already used in orthopaedics with good results [37,60]. New ultra-highly roughness and dense VPS titanium coatings provided good biological in vitro response and it behaved similarly to the coatings used in orthopaedic practice ( $R_a = 74 \mu\text{m}$ ) [170]. On the other hand, the stability of the integrated implants can be also achieved by mechanical interlocking using porous coatings which offer pore sizes bigger than  $100 \mu\text{m}$  and porosities of 30 to 40%. In vivo investigations showed that after 8 weeks implantation period, the bone tissue is in direct contact. Moreover, bone tissue grows into open pores of the VPS coating [60,176]. Although nano-scale seems to have more direct effects, global and micro roughness have an indirect influence on cellular activity, so the ideal roughness would be the one that combines all of them, micro- and nano-scale [177].

As an alternative of VPS, it is already demonstrated the feasibility of the production of highly rough CP-Ti coatings by CS with higher rough surfaces and overcoming with ASTM standards for hip, knee and shoulder joint prosthesis applications. In addition, the use of CS does not only provide a high roughness but also a micro- nano-roughness coming from morphological features of the feedstock powder and certain internal porosity that is formed by spraying coarse titanium particles showing little deformation upon impact. Actually, such texturization rather than macro roughness can be determining on cell adhesion and proliferation [178]. Therefore, the obtaining of CS CP-Ti coatings is produced in a friendly environment process and the low-cost coating production.

#### b) Cell viability and proliferation

HOB viability and proliferation were qualitatively analyzed by Live/Dead (Fig. 4.97) and measured quantitatively by MTS assays (Fig. 4.98) after 1, 7 and 14 days of cell culture on SB titanium surface and the optimal CS CP-Ti coating (IEc-sample 7), in order to observed the influence of roughness on cell response. It was observed that for both surfaces, most cells were alive after 14 days of culture. No significant number of dead cells was found in both samples tested.

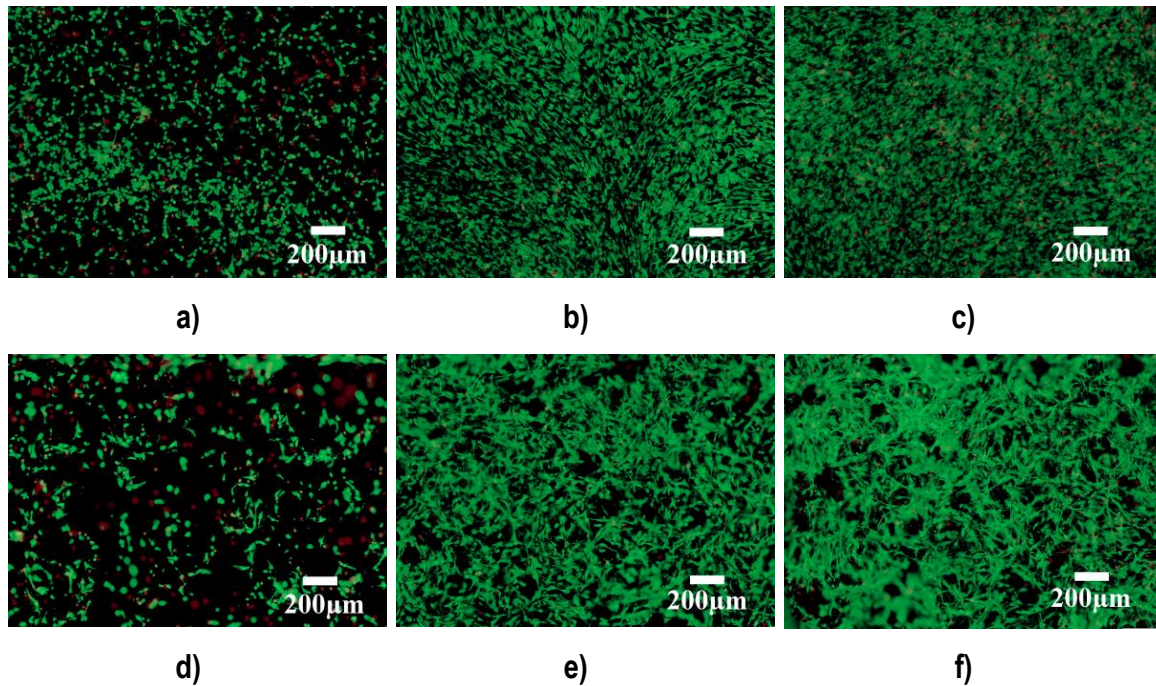


**Figure 4.97.** Live/Dead assay for a-b-c) SB surface and d-e-f) CS CP-Ti coating at 1, 7 and 14 days of cell culture (from left to right) (n=3)

A sign of successful implant material response in a first stage is a proper biomolecule in vivo adsorption, which is influenced by the physico-chemical interactions between adsorbent surface and macromolecule. Surface energy, which is intimately related to wettability [179], is a useful quantity that has often correlated strongly with biological interaction. Hence, implant wettability can become determining for the protein adsorption and consequently, for the cell adhesion. It is usually reported that biomaterial surfaces with moderate hydrophilicity, provide better cell growth and higher biocompatibility [180]. Surface wettability is considered to increase production of osteoblastic factors and bone formation as well as roughness [169]. Figure 4.98 shows MTS activity of SB surface and CS CP-Ti coating. MTS activity increased with the cell culture time indicating that cells are proliferating on the different specimens. Low differences between SB surface and CS CP-Ti coating were detected after 1 day of cell culture, but after 7 days, the HOB cell number increased for CS CP-Ti surfaces. This low difference at 1 day of culture may come from the superhydrophilicity of CS CP-Ti coating. At 14 days, the difference of the amount of cells decrease because CS CP-Ti coating enter in confluence and cell proliferation stopped.

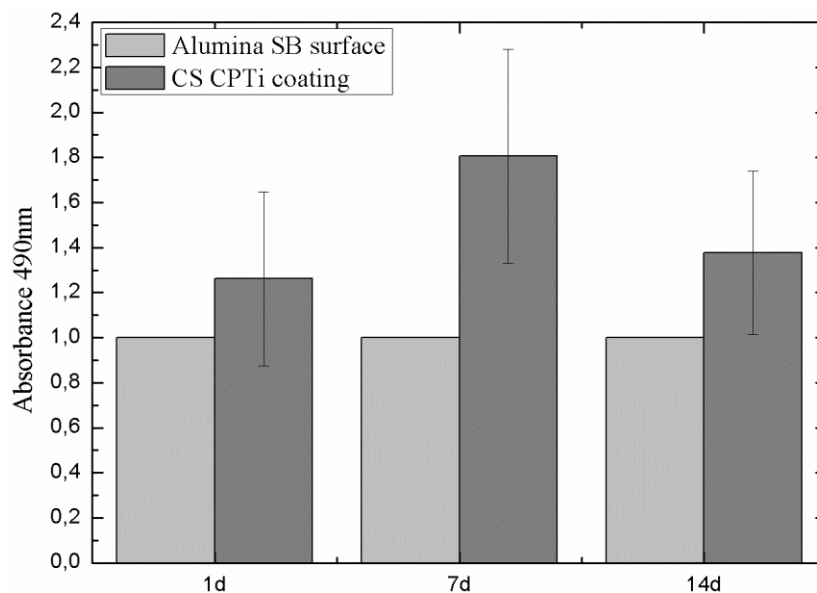


**Figure 4.98.** Cell viability measured by MTS assay after culturing for 1, 7 and 14 days of cell culture on SB surface and CS CP-Ti coating (n=3)

The high free surface area and the high wettability may contribute in obtaining higher values for CS CP-Ti coatings than SB surface. Therefore, both parameters are related with surface energy, which also contributes in cell response. Feng et al. [181] report that surface energy increased with the increase of surface roughness. Generally, greater surface roughness leads to greater specific area and higher surface energy. This would produce more surface active sites on titanium and higher reaction potential in thermodynamics, and then would be more favorable for cell attachment and proliferation.

Rough VPS Ti coatings have shown to be hydrophilic too [182]. A comparison study between rough VPS titanium coatings and different titanium surfaces were studied according to their roughness and wettability [182]. It was observed that the highest surface roughness ( $S_a = 27.8\mu\text{m}$ ) and hydrophilicity ( $37^\circ$ ) was obtained by rough VPS Ti coating, thus making it a possible candidate as a bone implant surface.

The present results show a good cell viability and cell proliferation in both surfaces along 14 days of culture. Therefore, the CS CP-Ti rough surface shows from 1 day of cell culture more cell proliferation that increases more rapidly up to 7 days of culture in comparison with SB surface. If CS CP-Ti coating would not have been in confluence, probably would increase fast, leading to a higher difference with the obtained SB surface values. Boyan et al. [171] observed that cell proliferation increased with the increase of surface topography too.

### c) Cell differentiation

The ALP is an early marker of cell differentiation that allows us to monitor the cell status. The ALP activity of CS CP-Ti coating is maintained at twice higher value than SB surface at 1 and 7 days of culture (Fig. 4.99). At 14 days of culture, a light decrease of ALP activity was found for CS CP-Ti coating compared to SB surface due to samples achieve cell confluence. It can be observed that at 1 day of culture the proliferation of CS CP-Ti coating was not double the proliferation of SB surface, but yes ALP activity, indicating that the increase of roughness leads to an increase of cell differentiation in comparison with low roughness surface.

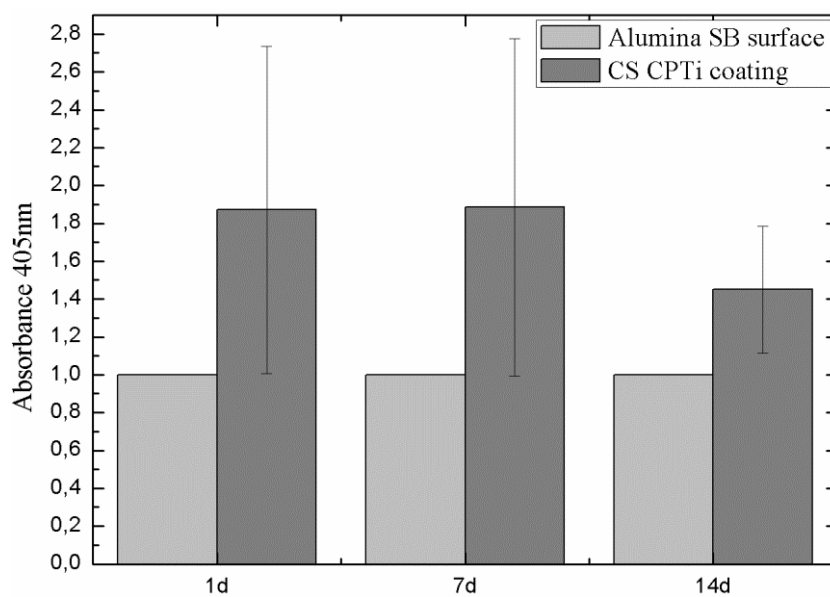


**Figure 4.99.** Cell differentiation measured by ALP activity at 1, 7 and 14 days of cell culture on SB surface and CS CP-Ti coating coating (n=3)

Therefore, it was detected a high cell mineralization on rough CS CP-Ti coating (Fig. 4.100), in which was observed a high amount of calcium phosphate deposits along the surface. Quantitatively, at 28 days of cell culture, CS CP-Ti coating doubles the amount of cell mineralization of SB surface. Mariscal-Muñoz et al [183] compared two different titanium grade 4 surfaces, one polished with a  $R_a=0.3\mu\text{m}$ , and a second one roughened by laser irradiation with and  $R_a=10.6\mu\text{m}$ . It was observed an increase of cell differentiation as well of cell mineralization with the increase of surface roughness; the mixed roughness features of highly rough CS CP-Ti coating leads to an increase of cell proliferation as well as cell differentiation. Mendonça et al. [184] reported an increase of mineralization with an increase of surface roughness on titanium surfaces. Moreover, a rough surface topography positively

modulates expression of genes related to collagen biosynthesis and cross-linking in adherent cells associated with an increased deposition of collagen-rich matrix [106].

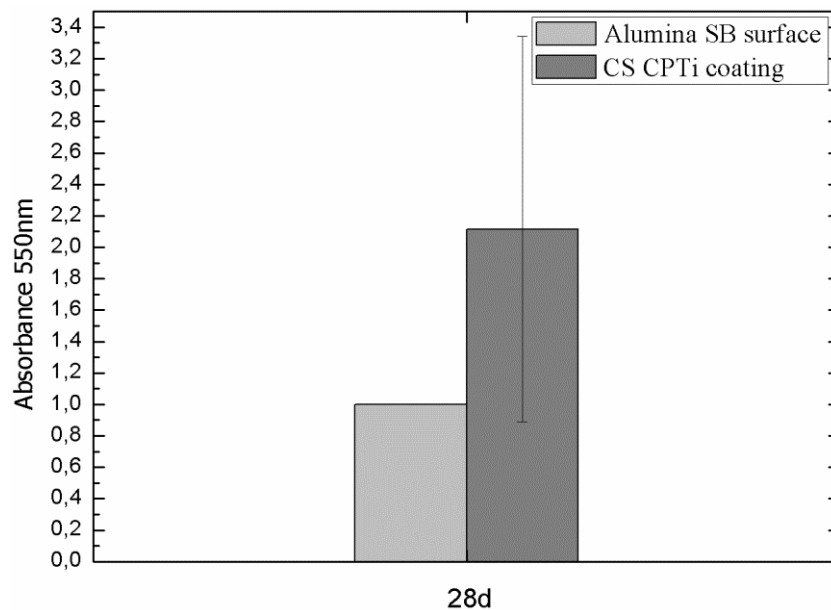


**Figure 4.100.** Alizerine red assay at 28 days of cell culture on SB surface and CS CP-Ti coating

#### d) Cell morphological aspects

Fluorescence micrographs provided information concerning the actin cytoskeleton (red colour) and the nucleus (blue colour) of the HOB. These images were taken after 1, 7 and 14 days of cell culture (Fig. 4.101). HOB were flattened and spread on rough surfaces after 1 day of culture and increase cytoplasmatic extensions during the days of culture. The osteoblast cells connected to each other after 1 day of culture. No significant morphological differences were observed between SB surface and CS CP-Ti coating.

In terms of cell morphology, in our study, osteoblasts were flattened, displaying a large and thin cytoplasmatic layer and numerous extended filopodia onto the Ti surfaces.

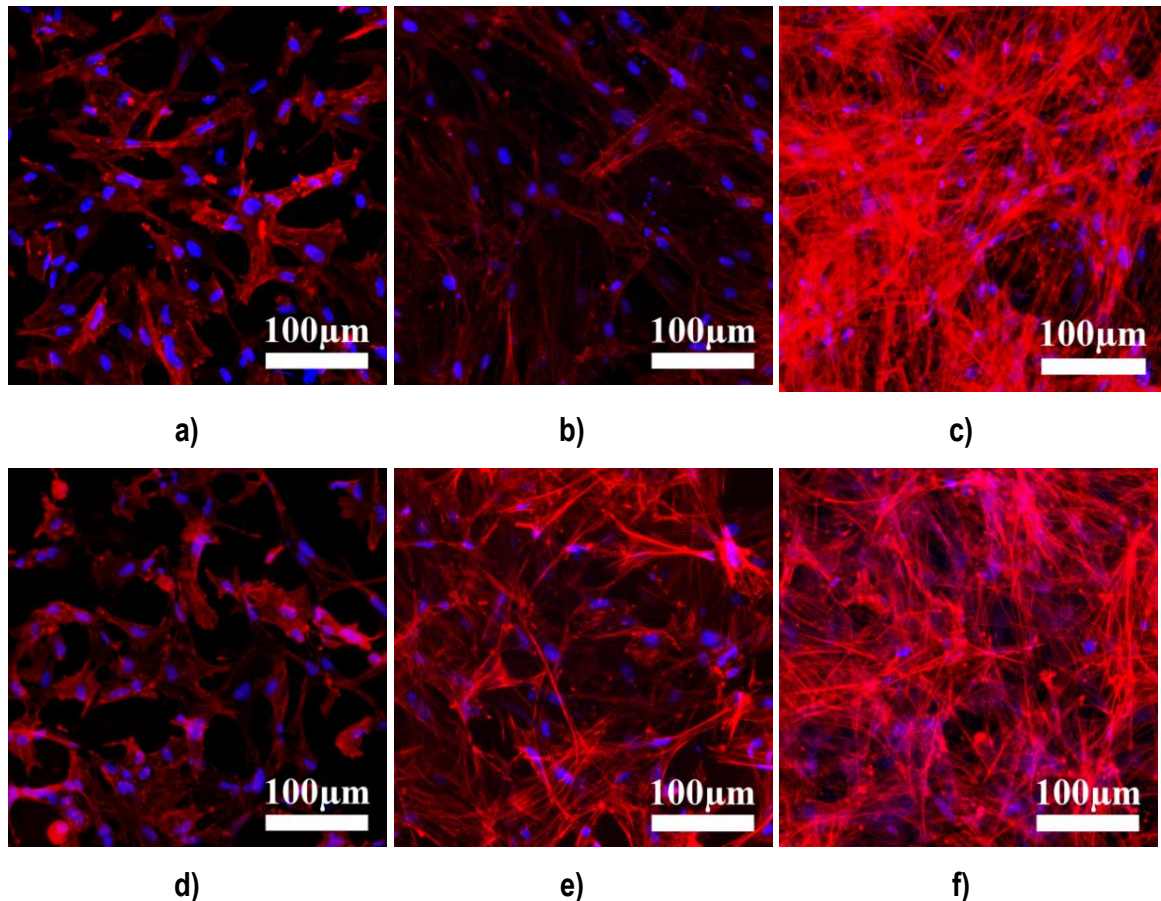


**Figure 4.101.** Phalloidin staining for a-b-c) SB surface and d-e-f) CS CP-Ti coating at 1, 7 and 14 days of cell culture (from left to right) (n=3)

#### 4.2.4.2. In vitro comparison of different nanotextured treatments onto highly rough commercial pure titanium coating by cold spray

##### a) Introduction

It is already reported that the combination of different topographies (micro- and nano-) significantly promote initial cell adhesion, proliferation and differentiation [185]. An important aspect of this phenomenon with nanosurfaces is their enhanced surface area and its roughness with nanometer dimensions [186]. Another factor is their high number of atoms at the surface, increased surface defect density and larger proportions of surface electron delocalization [187,188]. This enhanced surface energy, hence enhanced hydrophilicity, has been associated with increased protein adsorption and, consequently, osteoblast adhesion [189], which is a necessary prerequisite for subsequent functions, such as deposition of calcium-containing mineral. Daugaard et al. [190] used dual acid-etched Ti surfaces in a canine study and also found better osseointegration of the nanostructured surface in

comparison to conventional microtextured surfaces; the nanotextured surfaces show good cell response in comparison with smooth surfaces. Well-developed cell filopodia directly entered nanometer-sized pores for the initial attachment of the osteoblastic cells. These nanometer structures may also give the cells positive guidance by means of the selective attachment of osteoblasts to the implant surface [39].

#### b) Cell viability and proliferation

Figure 4.102 shows the image results of Live/Dead test of CS CP-Ti coating (Fig. 4.102a-d), after anodic oxidation with thermal treatment (Fig. 4.102b-e) and alkaline (Fig. 4.102c-f) treatments onto CS CP-Ti coating at 3 and 10 days of cell culture. In all cases there is an increase of cell proliferation but especially on the surfaces in which nanotextured treatments were performed. The anodic oxidation treatment is the one that shows higher cell proliferation, followed by the alkaline treatment.

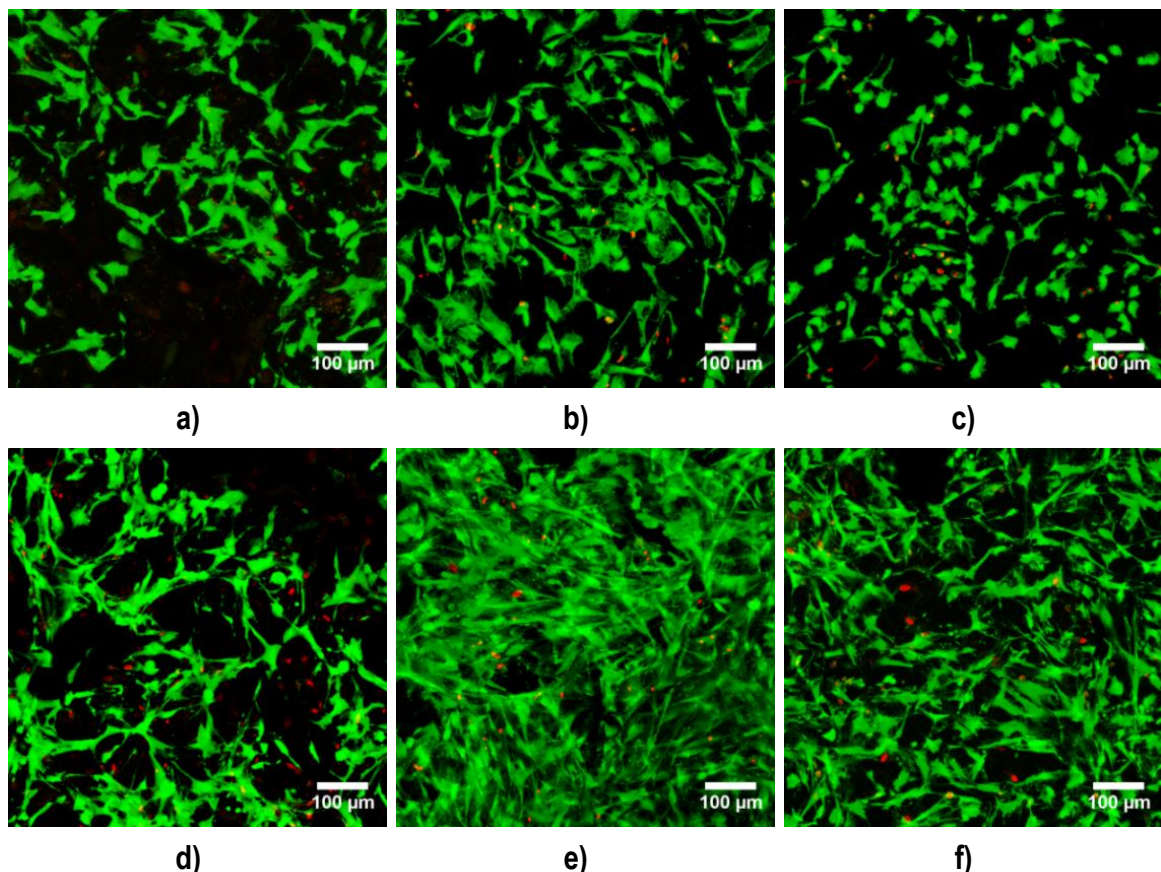


**Figure 4.102.** Live/Dead assay at 3 and 10 days (from up to down) of cell culture onto CS CP-Ti coating after (a,d) anodic oxidation (b,e) and alkaline treatment (c,f) (n=3)

The MTS assay corroborates the results observed in the Live/Dead assay (Fig. 4.103). At 3 days of culture it was observed very similar cell amount all substrates, which start to differ up

after 10 days of culture. In terms of surface wettability all surfaces show superhydrophilic behavior, leading to an initial good interaction between the liquid and the substrate. In terms of surface microtopography, no significant changes were observed among all samples. This means, that cell proliferation may be influenced by: surface energy or nanotopography features.

Feng et al. [181] studied the adhesion of osteoblasts on titanium and different surface oxide titanium films through the calculation of surface energy values, considering a contribution of dispersion components ( $\gamma^d$ ) and polar components ( $\gamma^p$ ).

They indicate that dispersion components ( $\gamma^d$ ) in surface energies were similar, whereas the polar components ( $\gamma^p$ ) presented were significantly different. ( $\gamma^p$ ) increased in order of: pure titanium < oxide titanium surface (produced by thermal treatment 600°C during 30min in air) < oxide titanium surface (produced by thermal treatment 600°C during 30min in oxygen), the same as the order of the number of adhered cells and ALP activity. These results indicate that ( $\gamma^p$ ) influenced the behavior of the HOB on Ti surfaces more strongly compared to ( $\gamma^d$ ), which was probably attributed to the fact that  $\text{TiO}_2$  and (OH)s groups on the surfaces and the compositions in cells and the culture medium are polar. Higher ( $\gamma^p$ ) leads to higher interaction energy and the products would be more stable leading good cell attachment and spreading on hydrophilic surfaces. Although both nanotextured treatments lead to superhydrophilic behavior, further surface energy tests should be performed in order to corroborate the small difference on the cell proliferation increase at 10 days of cell culture.

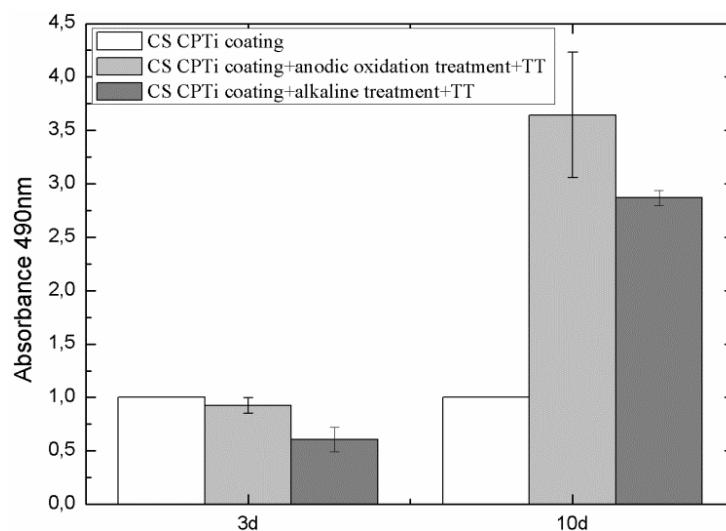


**Figure 4.103.** Cell viability measured by MTS assay at 3 and 10 days of cell culture onto CS CP-Ti coating and after anodic oxidation and alkaline treatments (n=3)

The obtaining of micro/nano-textured surfaces is a suitable topography modification that retains the mechanical interlocking ability of the microtopography thereby bonding well for osseointegration, and the good cell response of the nanotopography [55]. For the comparison of these two samples, one should consider the differences in nanotopography, i.e.  $1.2\pm 0.2\text{nm}$  and  $36.8\pm 4.6\text{nm}$  for the alkaline treatment and anodization+annealing respectively, as well as the differences in composition, i.e. sodium titanate and anatase respectively. Similar studies of micro/nano-textured titanium surface topographies were performed with  $\text{TiO}_2$  NTs by simple acid etching followed by anodic oxidation to mimic the hierarchical structure of bone tissues [191]. It was also reported in vivo the improvement of osseointegration in sheep 12 weeks after implantation [192]. The same happens with the combination of grid-blasting followed by alkaline treatment/heat treatment at  $600\text{ }^\circ\text{C}$  for 1h [193]. The higher cell increase of the nanotextured surface in comparison with the as-sprayed CS CP-Ti coating could be that cell filopodia has facility to directly anchor to the nanosurface porous along the top surface area. The cell proliferation differences between NTs and sodium titanate layers may be explained by the nanopattern [39].

The thermal treatments in both nanotextured surfaces also play an important role in the enhancement of biological properties, as could be the transformation from amorphous to crystalline surface structure. Wei et al. [79] reported that the alkaline treatment on Ti surfaces and subsequent heat treatment leads to the most rapid formation of apatite. On the other hand, in vitro studies [92] noted that at the early stage, eg. 2-12h of cell incubation, there was no difference in the data among the Ti, amorphous anodized and crystalline anodized surfaces. However, the number of attached cells on the  $\text{TiO}_2$  NTs markedly increases as the culture time is extended to 24 and 48 h. It is not clear why the amorphous  $\text{TiO}_2$  NTs provides slightly reduced cell proliferation rate than the  $\text{TiO}_2$  anatase. Residual fluorine within the pores of unannealed amorphous NTs (introduced during the HF anodic oxidation process) might be a factor; however, further studies are required to clearly understand the cause for the observed difference in the cell behavior.

Regarding  $\text{TiO}_2$  NTs layer, there is a lot of studies that discuss the optimal NT diameter [52, 98, 194]. Even so, an optimum size of a  $\text{TiO}_2$  NTs for osteoconductivity and osseointegration ability has been reported as 70nm after different in vivo assessments [195], but it is not complete consistent with the studies mentioned above; therefore, it should be considered the

antibacterial properties of TiO<sub>2</sub> NTs layer. As the NTs diameter increased, bacterial adhesion decreased and reached the lowest value for a 200nm NT diameter [102]. Ercan et al. [196] perform a comparison studio with different NT diameters (20-40-60-80 nm) and confirms that heat treatment of 80 nm diameter titanium tubes produced the most robust antimicrobial effect of all surface treatment parameters tested, and not just due to NT diameter, also for the crystallinity of the layer. Contrarily, Narendrakumar et al. [197] obtained the lowest adhesion of *S. sanguinis* and *S. mutans* on TiO<sub>2</sub> nanostructured surfaces and the highest osteoblast adhesion on small 15 nm diameter nanotubular/nanoporous. Therefore, there seems to be a high controversy on the optimal nanotube diameter that is suitable for cell interaction and the decrease of bacteria attachment.

### c) Cell differentiation

Although cell proliferation is higher for TiO<sub>2</sub> NTs layer than sodium titanate hydrogel, cell differentiation is high onto CS CP-Ti coating after alkaline treatment (Fig. 4.104).

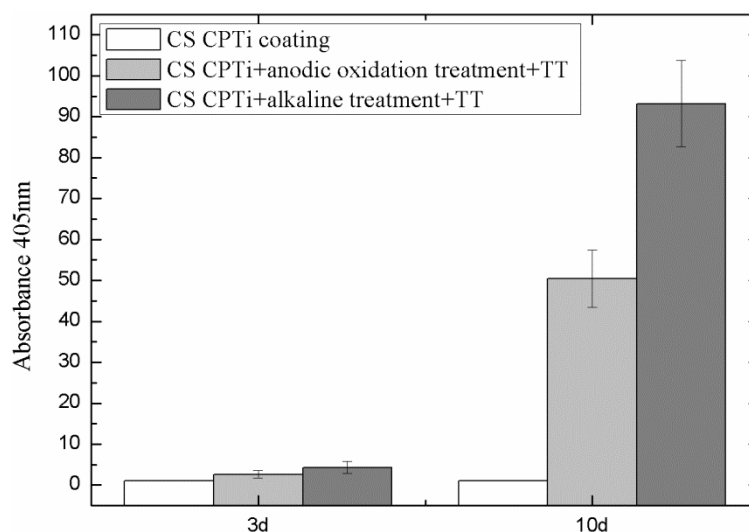


**Figure 4.104.** Cell differentiation measured by ALP activity at 1, 7 and 14 days of cell culture on nanotextured treatments onto CS CP-Ti coating (n=3)

The ALP activity of CS CP-Ti coating with nanotextured treatments coating increases significantly up to 10 days in comparison with the as-sprayed CS CP-Ti coating. The high surface area produced by the micro and nanoroughness leads to better cell attachment [198]. F-actin fibers play a crucial role in modulating cell modulus, elasticity and maintenance of cell shape. Observations that nanoscale topographies induce increased expression of actin stress fibers relative to flat surfaces may thus explain the mechanism by which surface nanoscale

roughness affects cellular surface attachment [199]. The ALP activity also is influenced by the surface energy; in both nanotextured surfaces, it might result in high surface energy (polar components ( $\gamma^p$ )) due to the presence of titanium oxides, leading a better cell attachment and cell differentiation. Therefore, the increase of ALP activity is related with the increase of roughness (micro- and nano-), thus anodic and alkaline treatments show higher cell differentiation in comparison with as-sprayed CP-Ti coating [181]. Surface nanoroughness might induce the difference in cell differentiation as, TiO<sub>2</sub> NTs layer lead to a nanoroughness of Ra= 36.8nm while sodium titanate layer to a Ra =1.2 nm.

#### **4.2.4.3. In vitro comparison between highly rough commercial pure titanium coating and hydroxyapatite coatings by cold spray**

##### a) Introduction

The use of bioceramics, such as calcium phosphates, and porous metals like titanium is well reported in cementless joint prosthesis. Calcium phosphates are known to be osteoconductive while unalloyed titanium can be osteopductive if a suitable previous surface treatment is done. There exists an extended work in the literature dealing with the application of calcium phosphates as bioactive layers by many several methodologies, especially concerning HAs due to their osteogenic properties and the ability to form strong bonds with host bone tissues. The bioactivity and biodegradation of HA are critical parameters to achieve a good HA coatings that mainly depend on Ca/P ratio, phase and crystallinity.

Surface chemistry, as could be the formation of sodium titanate hydrogel on the surface of the implant due to an alkaline treatment [79] or the deposition of calcium phosphates such HA [137], should allow for earlier load bearing of prostheses following implantation. Specifically, HA surfaces seem desirable due the induction of bone like apatite formation, which is considered to be a reason for better osseointegration [200]. As already explained in the previous section, cells are sensitive to small surface features; therefore, the use of agglomerate HA) is becoming a topic of special interest due its similar crystal bone size microstructure. Agglomerate HA powder provides high surface area which induces better bioactivity than coarse crystals [201]. Webster et al. [202] reported that osteoblast functions

on ceramics with grains smaller than 100nm were significantly enhanced compared with larger grains.

Highly rough titanium coating was compared in-vitro with the optimal sintered and agglomerate HA coatings produced by CS.

#### b) Cell viability and proliferation

The results of the Live/Dead assay are shown in figure 4.105. In general overview, all coatings show a good viability, there is no significant number of dead cells for all coatings and for all days of cell culture. No significant cell mortality was observed in all samples. The CS CP-Ti coating shows a continuous increase of cell proliferation along the surface (Fig. 4.105 a,b,c) in comparison with HA coatings, which show a decrease of the number of cells between 1 and 7 days of cell culture, followed by an cell proliferation increase from 7 to 14 days of cell culture, more remarkable in agglomerate HA coating than sintered HA coating (Fig. 4.105 d,e,f). It should be pointed that for sintered HA coating, it is observed a clear tendency of cell group-joining for all days of culture, showing non-coated zones onto the sintered HA surface (Fig. 4.105 g,h,i).

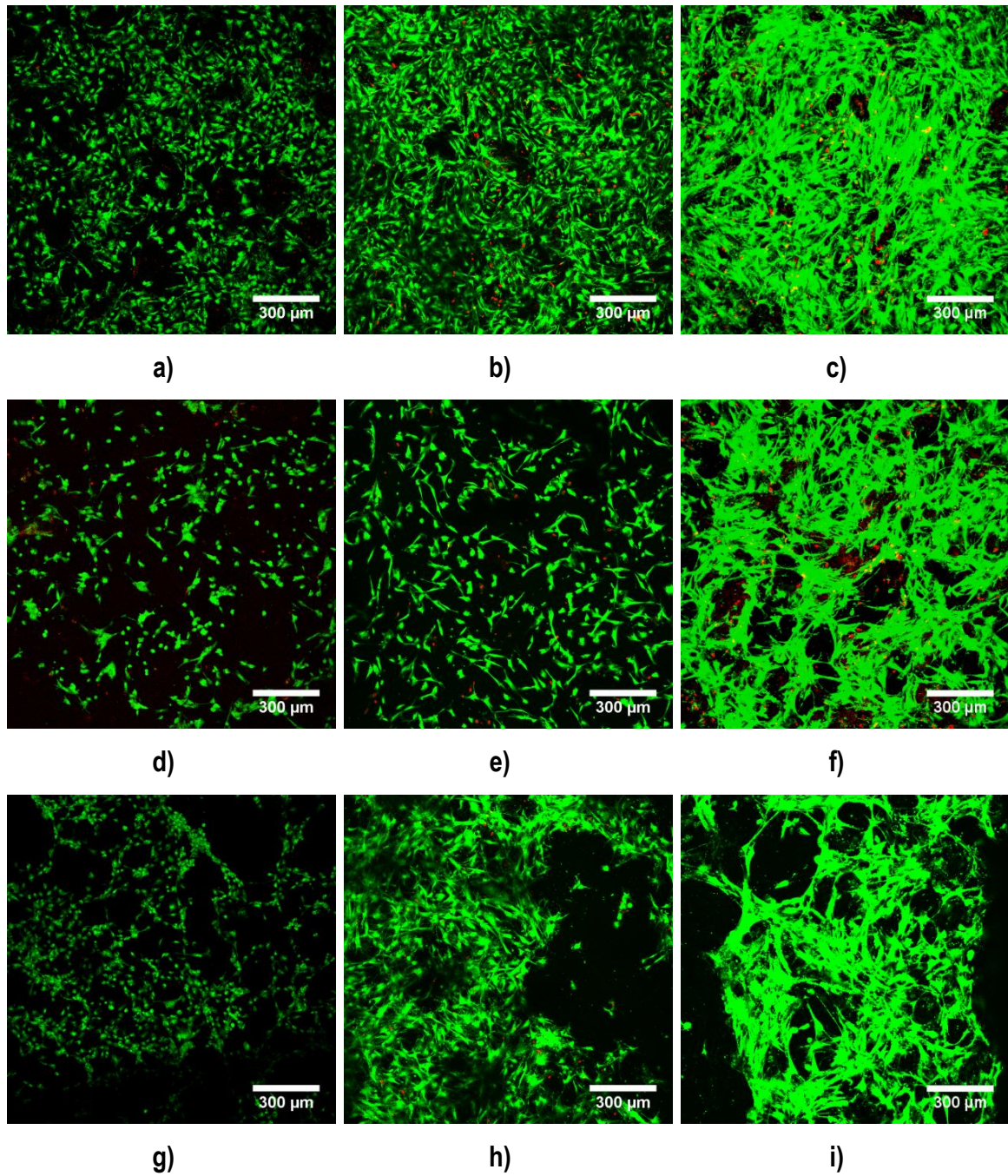


**Figure 4.105.** Live/Dead assay for a-c) CP-Ti, d-f) agglomerate HA and g-i) sintered-HA coatings at 1, 7 and 14 days of cell culture (from left to right) (n=3)

Figure 4.106 shows the MTS results, which match with the ones obtained in the Life/Dead assay (Fig. 4.105). Although cells on HA coating start proliferating up to 7 days, it should be taken into account the faster cell proliferation between 7 to 14 days, probably overcoming with the cell proliferation rate above 14 days, especially for the agglomerate HA coating.

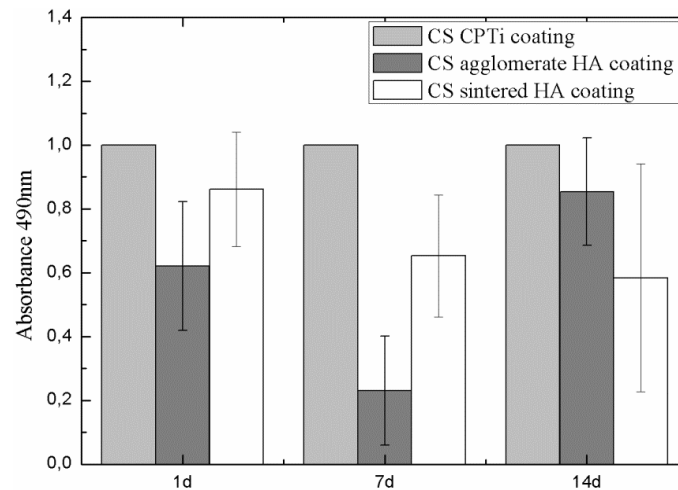


**Figure 4.106.** Cell viability measured by MTS assay after culturing for 1, 7 and 14 days of cell culture on CS CP-Ti, agglomerate and sintered HA CS coatings (n=3)

### c) Cell morphological aspects

In general, microstructured surfaces affect cell morphology and cytoskeletal structure, while nanostructured surfaces influence cell functions, including proliferation, differentiation and alignment [203]. As it has been reported that osteoblastic cells attached and spread more rapidly on smooth surfaces than on rough surfaces [204]. The roughness at microscale level has been reported to be very similar for all three samples ( $R_a \sim 45 \mu\text{m}$ ), while the roughness at the nanoscale level has been reported to be  $R_a = 58.2 \text{ nm}$  and  $39.1 \text{ nm}$  for sintered HA and agglomerate HA coatings respectively. It could be observed onto the as-sprayed rough CS CP-Ti coating that the cytoskeleton of HOB cells display spread morphology showing flattened cytoplasm and extended actin filopodia during all days of culture (Fig. 4.107a-b-c). Contrary, HOBs onto HA surfaces show nodular morphology and some of them one direction elongated cytoplasm at 1 day of cell culture (Fig. 4.107d-g). The CS CP-Ti coating shows a higher complex surface composed by micro-roughness produced by the use of coarse CP-Ti particles and a nano-roughness provided by the irregular morphology and the asperities of CP-Ti particles. The rough Ti surface produced by CS is fully composed by a diversity of random groves and ridges. The complex surface structure of CS CP-Ti coating in comparison of the HA coatings suggests a better anchoring for cells due to the different surface irregularities that they show onto the different surfaces. It was also confirmed by Rosales-Leal et al. [178] that cell adhesion and proliferation on the textured titanium surfaces with similar surface chemistry (acid-etched and blasted-etched surfaces) were driven by topography features. Khang et al. [205] showed that the individual role of sub-micron and nano-features

in roughness, in relation to the adhesion of bone cells, selectively adhered more on both sub-micron (400% increase) and nanometer (50% increase) surface structures than on flat surfaces. On the other hand HA coatings do not show as complex topography as CPTi coatings as HA deposition covers the surface irregularities of CS CP-Ti surface.

Although all CS coatings show similar micro- and nano- surface roughness, HOB have a better cell response on CS CP-Ti coating at 1 day of cell culture. Even so, topography is just one parameter that influence cell response, parameters such as surface composition, wettability and energy should be taken into account. Results have shown for all CS coatings a superhydrophilic behavior, that “should lead to” good cell response. As mentioned in the chapter of the results, the superhydrophilicity of CS CP-Ti coating comes from the high roughness and the favourable surface energy, on the other hand, the superhydrophilicity of HA coatings is due to the coating porosity, in which absorbs the droplet of contact angle measurement, but because of a favourable surface energy. In the case of HA coatings, surface energy plays an important role. Although it were not performed surface energy assays, it is already reported [183] that the behavior of HOB on the surface of HA and carbonated HA is greatly influenced by the polar component in surface energy, which a very low polar component would inhibit the osteoblast attachment [206]. The surface energy of a biomaterial greatly influences the initial cell attachment and spreading of human osteoblastic cells at the surface [207]. For that reason, cells onto HA coatings show a nodular morphology, due to the bad initial cell attachment..

At 7 days of culture, HOBs onto CS CP-Ti coating keep proliferating due to the good initial cell attachment at 1 day of cell culture (Fig.4.107b). On the other hand, cells seeded onto HA coatings turn from a nodular to osteoblastic morphology (Fig.4.107e-h), especially for the agglomerate HA powder, showing a good attachment onto the surface. From then on, cells on HA coatings starts to proliferate, especially on the agglomerate HA coatings, which gets closer cell proliferation values to CS CP-Ti coating at 14 days of cell culture; at that point , cells onto CS CP-Ti and agglomerate HA coatings show complete surfaces of HOB (Fig.4.107c-f).

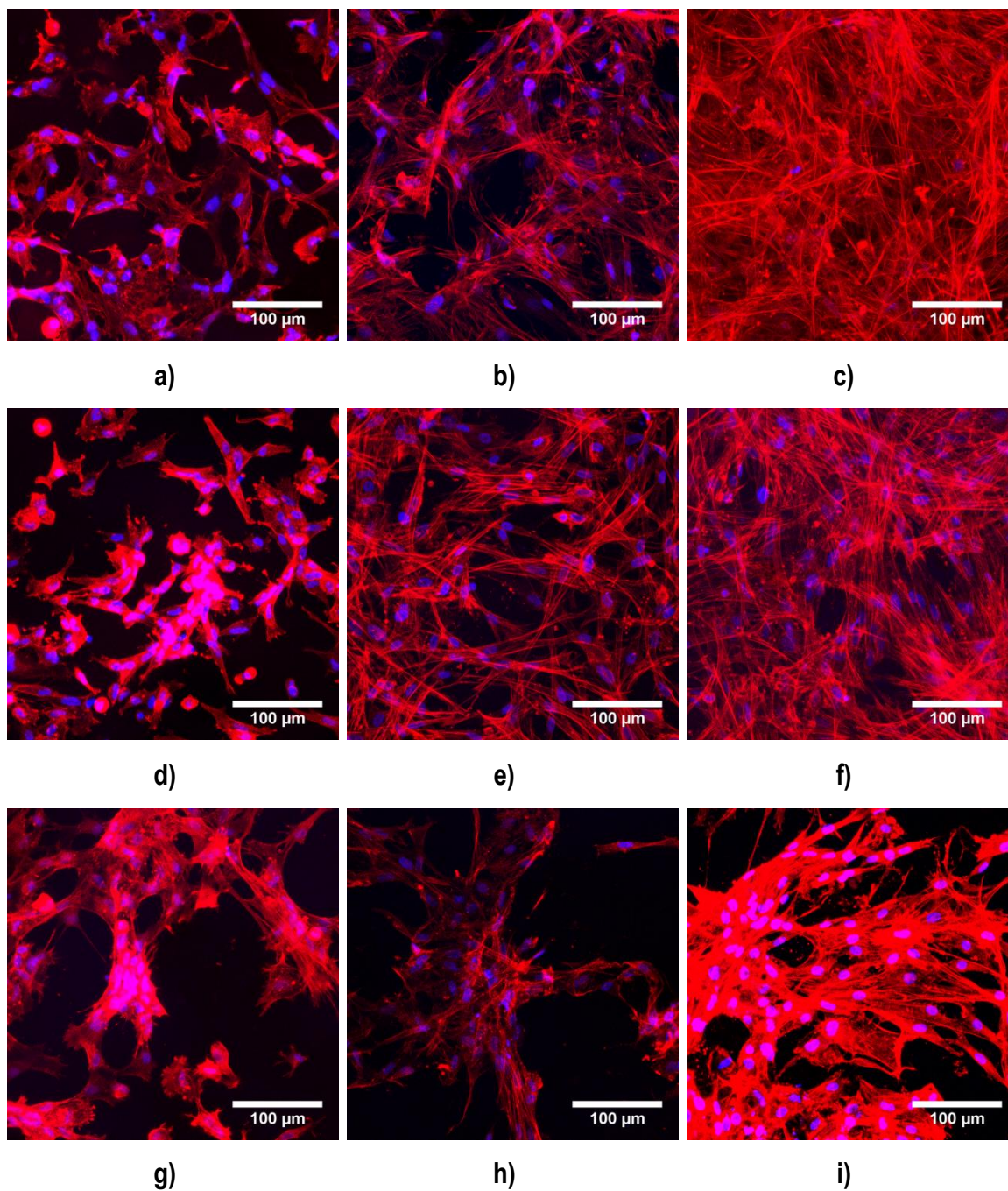


**Figure 4.107.** Phalloidin staining for a-b-c) CP-Ti, d-e-f) agglomerate HA and f-h-i) sintered HA CS coatings at 1, 7 and 14 days of cell cell culture (from left to right) (n=3)

Between 7 and 14 days of cell culture, cells on sintered HA coating also proliferate, but not as fast as in agglomerate HA coating. It can be observed that HOB cells on agglomerate HA coating show extended cytoplasm and elongated actin filopodia along the surface (at 7 days of culture) (Fig.4.107e), as well as HOB on sintered HA coating (Fig.4.107b). The higher increase of cell proliferation on agglomerate HA coating in comparison with sintered HA coating is suggested by: (i) small crystal size and (ii) HA phases. HOB functions onto

grains smaller than 100nm are significantly enhanced compared with larger grains leading to a faster bone ingrowth [202], and also provide high surface area which induces better bioactivity than coarse crystals [201]. The nanocrystalline structure together with the small amount of amorphous calcium phosphate (ACP) in which is composed agglomerate HA powder, allows physiologically produced HA to precipitate on the coating and enhance the bone ingrowth [208]. From that point, it was able to see a high proliferation onto agglomerate HA coating at 14 days of cell culture, getting closer to CP-Ti values, and probably overcoming them above 14 days of cell culture.

### c) Cell differentiation

The cell differentiation of CS CP-Ti and HA coatings is shown in figure 4.108. HA coatings show lowest values in comparison with CS CP-Ti coating. Between HA coatings, sintered HA coating is the one that shows the highest value in comparison with agglomerate HA coating along all cell culture days.

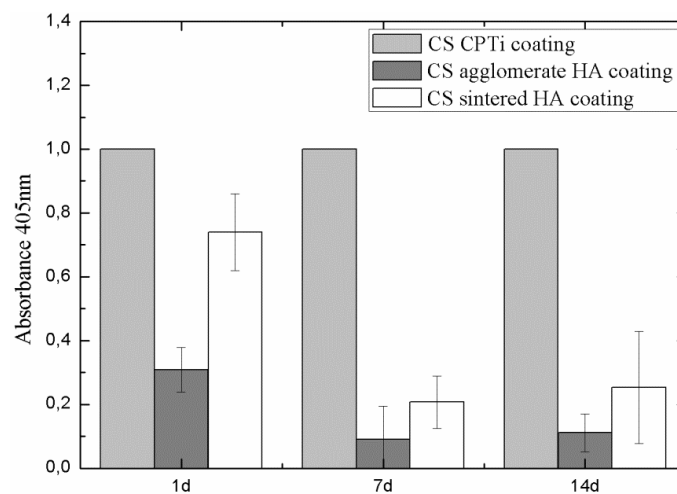


**Figure 4.108.** Cell differentiation measured by ALP activity at 1, 7 and 14 days of cell culture on CS CP-Ti, agglomerate HA and sintered HA coatings (n=3)

Rough surfaces have been well-known recognized for its stimulation on osteoblast differentiation [183]. A combination of micro- and nano-roughness has been demonstrated to enhance cell differentiation. Rolando et al. [209] develop a simple oxidation treatment for generating controlled nanoscale topographies on Ti surfaces, while retaining the starting micro-/submicro-scale roughness. The introduction of such nanoscale structures in combination with micro-/submicro-scale roughness improves osteoblast differentiation and local factor production, which, in turn, indicates the potential for improved implant

osseointegration in vivo. Moreover, it is reported that nano-to micro surface roughness ( $R_a=10.57\mu\text{m}$ ) enhance mineralization [183]. Actually, the high-waviness profile of those coatings increases the free surface contact area between host-bone and the implant [178]. It was found as an advantage the production of porous coatings with an open-cell structure, a pore size up to 150 and a 60-65% of macroporosity [69] in order to enhance bone ingrowth and a good mechanical fixation; the osteogenic-angiogenic responses to titanium alloy were greater on rough titanium alloy than on smooth titanium alloy. Surface features regulated expression of integrins important in collagen recognition. These factors may increase bone formation, enhance integration, and improve implant stability in interbody spinal fusions [210]. Rough CP-Ti coating produced by CS surface show the highest cell differentiation values for all days cell cultured in comparison with HA coatings. On the other hand, small differences were found between HA coatings. Sintered HA coatings stimulate more osteoblastic differentiation in comparison with agglomerate HA coating. As there are no significant topographic differences between agglomerate HA and sintered HA surfaces, but yes in phase composition and crystal size, it is suggested that osteoblast differentiation is sensible to crystal size.

#### **4.2.4.4. In vitro comparison of hydroxyapatite coatings obtained by plasma spray and cold spray**

##### a) Introduction

Plasma Spraying (PS) is a well-established process for commercial prosthesis for the production of HA coatings. Even so, the use of high temperatures produces changes in its microstructure and mechanical properties leading to implant failure. Several solutions preparations or post-treatments were proposed in order to solve that problem. Heat treatment and rough surfaces to spray were a good alternative in order to transform the amorphous HA phases into crystalline face or enhance mechanical properties due to the interlocking induced by the roughness of the substrate [208,211].

In order to control HA composition, low-temperature coating deposition processes were purpose such as AD [120,121] and NPDS [152], but with the use of sub-micron sized particles achieving thin very layers. Dense nanostructured HA coatings were obtained by AD with a 98.5% density and a tensile adhesion of  $30\pm 1$  MPa. However, further thermal treatment up to

400°C needs to be applied in order to avoid amorphous phases. Thermal treatments up to 400°C increase HA crystal size from 16.2 nm to 29.3 nm, increasing also biological properties. But, above 400°C, HA crystal size increase up to 99.7 nm decreasing biological properties [212]. As it is reported, osteoblast cells are sensible to grain size under 100 nm [202]. Both HA coatings showed good biocompatibility promoting osseointegration, however, it was suggest a successful outcome without post-heating treatment showing a high bone implant contact length [121]. Moreover, by AD, different HA surface roughnesses were achieved by manipulating the particle size distribution of the feedstock powder. An increase of roughness was perceived from 0.65 to 1.03  $\mu\text{m}$  together with a thickness increase up to 10  $\mu\text{m}$ . It was found that the optical biological performance was for 5  $\mu\text{m}$  thick HA coating with an intermediate surface roughness of 0.82  $\mu\text{m}$  [213].

As mentioned before, CS is a suitable technique to spray oxygen and temperature sensitive materials due to the temperature of feedstock powder it is under its melting point. This main advantage leads to the option to spray customized coatings with the desired microstructure and composition, beneficial in biomedical field [214].

This subpart aims to ascertain how different coating processes (PS and CS) affects HA coatings (eg. surface topography and chemistry, phase composition and microstructure) and thus, cell response. Optimal spraying PS HA conditions were chosen from previous research [215] while agglomerate HA coating by CS, due to its better cell response in comparison with sintered HA coating, was chosen for this study.

#### b) Cell viability and proliferation

HOB cell viability and proliferation were qualitatively analysed by Live/Dead (Fig. 4.109) and measured by MTS activity (Fig. 4.110) after 1, 7 and 14 days of culture. Live/Dead images of PS HA coating show a constant cell proliferation along all days of culture. Contrary, CS HA coating shows a decrease of the number of cells up to 7 day of cell culture, followed by a fast increase up to 14 days of cell culture, overcoming the results obtained for PS HA coating. For all coatings, no significant number of dead cells was found along days of culture.

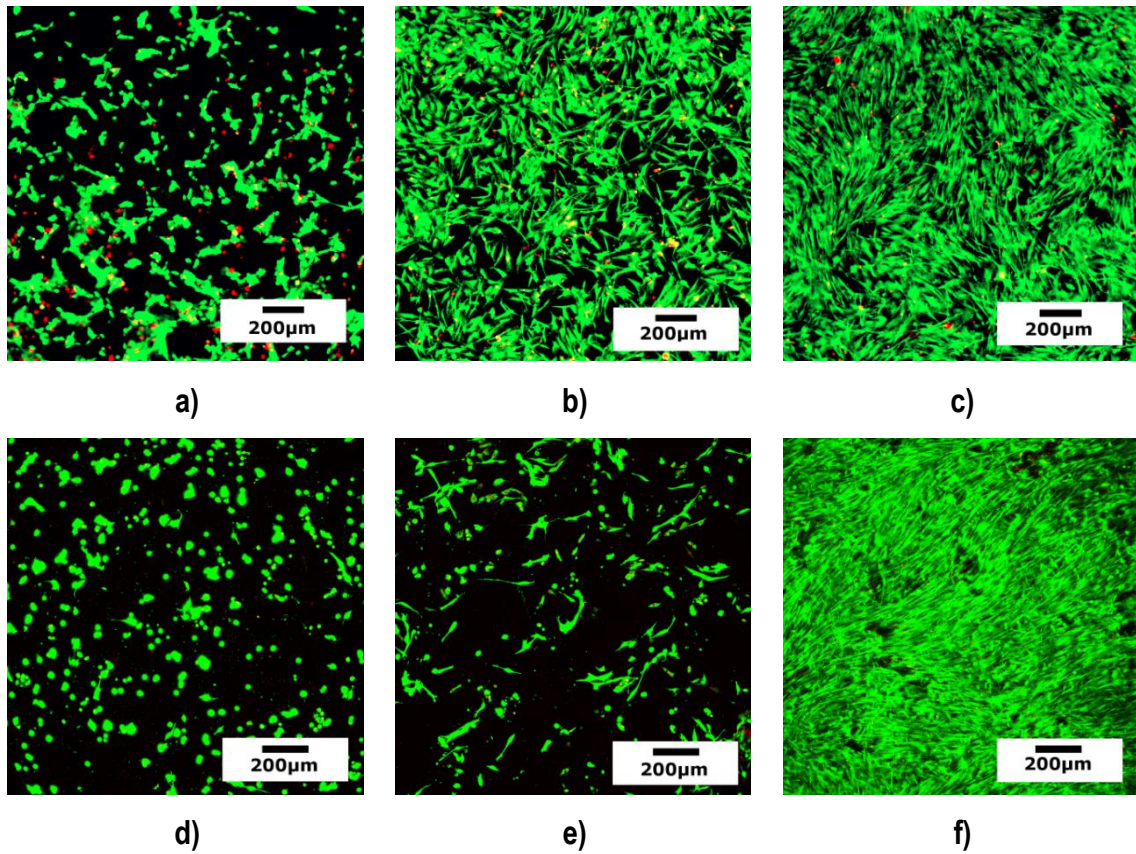


Figure 4.109. Life/Dead assay at 1, 7 and 14 days (from left to right) of cell culture of (a,b,c) PS and (d,e,f) CS HA coatings (n=3)

Figure 4.110 shows the MTS assay, in which confirms the results obtained from Live/Dead assay.

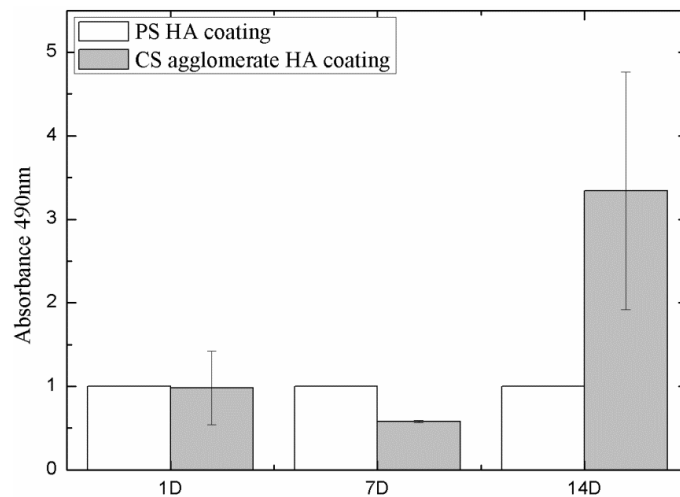


Figure 4.110. MTS assay at 1, 7 and 14 days (from left to right) of cell culture onto PS and CS HA coatings (n=3)

The microstructural characterization results of PS HA coating indicates surface roughness of  $R_a = 5.8 \mu\text{m}$ , a crystallinity of 62.4% and a porosity of 21-23%. As previously mentioned, cell attachment is enhanced by surface roughness and surface energy (among other parameters). Although CS HA coatings show a higher roughness than PS HA coatings, the surface tension of a dense PS HA coating, in comparison with the nanoporous CS HA coatings, results in a decrease of surface energy, thus favouring initial cell attachment and spreading of cells [216]. Superhydrophilicity of CS HA coating is not related to the surface energy, as it acts as a "sponge" absorbing the droplet of the contact angle measurement. It seems that cell attachment is mostly influenced by surface energy rather than surface composition and topography; at 1 day of cell culture, as previously reported, cells onto CS HA coating show a nodular morphology indicating initial bad attachment in comparison with the HOB onto PS HA coating.

At 7 days of cell culture, once cells are attached onto the substrate, cell proliferation mostly depends on surface composition as well as surface topography. HOB onto CS HA coating acquired osteoblastic morphology with extended filopodia and spread cytoplasm, leading to a higher cell proliferation up to 14 days of cell culture, overcoming the value of PS HA coating. CS HA coating, which has higher crystallinity yielded higher rates of cell proliferation than PS HA coating, as amorphous HA coatings yield a slightly higher cell attachment efficiency than crystalline HA coatings [217]. Moreover, cell proliferation is also influenced by the size of crystal grain, as cell response is sensitive to nanocrystal  $<100\text{nm}$  [202].

### c) Cell morphology aspects

FESEM micrographs of PS coatings already show a well-adhered cell attachment onto the surface from 1 day of culture and cell proliferation increases constantly (Fig. 4.111a,b). Cells show a flattened cytoplasm with long filopodia attached onto the surface, while at 7 days of culture cells start connecting their filopodia between them (Fig. 4.112a,b). Contrary, cells onto CS HA show an initial nodular morphology at 1 day of cell culture (Fig. 4.111c,d), but it turns to osteoblastic morphology up to 7 days of cell culture, achieving flattened and adherent morphology with more extended filopodia than cells onto PS HA surfaces (Fig. 4.112c,d).

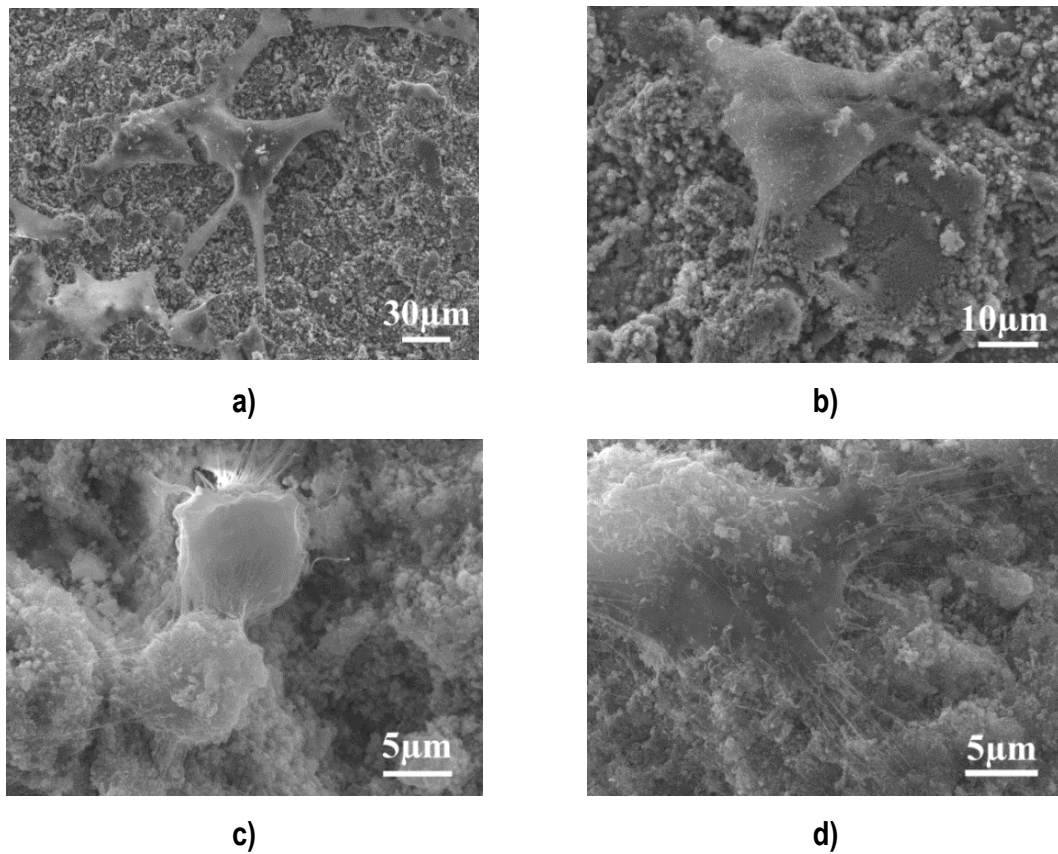


**Figure 4.111.** FESEM micrographs of cells at 1 day of cell culture onto a-b) PS, c-d) CS HA coatings (n=3)

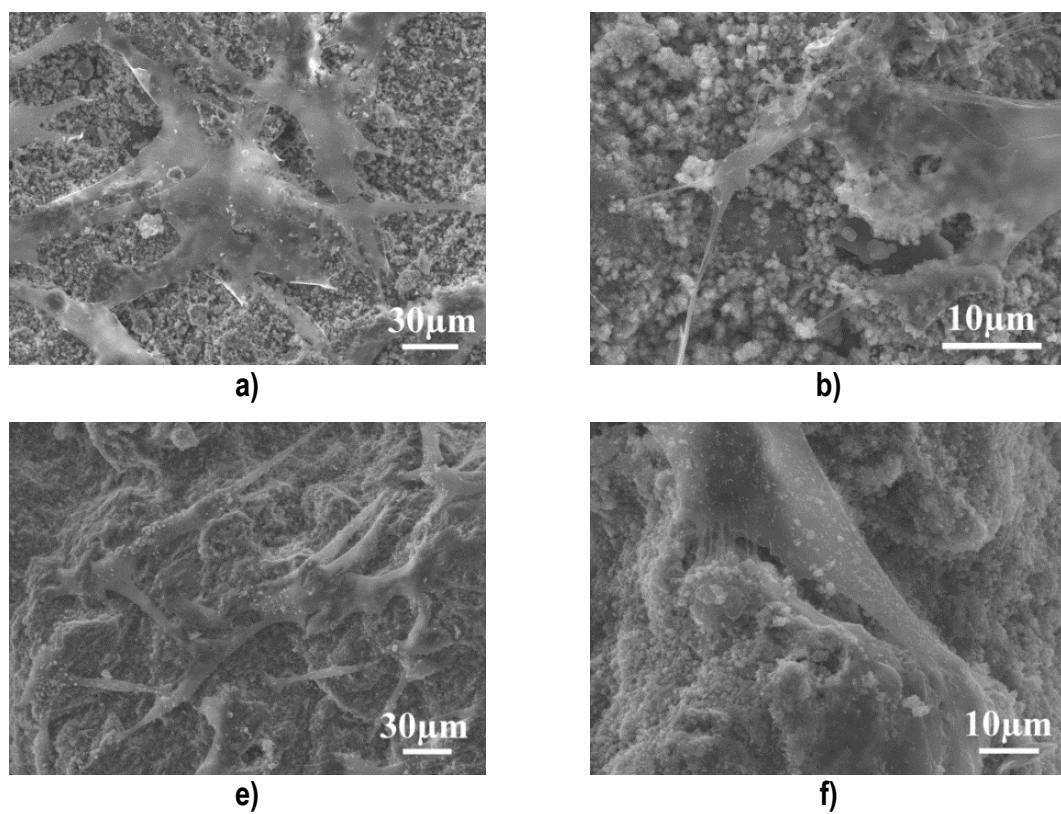


**Figure 4.112.** FESEM micrographs of cells at 7 day of cell culture onto a-b) PS, c-d) CS HA coatings(n=3)

#### d) Cell differentiation

The ALP activity is an early marker of cell differentiation that allows us to monitor the cell status (Fig. 4.113). The ALP activity of HA surfaces is maintained very constantly along 1 and 7 days of culture. No significant changes are perceived.

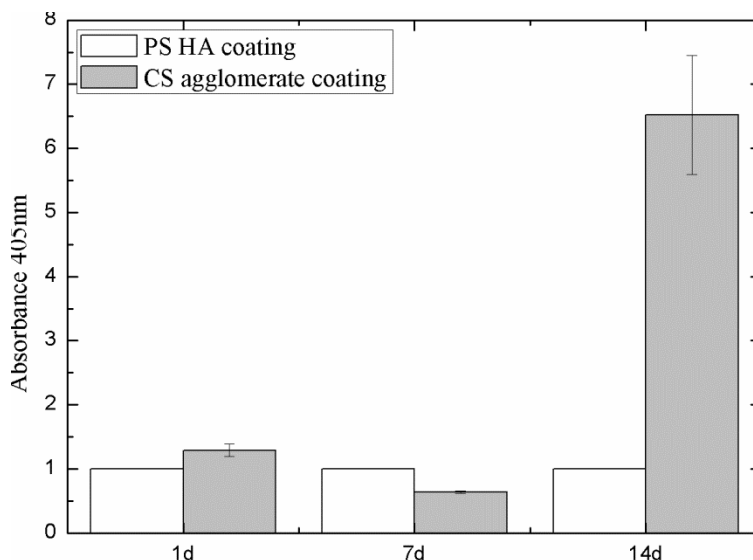


**Figure 4.113.** Cell differentiation measured by ALP activity at 1, 7 and 14 days of cell culture on PS and CS HA coatings (n=3)

Regarding cell differentiation, a lot of in vitro studies show that osteogenic differentiation is higher in cultures of ACP substrates compared to crystalline substrates [218]. In contrast, other in vitro and in vivo studies found that the dissolution of the amorphous phase inhibited the osteogenic differentiation and bone formation [219,220]. During 1 and 7 days of culture, cell differentiation values remain very similar. It is already reported that cell differentiation is enhanced by crystalline than amorphous HA phases, and even more, with a small crystall size [221]. That is the reason why PS HA coatings maintain low ALP activity during all days of cell culture. On the other hand, it could be observed that cells on CS HA coating do not show high cell differentiation up to 14 days of culture, which is because of the bad cell attachment previously mentioned. However, once cells attach properly on CS HA coating, it can be observed a higher increase of cell differentiation, due to the high percentage of crystallinity.

#### 4.2.4.5. In vitro dynamic testing of cell attachment onto hydroxyapatite surface

##### a) Introduction

Although a lot of in vitro and in vivo assays have been performed during the last few decades years for HA bioactive coatings, there is a lack of exploitation of real-time in vitro interaction measurements.

Among different surface detection methods (optical, mechanical, electrochemical), the optical ones are the most surface-sensitive label-free methods [222]. Surface Plasmon Resonance (SPR) is an optical detection method that has been used for a few decades for biomolecular interaction studies, like drugs and proteins [223]. SPR has reached popularity due to its high sensitivity and real-time measurements, which enables determination, not only of affinity, but also kinetics of the molecular interactions.

SPR is based on an optical interfacial property, called the evanescent field, created into a dielectric interface under total internal reflection conditions. For measurement proposes, the evanescent field is enhanced with free electron excitation on a dielectric–metal interface. The evanescent field detects the optical density or a change in it, inside the evanescent field, which extends a wavelength ( $\lambda$ ) of the incident light approximately to the measurement medium. The basic applications are the determination of kinetics and binding affinity between molecule interactions [222].

Physical SPR phenomena are not limited to molecular interactions but are also sensitive to other surface changes and applicable in the biomedical field [224,225]. In Multi-Parametric Surface Plasmon Resonance (MP-SPR) instruments, detection is based on the SPR principle utilizing the Kretschmann configuration and angle scanning optical arrangement (Fig. 4.114a). The SPR curve is detected when surface plasmons form on the metal surface that let a drop in the reflected intensity (Fig. 4.114b). The position of the SPR curve depends on the wavelength of the light, the refractive index on the measured surface and measurement media, such as air or water. MP-SPR measures full SPR curves on a wide angle range (laser rotates 38 degrees) and with two wavelengths of light (such as 670 nm and 980 nm). When binding on the surface is occurring, an SPR curve shift is detected due to the change in the refractive index near the surface. When the coating thickness increases up to hundreds of nanometers, the first SPR curve goes out of the measured angle range. However, two

wavelengths used for measurement increase flexibility related to coating thicknesses due to the second SPR curve still in the measured angle range. The measurement of the wide angle range of MP-SPR also enables the measurement in a so-called waveguide mode, which can be utilized in SPR sensing when the thickness of the sample layer is  $>\lambda^{-1}$  of the incident light. The MP-SPR optical setup makes the method suitable for a wide range of coating materials such as hydroxyapatite. The MP-SPR instrument is proved to be suitable for the molecule–material interaction measurements and cell interaction studies such as a protein or block copolymers adsorption on a nanocellulose surface, a drug interaction with living cell monolayer and a cell binding to peptide functionalized surfaces [226,227,228]. SPR is extensively utilized in interaction studies; however, recent research of protein or cell adsorption on hydroxyapatite coatings for prostheses applications was not found.

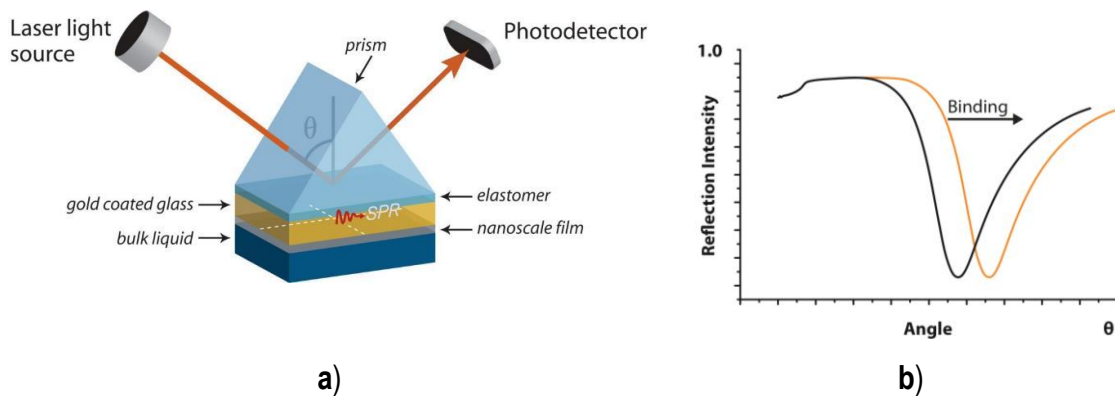


**Figure 4.114.** a) Measurements are performed on a sensor slide, typically a gold-coated glass slide that is placed between the prism and flow-cell. MP-SPR consists of an incident beam of *p*-polarized light that strikes electrically, and conducting sensors slide at the interface with high refractive index and an external medium (gas or liquid) with low refractive index. The incident beam jet moves at different angles and the determinate angle where surface plasmons exits take place, resulting in a reduced intensity of the reflected light and indicating changes in SPR signal due to surface molecular interactions; b) the graph shows a shift in SPR due to formation of a layer at the surface. The x-axis is the angle at which the laser excites plasmons. The y-axis shows the level of light intensity reflected from the surface. The dip in the curve (lowest light intensity) shows when the plasmons are excited

In this part, the MP-SPR was used to measure lysozyme protein and Human mesenchymal stem cells derived from adipose tissue (AD-MSC) interaction to the PS HA coating. It was not able to study the cell interaction of CS HA coatings, due to the higher kinetics of their deposition. The slide sensors of MP-SPR are too thin and fragile to deposit HA coatings by CS technic. So, a comparison between the standard gold sensor and PS HA coated were assayed.

### b) Multi-Parametric Surface Plasmon Resonance protein measurement

Lysozyme binding to HA coating was measured with the MP-SPR (Fig. 4.115). Figure 4.114a shows SPR curve before and after lysozyme injection where curve displacement to the right is observed due to protein binding. Figure 4.115b shows centroid sensogram during interaction measurement; it presents changes in SPR peak minimum position during binding. Lysozyme injection is started at 7.5 min, and, due to the advantage of real-time measurement, it is observed that lysozyme binds readily on the HA coating (association curve) with used concentration reaching plateau a couple minutes after injection (Fig. 4.115b). Since injection is ended at 14.5 min, protein starts dissociating from the surface and reaches a plateau after approximately 20min dissociation (time point 34.5 min).

Regarding the previous mentioned techniques, it was also proved that the applicability of physical vapor deposition (PVD) and electrophoretic deposition (EPD) time for surface acoustic wave (SAW) biosensor functionalization. Moreover, it was demonstrated that protein adsorption such as fibronectin can be detected on these metallic and ceramic (HA) surfaces [229]. In addition, other studies indicate that HA coated sensor technique by EPD is applicable for qualitative and conformational analysis of protein adsorption with quartz crystal microbalance with dissipation (QCM-D) techniques [230]. Studies were performed in order to study the effect of crystallite size, and it was found that the adsorption amount of human serum albumin was affected by crystal size but not that of bovine plasma fibrogen [231].

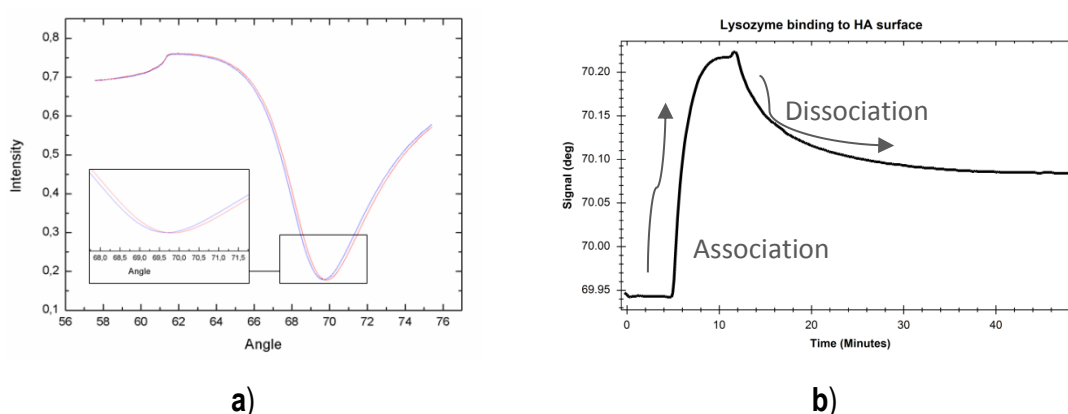


**Figure 4.115.** a) Full SPR curve before lysozyme protein injection (blue curve) and after protein deposition (red curve) on an HA coating; b) sensogram showing SPR Peak Minimum Angle changes during lysozyme interaction.

### c) Multi-Parametric Surface Plasmon Resonance cell measurement

AD-MSC adsorption on the HA coating and reference gold surface were measured using MP-SPR. Full SPR curve in cell culture medium at wavelenths of 670 and 980 nm was measured before cell attachment on the gold sensor slide (Fig. 4.116a) and HA surface on a TiO<sub>2</sub> coated gold sensor slide (Fig. 4.116b). HA coated surface was compared to the gold surface (Fig. 4.116c). HA surface shows faster increase of signals than gold surface indicating faster attachment of the cells as seen during the first minutes of the cells injection (from time point of 0) (Fig 4.116c). Cells attach over time on the HA surface until reaching plateau value at 90 min, whereas on a gold surface, the plateau value is reached only after 10 min. Despite that, AD-MSC cells have a good tendency to attach easily on surface: results show that HA surface favors attachment on the cells compared to the gold surface. The HA is porous material, and it is expected that HA coatings have more binding capacity on the surface compared to the smooth gold surface. However, higher porosity is not solely explaining detected differences on the cells attachment.

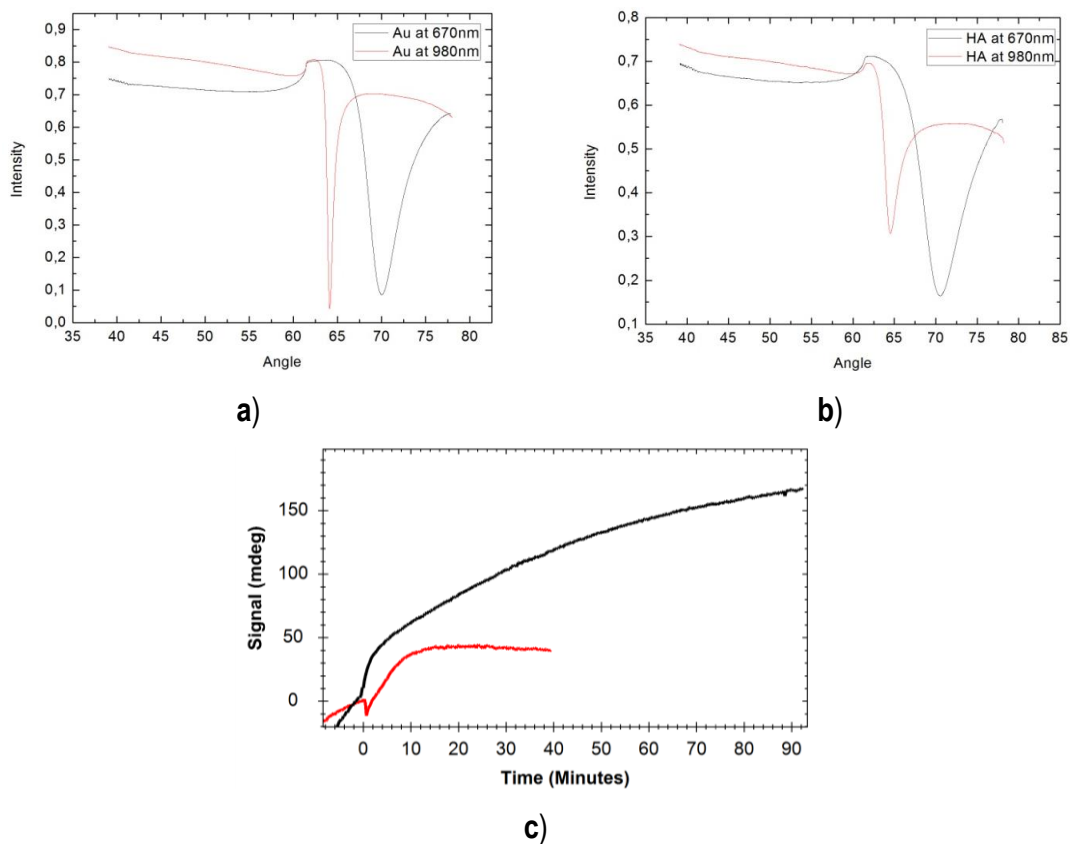


**Figure 4.116.** Full SPR curves measured in cell culture medium of a) pure gold and b) HA coated sensor slide; and c) measured peak minimum angle sensograms during AD-MSC adsorption on the HA coating (black) and the gold (red) surface. Measured with 670 nm wavelength

### 4.3 REFERENCES

- 
- [1] Fauchais P, Montavon G, Bertrand G (2010) From Powders to Thermally Sprayed Coatings. *J Therm Spray Technol* 19:56–80.
- [2] Fernandes DJ, Elias CN, Valiev RZ (2015) Properties and Performance of Ultrafine Grained Titanium for Biomedical Applications. *Mater Res* 18:1163–1175.
- [3] Elias CN, Meyers MA, Valiev RZ, Monteiro SN (2013) Ultrafine grained titanium for biomedical applications: An overview of performance. *J Mater Res Technol* 2:340–350.
- [4] Pateyron B, Pawłowski L, Calve N, et al (2013) Modeling of phenomena occurring in plasma jet during suspension spraying of hydroxyapatite coatings. *Surf Coat Technol* 214:86–90.
- [5] d'Haese R, Pawłowski L, Bigan M, et al (2010) Phase evolution of hydroxapatite coatings suspension plasma sprayed using variable parameters in simulated body fluid. *Surf Coat Technol* 204:1236–1246.
- [6] ASTM B-212-09 - Standard Test Method for Apparent density of Free-Flowing Metal Powders using the Hall Flowmeter Funnel.
- [7] ASTM B-527-93 - Standard Test Method for Determination of Tap Density of Metallic Powders and Compounds.
- [8] ASTM B-962-08 Standard Test Methods for Density of Compacted or Sintered Powder Metallurgy (PM) Products Using Archimedes' Principle
- [9] De Groot, K., Klein, C. P. A. T., Wolke, J. D., & de Blicck-Hogervorst, J. M. A. (1990). Chemistry of calcium phosphate bioceramics. *Handbook of bioactive ceramics*, 2, 3-16.
- [10] Ramesh S, Tan CY, Hamdi M, et al (2007) The influence of Ca/P ratio on the properties of hydroxyapatite bioceramics. *Int Conf smart Mater Nanotechnol Eng.* p 64233A
- [11] Kumar R, Prakash KH, Cheang P, Khor KA (2004) Temperature Driven Morphological Changes of Chemically Precipitated Hydroxyapatite Nanoparticles. *Langmuir* 20:5196–5200.

- 
- [12] El Idrissi BC, Yamni K, et al (2014) A novel method to synthesize nanocrystalline hydroxyapatite: Characterization with x-ray diffraction and infrared spectroscopy. *IOSR J Appl Chem* 7:107–112.
- [13] Rehman I, Bonfield W (1997) Characterization of hydroxyapatite and carbonated apatite by photo acoustic FTIR spectroscopy. *J Mater Sci Mater Med* 8:1–4.
- [14] Venkateswarlu K, Chandra Bose A, Rameshbabu N (2010) X-ray peak broadening studies of nanocrystalline hydroxyapatite by Williamson–Hall analysis. *Physica B: Condensed Matter* 405:4256–4261.
- [15] Villa M (2013) Metallic coatings deposited by cold gas spray onto light alloys PhD thesis. Universitat de Barcelona.
- [16] Gil FJ, Ginebra MP, Planell JA (2002) Surface hardening by anodizing and heat treatments of Ti6Al4V alloys for articular prostheses. *Biomed Mater Eng* 12:271–281.
- [17] Moridi A, Hassani-Gangaraj SM, Guagliano M, Dao M (2014) Cold spray coating: review of material systems and future perspectives. *Surf Eng* 30:369–395.
- [18] Hussain T, McCartney DG, Shipway PH, Marrocco T (2011) Corrosion Behavior of Cold Sprayed Titanium Coatings and Free Standing Deposits. *J Thermal Spray Technol* 20:260–274.
- [19] Bae G, Kumar S, Yoon S, et al (2009) Bonding features and associated mechanisms in kinetic sprayed titanium coatings. *Acta Mater* 57:5654–5666.
- [20] Zahiri SH, Antonio CI, Jahedi M (2009) Elimination of porosity in directly fabricated titanium via cold gas dynamic spraying. *J Materials Processing Tech* 209:922–929.
- [21] Luo X-T, Li C-X, Shang F-L, et al (2014) High velocity impact induced microstructure evolution during deposition of cold spray coatings: A review. *Surf Coat Technol* 254:11–20.
- [22] Guilemany, JM, Cinca, N., Dosta, S., Garcia-Cano, I. Intellectual Property: Feasibility of cold gas spraying to produce high roughness high porous titanium coatings for metallic prosthesis, Ref Number 1870 - . Universitat de Barcelona. Legal Deposit: 17/10/2014, Spain, 2014

- 
- [23] Van Steenkiste TH, Smith JR, Teets RE (2002) Aluminum coatings via kinetic spray with relatively large powder particles. *Surf Coat Technol* 154:237–252.
- [24] Schmidt T, Gärtner F, Assadi H, Kreye H (2006) Development of a generalized parameter window for cold spray deposition. *Acta Mater* 54:729–742.
- [25] Cinca N, Rebled JM, Estradé S, et al (2013) Influence of the particle morphology on the Cold Gas Spray deposition behaviour of titanium on aluminum light alloys. *J Alloys and Compd* 554:89–96.
- [26 ] Jahedi, M., 2013. Cold spray news from down under. In: V.Fridici et al. (Ed.), *Proceedings of 26th Int. Conf. on 'Surface modification technologies (SMT 26)'*, Écully, France. (ed. V.FRIDICI et al.); .
- [27] Binder K, Gottschalk J, Kollenda M, et al (2011) Influence of Impact Angle and Gas Temperature on Mechanical Properties of Titanium Cold Spray Deposits. *J Therm Spray Technol* 20:234–242.
- [28] Goldbaum D, Chromik RR, Brodusch N, Gauvin R (2015) Microstructure and Mechanical Properties of Ti Cold-Spray Splats Determined by Electron Channeling Contrast Imaging and Nanoindentation Mapping. *Microsc Microanal* 21:570–581.
- [29] Wong W, Rezaeian A, Yue S, Irissou E, Legoux J-G (2009) Effects of gas temperature, gas pressure, and particle characteristics on Cold Sprayed Pure titanium Coatings, in: *Proceedings of Thermal Spray: Expanding Thermal Spray Performance to New Markets and Applications*, United States.
- [30] Pattison J, Celotto S, Khan A, O'Neill W (2008) Standoff distance and bow shock phenomena in the Cold Spray process. *Surf Coat Technol* 202:1443–1454.
- [31] Li W-Y, Zhang C, Guo X, et al (2007) Study on impact fusion at particle interfaces and its effect on coating microstructure in cold spraying. *App Surf Sci* 254:517–526.
- [32] King, PC, MJahedi, M, 2010. Transmission electron microscopy of cold gas sprayed titanium, in: *Proceedings of Thermal Spray: Global Solutions for Future Application*, Singapore.

- 
- [33] Zhu KY, Vassel A, Brisset F, et al (2004) Nanostructure formation mechanism of  $\alpha$ -titanium using SMAT. *Acta Mater* 52:4101–4110.
- [34] Buser D, Schenk RK, Steinemann S, et al (1991) Influence of surface characteristics on bone integration of titanium implants. A histomorphometric study in miniature pigs. *J Biomed Mater Res* 25:889–902.
- [35] Becker W, Becker BE, Ricci A, et al (2000) A prospective multicenter clinical trial comparing one- and two-stage titanium screw-shaped fixtures with one-stage plasma-sprayed solid-screw fixtures. *Clin Implant Dent Relat Res* 2:159–165.
- [36] Wennerberg A, Hallgren C, Johansson C, Danelli S (1998) A histomorphometric evaluation of screw-shaped implants each prepared with two surface roughnesses. *Clin Oral Implants Res* 9:11–19.
- [37] Technical file specifications from: <http://www.terolabsurface.com/>. Accessed: 08 February 2014.
- [38] Brett P., Harle J, Salih V, et al (2004) Roughness response genes in osteoblasts. *Bone* 35:124–133.
- [39] Le Guéhennec L, Soueidan A, Layrolle P, Amouriq Y (2007) Surface treatments of titanium dental implants for rapid osseointegration. *Dental Mater* 23:844–854.
- [40] Citeau A, Guicheux J, Vinatier C, et al (2005) In vitro biological effects of titanium rough surface obtained by calcium phosphate grid blasting. *Biomater* 26:157–165.
- [41] Nishiguchi S, Nakamura T, Kobayashi M, et al (1999) The effect of heat treatment on bone-bonding ability of alkali-treated titanium. *Biomater* 20:491–500.
- [42] Zhao G, Zinger O, Schwartz Z, et al (2006) Osteoblast-like cells are sensitive to submicron-scale surface structure. *Clin Oral Implants Res* 17:258–264.
- [43] Zhao G, Raines A, Wieland M, et al (2007) Requirement for both micron- and submicron scale structure for synergistic responses of osteoblasts to substrate surface energy and topography. *Biomater* 28:2821–2829.

- 
- [44] Rønold HJ, Lyngstadaas SP, Ellingsen JE (2003) Analysing the optimal value for titanium implant roughness in bone attachment using a tensile test. *Biomater* 24:4559–4564.
- [45] Conforto E, Aronsson B-O, Salito A, et al (2004) Rough surfaces of titanium and titanium alloys for implants and prostheses. *Mater Sci Eng C* 24:611–618.
- [46] Lima RS, Kucuk A, Berndt CC, Karthikeyan J, Kay CM, Lindemann J. (2002) Deposition efficiency, mechanical properties and coating roughness in cold-sprayed titanium. *J Mater Sci Lett* 21:1687–9.
- [47] Choudhuri A, Mohanty PS, Karthikeyan J (2009) Bio-ceramic composite coatings by cold spray technology. In: *Proceedings of the International Thermal Spray Conference, United States*.
- [48] Yang YZ, Tian JM, Tian JT, Chen ZQ, Deng XJ, Zhang DH (2000) Preparation of graded porous titanium coatings on titanium implant materials by plasma spraying. *J Biomed Mater Res* 52:333–337
- [49] Lautenschlager, EP., Monaghan, P. (1993) Titanium and titanium alloys as dental materials. *Int Dent J* 43, 245-53.
- [50] Kang, BS., Sul, YT., Lee, HJ., Albrektsoon, T. (2009) XPS, AES and SEM analysis of recent dental implants. *Acta Biomater* 5, 2222-2229.
- [51] Diebold, U., Madey, TE., (1996) TiO<sub>2</sub> by XPS. *Surf Sci Spectra* 4, 227
- [52] Minagar S, Wang J, Berndt CC, et al (2013) Cell response of anodized nanotubes on titanium and titanium alloys: Cell Response of Anodized TITANIA Nanotubes. *J Biomed Mater Res A* 101A:2726–2739.
- [53] Law K-Y, Zhao H (2016) *Surface Wetting*. Springer International Publishing, Cham
- [54] Rupp F, Scheideler L, Rehbein D, et al (2004) Roughness induced dynamic changes of wettability of acid etched titanium implant modifications. *Biomater* 25:1429–1438.
- [55] Zhao L, Mei S, Chu PK, et al (2010) The influence of hierarchical hybrid micro/nano-textured titanium surface with titania nanotubes on osteoblast functions. *Biomater* 31:5072–5082.

---

[56] ASTM C-633-01 - Standard Test Method for Adhesion or Cohesion Strength of Thermal Spray Coatings.

[57] ASTM F 2068-05 Standard Specification for Femoral Prostheses— Metallic Implants

[58] ASTM F 2083-12 Standard Specification for Knee Replacement Prosthesis

[59] ASTM F 2083-12 Standard Specification for Shoulder Prosthesis

[60] Coating research and eveloping IT. VPS Titanium Coatings. [http://www.eurocoating.it/plasma\\_spray\\_coatings/vacuum\\_plasma\\_spray\\_titanium\\_coatings/default.aspx](http://www.eurocoating.it/plasma_spray_coatings/vacuum_plasma_spray_titanium_coatings/default.aspx) Accessed 22 March 2016

[61] Titanium Plasma Spray <https://www.exac.com/resource-library/hip/reference-papers/titanium-plasma-spray> file. Accessed 31 May 2016

[62] Gardon M, Concustell A, Dosta S, et al (2014) Improved bonding strength of bioactive cermet Cold Gas Spray coatings. *Mate Sci Eng C* 45:117–121.

[63] Sun J, Han Y, Cui K (2008) Innovative fabrication of porous titanium coating on titanium by cold spraying and vacuum sintering. *Mater Lett* 62:3623–3625.

[64] Li H, Khor KA, Cheang P (2007) Adhesive and bending failure of thermal sprayed hydroxyapatite coatings: Effect of nanostructures at interface and crack propagation phenomenon during bending. *Eng Fract Mech* 74:1894–1903.

[65] Li W-Y, Zhang C, Wang H-T, et al (2007) Significant influences of metal reactivity and oxide films at particle surfaces on coating microstructure in cold spraying. *App Surf Sci* 253:3557–3562.

[66] ASTM 1044-99 - Standard Test Method for Shear Testing of Calcium Phosphate Coatings and Metallic Coatings.

[67] Nishiguchi S, Kato H, Neo M, et al (2001) Alkali- and heat-treated porous titanium for orthopedic implants. *J Biomed Mater Res* 54:198–208.

---

[68] Aebli N, Krebs J, Stich H, et al (2003) In vivo comparison of the osseointegration of vacuum plasma sprayed titanium- and hydroxyapatite-coated implants. *J Biomed Mater Res* 66A:356–363.

[69] Qiu D, Zhang M, Grøndahl L (2013) A novel composite porous coating approach for bioactive titanium-based orthopedic implants. *J Biomed Mater Res A* 101A:862–872.

[70] ASTM 1978-00 - Standard Test Method for Measuring Abrasion Resistance of Metallic Thermal Spray Coatings by Using the Taber Abraser.

[71] Kennedy D, Hashmi MS (1998) Methods of wear testing for advanced surface coatings and bulk materials. *J Mater Process Technol* 77:246–253.

[72] Theeratatpong K., Danchaivijit, S, Boonyongmaneerat, Y (2013) Comparison of ball-on-disc and Taber wear tests in assessing wear performance of electrolessly-deposited alloys. *J Metals Mater Miner* 23:75-79.

[73] McKellop HA, Hart A, Park S-H, et al (2014) A lexicon for wear of metal-on-metal hip prostheses: Metal-on-metal wear Lexicon. *J Orthopaedic Res* 32:1221–1233.

[74] Jäger M, Zilkens C, Zanger K, Krauspe R (2007) Significance of Nano- and Microtopography for Cell-Surface Interactions in Orthopaedic Implants. *J Biomed Biotechnol* 2007:1–19.

[75] Jayaraman M, Meyer U, Bühner M, et al (2004) Influence of titanium surfaces on attachment of osteoblast-like cells in vitro. *Biomater* 25:625–631.

[76] Zhang R, Wan Y, Ai X, et al (2016) Fabrication of micro/nano-textured titanium alloy implant surface and its influence on hydroxyapatite coatings. *Journal of Wuhan University of Technology-Mater Sci Ed* 31:440–445.

[77] Orsini G, Assenza B, Scarano A, et al (2000) Surface analysis of machined versus sandblasted and acid-etched titanium implants. *Int J Oral Maxillofac Implants* 15:779–784.

[78] Kulkarni M, Mazare A, Schmuki, Iglič A, (2014) Biomaterial surface modification of titanium and titanium alloys for medical applications In book: *Nanomedicine, Chapter: Biomaterial Surface Modification Of Titanium and Titanium Alloys for Medical Applications*,

---

Publisher: One Central Press, Editors: Alexander Seifalian, Achala de Mel, Deepak M. Kalaskar, pp.111-136

[79] Wei M, Kim H-M, Kokubo T, Evans JH (2002) Optimising the bioactivity of alkaline-treated titanium alloy. *Mater Sci Eng C* 20:125–134.

[80] Sykaras N, Iacopino AM, Marker VA, et al (2000) Implant materials, designs, and surface topographies: their effect on osseointegration. A literature review. *Int J Oral Maxillofac Implants* 15:675–690.

[81] Ghicov A, Schmuki P (2009) Self-ordering electrochemistry: a review on growth and functionality of TiO<sub>2</sub> nanotubes and other self-aligned MO<sub>x</sub> structures. *Chem Comm* 2791.

[82] Taveira LV, Macák JM, Tsuchiya H, et al (2005) Initiation and Growth of Self-Organized TiO<sub>2</sub> Nanotubes Anodically Formed in NH<sub>4</sub>F/(NH<sub>4</sub>)<sub>2</sub>SO<sub>4</sub> Electrolytes. *J Electrochem Soc* 152:B405.

[83] Pacheco, I. (2015). Study of the Titanium anodization process to produce biocompatible surfaces. Universitat de Barcelona, 1-47.

[84] Santiveri, C. (2016). Anodizing of titanium coatings with different roughnesses, 1-67.

[85] Ghicov A, Tsuchiya H, Macak JM, Schmuki P (2005) Titanium oxide nanotubes prepared in phosphate electrolytes. *Electrochem Commun* 7:505–509.

[86] Xie Y, Ao H, Xin S, et al (2014) Enhanced cellular responses to titanium coating with hierarchical hybrid structure. *Mater Sci Eng C* 38:272–277.

[87] Tian T, Dong H, Tian X, Hao Y (2013) Fabricated Antibacterial and Bioactive Titania Nanotube Arrays Coating on the Surface of Titanium. *OJSST* 3:59–62.

[88] Lorenzetti M, Dogša I, Stošicki T, et al (2015) The Influence of Surface Modification on Bacterial Adhesion to Titanium-Based Substrates. *ACS APPL MATER INTER* 7:1644–1651.

[89] Bose S, Banerjee D, Robertson S, et al (2015) Drug Delivery From Surface Modified Titanium Alloy for Load-Bearing Implants. In: Narayan R, Bose S, Bandyopadhyay A (eds)

---

Biomaterials Science: Processing, Properties, and Applications V. John Wiley & Sons, Inc., Hoboken, NJ, USA, pp 129–136

[90] Losic D, Aw MS, Santos A, et al (2015) Titania nanotube arrays for local drug delivery: recent advances and perspectives. *Expert Opin Drug Deliv* 12:103–127.

[91] Verket A, Tiainen H, Haugen HJ, et al (2012) Enhanced Osteoblast Differentiation on Scaffolds Coated with TiO<sub>2</sub> Compared to SiO<sub>2</sub> and CaP Coatings. *Biointerphases* 7:1–10.

[92] Oh S, Daraio C, Chen L-H, et al (2006) Significantly accelerated osteoblast cell growth on aligned TiO<sub>2</sub> nanotubes. *J Biomed Mater Res A* 78A:97–103.

[93] Liu X, Chub PK, Ding C (2004) Surface modification of titanium, titanium alloys, and related materials for biomedical Applications. *Mater Sci Eng R* 47:49–121

[94] Mor GK, Varghese OK, Paulose M, et al (2006) A review on highly ordered, vertically oriented TiO<sub>2</sub> nanotube arrays: Fabrication, material properties, and solar energy applications. *Sol Energ Mat Sol* 90:2011–2075.

[95] Zhang S (2011) Biological and biomedical coatings handbook. CRC Press, Boca Raton, FL

[96] Regonini D, Jaroenworuluck A, Stevens R, Bowen CR (2010) Effect of heat treatment on the properties and structure of TiO<sub>2</sub> nanotubes: phase composition and chemical composition. *Surf Interface Anal* 42:139–144.

[97] Regonini D, Bowen CR, Jaroenworuluck A, Stevens R (2013) A review of growth mechanism, structure and crystallinity of anodized TiO<sub>2</sub> nanotubes. *Mat Sci Eng R* 74:377–406.

[98] Brammer KS, Oh S, Cobb CJ, et al (2009) Improved bone-forming functionality on diameter-controlled TiO<sub>2</sub> nanotube surface. *Acta Biomater* 5:3215–3223.

[99] Groth T, Altankov G (1996) Studies on cell-biomaterial interaction: role of tyrosine phosphorylation during fibroblast spreading on surfaces varying in wettability. *Biomater* 17:1227–1234.

---

[100] Faucheux N, Schweiss R, Lützow K, et al (2004) Self-assembled monolayers with different terminating groups as model substrates for cell adhesion studies. *Biomater* 25:2721–2730.

[101] Ikada Y (1994) Surface modification of polymers for medical applications. *Biomater* 15:725–736.

[102] Xu Z, Lai Y, Wu D, et al (2015) Increased Mesenchymal Stem Cell Response and Decreased *Staphylococcus aureus* Adhesion on Titania Nanotubes without Pharmaceuticals. *BioMed Res Inter* 2015:1–9.

[103] Tugulu S, Löwe K, Scharnweber D, Schlottig F (2010) Preparation of superhydrophilic microrough titanium implant surfaces by alkali treatment. *J Mater Sci Mater Med* 21:2751–2763.

[104] Kokubo T, Miyaji F, Kim H-M, Nakamura T (1996) Spontaneous Formation of Bone-like Apatite Layer on Chemically Treated Titanium Metals. *J Am Ceram Soc* 79:1127–1129.

[105] Kim H-M, Miyaji F, Kokubo T, Nakamura T (1997) Apatite-Forming Ability of Alkali-Treated Ti Metal in Body Environment. *J Ceram Soc Jpn* 105:111–116.

[106] Melero H, Garcia-Giralt N, Fernández J, et al (2014) Comparison of in vitro behavior of as-sprayed, alkaline-treated and collagen-treated bioceramic coatings obtained by high velocity oxy-fuel spray. *Appl Surf Sci* 307:246–254.

[107] Xue W, Liu X, Zheng X, Ding C (2005) In vivo evaluation of plasma-sprayed titanium coating after alkali modification. *Biomater* 26:3029–3037.

[108] Ha SW, Eckert KL, Wintermantel E, et al (1997) NaOH treatment of vacuum-plasma-sprayed titanium on carbon fibre-reinforced poly(etheretherketone). *J Mater Sci Mater Med* 8:881–886.

[109] Liang F, Zhou L, Wang K (2003) Apatite formation on porous titanium by alkali and heat-treatment. *Surf Coat Technol* 165:133–139.

- 
- [110] Liu X, Chu P, Ding C (2004) Surface modification of titanium, titanium alloys, and related materials for biomedical applications. *Mater Sci Eng R* 47:49–121.
- [111] T. Kokubo, H. M. Kim, M. Kawashita (2003) Novel bioactive materials with different mechanical properties. *Biomater*, 24 2161-2175
- [112] Gil FJ, Planell JA (2000) Behaviour of normal grain growth kinetics in single phase titanium and titanium alloys. *Mater Sci Eng A* 283:17–24.
- [113] Tsuji H, Ishida T, Fukuda N (2003) Surface hydrophilicity and enzymatic hydrolyzability of biodegradable polyesters: 1. effects of alkaline treatment. *Polym Int* 52:843–852.
- [114] Lim YJ, Oshida Y, Andres CJ, Barco MT (2001) Surface characterizations of variously treated titanium materials. *Int J Oral Maxillofac Implants* 16:333–342.
- [115] Chun D-M, Ahn S-H (2011) Deposition mechanism of dry sprayed ceramic particles at room temperature using a nano-particle deposition system. *Acta Mater* 59:2693–2703.
- [116] Chun D-M, Choi J-O, Lee CS, Ahn S-H (2012) Effect of stand-off distance for cold gas spraying of fine ceramic particles (<math>\leq 5\mu\text{m}</math>) under low vacuum and room temperature using nano-particle deposition system (NPDS). *Surf Coat Technol* 206:2125–2132.
- [117] Akedo J (2006) Aerosol Deposition of Ceramic Thick Films at Room Temperature: Densification Mechanism of Ceramic Layers. *J Am Ceram Soc* 89:1834–1839.
- [118] Akedo J (2008) Room Temperature Impact Consolidation (RTIC) of Fine Ceramic Powder by Aerosol Deposition Method and Applications to Microdevices. *J Therm Spray Technol* 17:181–198.
- [119] Miyoshi T (2008) Preparation of Full-Dense  $\text{Pb}(\text{Zr,Ti})\text{O}_3$  Ceramics by Aerosol Deposition. *J Am Ceram Soc* 91:2098–2104.
- [120] Hahn B-D, Park D-S, Choi J-J, et al (2009) Dense Nanostructured Hydroxyapatite Coating on Titanium by Aerosol Deposition. *J Am Ceram Soc* 92:683–687.
- [121] Park D-S, Kim I-S, Kim H, et al (2010) Improved biocompatibility of hydroxyapatite thin film prepared by aerosol deposition. *J Biomed Mater Res B: Appl Biomater* n/a-n/a.

- 
- [122] Park H, Cao F, Kwon J, Lee C (2013) The Effect of Shock-Induced Plastic Deformation on Alumina Deposition During Vacuum Kinetic Spraying, in Thermal Spray 2013: Proceedings of the International Thermal Spray Conference, Busan, South Korea
- [123] Lee D-W, Kim H-J, Kim Y-H, et al (2011) Growth Process of  $\alpha$ -Al<sub>2</sub>O<sub>3</sub> Ceramic Films on Metal Substrates Fabricated at Room Temperature by Aerosol Deposition: Growth Process of  $\alpha$ -Al<sub>2</sub>O<sub>3</sub> Ceramic Films on Metal Substrates. *J Am Ceram Soc* 94:3131–3138.
- [124] Yamada M, Isago H, Shima K, Nakano H, Fukumoto M (2010) Deposition of TiO<sub>2</sub> Ceramic Particles on Cold Spray Process, in Thermal Spray 2010: Proceedings of the International Thermal Spray Conference , Singapore
- [125] Seo D, Sayar M, Ogawa K (2012) SiO<sub>2</sub> and MoSi<sub>2</sub> formation on Inconel 625 surface via SiC coating deposited by cold spray. *Surf Coat Technol* 206:2851–2858.
- [126] Kliemann J-O, Gutzmann H, Gärtner F, et al (2011) Formation of Cold-Sprayed Ceramic Titanium Dioxide Layers on Metal Surfaces. *J Therm Spray Technol* 20:292–298.
- [127] Chen MW, McCauley JW, Dandekar DP, Bourne NK (2006) Dynamic plasticity and failure of high-purity alumina under shock loading. *Nature Mater* 5:614–618.
- [128] Longy F, Cagnoux J (1989) Plate-Impact Recovery Experiments of Ceramics, in *APS Proc- Shock Waves in Condensed Matter*, Edited by S.C. Schmidt, J. N. Johnson, and L. W. Davison. Elsevier
- [129] Vilardell AM, Cinca N, Dosta S, Cano IG, Guilemany JM (2015) Multifunctional Micro-Nano Structured Hydroxyapatite Coatings on Titanium Ti6Al4V for Biomedical Applications by Cold Gas Spray. *Acta. de Protocolarización num.*, ???, 809
- [130] El Bied A, Sulem J, Martineau F (2002) Microstructure of shear zones in Fontainebleau sandstone. *J Rock Mech Min Sci* 39:917–932.
- [131] Du Bernard X, Eichhubl P, Aydin A (2002) Dilation bands: A new form of localized failure in granular media: DILATION BANDS. *Geophys Res Lett* 29:29-1-29–4.

---

[132] Curran DR, Seaman L, Cooper T, Shockey DA (1993) Micromechanical model for comminution and granular flow of brittle material under high strain rate application to penetration of ceramic targets. *I J Impact Eng* 13:53–83.

[133] He L-H, Standard OC, Huang TTY, et al (2008) Mechanical behaviour of porous hydroxyapatite. *Acta Biomater* 4:577–586.

[134] Ivchenko NV, Kuznetsov RI, Beresnev BB (1986) Effect of Hydrostatic Pressure on the Recrystallization of CsJ(T1) Crystals. *Fiz Tekh Vysokikh Davlenii*, 21, 30–7

[135] Singh RP, Batra B (2013) Effect of Cold Spraying Parameters and Their Interaction and Hydroxyapatite Deposition. *J Appl Fluid Mech* 6, 555–61

[136] Kim K, Watanabe M, Kuroda S (2009) Jetting-Out Phenomenon Associated with Bonding of Warm-Sprayed Titanium Particles onto Steel Substrate. *J Therm Spray Technol* 18:490–499.

[137] Cinca N, Vilardell AM, Dosta S, et al (2016) A New Alternative for Obtaining Nanocrystalline Bioactive Coatings: Study of Hydroxyapatite Deposition Mechanisms by Cold Gas Spraying. *J Am Ceram Soc* 99:1420–1428.

[138] Yao H-L, Yang G-J, Fan S-Q, et al (2015) Ceramic Nano-particle/Substrate Interface Bonding Formation Derived from Dynamic Mechanical Force at Room Temperature: HRTEM Examination. *J Therm Spray Technol* 24:720–728.

[139] Syed MA, Hutt NJ, Shah N, Edge AJ (2015) Hydroxyapatite ceramic-coated femoral components in young patients followed up for 17 to 25 years: an update of a previous report. *Bone & Jt J* 97–B:749–754.

[140] Gadow R, Killinger A, Stiegler N (2010) Hydroxyapatite coatings for biomedical applications deposited by different thermal spray techniques. *Surf Coat Technol* 205:1157–1164.

[141] Ferraz MP, Monteiro FJ, Serro AP, et al (2001) Effect of chemical composition on hydrophobicity and zeta potential of plasma sprayed HA/CaO-P2O5 glass coatings. *Biomateri* 22:3105–3112.

- 
- [142] Lopes MA, Monteiro FJ, Santos JD, Serro AP, Saramago B (1999) Hydrophobicity, surface tension, and zeta potential measurements of glass-reinforced hydroxyapatite composites. *J Biomed Mater Res* 45:370-5
- [143] Mamalis A, Vottea I, Manolakos D (2001) On the modelling of the compaction mechanism of shock compacted powders. *J Mater Process Tech* 108:165–178.
- [144] Schmidt T, Assadi H, Gärtner F, et al (2009) From Particle Acceleration to Impact and Bonding in Cold Spraying. *J Therm Spray Technol* 18:794–808.
- [145] Dewar MP, McDonald AG, Gerlich AP (2012) Interfacial heating during low-pressure cold-gas dynamic spraying of aluminum coatings. *J Mater Sci* 47:184–198.
- [146] Roland T, Pelletier H, Krier J (2013) Scratch resistance and electrochemical corrosion behavior of hydroxyapatite coatings on Ti6Al4V in simulated physiological media. *J Appl Electrochem* 43:53–63.
- [147] Łatka L, Pawlowski L, Chicot D, et al (2010) Mechanical properties of suspension plasma sprayed hydroxyapatite coatings submitted to simulated body fluid. *Surf Coat Technol* 205:954–960.
- [148] Cui, F.Z., Luo, Z.S., & Feng, Q. L. (1997). Highly adhesive hydroxyapatite coatings on titanium alloy formed by ion beam assisted deposition. *J Mater Sci: Mater Med*, 8: 403-5.
- [149] Fernández-Pradas JM, Cléries L, Martínez E, et al (2001) Influence of thickness on the properties of hydroxyapatite coatings deposited by KrF laser ablation. *Biomater* 22:2171–2175.
- [150] Champagne VK, *The cold spray materials deposition process: fundamentals and applications*, Woodhead; CRC Press, Cambridge: Boca Raton, 2007. <http://search.library.wisc.edu/catalog/ocn163617979>.
- [151] Fan S-Q, Yang G-J, Li C-J, et al (2006) Characterization of Microstructure of Nano-TiO<sub>2</sub> Coating Deposited by Vacuum Cold Spraying. *J Therm Spray Technol* 15:513–517.

---

[152] Kim M-S, Chun D-M, Choi J-O, et al (2011) Room temperature deposition of TiO<sub>2</sub> using nano particle deposition system (NPDS): Application to dye-sensitized solar cell (DSSC). *IJPEM* 12:749–752.

[153] Kergourlay E, Grossin D, Cinca N, et al (2016) First Cold Spraying of Carbonated Biomimetic Nanocrystalline Apatite on Ti6Al4V: Physical-Chemical, Microstructural, and Preliminary Mechanical Characterizations: First Cold Spraying of Carbonated Biomimetic Nanocrystalline. *Adv Eng Mater* 18:496–500.

[154] Yamada M, Isago H, Shima K, Nakano H and Fukumoto M, Toyohashi J (2010) Deposition of TiO<sub>2</sub> Ceramic Particles on Cold Spray Process. *Proceedings of the International Thermal Spray Conference, Singapore*, 342-347.

[155] Landi E, Tampieri A, Celotti G, Sprio S (2000) Densification behaviour and mechanisms of synthetic hydroxyapatites. *J Euro Ceram Soc* 20:2377–2387.

[156] Cacciotti I, Bianco A, Lombardi M, Montanaro L (2009) Mg-substituted hydroxyapatite nanopowders: Synthesis, thermal stability and sintering behaviour. *J Euro Ceram Soc* 29:2969–2978.

[157] Gross KA, Gross V, Berndt CC (2005) Thermal Analysis of Amorphous Phases in Hydroxyapatite Coatings. *J Am Ceram Soc* 81:106–112.

[158] Sōmiya S (2013) *Handbook of advanced ceramics: materials, applications, processing, and properties*, Second edition. Academic Press, imprint of Elsevier, Amsterdam ; Boston

[159] Biocollagen technologies: <http://www.bio-coll.com/products.php?action=more&id=4>  
Accessed: 06 July 2016

[160] Basic-healthcare healthy foundation: <http://www.b-ostin.com/basic-healthcare-biomaterials.htm> Accessed: 06 July 2016

[161] ExacTECH company: <https://www.exac.com/products/biologics/ossigen-collagen-composite> Accessed: 06 July 2016

[162] Bauer S, Schmuki P, von der Mark K, Park J (2013) Engineering biocompatible implant surfaces. *Progress in Mater Sci* 58:261–326.

- 
- [163] Elias CN, Lima JHC, Valiev R, Meyers MA (2008) Biomedical applications of titanium and its alloys. *JOM* 60:46–49.
- [164] Pramanik S, Agarwal AK, Rai KN (2005) Chronology of Total Hip Joint Replacement and Materials Development. *Trends Biomater, Artif. Organs*. 19 15-26.
- [165] Mjöberg B (1994) Theories of wear and loosening in hip prostheses. Wear-induced loosening vs loosening-induced wear--a review. *Acta Orthop Scand* 65:361–371.
- [166] Rupp F, Scheideler L, Olshanska N, et al (2006) Enhancing surface free energy and hydrophilicity through chemical modification of microstructured titanium implant surfaces. *J Biomed Mater Res A* 76A:323–334.
- [167] Gnedenkov SV, Sinebryukhov SL, Egorkin VS, et al (2011) Wetting and electrochemical properties of hydrophobic and superhydrophobic coatings on titanium. *Colloids Surf A: Physicochem Eng Asp* 383:61–66.
- [168] Mekayarajjananonth T, Winkler S (1999) Contact angle measurement on dental implant biomaterials. *J Oral Implantol* 25:230–236.
- [169] Hotchkiss KM, Reddy GB, Hyzy SL, et al (2016) Titanium surface characteristics, including topography and wettability, alter macrophage activation. *Acta Biomater* 31:425–434.
- [170] Borsari V, Giavaresi G, Fini M, et al (2005) Comparative in vitro study on a ultra-high roughness and dense titanium coating. *Biomater* 26:4948–4955.
- [171] Boyan BD, Bonewald LF, Paschalis EP, et al (2002) Osteoblast-Mediated Mineral Deposition in Culture is Dependent on Surface Microtopography. *Calcif Tissue Int* 71:519–529.
- [172] Endres S, Wilke M, Knöll P, et al (2008) Correlation of in vitro and in vivo results of vacuum plasma sprayed titanium implants with different surface topography. *J Mater Sci: Mater Med* 19:1117–1125.
- [173] Wennerberg A, Albrektsson T (2009) Effects of titanium surface topography on bone integration: a systematic review. *Clin Oral Implants Res* 20:172–184.

- 
- [174] Alla RK, Ginjupalli K, Upadhya N, et al (2011) Surface Roughness of Implants: A Review. *Trends Biomater. Artif. Organs*, 25(3), 112-118
- [175] Wu Y, Zitelli JP, TenHuisen KS, et al (2011) Differential response of Staphylococci and osteoblasts to varying titanium surface roughness. *Biomater* 32:951–960.
- [176] Frauchiger VM, Eitel F, Tommasin R, Jaeggi C, Wippich T, Jaeggi S. An Open-Porous Titanium Coating for Advanced Osseointegration. 55th Annual Meeting of the Orthopaedic Research Society
- [177] Pachauri P, Bathala LR, Sangur R (2014) Techniques for dental implant nanosurface modifications. *J Adv Prosthodont* 6:498.
- [178] Rosales-Leal JI, Rodríguez-Valverde MA, Mazzaglia G, et al (2010) Effect of roughness, wettability and morphology of engineered titanium surfaces on osteoblast-like cell adhesion. *Colloids Surf A: Physicochem Eng Asp* 365:222–229.
- [179] Adamson AW, Gast AP (1997) *Physical chemistry of surfaces*, 6th ed. Wiley, New York
- [180] Janssen MI, van Leeuwen MBM, van Kooten TG, et al (2004) Promotion of fibroblast activity by coating with hydrophobins in the beta-sheet end state. *Biomater* 25:2731–2739.
- [181] Feng B, Weng J, Yang BC, et al (2003) Characterization of surface oxide films on titanium and adhesion of osteoblast. *Biomater* 24:4663–4670
- [182] Influence of topography and wettability on biocompatibility
- [183] E. Mariscal-Muñoz, C.A.S. Costa, H.S. Tavares, J. Bianchi, J. Hebling, J.P.B. Machado, U.H. Lerner, P.P.C. Souza, Osteoblast differentiation is enhanced by a nano-to-micro hybrid titanium surface created by Yb:YAG laser irradiation, *Clin Oral Investig.* 20 (2016) 503–511.
- [184] Mendonça DBS, Miguez PA, Mendonça G, et al (2011) Titanium surface topography affects collagen biosynthesis of adherent cells. *Bone* 49:463–472.
- [185] Wang T, Wan Y, Liu Z (2016) Fabrication of hierarchical micro/nanotopography on bio-titanium alloy surface for cytocompatibility improvement. *J Mater Sci* 51:9551–9561.

- 
- [186] Streicher RM, Schmidt M, Fiorito S (2007) Nanosurfaces and nanostructures for artificial orthopedic implants. *Nanomed* 2:861–874.
- [187] Siegel RW: Creating nanophase materials. *Sci. Am.* 275, 42–47 (1996). 49.
- [188] Klabunde KJ, Stark J, Koper O, et al (1996) Nanocrystals as Stoichiometric Reagents with Unique Surface Chemistry. *J Phys Chem* 100:12142–12153.
- [189] Davies J, “The Importance and Measurement of Surface Charge Species in Cell Behaviour Interface,” In B. D. Ratner, Ed., *Surface Characterization of Biomaterials*, Elsevier, New York, 1988, pp. 219-234.
- [190] Daugaard H, Elmengaard B, Bechtold JE, Soballe K: The effect of dual acid texturing implants on bone ongrowth – an unloaded implant model in an experimental canine study. 52nd Annual Meeting of the Orthopaedic Research Society
- [191] Wang XP, Yu Y, Hu XF, Gao Lian (2000) Hydrophilicity of TiO<sub>2</sub> films prepared by liquid phase deposition. *Thin Solid Films* 371:148–152.
- [192] Xiao J, Zhou H, Zhao L, et al (2011) The effect of hierarchical micro/nanosurface titanium implant on osseointegration in ovariectomized sheep. *Osteoporosis Int* 22:1907–1913.
- [193] Fawzy AS, El-Askary FS (2009) Effect acidic and alkaline/heat treatments on the bond strength of different luting cements to commercially pure titanium. *J Dent* 37:255–263.
- [194] Park J, Bauer S, von der Mark K, Schmuki P (2007) Nanosize and Vitality: TiO<sub>2</sub> Nanotube Diameter Directs Cell Fate. *Nano Letters* 7:1686–1691.
- [195] Wang N, Li H, Lü W, et al (2011) Effects of TiO<sub>2</sub> nanotubes with different diameters on gene expression and osseointegration of implants in minipigs. *Biomater* 32:6900–6911.
- [196] Ercan B, Taylor E, Alpaslan E, Webster TJ (2011) Diameter of titanium nanotubes influences anti-bacterial efficacy. *Nanotechnology* 22:295102.
- [197] Narendrakumar K, Kulkarni M, Addison O, et al (2015) Adherence of oral streptococci to nanostructured titanium surfaces. *Dental Mater* 31:1460–1468.

---

[198] Puckett S, Pareta R, Webster TJ (2008) Nano rough micron patterned titanium for directing osteoblast morphology and adhesion. *Int J Nanomedicine* 3:229–241.

[199] Hansen JC, Yul Lim J, Xu L-C, et al (2007) Effect of surface nanoscale topography on elastic modulus of individual osteoblastic cells as determined by atomic force microscopy. *J Biomech* 40:2865–2871.

[200] Mucalo M (2015) Hydroxyapatite (HAp) for biomedical applications. Elsevier/Woodhead Publishing, Woodhead Publishing is an imprint of Elsevier, Amsterdam ; Boston

[201] Mobasherpour I, Heshajin MS, Kazemzadeh A, Zakeri M (2007) Synthesis of nanocrystalline hydroxyapatite by using precipitation method. *J Alloy Compd* 430:330–333.

[202] Webster T (2000) Enhanced functions of osteoblasts on nanophase ceramics. *Biomater* 21:1803–1810.

[203] Jeon H, Simon CG, Kim G (2014) A mini-review: Cell response to microscale, nanoscale, and hierarchical patterning of surface structure: A Mini-Review. *Journal of Biomedical Materials Research Part B: Appl Biomater* 102:1580–1594.

[204] Le Guehenec L, Lopez-Heredia M-A, Enkel B, et al (2008) Osteoblastic cell behaviour on different titanium implant surfaces. *Acta Biomater* 4:535–543.

[205] Khang D, Lu J, Yao C, et al (2008) The role of nanometer and sub-micron surface features on vascular and bone cell adhesion on titanium. *Biomater* 29:970–983.

[206] Redey SA, Razzouk S, Rey C, et al (1999) Osteoclast adhesion and activity on synthetic hydroxyapatite, carbonated hydroxyapatite, and natural calcium carbonate: relationship to surface energies. *J Biomed Mater Res* 45:140–147.

[207] Redey SA, Nardin M, Bernache-Assolant D, et al (2000) Behavior of human osteoblastic cells on stoichiometric hydroxyapatite and type A carbonate apatite: role of surface energy. *J Biomed Mater Res* 50:353–364.

[208] Sun L, Berndt CC, Gross KA, Kucuk A (2001) Material fundamentals and clinical performance of plasma-sprayed hydroxyapatite coatings: A review. *J Biomed Mater Res* 58:570–592.

---

[209] Gittens RA, McLachlan T, Olivares-Navarrete R, et al (2011) The effects of combined micron-/submicron-scale surface roughness and nanoscale features on cell proliferation and differentiation. *Biomater* 32:3395–3403.

[210] Olivares-Navarrete R, Hyzy SL, Gittens RA, et al (2013) Rough titanium alloys regulate osteoblast production of angiogenic factors. *Spine J* 13:1563–1570.

[211] Tsui YC, Doyle C, Clyne T. (1998) Plasma sprayed hydroxyapatite coatings on titanium substrates Part 2: optimisation of coating properties. *Biomater* 19:2031–2043.

[212] Hahn, B.-D., Park, D.-S., Choi, J.-J., Ryu, J., Yoon, W.-H., Kim, K.-H., Park, C. and Kim, H.-E. (2009), Dense Nanostructured Hydroxyapatite Coating on Titanium by Aerosol Deposition. *J Am Ceram Soc*, 92: 683–687.

[213] Hahn B-D, Park D-S, Choi J-J, et al (2011) Preparation and in vitro characterization of aerosol-deposited hydroxyapatite coatings with different surface roughnesses. *Appl Surf Sci* 257:7792–7799.

[214] Vilardell AM, Cinca N, Concustell A, et al (2015) Cold spray as an emerging technology for biocompatible and antibacterial coatings: state of art. *J Mater Sci* 50:4441–4462.

[215] Gaona M (2007) Recubrimientos biocompatibles obtenidos por Proyección Térmica y estudio in vitro de la función osteoblástica. PhD thesis. Universitat de Barcelona

[216] Li H, Khor KA, Chow V, Cheang P (2007) Nanostructural characteristics, mechanical properties, and osteoblast response of spark plasma sintered hydroxyapatite. *J Biomed Mater Res A* 82A:296–303.

[217] Chou L, Marek B, Wagner WR (1999) Effects of hydroxylapatite coating crystallinity on biosolubility, cell attachment efficiency and proliferation in vitro. *Biomater* 20:977–985.

[218] Maxian SH, Di Stefano T, Melican MC, et al (1998) Bone cell behavior on Matrigel-coated Ca/P coatings of varying crystallinities. *J Biomed Mater Res* 40:171–179.

[219] Ferraz MP, Fernandes MH, Santos JD, Monteiro FJ (2001) HA and double-layer HA-P2O5/CaO glass coatings: influence of chemical composition on human bone marrow cells osteoblastic behavior. *J Mater Sci Mater Med* 12:629–638.

- 
- [220] MacDonald DE, Betts F, Stranick M, et al (2001) Physicochemical study of plasma-sprayed hydroxyapatite-coated implants in humans. *J Biomed Mater Res* 54:480–490.
- [221] Hu Q, Tan Z, Liu Y, et al (2007) Effect of crystallinity of calcium phosphate nanoparticles on adhesion, proliferation, and differentiation of bone marrow mesenchymal stem cells. *J Mater Chem* 17:4690.
- [222] Granqvist, N (2014) Biomimetic Interfaces for Surface Sensitive Drug Discovery Techniques. PhD thesis. University of Helsinki.
- [223] Schasfoort RBM, Tudos AJ (2008) Handbook of Surface Plasmon Resonance. Royal Society of Chemistry, Cambridge.
- [224] Canovi M, Lucchetti J, Stravalaci M, et al (2012) Applications of surface plasmon resonance (SPR) for the characterization of nanoparticles developed for biomedical purposes. *Sensors (Basel)* 12:16420–16432.
- [225] Kausaite A, Ramanaviciene A, Mostovojus V, Ramanavicius A (2007) Surface plasmon resonance and its application to biomedical research. *Medicina (Kaunas)* 43:355–365.
- [226] Etayash H, Jiang K, Azmi S, et al (2015) Real-time Detection of Breast Cancer Cells Using Peptide-functionalized Microcantilever Arrays. *Scientific Reports* 5:13967.
- [227] Orelma H, Filpponen I, Johansson L-S, et al (2011) Modification of Cellulose Films by Adsorption of CMC and Chitosan for Controlled Attachment of Biomolecules. *Biomacromolecules* 12:4311–4318.
- [228] Nishiguchi A, Matsusaki M, Akashi M (2015) Structural and Viscoelastic Properties of Layer-by-Layer Extracellular Matrix (ECM) Nanofilms and Their Interactions with Living Cells. *ACS Biomaterials Science & Engineering* 1:816–824.
- [229] Meininger M, Schmitz T, Wagner T, et al (2016) Real-time measurement of protein adsorption on electrophoretically deposited hydroxyapatite coatings and magnetron sputtered metallic films using the surface acoustic wave technique. *Mater Sci Eng C* 61:351–354.

---

[230] Monkawa A, Ikoma T, Yunoki S, et al (2006) Fabrication of hydroxyapatite ultra-thin layer on gold surface and its application for quartz crystal microbalance technique. *Biomater* 27:5748–5754.

[231] Ikoma T, Tagaya M, Hanagata N, et al (2009) Protein Adsorption on Hydroxyapatite Nanosensors with Different Crystal Sizes Studied In Situ by a Quartz Crystal Microbalance with the Dissipation Method. *J Am Ceram Soc* 92:1125–1128.

# CHAPTER 5

## *Conclusions*

---



In the present thesis, titanium and hydroxyapatite coatings have been obtained by means of cold spray (CS) providing their performance and in-vitro feasibility, as well as the production of nanotextured treatments onto such titanium coatings.

With regard to the highly titanium coatings:

1. The CS process has been employed to obtain highly rough porous pure titanium (CP-Ti) coatings with irregular and coarse powders, which may be competitive with current VPS commercial coatings in a more cost effective and environmental friendly manner. The optimization of the spraying parameters has allowed obtaining a coating free of oxidation in comparison with conventional thermal spray techniques, and with inner porosity suitable for biomedical applications.
2. The as-sprayed highly rough porous CP-Ti coatings show a good interparticle and coating-substrate bonding. The internal structure preserves the nanocrystalline features already observed in the feedstock. The porous structure is formed by particle bonding at local points where metallurgical contacts are produced. At those points, the bonding is most probably produced by adiabatic shear instabilities, this is when thermal softening dominates over work hardening during lateral flow upon impact at high strain rates; this process is highly localized at the interfaces.
3. The top surface particles show less plastic deformation in comparison with the first ones to arrive, but provide high roughness. On the other hand, the fracture surface of CP-Ti shows that it failed at particle-particle interface through descohesion.
4. The optimal highly rough porous CP-Ti coating overcomes the mechanical requirements with ASTM standard specifications for hip, knee and joint replacements. The mechanical values result in a tensile strength of  $40\pm 5\text{MPa}$  ( $>20\text{MPa}$ ), a shear strength of  $39\pm 2\text{MPa}$  ( $>20\text{MPa}$ ) and a weight loss of  $37\pm 5$  ( $<65\text{mg}/100\text{cycles}$ ).
5. All CP-Ti coatings show high roughness profile with  $R_a = 27\text{-}40\ \mu\text{m}$  and  $R_z = 160\text{-}235\ \mu\text{m}$ . However, in all cases, the spraying conditions did not much affect on  $R_a$  and  $R_z$  roughness values. The selection of an optimum was based on the tensile strength

values ( $40\pm 5$  MPa), with a  $R_a=40\pm 12$   $\mu\text{m}$  and  $R_z=235\pm 44$   $\mu\text{m}$ . Moreover, the surface area was increased x2.7 times in comparison with #240 grinded surface.

6. The high CS CP-Ti roughness leads to superhydrophilic ( $0^\circ$ ) behavior in comparison with #240 grinded surface and sand blasted (SB) surface.

With regard to the nanotextured surface treatments on cold gas titanium coatings:

7. The anodic oxidation treatment has been successfully applied onto the obtained optimal highly rough CS CP-Ti coating (not just on smooth titanium foils as it is reported in the literature), leading to the formation of a layer of amorphous  $\text{TiO}_2$  nanotubes with a mean diameter between 50-100 nm, leading to a nanoroughness of  $R_a=36.8\pm 4.6$  nm.
8. An alkaline treatment can be reproduced onto the as-sprayed CS CP-Ti coating as well, with a smaller nanoroughness than that with the anodizing treatment, e.g.  $1.2\pm 0.2$  nm.
9. Both nanostructured surface treatments show superhydrophilic ( $0^\circ$ ) surface behavior due to the high roughness of the CP-Ti coating, as well as the presence of the anatase  $\text{TiO}_2$  phase after thermal treatments.

With regard to the hydroxyapatite coatings:

10. CS is a suitable process to obtain crystalline and nanocrystalline hydroxyapatite (HA) coatings maintaining the feedstock powder microstructure and composition. No additional amorphization is obtained after cold spraying.
11. The deposition of a sintered porous HA powder is explained in terms of porous collapse, fragmentation and densification under the shock compressive loading from the high CS kinetics.

12. The presence of the CP-Ti coating enables the uniform deposition of a thin layer of sintered HA powder, contrary to #240 grinded and the SB titanium substrates.
13. Contrary to sintered HA powder, the CS impact of nanocrystalline agglomerate HA powder produces compaction of the nanocrystalline grains within the particle. A consolidation between particles is caused by the tamping effect produced by the continuous impact of incoming particles onto the already adhered ones.
14. The build up of thick HA coatings from the agglomerate HA powder is possible due to the combination of: (i) the compaction mechanism of the feedstock nanocrystalline powder and (ii) the surface activation of the substrate by the high surface roughness.
15. The adhesion properties of agglomerate HA powder depends on coating compaction. For agglomerate HA coatings it was observed an increase of scratch adhesion between particles as thickness does.
16. Both HA coatings show superhydrophilic ( $0^\circ$ ) behavior, not just because of the high roughness of CP-Ti coating, also from the good wettability of HA coatings.

*With regard to the biological properties of the coatings:*

*The effect of surface roughness...*

17. The cell morphology is not affected in terms of different roughnesses between SB surface and CP-Ti coating. Cells on SB surfaces ( $R_a=4\pm 1 \mu\text{m}$  and  $38\pm 5 \mu\text{m}$ ) and CS CP-Ti coatings show similar morphologies, acquiring in both cases an osteoblastic morphology with extended actin filaments along the roughness.
18. In vitro, the increase of surface roughness results in an increase of cell response. Higher cell viability and cell proliferation were observed for CS CP-Ti coating in comparison with SB surface.

19. Cell differentiation and mineralization also increases with the surface roughness. CP-Ti coatings show higher values than SB surface, especially in cell mineralization, in which it doubles the value at 28 days of cell culture, indicating a higher amount of calcium phosphate deposits.
20. The nanotextured features onto CS CP-Ti coating stimulate cell response. The nanotextured surface treatments onto rough CS CP-Ti coating lead to a significant enhance of cell response in comparison with the as-sprayed CS CP-Ti coating.
21. The nanotextured surfaces also induce higher cell differentiation in comparison with the as-sprayed CP-Ti coating. In terms of surface roughness, a higher cell differentiation for the lowest surface nanoroughness can be observed. However, surface composition should be considered in future research.

*The effect of surface composition...*

22. Cell proliferation depends on cell attachment, thus cell morphology. Cells onto CS CP-Ti coating show an osteoblastic morphology since 1 day of cell culture and cell proliferation along all days of cell culture. On the other hand, cells on HA coatings show an initial nodular morphology, with bad surface attachment. Cells on HA coatings starts a faster proliferation up to 7 days of culture (in which acquires osteoblastic morphology), probably overcoming the cell proliferation values of CS CP-Ti above 14 days of cell culture.
23. The size of HA crystal and HA composition are related with cell proliferation. The nanocrystalline agglomerate HA coating with a small percentage of amorphous phase shows higher cell proliferation in comparison with pure crystalline sintered HA coatings.
24. The CP-Ti coating shows higher cell differentiation than HA coatings due to the surface energy. Even so, between HA coatings, cell differentiation is higher for the crystalline sintered HA coating, who has a highes crystallinity percentage.

*The effect the thermal spray technique on hydroxyapatite coatings...*

25. Cell proliferation increases with the decrease of crystal size and the increase of HA crystallinity (CS>PS), although cells deposited onto CS HA coatings start proliferate from 7 days of culture on, that is when cells already acquire an osteoblastic morphology.
26. Cell differentiation between HA coatings increases with the increase of HA crystallinity (CS>PS).

*Regarding in vitro dynamic testing...*

27. The in vitro evaluation of PS HA coating at real-time demonstrate to be feasible to observe cell viability and proliferation, leading to a better understanding approach of cell interaction.



# **APPENDIX I**

## ***PUBLICATIONS***

---



## **I.1. ARTICLES**

### **I.1.1. PUBLISHED ARTICLES**

1. AM. Vilardell, N. Cinca, A. Concustell, S. Dosta, IG. Cano, JM. Guilemany, Cold spray as an emerging technology for biocompatible and antibacterial coatings: state of art, *J Mater Sci.* 50 (2015) 4441–4462. doi:10.1007/s10853-015-9013-1.
2. N. Cinca, AM. Vilardell, S. Dosta, A. Concustell, IG. Cano, JM. Guilemany, S. Estradé, A. Ruiz, F. Peiró, A New Alternative for Obtaining Nanocrystalline Bioactive Coatings: Study of Hydroxyapatite Deposition Mechanisms by Cold Gas Spraying, *J Am Ceram Soc.* (2016) 1420–1428. doi:10.1111/jace.14076.
3. A. Vilardell, N. Cinca, A. Jokinen, N. Garcia-Giralt, S. Dosta, I. Cano, J. Guilemany, Real-Time Protein and Cell Binding Measurements on Hydroxyapatite Coatings, *J Funct Biomater* 7 (2016) 23. doi:10.3390/jfb7030023.

### **I.1.2. SUBMITTED/ACCEPTED ARTICLES**

4. AM. Vilardell, N. Cinca, IG. Cano, A. Concustell, S. Dosta , JM. Guilemany, Dense Nanostructured Hydroxyapatite Coating on Titanium by Cold Spray [State: Accepted in *J Eur Ceram Soc*]
5. AM.Vilardell, N. Cinca, A. Concustell, S. Dosta, IG. Cano, JM. Guilemany, On the microstructural and mechanical characterization of optimized high-rough titanium coatings by Cold Spray for biomedical applications [State: Submitted in *Surf Coat*]
6. AM.Vilardell, N. Cinca, S. Dosta, IG. Cano, JM. Guilemany, Feasibility of using low pressure cold gas spray for the spraying of ceramic hydroxyapatite coatings [State: Submitted in *Mat Lett*]

**I.1.3. TO SEND TO JOURNALS**

7. AM.Vilardell, N. Cinca, N. Garcia-Giralt, A. Díez-Pérez, S. Dosta, IG. Cano, JM. Guilemany, Osteoblastic cell response on high-rough titanium coatings by Cold Spray State [State: To send to *Appl Surf Sci*]
8. AM.Vilardell, N. Cinca, N. Garcia-Giralt, A.Díez-Pérez, S.Dosta, IG.Cano, JM.Guilemany, Functionalized coatings by Cold Spray: an In-Vitro Study of Hydroxyapatite vs. Porous Titanium [State: To send to *Biomater*]
9. AM.Vilardell, N. Cinca, N. Garcia-Giralt, A.Díez-Pérez, S.Dosta, IG.Cano, JM.Guilemany, In-vitro study of hydroxyapatite coatings obtained by Cold Spray in comparison with conventional thermal spray techniques.
10. AM.Vilardell, N. Cinca, N. Garcia-Giralt, A.Díez-Pérez, S.Dosta, IG.Cano, JM.Guilemany, In-vitro study of nanotextured treatments on highly rough titanium coating by cold spray.
11. A.M. Vilardell, N. Cinca, I. Pacheco, C. Santiveri, S. Dosta, I.G.Cano, JM. Guilemany, M. Sarret, C. Muller, Characterization of as-sprayed CGS titanium coatings and their functionalization for biomedical applications.

**I.2. CONGRESSES**

1. A.M.Vilardell, N.Cinca, S.Dosta, J.M.Guilemany, Obtención de recubrimientos de HAp obtenidos por Proyección Fría (CGS). XIII Congreso Nacional de Materiales (2014). Oral communication.
2. A.M.Vilardell, N. Cinca, J. M. Guilemany, On the understanding of an hydroxyapatite layer formation by cold gas spray onto titanium substrates. *Bioceramics26* (2014). Poster.
3. A.M. Vilardell, N. Cinca, A.Concubell, S.Dosta, I.Garcia-Cano, J. M. Guilemany, Chemical and Morphological Changes of hydroxyapatite Cold Gas Spray coatings

- during Immersion in Simulated Physiological Solutions. Euro BioMAT (2015). Oral Poster
4. N.Cinca, S.Dosta, A.Concstell, G.Ma, M.Couto, A.M.Vilardell, IG.Cano, JM Guilemany, Metal, ceramic and cermet interface deposition features by cold gas spray at nanoscale. Materials (2015). Oral communication.
  5. A.M.Vilardell, Biocompatible coatings to lifespan the use of prostheses. Innovation Workshop on Cold Gas Spray. (2015). Oral communication
  6. N.Cinca, AM.Vilardell, S.Dosta, A.Concstell, IG.Cano, JM Guilemany, Deposition process and cahracterization of Hydroxyapatite coatings by Cold Gas Spray. RIPT (2015). Oral communication.
  7. A.M.Vilardell, N.Cinca, S.Dosta, I.G.Cano, J. M. Guilemany, Influence of HA microstructure on layer build.up coatings by cold spray. ITSC (2016). Poster
  8. A.M.Vilardell, N. Cinca, S.Dosta, I.G.Cano, J. M. Guilemany, N.Garcia-Giralt, A. Díez-Pérez, Osteoblastic Cell Responce on Titanium Coatings produced by Cold Spray. XIV Congreso Nacional de Materiales (2016). Oral communication
  9. José M<sup>a</sup>. Gómez de Salazara, José M<sup>a</sup>. Guilemany, A.M. Vilardell, N. Cinca, M.I. Barrena, Dopado de hidroxyapatita con nanopartículas de Ag, para aplicaciones biomédicas, mediante procesos de proyección térmica. XIV Congreso Nacional de Materiales (2016). Oral communication
  10. A.M. Vilardell, N.Cinca, S. Dosta, I.G.Cano, J. M. Guilemany, C. Santiveri, M. Sarret, C. Muller, Characterization of as-sprayed CGS titanium coatings and their funtionalization for biomedical applications. SMT30 (2016). Oral communication.

**I.3. TRADE SECRETS**

1. A.M. Vilardell, N. Cinca, S. Dosta, I.G. Cano, and J.M. Guilemany, "Multifunctional Miro-Nano Structured Hydroxyapatit Coatings Onto titanium Ti6Al4V for Biomedical Applications by Cold Gas Spray," Acta. de Protocolarización num., 809 (2015).

# **APPENDIX II**

***ON THE UNDERDSTANDING OF COLD SPRAY***

---



## II.1. INTRODUCTION

Cold spray (CS) is a solid state spray deposition technology included in the larger family of thermal spray process. The basic principle of the CS process is that is based on the high velocity (up to 1100m/s) of a gas jet (air/nitrogen/helium) formed by using a deLaval or similar converging/diverging nozzle, to accelerate powder particles (1-50 $\mu$ m) towards a substrate (Fig. II.1). During the impact with the substrate, particles undergo plastic deformation on impact and form splats due to the high kinetic energy of the particles rather than high temperature. Particles bond each other producing a coating and thereby avoids or minimases shortcomings of traditional thermal spray methods, such as high-temperature oxidation, evaporation, melting, crystallization, residual stresses and gas release. Particles are always propelled through a gas at temeprature lower than the melting point of the feedstock powder material [1,2]. Some other characteristics of CS process are the onces that follow:

- a) The amount of heat delivered to the coated part is small so that microstructural changes in the substrate material are non-existent.
- b) Absence of oxidation and other chemical reactions, thermally and oxygen sensitive deposition materials can be cold sprayed.
- c) Nanophase, intermetallic or amorphous materials can be sprayed.
- d) Formation of embrittling phases is avoided.
- e) Segregation (macro and micro) is also avoided.
- f) Peening effects are introduced on the interface which is beneficial for adhesion (compressive stresses).
- g) It has large possibilities of cost-effective and environmentally friendly alternatives to other technologies as electroplating, painting and so on.

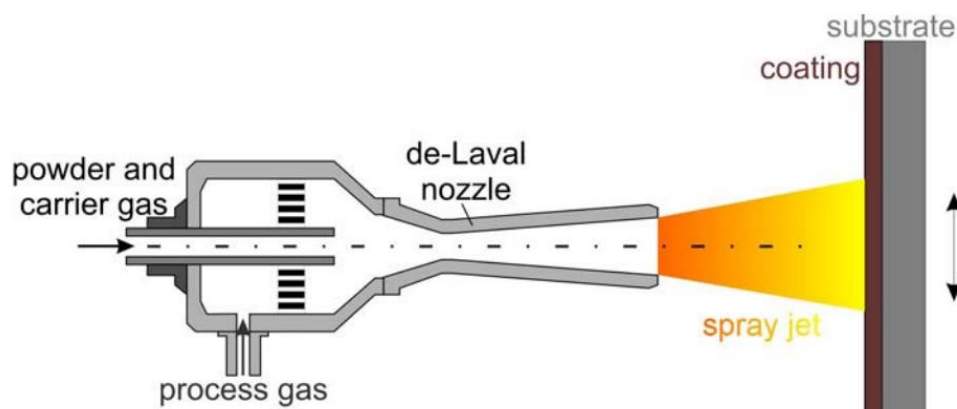


Figure II.1. Principle of CS spraying process

## II.2. COLD SPRAY SYSTEMS

### II.2.1. LOW PRESSURE COLD SPRAY

In low pressure cold spray (LPCS), particles are accelerated usually with air or nitrogen, and spraying parameters, such as pressure and preheating temperature, are limited up to 10 bars and 550°C. Normally the gas is accelerated between the range of 300-600 m/s. Solid powder particles are radially introduced downstream of the throat section of the supersonic nozzle and accelerated toward the substrate as shown in the figure II.2. The particles are effectively drawn in from the powder feeder by Venturi effect, i.e. by keeping the static pressure within the nozzle below the atmospheric pressure. The use of low pressures improves its operational safety, the system is more portable and also the spraying cost is reduced significantly in comparison with high pressure cold spray [3].

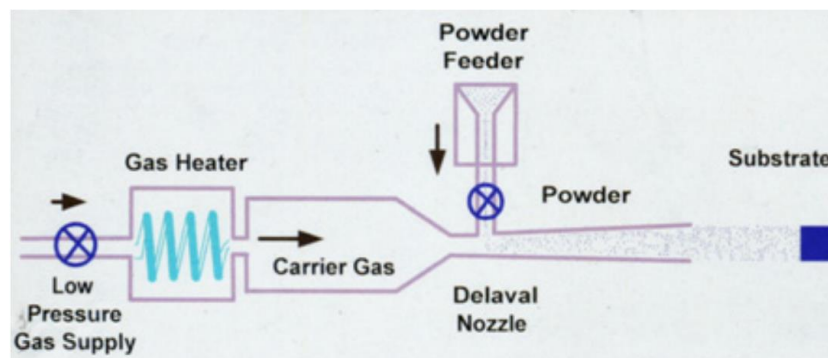


Figure II.2. Operating principle of LPCS

### II.2.2. HIGH PRESSURE COLD SPRAY

In high pressure cold spray (HPCS), particles are accelerated by helium or nitrogen gas up to higher pressures (40 bars) and preheating temperatures (up to 1100°C). The expansion of the gas at the nozzle produces the conversion of enthalpy into kinetic energy, which achieves supersonic gas flows up to 1200m/s. In comparison with LPCS, the solid powder feedstock particles mix with the propellant gas in the pre-chamber zone and are then axially fed into the gas stream, upstream of the converging section of the nozzle at a higher pressure than the accelerating gas to prevent backflow of the carrier gas to the powder feeder as shown in figure II.3. The use of high pressures leads to higher efficiency up to 90% in comparison with the 50% of LPCS system [3].

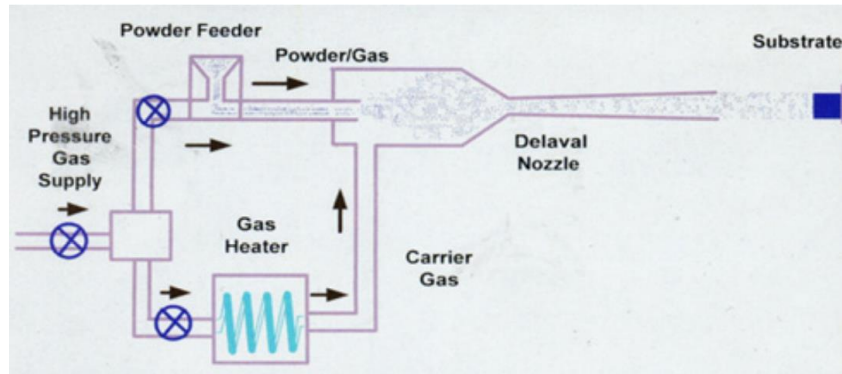
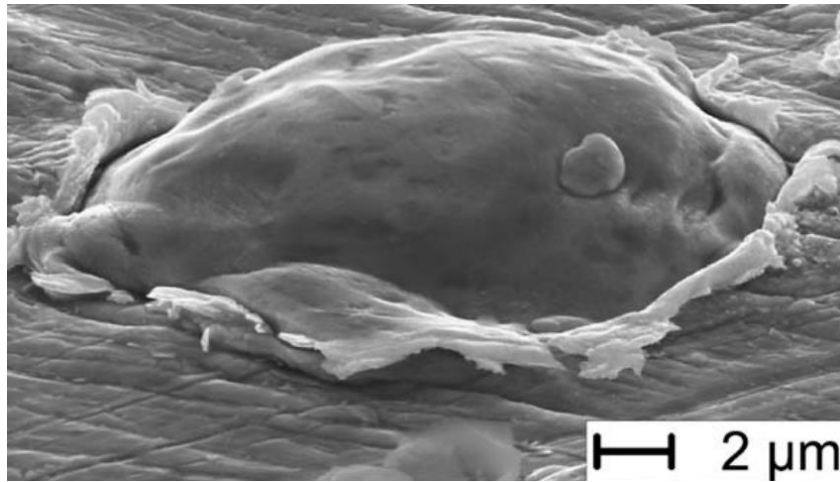


Figure II.3. Operating principle of HPCS

### II.3. DEPOSITION MECHANISM

The most prevailing bonding theory in CS is attributed to adiabatic shear instability which occurs at the interface particle-substrate at or beyond a certain velocity called critical velocity ( $V_c$ ). The initiation of adiabatic shear instability is usually described by thermal softening in competition with rate effects and work hardening. When a spherical particle travelling at  $V_c$  impacts a substrate, a strong pressure field propagates spherically into the particle and substrate from the point of contact. During work hardening, the distortion of grain structure and the generation and glide of dislocations occur. The rest of the plastic work, which can be as much as 90% of the total, is dissipated as heat. Heat generated by plastic work softens the material. At a certain point, thermal softening dominates over work hardening such that eventually stress falls with increasing strain. As a result, the material becomes locally unstable and additional imposed strain tends to accumulate in a narrow band. Consequently, an interfacial jet composed of the highly deformed material is formed (Fig. II.4). This adiabatic shear instability phenomena results in viscous flow of material at an outward flowing direction with temperatures close to melting temperature of the material. This material jetting is also a known phenomenon in explosive welding of materials. Experimental results show that the minimal particles impact velocity needed to produce shear localisation at the particles/substrate interface correlates quite well with the critical velocity for particle deposition by the CS process in a number of metallic materials. So far adiabatic shear instability is the most prevailing bonding theory in CS [4,5].



**Figure II.4.** Scanning electron micrograph of wipe test samples of a copper particle on a copper substrate [6]

The technology has developed from the spraying of ideal metallic materials with relatively low melting point and lower mechanical strength such as aluminum, and copper, to higher strength materials such as iron, titanium, as well as tantalum and even cermet and ceramic materials [7,8]. However, still the use of CS for ceramic materials has been observed as a non-feasible approach, leading to very fine or non-homogeneous layers [8,9].

#### **II.4. PARTICLE VELOCITY AND CRITICAL VELOCITY**

Particle velocity prior to impact is one of the most important parameters in cold spraying. Adiabatic shear instability occurs when particles travel at a sufficient high velocity called the critical velocity. It determines whether deposition of a particle or erosion of a substrate occurs on the impact of a spray particle. Generally, for a given material, there exist a minimum particle velocity commonly known as critical velocity, which must be achieved for the transition from erosion of the substrate to deposition the particle occurs (Fig. II.5). Deposition efficiency is the mass ratio of deposited to impacting particles. Particles traveling below a certain velocity will result in abrasion of the substrate upon the impact. However, particles travelling at or above that certain velocity will result in deposition and coating formation. This particle velocity depends on different factors such as, particle size and microstructure, the material of the particle and the substrate, and the spraying conditions [10].

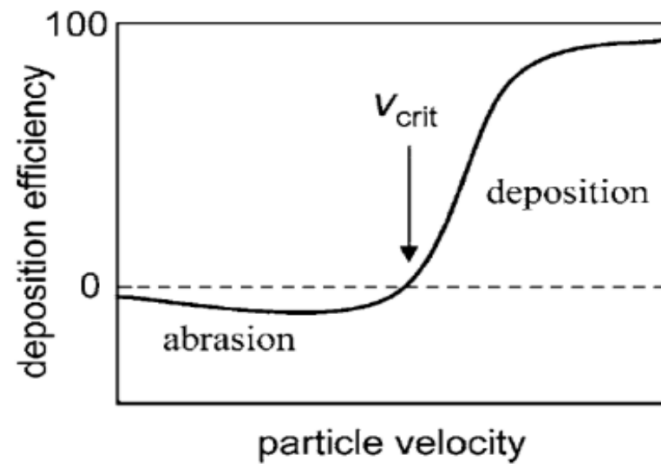


Figure II.5. Scanning electron micrograph of wipe test samples of a copper particle on a copper substrate [3]

**II.5. INFLUENCE OF SPRAYING PARAMETERS**

For a successful spraying of a metal onto metal substrate, it is necessary that whatever the spraying conditions are, there is a suitable metallurgical bonding between the two materials, this is that they show a capability to deform and disrupt any possible native oxide layer upon impact so that direct contact is promoted. For this to occur, usually particle velocities need to be within a window of deposition. Figure II.6 shows a macroscopic example given by 20 mm copper balls in homemade projectiles impacting onto a steel plate. Amount of explosives defined speed of the ball [11]. Usually, the particles do not instantly adhere but rather there is a delay time.

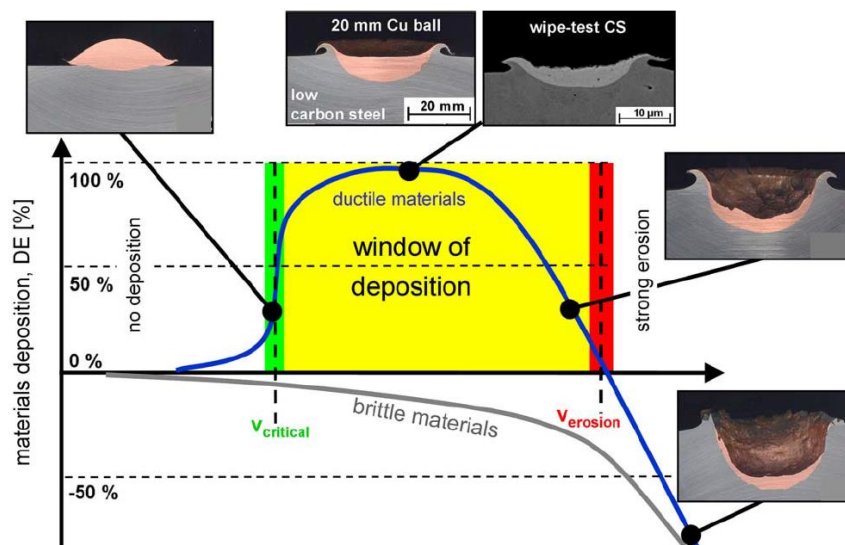


Figure II.6. Schematic correlation between particle velocity, deposition efficiency and impact effects for a constant impact temperature. Deposition is only observed for ductile materials in a certain velocity range for a given powder size and temperature, the so-called “window of deposition” [12]

### **II.5.1. GAS TEMPERATURE AND GAS PRESSURE**

Cold spray process is influenced by temperature in two different manners. First, the particle velocity increases with an increase in gas temperature. The pre-heating of the gas provides higher particle velocity, but also increases the risk of oxidation which it can be detrimental for the functionality of the coating. Second, temperature affects the elastic and plastic properties of materials, thus enhancing thermal softening, which is important for the bonding mechanism. Due to that, it is reported that critical velocity decreases with the increase of particle temperature [13]. As well as gas temperature, gas pressure usually leads to higher particle velocities, which is beneficial whenever they are found within the window of deposition, defined as the area between critical velocity and the erosion velocity of a particle which particle deposits.

### **II.5.2. STAND OFF DISTANCE AND SPRAYING ANGLE**

Particle velocity increases outside the nozzle and loses velocity during the flight, although it could be further reduced due to the shock wave resulting from the previous particles impacting onto the substrate (Bow shock). The bow shock depends on the stand-off distance, at small distances particle deposition is reduced due to the high strength of the bow shock. Contrary, large stand-off distances particles are propelled unhindered [14].

There can be distinguished three stand-off regions (Fig. II.7):

- 1) Small stand-off region: when the presence of the bow shock adversely affects deposition performance
- 2) Medium stand-off region, where the bow shock has disappeared and, if the gas velocity remains above the particle velocity, the deposition efficiency continues to increase.
- 3) Large stand-off region, where the gas velocity has fallen below the particle velocity, and the particles begin to decelerate. For optimal deposition performance, the stand-off distance should be set within region 2.

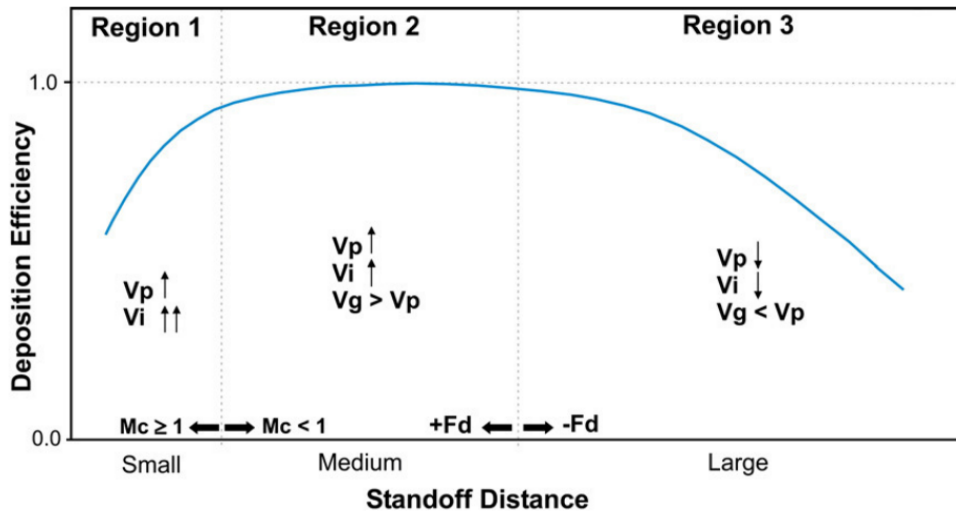


**Figure II.7.** Chart showing the effect of stand-off distance on deposition efficiency. Here  $F_d$  is the drag force,  $M_c$  is the centerline mach number,  $V_g$  is the gas velocity,  $V_i$  is the particle impact velocity and  $V_p$  is the in-flight particle velocity [14]

The impact angle of the particles has an important influence on the properties of the coating and deposition efficiency. As the angle decreases from the normal angle called off-normal angle ( $\theta$ ), then deposition of particle depend upon the normal component of the velocity and only the particles with the normal velocity components higher than the critical velocity will be deposited during impact. When the normal component of the particle velocity is lower than the critical velocity, the particle would not be able to adhere to the substrate (Fig. II.8). Therefore, it should be considered that the contact angle has influence on the deposition and the coating microstructure, since the deformation of the particles at the moment of impact depends primarily on the impact velocity.

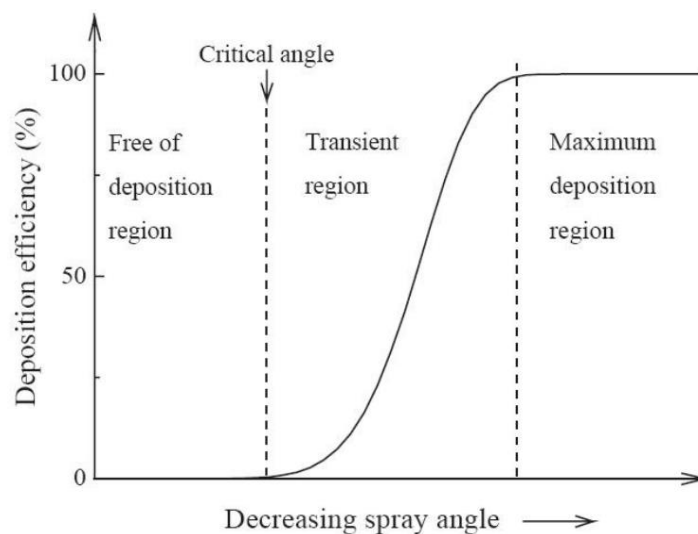


**Figure II.8.** View of the different region of particles on substrate while changes spraying angle in front of deposition efficiency [1]

### **II.5.3. FEEDING RATE**

The thickness in CS coatings increases linearly with an increase of the feeding rate, until a maximum that indicates that there are too many particles impacting on the substrate surface, creating excessive residual stresses, which can cause coating detachment.

### **II.5.4. SPRAYING POWDER SIZE AND MORPHOLOGY**

In general, smaller particle size, have in average a higher particle velocity. This is because the acceleration which prints the gas to the particles is inversely proportional to the particle diameter. Theoretically this implies that a smaller diameter, higher is the acceleration experienced by the particle and therefore higher is the velocity of the particle at impact time. However, in the same way that the smaller particles are accelerated more easily, also their deceleration is faster, while with larger particles, speed is maintained for a longer period of time.

Another important aspect is the powder morphology. Non-spherical particles with irregular and roughened surfaces have a different flight and impact behaviour than spherical particles. An irregular morphology increases the stresses concentration during the impact due to the fact that the load is not uniformly distributed as in the spherical particles. This stresses concentration can facilitate the emergence of deformations which lead to the break of the thin oxide layer present on the material surface and therefore causing a greater contact between the particle and the substrate.

### **II.5.5. GAS TYPE**

Pure nitrogen gas is generally preferred as the inert gas in cold spray processes for its low cost and availability. Though, the more expensive helium gas is occasionally used instead of nitrogen to improve the adhesion and the coating quality of high-grade alloys of aluminum, steel, nickel, titanium, etc. Helium (He) has preferable thermal properties that brings the gas to higher Mach numbers and increases particle impact velocities accordingly. The specific heat ratio and the specific gas constant of the helium gas are much higher than that of nitrogen. Porosity, metallurgical homogeneity and strength of the coatings improve when the particle kinetic energy upon impact is increased to sufficient levels.

## II.6. REFERENCES

- 
- [1] Ghelichi R, Guagliano M (2009) Coating by the cold spray process: a state of the art. *Fratt Integr Strutt* 8:30–44
- [2] Moridi A, Hassani-Gangaraj SM, Guagliano M, Dao M (2014) Cold spray coating: review of material systems and future perspectives. *Surf Eng* 30:369–395.
- [3] Singh HR, Sidhu TS, Kalsi SBS (2012) Cold spray technology: future of coating deposition processes. *Frat Integr Strutt* 22:69–84
- [4] Hussain T (2012) Cold Spraying of Titanium: A Review of Bonding Mechanisms, Microstructure and Properties. *Key Eng Mater* 533:53–90.
- [5] Grujicic M, Zhao C., DeRosset W., Helfritsch D (2004) Adiabatic shear instability based mechanism for particles/substrate bonding in the cold-gas dynamic-spray process. *Materials & Design* 25:681–688.
- [6] Assadi H, Gärtner F, Stoltenhoff T, Kreye H (2003) Bonding mechanism in cold gas spraying. *Acta Mater* 51:4379–4394.
- [7] Schmidt T, Gärtner F, Assadi H, Kreye H (2006) Development of a generalized parameter window for cold spray deposition. *Acta Mater* 54:729–742.
- [8] Dosta S, Couto M, Guilemany JM (2013) Cold spray deposition of a WC-25Co cermet onto Al7075-T6 and carbon steel substrates. *Acta Mater* 61:643–652.
- [9] Kergourlay E, Grossin D, Cinca N, et al (2016) First Cold Spraying of Carbonated Biomimetic Nanocrystalline Apatite on Ti6Al4V: Physical-Chemical, Microstructural, and Preliminary Mechanical Characterizations: First Cold Spraying of Carbonated Biomimetic Nanocrystalline. *Adv Eng Mater* 18:496–500.
- [10] Marrocco T, (2008) Development of improved cold spray and hvof deposited coatings. PhD thesis. University of Nottingham
- [11] Schmidt T, Assadi H, Gärtner F, et al (2009) From Particle Acceleration to Impact and Bonding in Cold Spraying. *J Therm Spray Technol* 18:794–808.

[13] Li C-J, Li W-Y, Liao H (2006) Examination of the Critical Velocity for Deposition of Particles in Cold Spraying. *J Therm Spray Technol* 15:212–222.

[14] Fernandez MM, (2008) Cold Spray Deposition of Titanium onto Aluminum Substrates. Master dissertation

# APPENDIX III

## *REFINEMENT OF X-RAY DATA*

---



### III.1. INTRODUCTION

The x-ray diffraction (XRD) data was processed in many ways in order to get information from the hydroxyapatite and titanium powders and coatings diffractograms, first to analyze the grain size before and after the cold gas spraying, and second to calculate the percentage of crystalline and amorphous phases of hydroxyapatite powders and coatings.

To evaluate the grain size an individual x-ray peak fitting was performed, while a whole x-ray spectrum fitting was done by Rietveld's method to evaluate the percentage of crystalline and amorphous phases.

### III.2. FREE PROFILE FITTING

One or some of the peaks of the analyzed x-ray spectra are fitted without using any structural information by means of the pseudo-voigt (pV) function included in the XRFit program (WinPLOT software pack). Assuming linear background, such function is a linear combination of the two possible peak shape functions: Gaussian (G) and Lorentzian (L). Hence, pV results in (eq.III.1):

$$(eq.III.1) \quad pV = hG + (1 - h)L$$

Both G and L depend directly on the full width at half maximum of the peak (FWHM) and ( $2\Theta - 2\Theta_h$ ). The best fit sought is the best least-squares fit to all  $y_i$ 's simultaneously. The quantity minimized in the least-squares refinement is the residual  $X^2$  (eq.III.2):

$$(eq. III.2) \quad X^2 = \sum_i w_i (y_i^{obs} - y_i^{calc})^2$$

Where  $y_i^{obs}$ ,  $y_i^{calc}$  and  $w_i$  are observed and calculated intensities at the  $i$ th step and weight respectively. Figure III.1 shows an example of output profiles of individual x-ray peak fitting, where the red points are the experimental data, the black line is the calculated profile and the blue line the difference.

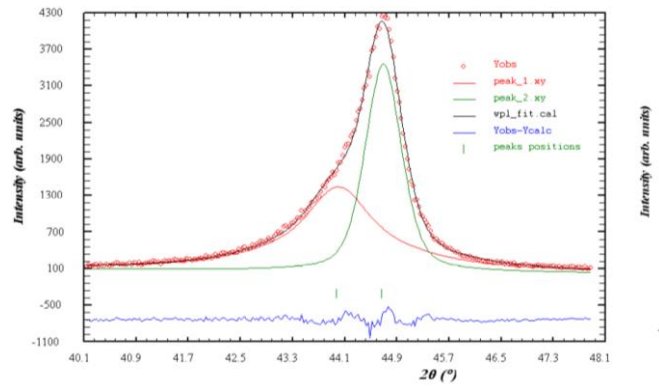


Figure III.1. Example of the output profiles individual x-ray peak fitting

The output data consists of the angular position ( $2\Theta_h$ ) for a certain reflection, the integrated intensity, FWHM,  $\eta$  and  $H_G$  and  $H_L$  contributions to the global breadth  $H$ . A continuous refinement is carried out until the convergence criterion is reached, achieving a minimum for  $\chi^2$ .

By using the Bragg law, the  $d_{hkl}$  reflections are calculated and these are introduced in the Scherrer formula (eq. III.3).

$$\text{(eq. III.3)} \quad \beta = \frac{C\lambda}{D \cos\theta}$$

where  $\beta$  is the full width at half maximum of the peak,  $\lambda$  is the wavelength of the x-ray,  $\Theta$  is the Bragg angle,  $C$  is a unit cell geometry-dependent constant whose value is typically between 0.85 and 0.99 and,  $D$  is the grain size.

### III.3. RIETVELD'S METHOD

The XRD analysis is one of the most used to quantify crystalline phases (and eventually amorphous phases). In the previous method, profiles were refined, but here crystal structures. Rietveld's method performs a global adjustment of the x-ray profile to quantify each crystalline phase (FullProf\_Suite software). In the present research it was used to quantify the percentage of amorphous and crystalline phases of hydroxyapatite powders and coatings.

In the Rietveld's method the least-squares refinements are carried out until the best fit is obtained between the entire observed powder diffraction pattern taken as a whole and the entire calculated pattern based on the simultaneously refined models. Figure III.2 shows an

example of output profiles obtained with Rietveld's method, where the red points are the experimental data, the black line is the calculated profile and the blue line the difference

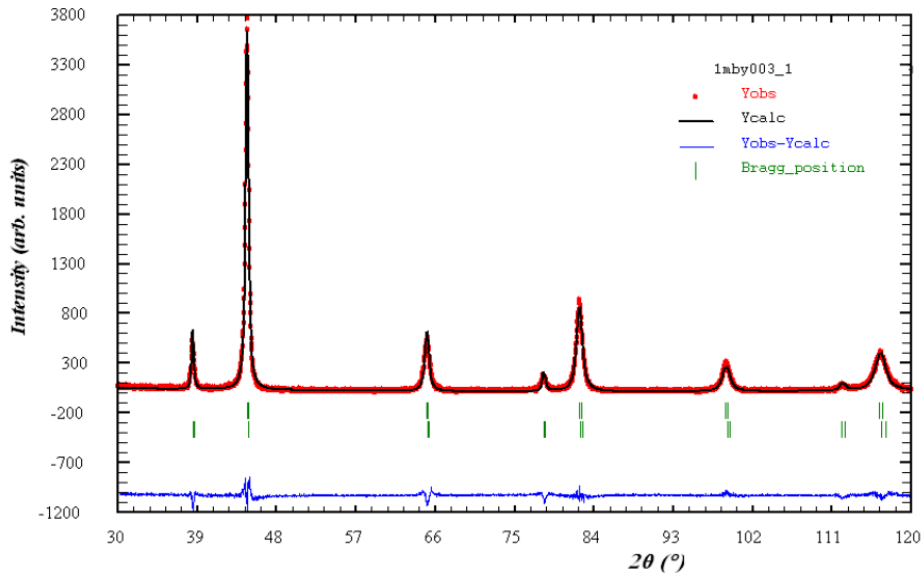


Figure III.2. Example of the output profiles obtained with Rietveld method

There is an extensive mathematic background around these methods but here, it will be explained briefly introducing just the most important formula. It is possible to calculate directly the weigh fractions  $W_J$  from the crystalline phases and the global weight fraction  $W_{AM}$  from the amorphous and non-identified phases, just knowing the real weigh fraction  $W_P$  from a known pattern and from other weight fraction values  $W_J$  resulting from Rietveld fitting from all quantified phases (including the known pattern with the adjusted weight fraction  $W_P^0$ ).

$$\text{(eq. III.4)} \quad W_J = \frac{W_J^0 W_P}{W_P^0 (1 - W_P)}$$

$$\text{(eq. III.5)} \quad W_{AM} = \frac{W_P^0 W_P}{W_P^0 (1 - W_P)}$$



## **RESUMEN**

El propósito de esta tesis doctoral es investigar la viabilidad y desarrollo de recubrimientos funcionales para prótesis articulares por medio de la tecnología de proyección fría o cold spray (CS). La razón de la elección de este tema es explorar las ventajas de la técnica con el fin de alcanzar y mejorar los inconvenientes que presentan las tecnologías de proyección térmica convencionales en el ámbito biomédico.

El uso de prótesis articulares está aumentando hoy en día con el aumento de esperanza de vida y las enfermedades crónicas. En términos ortopédicos, más y más pacientes requerirán el uso de prótesis para sustituir una parte fundamental de su esqueleto. La proyección por plasma (PS) es la técnica de deposición utilizada hoy en día para este propósito. El Centro de proyección térmica ha investigado en los últimos años esta línea, para mejorar la osteointegración entre la prótesis y el tejido óseo, al igual que las propiedades mecánicas y biológicas. Sin embargo, la mayor desventaja de ambas técnicas es la temperatura de trabajo, que puede producir oxidación en el caso de materiales metálicos o descomposición en fases secundarias en materiales nanoestructurados, amorfos o sensibles a la temperatura como es el caso de la hidroxiapatita (HA).

Como alternativa, se propone el CS, para la obtención de recubrimientos en estado sólido. El interés industrial de la utilización de esta técnica en el campo biomédico reside en su deposición a baja temperatura (por debajo de la temperatura de fusión del material), ofreciendo la posibilidad de proyectar materiales sensibles a la temperatura, al oxígeno y con bajo punto de fusión. CS ofrece la posibilidad de proyectar diferentes tipos de materiales, a bajo coste, en una atmosfera agradable, y manteniendo la microestructura del polvo partida en el recubrimiento, pudiendo obtener así recubrimientos personalizados.

El objetivo principal de esta tesis doctoral es la obtención y optimización de recubrimientos de titanio rugoso y HA sobre sustratos de Ti6Al4V mediante CS, manteniendo la microestructura y la composición de los polvos de partida al recubrimiento. Los recubrimientos se han caracterizado a nivel microestructural, mecánico y biológico; secundariamente, se han realizado recubrimientos nanotexturizados sobre el recubrimiento óptimo del titanio para comparar como afecta este tipo de rugosidad a nivel celular; finalmente, a nivel biológico, se han realizado un total de 4 estudios comparativos con test

estáticos in vitro, donde se compara: (i) el efecto de la rugosidad del recubrimiento (ii) el efecto de la nanorugosidad, (iii) el efecto de la composición superficial del recubrimiento y (iv) el efecto de la técnica de proyección utilizada para la obtención de los recubrimientos de HA. Finalmente, en colaboración con la universidad de Tampere, se realizó un primer estudio de test dinámico los recubrimientos de HA por PS.

## 1. INTRODUCCIÓN

### 1.1. LA PROYECCIÓN TÉRMICA

La proyección térmica es un grupo de procesos para producir recubrimientos metálicos y no metálicos. El material a proyectar (en forma de polvo o hilo), es fundido mediante una energía obtenida a partir de la combustión de gases, de un arco voltaico o de una recombinación de gases plasmógenos, según la técnica empleada. El material fundido es proyectado seguidamente sobre la pieza a recubrir en estado plástico a elevada energía cinética y térmica. A través de la solidificación de las partículas fundidas en el impacto con el sustrato, se crean uniones cohesivas entre sí y el adhesivo lazos con el sustrato. Las partículas fundidas impactan y empiezan a adherirse sobre el sustrato debido a la alta velocidad de enfriamiento, por lo general superiores a  $10^6$  K/s para los metales. Las técnicas de proyección térmica se dividen en tres grandes subgrupos según la fuente de energía utilizada (Fig. 1.1)

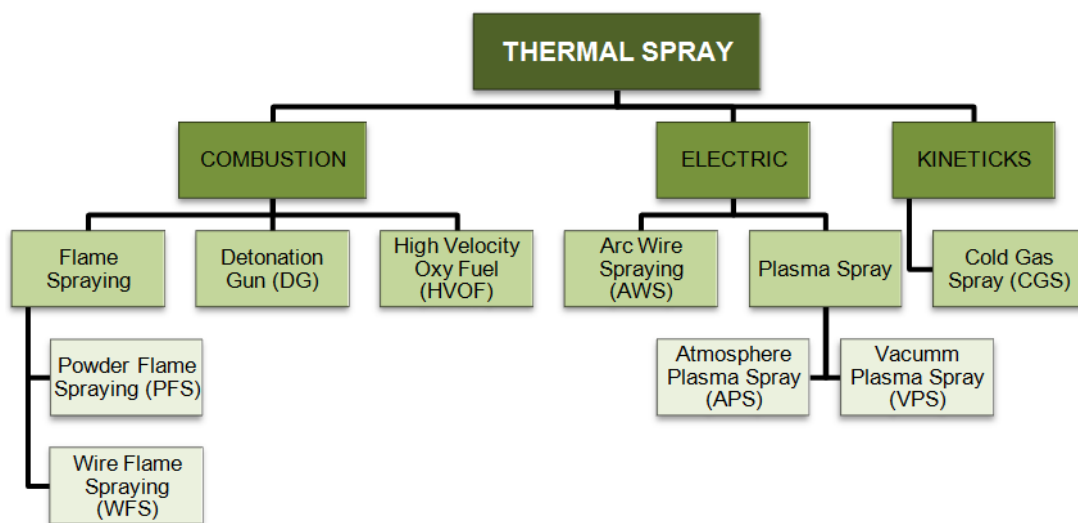
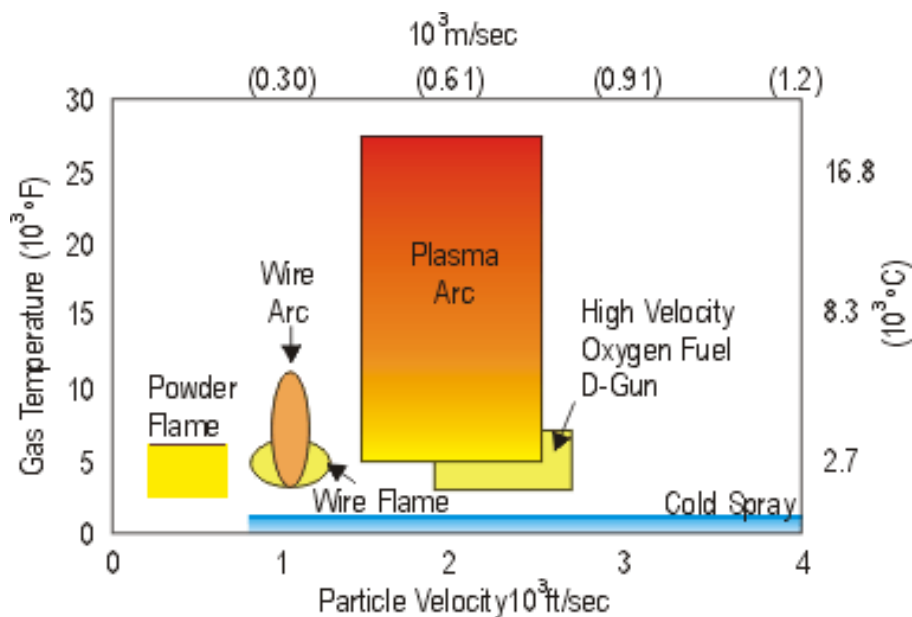


Figure 1.1. Esquema de las técnicas de proyección térmica según la fuente de energía utilizada

Una gran ventaja de los procesos de proyección térmica es la capacidad de depositar una gama extremadamente amplia de materiales. Además de los metales, cerámicas, vidrios y polímeros, los recubrimientos de proyección térmica se han aplicado con éxito a muchos otros materiales de substrato incluyendo madera. La proyección térmica ofrece también la ventaja de las grandes velocidades de deposición, superiores a la de las tecnologías de recubrimientos alternativos, tales como electrodeposición o deposición de vapor, donde la deposición se produce a nivel atómico o molecular. Como principal desventaja encontramos la elevada temperatura del propio proceso. Las elevadas temperaturas causan inclusiones de óxido (materiales metálicos sobretudo), así como la descomposición / degradación en materiales sensibles al oxígeno tales titanio o la HA.

## 1.2. LA PROYECCIÓN FRÍA

La proyección fría, es una técnica muy novedosa para la obtención de recubrimientos en el ámbito de la proyección térmica. El uso de bajas temperaturas de trabajo (siempre por debajo del punto de fusión del material) es lo que la hace diferente respecto al resto de técnicas convencionales, ya que la hace ideal para depositar materiales sensibles a la temperatura (ej. materiales nanoestructurados y amorfos) o reactivos al oxígeno (ej. titanio). Además tiene un gran potencial a nivel económico y ambiental por ser un proceso eficiente y respetuoso con el medio ambiente.



**Figure 1.2.** Esquema de la temperaturas de gas frente a la velocidad de partícula de las diferentes técnicas de proyección térmica

### 1.2.1. Mecanismo de deposición

El mecanismo de deposición de CS se atribuye a las conocidas "adiabatic shear instabilities" (ASIs), que se producen en la interfaz entre el sustrato y la partícula al superar esta la velocidad crítica. El inicio de las ASIs es usualmente descrito por el ablandamiento térmico. Cuando una partícula esférica que viaja a velocidad crítica impacta sobre el sustrato, establece un fuerte campo de presión propagándose en la partícula y el sustrato desde el punto de inicio de contacto. Durante el impacto, se produce endurecimiento del material por trabajo en frío, donde se genera una distorsión de la estructura de grano que provoca la generación y movimiento de dislocaciones. El resto del trabajo plástico, que puede ser tanto como 90% del total, se disipa como calor. El calor generado por el trabajo plástico reblandece material. En un momento determinado, el ablandamiento térmico domina sobre el endurecimiento de trabajo de tal manera que, finalmente, el estrés disminuye al aumentar la tensión. Como resultado, el material se vuelve inestable y localmente deforma. Por consiguiente, da resultado a un "jet" del material (Fig. 1.3). Las ASIs resultan en un flujo viscoso de material en dirección hacia fuera que fluye a temperaturas cercanas a las de la temperatura de fusión del material.

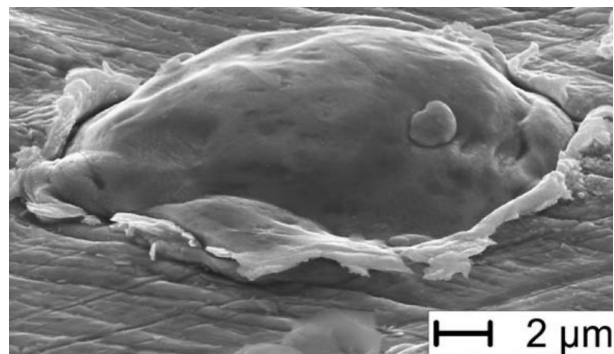


Figure 1.3. Micrografía MEB del impacto de una partícula de cobre sobre sustrato de cobre

### 1.2.2. Velocidad de partícula y velocidad crítica

La velocidad de la partícula antes del impacto es uno de los parámetros más importantes en el CS. Las ASIs se producen a una velocidad conocida como la velocidad crítica ( $V_c$ ), que determina si habrá deposición de partícula o erosión del sustrato durante el impacto de la partícula. Las partículas que viajan por debajo de una cierta velocidad darán lugar a la abrasión del sustrato en el impacto. Sin embargo, las partículas que viajan a o por encima de cierta velocidad darán lugar a la deposición y la formación de recubrimiento. La velocidad

de partícula depende de diferentes factores tales como, el tamaño de partícula y la microestructura, el material de la partícula y el sustrato, y las condiciones de proyección.

### **1.2.3. Influencia de los parámetros de proyección**

Para una buena adherencia entre la partícula y el sustrato, es necesario que haya una unión metalúrgica apropiada, demostrando una capacidad para deformar y alterar cualquier posible capa de óxido nativo.

#### **a) Temperatura y presión del gas**

El CS es influenciado por la temperatura de dos maneras distintas. En la primera, la velocidad de partícula aumenta junto con el aumento de la temperatura del gas. En segundo lugar, la temperatura afecta a las propiedades elásticas y plásticas del material, así como la formación de ASIs, que es importante para una buena unión entre partícula y sustrato. Al igual que la temperatura, la presión del gas por lo general, aumenta la velocidad de partícula, que es beneficioso cuando la partícula se encuentra dentro de la ventana de deposición, que se define como el área entre la velocidad crítica y la velocidad de erosión de una partícula, para que haya deposición de partícula.

#### **b) Distancia y ángulo de la pistola de proyección**

La velocidad de las partículas aumenta fuera de la pistola de proyección y pierden velocidad durante el vuelo, aunque podría reducirse aún más debido a la onda de choque resultante de las partículas anteriores al impactar sobre el sustrato. A cortas distancias, la deposición de partículas se reduce debido a la onda de choque, por lo contrario, a largas distancias, las partículas son propulsadas sin ningún obstáculo.

El ángulo de impacto de las partículas tiene una influencia importante en las propiedades de la eficiencia del recubrimiento y deposición. A medida que el ángulo disminuye desde el ángulo normal (perpendicular), la deposición de las partículas depende de la componente normal de la velocidad y sólo las partículas con los componentes de la velocidad normales mayor que la velocidad crítica serán depositadas durante el impacto. Cuando la componente normal de la velocidad de las partículas es inferior a la velocidad crítica, la partícula no sería capaz de adherirse al sustrato.

### c) Tasa de alimentación del polvo de proyección

El espesor de los recubrimientos aumenta linealmente con un aumento de la tasa de alimentación, hasta un máximo que indica que hay demasiadas partículas que impactan en la superficie del sustrato, creando tensiones residuales excesivas, que puede causar el desprendimiento de recubrimiento.

### d) Morfología del polvo de proyección

En general un rango de distribución de partículas estrecho y menor suele tener una velocidad media de partículas mayor. Esto es debido a que la aceleración que le imprime el gas a las partículas es inversamente proporcional al diámetro de la misma. Sin embargo se debe tener en cuenta que, del mismo modo que las partículas de menor tamaño se aceleran más fácilmente, también su deceleración es más rápida, mientras que las partículas de mayor tamaño, mantienen la velocidad durante un mayor periodo de tiempo. Cabe decir, que la morfología de la partícula también afectará a su velocidad, partículas con morfología irregular tenderán a acelerar más rápido que partículas esféricas por la conocida “drag force”.

## **2. MATERIALES**

Para la obtención de recubrimientos de titanio rugoso se seleccionó un polvo de titanio comercialmente puro (grado 2) con un gran tamaño de partícula y morfología irregular (MBN Nanomaterialia, Italia).

Para la obtención de recubrimientos de HA se utilizaron dos polvos:

- Polvo esférico cristalino obtenido por sinterización (Plasma Biotal, Reino Unido)
- Polvo esférico nanocristalino obtenido por aglomeración (Medicoat, Francia)

Todos los recubrimientos fueron proyectados sobre sustratos de la aleación Ti6Al4V (Technoalloy, España).

### **3. PROCEDIMIENTO EXPERIMENTAL**

#### **3.1. MÉTODOS DE CARACTERIZACIÓN DE LOS POLVOS**

Los polvos se caracterizaron principalmente mediante el tamaño de partícula, la composición y transformación de fases, la densidad, la morfología y la fluidez.

- **Tamaño de partícula:** La distribución granulométrica del polvo de partida se realizó a través de un análisis por difracción láser con un equipo Beckman Coulter LS 13320. Este equipo utiliza un láser con una potencia de 5mW y una longitud de onda de 750nm. El rango de tamaño de partícula que permite analizar esta comprendido entre 200nm y 2mm.
- **Densidad:** Hay tres métodos para medir la densidad:
  - Densidad aparente: Se calcula mediante la norma ASTM B-212-09.
  - Densidad vibrada: Se calcula mediante la norma ASTM B-527-93.
  - Densidad real: Se calcula mediante la norma ASTM B-962-08
- **Fluidez:** Determinado de acuerdo con la norma ASTM B-213-03.
- **Brauner-Emmet-Teller (BET):** La área superficial de las partículas se midió con un equipo Micrometrics, modelo TriStar equipado con nitrógeno como gas de adsorción.
- **Morfología:** Dos microscopios electrónicos de barrido (MEB) fueron utilizados para examinar la superficie libre y la sección transversal de los polvos, (i) JEOL 5510 y (ii) ProX Phenom, ambos equipados con microanálisis EDS.
- **Microestructura:** La microestructura de las partículas se determinó utilizando el equipo de microscopía electrónica de transmisión JEM JEOL 2100. Las muestras fueron preparadas con la técnica de Focused Ion Beam.
- **Composición de fases:** Para ello se utilizaron distintas técnicas:
  - Difracción de rayos X: El equipo utilizado fue Siemens D500 tipo Bragg Brentano  $\theta/2\theta$  con una radiación Cu K $\alpha$ . La cuantificación de fases se realizó aplicando el método Rietveld utilizando el programa FullProf.
  - Espectroscopia infrarroja transformada de Fourier: Los ensayos fueron realizados con el equipo Scientific Nicolet iZ10 MX,

- **Transformación de fases:** La termogravimetría fue analizada con el equipo SDT 2960 (TA instruments) para los polvos de hidroxiapatita en un rango entre 200°C y 1300°C.
- **Dilatometría:** Fue realizada con el equipo Setaram TMA Setsys 16/18 entre 25°C y 1600°C y una precisión de 0.01  $\mu\text{m}$

## **3.2. OBTENCIÓN DE RECUBRIMIENTOS**

### **3.2.1. Técnicas de proyección térmica**

Esta tesis se focaliza en la obtención de recubrimientos funcionalizados por CS, aun así, los recubrimientos de HA fueron obtenidos por PS y HVOF para compararlos con los obtenidos por CS.

- **High pressure cold spray (HPCS):** El equipo utilizado fue KINETICS® 4000 (Cold Gas Technology, Ampfing, Alemania), con una presión máxima de operación de 40 bares y una temperatura de 800 °C, y limitado al uso de nitrógeno como gas propulsor.
- **Low pressure cold spray (LPCS):** El equipo utilizado fue Dycomet 423 (Países Bajos), con una presión máxima de operación de 10 bares y una temperatura de 600 °C, y limitado al uso de aire como gas propulsor.
- **Proyección por Plasma:** El equipo utilizado para la proyección por plasma es un modelo A-3000 S de PLASME TECHNIK con una potencia máxima de 55kW y un voltaje de 70-80 V. La pistola de proyección es el modelo PLASME TECHNIK F4-MB con dos inyectores del polvo y posee un cátodo cilíndrico-cónico con punta de ThO<sub>2</sub> y un ánodo tubular refrigerado con agua.

### **3.2.2. Recubrimientos de nanotexturización**

- **Tratamiento de anodizado:** El anodizado del recubrimiento de titanio se realizó con una configuración de dos electrodos utilizando DELTA ELEKTRONIKA SM 400-AR-4 como fuente de alimentación, controlada por LabVIEW. Una lámina de acero inoxidable AA304 se utilizó como electrodo auxiliar. Se utilizó un baño de etilenglicol con 5% en peso de H<sub>2</sub>O y 0,5% en peso NH<sub>4</sub>F y se aplicaron 30 V y 1800 s.

Posteriormente se realizó un tratamiento térmico de 1h a 450°C en atmosfera controlada.

- **Tratamiento alcalino:** Para el tratamiento alcalino, las muestras de titanio se sumergieron 3 días a 5M NaOH a una temperatura de 80°C. Las muestras fueron lavadas con agua destilada y secadas en un horno a 40°C. Posteriormente se realizó un tratamiento térmico de 1h a 600°C en atmosfera controlada.

### 3.3. Métodos de caracterización de los recubrimientos

Los métodos de caracterización de los recubrimientos se dividen a nivel microestructural, mecánico, químico y biológico.

#### 3.3.1. Caracterización microestructural de los recubrimientos

- **Microscopía óptica:** El microscopio Leica DMI5000 M fue utilizado para analizar la estructura del recubrimiento, al igual que para la obtención de los valores de espesor y porosidad acorde con la normativa ASTM F-1854.
- **Microscopía confocal:** El microscopio confocal Leica DCM3D fue utilizado para calcular los perfiles 2D y 3D y su descomposición en rugosidad y ondulación.
- **Microscopía electrónica:** Los análisis superficiales fueron realizados mediante microscopía electrónica de barrido de emisión de campo con el equipo JEOL JSM 7100F; la microestructura de los recubrimientos se analizó por microscopía electrónica de transmisión JEM JEOL 2100, la cual de analizaron muestras preparadas previamente por FIB.
- **Ataque químico:** El reactivo Kroll fue utilizado para evaluar la deformación de los recubrimientos de titanio, al igual que la microestructura del sustrato Ti6Al4V.
- **Espectroscopía de fotoelectrones emitidos por rayos X:** El equipo utilizado fue PHI 5500 Multitechnique System (de Physical Electronics) con una fuente de rayos X monocromática (aluminio K $\alpha$  de 1486,6 energía eV y 350 W), situado perpendicular al eje del analizador y calibrado mediante la línea de 3d5/2 de Ag con una anchura total a la mitad del máximo (FWHM) de 0,8 eV. Todas las muestras fueron analizadas

antes y después de ser limpiadas con un bombardeo de iones de Ar para eliminar posible contaminación superficial.

- **Ángulo de contacto:** El goniómetro para medir el ángulo de contacto fue elaborado por la Universidad de Barcelona, y el programa utilizado para la captura de imágenes fue el imageJ. Los ensayos se realizaron con gotas de 2µl de agua MilliQ y solución de Hanks.

### 3.3.2. Caracterización mecánica de los recubrimientos

- **Adherencia de tracción de los recubrimientos:** Las adherencias de tracción de los recubrimientos fueron obtenidas siguiendo la norma ASTM F-1147-05
- **Adherencia de cizalla de los recubrimientos:** Las adherencias de cizalla de los recubrimientos fueron obtenidas siguiendo la norma ASTM F1044
- **Test de abrasión:** La abrasión de los recubrimientos fue obtenidas siguiendo la norma ASTM F-1978.
- **Test de scratch:** Los tests de scratch fueron obtenidos siguiendo la norma ASTM C1624-05.

### 3.3.3. Caracterización biológica de los recubrimientos

#### a) Tests estáticos

- **Cultivo celular:** Los osteoblastos se obtienen del hueso trabecular de la rodilla después de su reemplazamiento por una prótesis articular siguiendo el proceso de Nachter et al. El estudio fue aprobado por el comité ético del Parc de Salut Mar.
- **Viabilidad y proliferación celular:** Se analizó mediante el kit MTS (CellTiter 96® AQueous One Solution Cell Proliferation assay –Promega-), basado en la transformación de la sal de tetrazolio a formazán por parte de las células activas, y que da una medida de la cantidad de células vivas en superficie midiendo la intensidad del color con un espectrofotómetro (490nm). A nivel cualitativo, el test Life/Dead (LIFE/DEAD Viability/Cytotoxicity assay Kit for Mammalian Cells – Invitrogen-), permitió por simple observación superficial con un microscopio óptico

Leica DM1000 localizar la distribución de células vivas (citoplasma verde) y muertas (núcleo celular rojo).

- **Diferenciación celular:** La diferenciación celular se mide a través de la actividad de la fosfatasa alcalina (Abcam's Alkaline Phosphatase Assay Kit), que permite la medida a través de la intensidad de color mediante un espectrofotómetro (405nm).
- **Mineralización celular: Las células son fijadas con** 10% formamida durante 10 min, lavadas intensamente con PBS y teñidas con 300 µl of 40 mM/l Alizarin a un pH de 4.2. Acto seguido, se vuelven a lavar con PBS para extraer el exceso del tinte, y la mineralización celular se cuantifica mediante la disolución del precipitado rojo de alizerina con 10%cloruro de cetilpiridinio a temperatura ambiente al cabo de 30min. La cuantificación se realiza mediante espectrofotómetro a una longitud de onda de 550nm.
- **Morfología celular:** La morfología celular se examinó de dos modalidades distintas: (i) Tiñendo el núcleo y los filamentos de actina mediante DAPI y Phalloidin-Tetramethylrhodamine B isothiocyanate (Sigma-Aldrich) siguiendo el protocolo del fabricante y observándolas mediante microscopía confocal Leica DCM3D o (ii) Fijándolas mediante etanol y observándolas con el equipo JEOL JSM 7100F FESEM.

#### b) Tests dinámicos

En colaboración con la Universidad de Tampere (Finlandia), se ensayaron como primer intento los recubrimientos de HA por PS.

- **Multi Parametric Surface Plasmon Resonance (MP-SPR):** Mediante el equipo MP-SPR Navi™ 200 instrument (BioNavis Ltd., Tampere, Finland) en el modo de medición angular y a temperatura de 20-21°C, se hicieron ensayos dinámicos con proteínas y células para observar la viabilidad de los recubrimientos de HA. Las condiciones fueron las siguientes:
  - Para la interacción (0.2 mg/ml) con proteínas (Lisozima), circuló una solución de 0.15M NaCL con un caudal de 30 µL/min. Las mediciones se hicieron con una longitud de onda de 670 nm.

- Para las células (AD-MSK): Las medidas fueron tomadas simultáneamente usando longitudes de onda de 670 y 980 nm hasta alcanzar un valor estable.

## **4. RESULTADOS Y DISCUSIÓN**

### **4.1. RECUBRIMIENTOS RUGOSOS DE TITANIO**

El titanio es uno de los materiales que se ha estudiado bastante en gran medida por su deposición por CS debido a su potencial en la industria aeronáutica y aeroespacial, así como la protección anódica en ambientes corrosivos, y en los campos de restauración y reparación dimensionales. Estas aplicaciones requieren principalmente la formación de recubrimientos densos. Contrariamente, un recubrimiento de titanio poroso/rugoso es útil para aplicaciones biomédicas.

El uso de partículas gruesas facilita la obtención de recubrimientos porosos en comparación con las partículas finas debido a sus bajas velocidades, y las oquedades entre partículas, una vez éstas se depositan en el sustrato. El uso de partículas grandes implica menores tasas de enfriamiento, así como menores tasas de deformación. Todo esto, y teniendo en cuenta la baja difusividad térmica del titanio que facilita la retención local de calentamiento interfacial, puede favorecer la adherencia entre los puntos de contacto de partículas mediante deformación plástica.

Para la obtención de recubrimientos de titanio rugoso se realizó un diseño de experimentos teniendo como variables la temperatura y la presión (las condiciones de proyección para la obtención de titanio rugoso están bajo la protección de una propiedad intelectual). En todas las condiciones se obtuvieron recubrimientos rugosos de titanio libres de óxidos. Todas las superficies muestran elevados perfiles de rugosidad, siendo los valores mínimos de  $R_a=28\ \mu\text{m}$  y  $R_z=152\ \mu\text{m}$ , y los máximos de  $R_a=41\ \mu\text{m}$  y  $R_z=235\ \mu\text{m}$ . Esta microrugosidad produce un incremento de superficie libre de hasta 2.7 veces en comparación con una superficie de titanio desbastada a #240. El aumento de rugosidad debido a la elevada rugosidad da lugar a una superficie superhidrofílica ( $0^\circ$ ) en comparación a los sustratos de Ti6Al4V con y sin menor rugosidad (granallado), ideal para una fácil deposición celular.

Los recubrimientos de titanio tienen un rango de espesor entre 300-350 $\mu$ m y unas porosidades entre 8-15%. Las muestras proyectadas con condiciones más energéticas muestran menor porosidad y mayores puntos de contacto de las partículas de titanio y viceversa.

Se eligió un recubrimiento óptimo a partir de las propiedades mecánicas. Acorde con las normativas ASTM para prótesis articulares de cadera, rodilla y hombro, se realizaron test de esfuerzo a tracción, cizalla y test de abrasión. El recubrimiento de titanio rugoso óptimo dió unos valores de 40 $\pm$ 5 MPa (test tracción>20MPa), 39 $\pm$ 2MPa (test cizalla>20MPa) y una perdida de massa de 37 $\pm$ 5 mg/100ciclos (test abrasión<65mg/100ciclos), cumpliendo con las normativas. La superficie de fractura de las muestras después del test a tracción y cizalla, muestra principalmente una fractura cohesiva entre partículas. La superficie de desgaste (ensayo de abrasión) revela un desgaste dúctil; las ruedas abrasivas producen rasguños en los picos de rugosidad, promoviendo progresivamente una nivelación de ésta reduciéndola lentamente. La figura 1.4 muestra el recubrimiento óptimo de titanio.

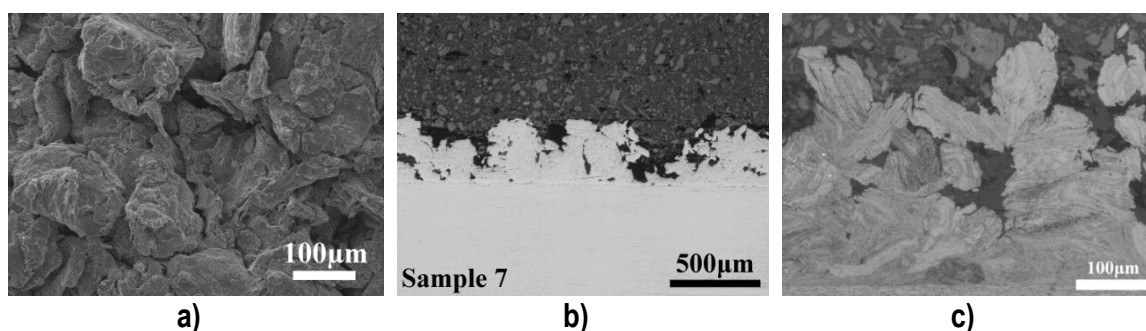


**Figura 1.4.** Micrografías de a) la superficie libre, b) la sección transversal antes y después de ser c) atacada con el reactivo Kroll del recubrimiento óptimo de titanio.

## **4.2. RECUBRIMIENTOS DE NANOTEXTURIZACIÓN**

Esta sección se centra en el desarrollo de tratamientos superficiales nanoestructurados, especialmente el tratamiento de anodización y el tratamiento alcalino sobre el recubrimiento rugoso de titanio (óptimo). La novedad está en la obtención de la nanotexturización sobre la superficie microrugosa del titanio obtenida por CS para comparar la respuesta celular (4.4. *Propiedades biológicas*).

#### 4.2.1. Tratamiento de anodización

La formación controlada de la capa de óxido a través de la anodización permite la formación de una morfología óptima tubular de óxido que contiene las matrices de poros altamente ordenadas. La formación de nanotubos (NTs) representa una combinación única de forma y funcionalidad. La obtención superficial de NTs mejora la biocompatibilidad y bioactividad; y por otra parte, actúa como barrera contra la corrosión del titanio, lo que mejora su resistencia a la corrosión.

En primer lugar, se realizó un primer anodizado para la formación de una capa de óxido densa, para en un segundo lugar, hacer crecer los NT mediante un segundo anodizado. El electrolito seleccionado consiste en un 0,5% en peso de  $\text{NH}_4\text{F}$  y 5% en peso agua MilliQ disuelto en etilenglicol. Para el anodizado fueron aplicadas las siguientes condiciones 40V durante 150s. Ésta capa está compuesta básicamente por subóxidos de  $\text{TiO}$ ,  $\text{Ti}_2\text{O}_3$  y  $\text{TiO}_2$ .

La capa de  $\text{TiO}_2$  NTs se produjo a 30V durante 45min en un electrolito que consiste en un 0,5% en peso de  $\text{NH}_4\text{F}$  y 5% en peso agua MilliQ disuelto en etilenglicol. Estas condiciones dan lugar a una geometría de nanotubular con porosidades entre 50-100nm y una longitud de  $2.4\mu\text{m}$  (Fig. 1.5a). Se observó que, a menor tiempo de anodizado (30min) había cantidad de remanentes en la superficie nanotubular, provenientes de la capa compacta formada durante los primeros segundos del anodizado, mientras que a mayor tiempo (60min), se observa una superficie limpia pero los NTs son atacados químicamente por el propio electrolito. Con las condiciones seleccionadas, no se observa ataque a los NTs, aunque persisten pocas cantidades remanentes de óxido (Fig. 1.5b).

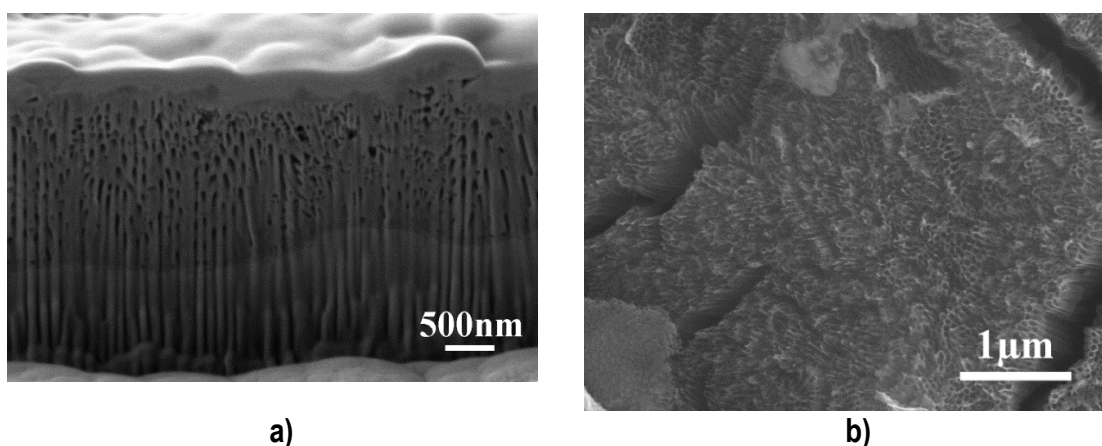


**Figura 1.5.** Micrografías de la a) un corte del recubrimiento y b) superficie libre de la capa de NTs sobre el recubrimiento de titanio rugoso

Una vez obtenida la capa amorfa de TiO<sub>2</sub> NTs, se le realizó un tratamiento térmico a 450°C durante 1h en atmosfera controlada para la obtención de una estructura cristalina, ya que da lugar a una mayor respuesta celular.

La nanotexturización de recubrimientos rugosos de titanio por anodizado, mantuvo de forma muy similar la microrugosidad proveniente del recubrimiento de titanio rugoso, pero además, dio lugar a nanorugosidades de Ra=36.8nm con una superficie superhidrofílica.

#### 4.2.2. Tratamiento alcalino

Este tratamiento es muy popular en el titanio puro para aplicaciones dentales y ortopédicas debido a sus propiedades mecánicas, mayor resistencia a la corrosión y mayor bioactividad debido a la inducción de una capa de apatita en fluido corporal. El tratamiento alcalino de los recubrimientos de titanio fue realizado tras la inmersión de las muestras en una solución durante 3 días a 5M NaOH a 80°C, acto seguido se realizó un tratamiento térmico en atmosfera controlada a 600°C durante 1h, en el cual se obtiene una capa nanoestructurada de titanato de sodio.

Los resultados muestran una nanocapa superhidrofílica (0°) con un tamaño de poro <100nm, un espesor de ~500nm y una nanorugosidad de Ra= 1.2nm (Fig. 1.6a), manteniendo así la microrugosidad proporcionada por la capa de titanio. La figura 1.6b muestra la sección transversal de éste recubrimiento, del cual se observan 4 regiones: región a) recubrimiento titanio rugoso, b) capa de TiO<sub>2</sub> cristalina, c) capa de difusión entre la capa de TiO<sub>2</sub> con la de la capa de la región d) de titanato de sodio.

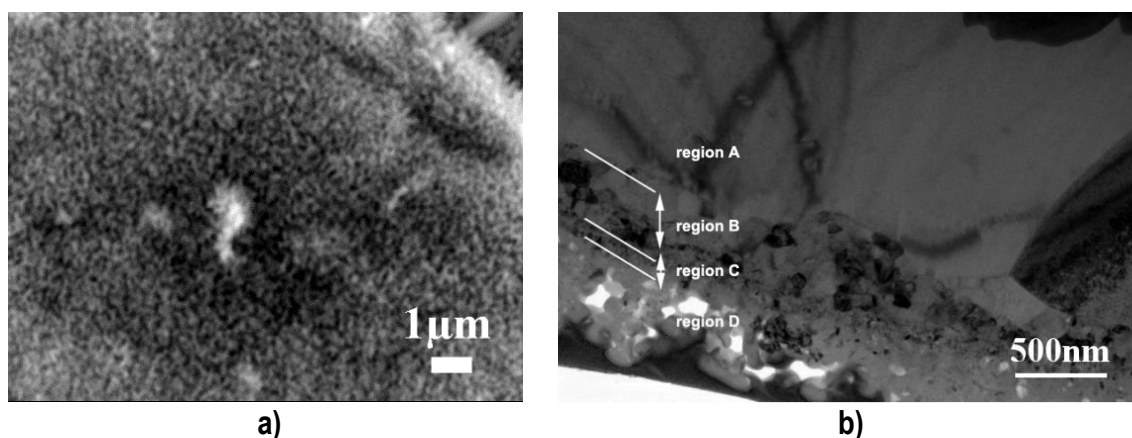


**Figura 1.6.** Micrografías de la a) un corte del recubrimiento y b) superficie libre de la capa de NTs sobre el recubrimiento de titanio rugoso

### **4.3. RECUBRIMIENTOS DE HYDROXYAPATITA**

El uso de recubrimientos biocerámicos, tales como los fosfatos de calcio, y los porosos, tales como el titanio han sido estudiado para el uso de prótesis articulares no cementadas. Los fosfatos de calcio son conocidos por su osteoconductividad. Diversos estudios afirman que la deposición de capas bioactivas, especialmente de HA, mejoran las propiedades osteogénicas y la capacidad para formar enlaces fuertes con el tejido óseo. La bioactividad y la biodegradación de la HA son parámetros críticos para lograr un buen recubrimiento de HA que dependen principalmente de la composición, la fase y la cristalinidad.

Aunque la deposición de materiales cerámicos es todo un reto mediante tecnología CS, sus fenómenos de unión sólidos también se han intentado por técnicas de deposición similares al CS a temperatura ambiente, tales como la deposición por aerosol (AD) y por sistema de nanopartículas (NPDS). Por el momento, se han conseguido depositar materiales cerámicos por CS sobre sustratos con bajo módulo elástico (magnesio y PEEK), el cual la deformación plástica de éste favorece la unión partícula-sustrato.

#### **4.3.1. Condiciones de proyección**

Las condiciones de proyección de la HA se optimizaron mediante un diseño de experimentos de "wipe test", que consiste en un movimiento rápido del sustrato frente a la proyección de la pistola, siendo los principales parámetros: la temperatura, la presión y la distancia de proyección.

Una vez determinadas las condiciones óptimas para la obtención de recubrimientos hidroxiapatita (las condiciones de proyección están bajo protección de una propiedad intelectual). Para ambas HA se consiguió optimizar una capa fina (~30-50µm) sobre el recubrimiento de titanio rugoso de titanio, ya que facilitaba el anclaje de las partículas de HA para la deposición de capa en comparación a una superficie de titanio desbastado o granallado. La figura 1.7 muestra micrografías de la superficie libre y sección transversal de los recubrimientos de HA óptimos por CS.

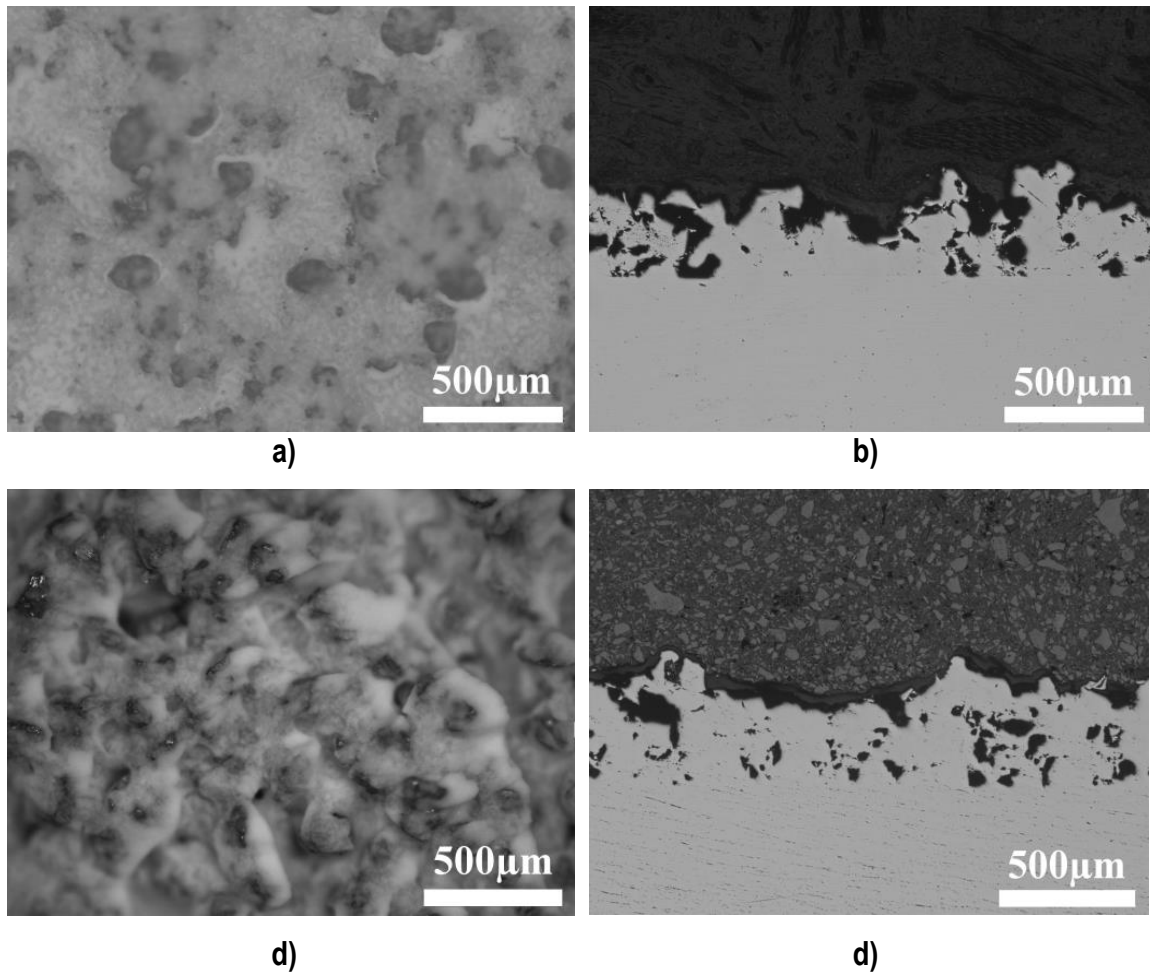
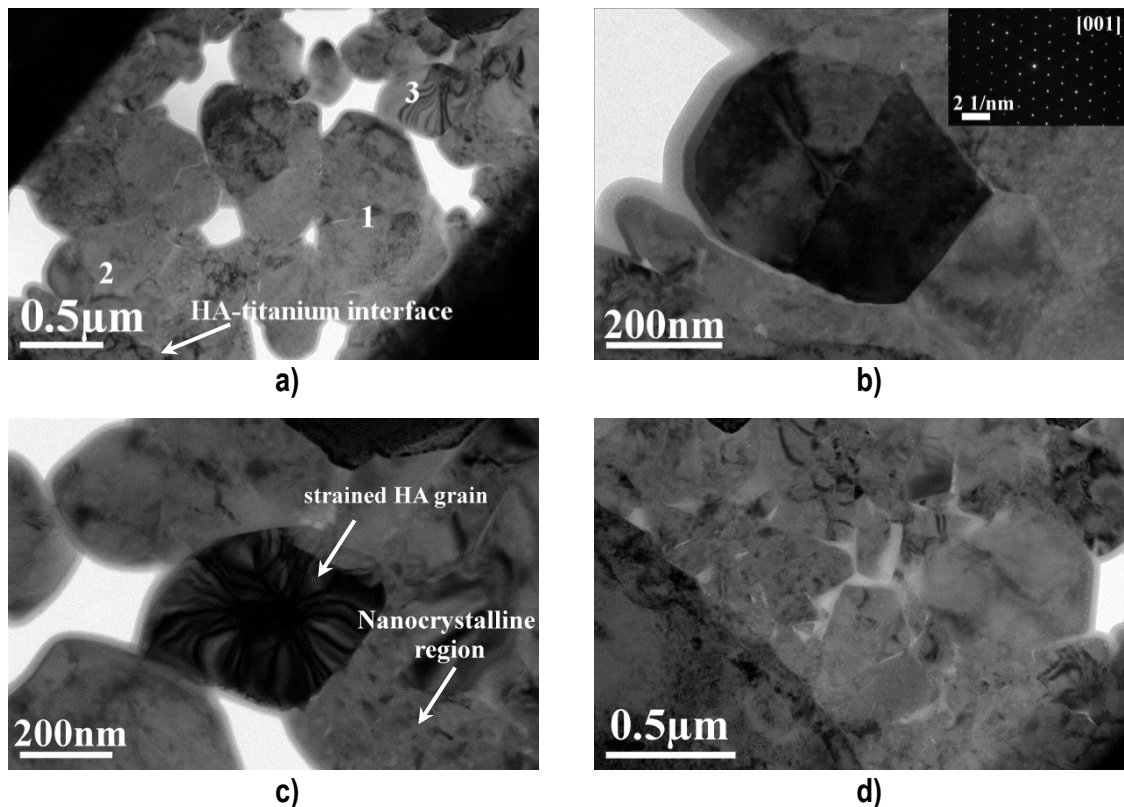


Figura 1.7. Micrografías de la a) superficie libre y b) sección transversal del recubrimiento óptimo de HA aglomerada

#### 4.3.2. Mecanismo de deposición de la hidroxiapatita sinterizada

Para estudiar el mecanismo de deposición de la HA, se analizó mediante microscopía electrónica de transmisión su microestructura una vez adherida la partícula al sustrato (splat).

La microestructura mostró que el mecanismo de deposición ocurrió a través de: (i) el colapso de poros, (ii) fragmentación dinámica por impacto y agrietamiento y (iii) reducción del tamaño de cristal por mecanismos de deformación plástica (Fig. 1.8). Por tal motivo, es imposible obtener espesores más grandes que  $\sim 20\mu\text{m}$  con HA obtenida por sinterización, tanto en sustrato desbastado o granallado con partículas de alúmina. En cambio, el uso de un recubrimiento microrugoso para la deposición de HA sinterizada ayuda a la obtención de un recubrimiento más homogéneo debido a la deposición de HA en los distintos valles de rugosidad de la capa de titanio rugoso.



**Figura 1.8.** Micrografías TEM de la a) parte central del splat de HA sobre Ti6Al4V, b) y c) detalle correspondiente a los puntos 1, 2, and 3 in “a”, d) fragmentación y agrietamiento de las áreas laterales del splat

### 4.3.3. Mecanismo de deposición de la hidroxiapatita aglomerada

El mismo estudio se realizó sobre una splat de HA aglomerada para estudiar el mecanismo de deposición por CS. En general se observan orientaciones al azar de nanocristales a lo largo de la partícula. Se observan claramente franjas de Moirée, donde el solapamiento de cristales parece tomar una importancia significativa. A lo largo de la interfaz entre la partícula y el sustrato, se observa una buena adhesión. Parece ser que el mecanismo de deposición se basa en la compactación de los nanocristales dentro de la partícula durante el impacto, preservando su nanoestructura inicial (Fig. 1.9). Añadir que el incremento de espesor conduce a un incremento de propiedades mecánicas (Scratch test).

Este mecanismo de deposición de HA aglomerada permite da lugar a la obtención de recubrimientos gruesos al igual que el crecimiento de capa. Aun así, para dicho recubrimiento es necesario la activación del sustrato mediante un recubrimiento microrugoso de las características del obtenido con el titanio. Las primeras partículas de HA proyectadas necesitan anclarse en el sustrato para poder compactar y hacer crecer la capa.

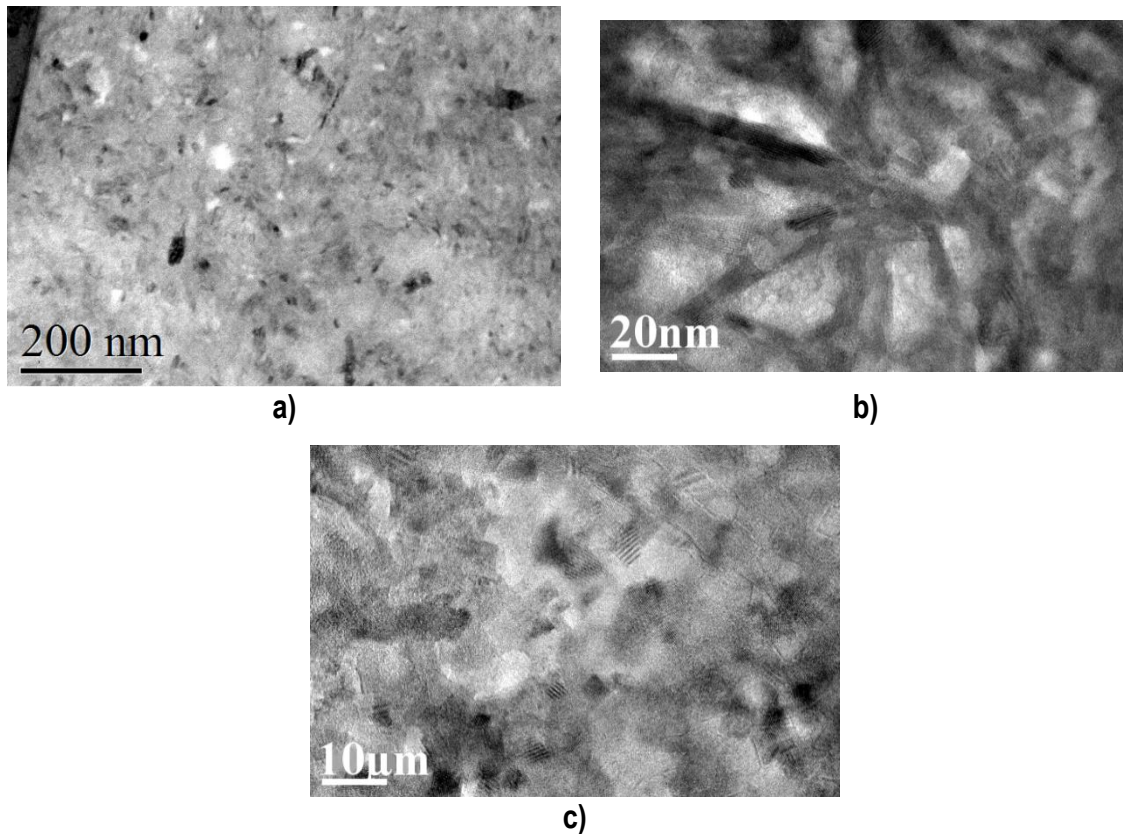


Figura 1.9. a) Micrografía de TEM representativa del splat, b) parte superior y c) parte central de la splat

#### 4.3.4. Aspectos generales

En todos los recubrimientos de HA por CS se mantuvieron las propiedades de los polvos de partida en el recubrimiento. No hay presencia de amorfización ni de fases secundarias en el recubrimiento. La microestructura se conserva a lo largo de la deposición por CS, aun así, por la HA sinterizada, hay una ligera reducción del tamaño de cristal debido al impacto de la propia técnica.

En ambos casos, la deposición de HA sobre los recubrimientos de titanio, hace que disminuya ligeramente la microrugosidad, pero manteniendo el comportamiento superhidrofílico. La nanorugosidad de los recubrimientos óptimos de HA fue calculada, dando lugar a valores bastante similares de de  $R_a = 58.2\text{nm}$  y  $R_a = 39.1\text{nm}$ .

#### 4.4. PROPIEDADES BIOLÓGICAS

Se llevaron a cabo ensayos de viabilidad y proliferación celular a nivel cualitativo (Live/Dead) y cuantitativo (MTS), juntamente con los de diferenciación (ALP) y mineralización celular.

Paralelamente, se realizó un análisis de la morfología celular mediante fijación de las células y observación por FESEM o por tinción del núcleo y los filamentos de actina y observación por confocal.

Hay un total de 4 estudios in vitro comparativos, donde se evalúa:

- El efecto de la rugosidad superficial
- El efecto de la nanorugosidad superficial
- El efecto de la composición superficial.
- El efecto de la técnica de proyección térmica utilizada para la elaboración de recubrimientos de HA.

Hay un quinto punto, dónde se evaluó la posibilidad de probar dinámicamente in-vitro la adhesión celular de los recubrimientos de HA en colaboración con la universidad de Tampere. Una primera aproximación se realizó con los recubrimientos de PS.

- 4.4.5. Test dinámico de adhesión celular

#### **4.4.1. Efecto de la rugosidad superficial**

El estudio se basa en la respuesta celular de una superficie de titanio granallada con alúmina, juntamente con la del titanio rugoso obtenido por CS.

Ambas muestras muestran una buena viabilidad y proliferación celular a lo largo de 14 días de cultivo, siendo la respuesta más significativa para las muestras de mayor rugosidad. A sí mismo, el incremento de rugosidad da considerables diferencias a nivel de diferenciación y mineralización celular, siendo éste último el doble de valor a 28 días de cultivo en las muestras de titanio rugoso. Para ambas muestras, no se observaron diferencias significativas a nivel de morfología celular. Las células muestran una morfología osteoblástica, dónde se observan extensos filamentos de actinas anclados en la rugosidad del material.

#### **4.4.2. Efecto de la nanorugosidad superficial**

Los tratamientos de nanotexturización sobre el titanio: el tratamiento de anodizado y el alcalino, se compararon entre sí juntamente con el recubrimiento rugoso de titanio sin tratar.

La respuesta celular sobre las superficies nanoestructuradas da lugar a un incremento significativo a nivel de viabilidad, proliferación y sobretodo diferenciación celular en comparación con el recubrimiento de titanio rugoso sin tratar. Entre ambas nanotexturaciones se observa una mayor pero no significativa proliferación celular sobre las muestras anodizadas, pero una mayor diferenciación celular en las muestras las cuáles se aplicó el tratamiento alcalino, posiblemente por la baja nanorugosidad que presenta en comparación al anodizado.

#### **4.4.3. Efecto de la composición superficial**

Los recubrimientos óptimos de titanio rugoso se compararon con los óptimos de HA sinterizada y aglomerada, la cual la rugosidad de todas las muestras era bastante similar y solo varía la composición del recubrimiento.

A día 1, las células muestran una morfología osteoblástica y extendida a lo largo de los diferentes picos de rugosidad del titanio (mostrando buena adherencia con el sustrato), por lo contrario, muestran una morfología esférica/nodular en ambos recubrimientos de HA (mostrando mala adherencia con el sustrato). La viabilidad y proliferación celular a día 1 es mucho más elevada para el recubrimiento de titanio que los de HA debido a la adhesión celular. Aun así, a día 7, las células de los recubrimientos de HA pasan a adquirir una forma osteoblástica (mostrando buena adherencia) y a proliferar más rápido que las células depositadas sobre el titanio (más por la HA aglomerada que dispone de una estructura nanocristalina que por la HA sinterizada que muestra una estructura cristalina). A día 14, se continúa observando un incremento de proliferación en los recubrimientos de HA, más por las de la microestructura nanocristalina que cristalina, pudiendo éstos superar los valores del titanio rugoso a mayores días de cultivo.

La HA induce una mayor rapidez en proliferación celular en comparación al titanio una vez las células adquieren la morfología osteoblástica. A nivel microestructural, la proliferación celular aumenta con el decrecimiento de tamaño de grano.

#### **4.4.4. Efecto de la técnica de proyección térmica utilizada para la elaboración de recubrimientos de HA**

En previas investigaciones se tomó optimizado el recubrimiento de HA de investigaciones previas por proyección por plasma (PS).

En este estudio se compararan ambos recubrimientos con los obtenidos por CS con el polvo de HA aglomerado que es el que dio mejores resultados a nivel biológico.

Los resultados in-vitro muestran mayor proliferación con las muestras de mayor porcentaje cristalinidad (CS>PS), al mismo tiempo, los valores de diferenciación celular son más elevados para las muestras cristalinas (HA por CS).

#### **4.4.5. Test dinámico de adhesión celular**

En esta primera aproximación se observó que la técnica de MP-SPR (Multi-Parametric Surface Plasmon Resonance), es una técnica viable para la medida de la adhesión celular en recubrimientos de HA. Los test in vitro dinámicos ofrecen una mayor aproximación in-vivo a tiempo real en comparación con los test in vitro estáticos.

Los resultados muestran una gran adhesión en el recubrimiento de HA por PS, tanto en proteínas como con células, en comparación a un sustrato no recubierto.